



## Non-classical electrostrictive response in bulk ceria: tailoring by microstructure and defect chemistry

Kabir, Ahsanul

*Publication date:*  
2020

*Document Version*  
Publisher's PDF, also known as Version of record

[Link back to DTU Orbit](#)

*Citation (APA):*  
Kabir, A. (2020). *Non-classical electrostrictive response in bulk ceria: tailoring by microstructure and defect chemistry*. Technical University of Denmark.

---

### General rights

Copyright and moral rights for the publications made accessible in the public portal are retained by the authors and/or other copyright owners and it is a condition of accessing publications that users recognise and abide by the legal requirements associated with these rights.

- Users may download and print one copy of any publication from the public portal for the purpose of private study or research.
- You may not further distribute the material or use it for any profit-making activity or commercial gain
- You may freely distribute the URL identifying the publication in the public portal

If you believe that this document breaches copyright please contact us providing details, and we will remove access to the work immediately and investigate your claim.

DTU Energy

Department of Energy Conversion and Storage

---

# Technical University of Denmark



Section for Functional Oxides

---

## Non-classical electrostrictive response in bulk ceria: tailoring by microstructure and defect chemistry

---

### Author

Ahsanul Kabir

### Supervisors

Prof. Vincenzo Esposito

Prof. Jacob R. Bowen

Prof. Ngo Van Nong

Submitted in partial fulfilment of the requirements for the degree of 'Doctor of Philosophy'

# Preface

---

I Ahsanul Kabir, hereby declare that the thesis entitled "Non-classical electrostrictive response in bulk ceria: tailoring by microstructure and defect chemistry" is an independent work and is submitted for the degree in 'Doctor of Philosophy' to the evaluation committee and the PhD school at the Technical University of Denmark (DTU). The work of this thesis is carried out from 15<sup>th</sup> April 2017 to 14<sup>th</sup> April 2020 at the Department of Energy Conversion and Storage at the Technical University of Denmark (DTU) under the direct supervision of Professor Vincenzo Esposito and partial supervision of Professor Ngo van Nong and Professor Jacob Bowen. Some parts of the experiments are performed at the following institutes:

- i. Ceramics Laboratory at the Swiss Federal Institute of Technology Lausanne (EPFL), Switzerland (Professor Paul Muralt).
- ii. Institute of Materials Science (I) at the University of Erlangen (FAU), Germany (PD Dr. Benoit Merle).
- iii. Department of Materials and Interfaces at the Weizmann Institute of Science (WIS), Israel (Maxim Varenik and Professor Igor Lubomirsky)

The research is financially supported by the Danish Council for Independent Research Technology and Production Sciences for the DFF-Research Project 2 (Grant No. 48293) and partially by the BioWings project funded by the European Union's Horizon 2020, Future and Emerging Technologies (FET) program (Grant No. 801267), Otto Mønsted Foundation (Denmark) and Reinholdt W. Jorck og Hustrus Foundation (Denmark).

# Acknowledgments

---

I would like to express my appreciation to principal supervisor Prof. Vincenzo Esposito and co-supervisor Prof. Ngo Van Nong and Prof. Jacob R. Bowen for allowing me to carry out the doctorate thesis at Department of Energy Conversion and Storage (DTU-Energy) at the Technical University of Denmark. Without their supervision, the research work would have been challenging to accomplish. More specifically, Vincenzo was a driving force during the thesis, pushed my research lot further than expectations with his excellent guideline and optimism. He started teaching me from the very first day about the theoretical background of the work and systematically followed the research track. His constant supervision built not only my research vision but also communication and writing skills. I am also grateful to Prof. Paul Muralt (EPFL, Lausanne) and Dr. Benoit Merle (FAU, Erlangen) for accepting me as a guest researcher in their institute. Additionally, I am very much thankful to Maxim Varenik and Prof. Igor Lubomirsky (WIS, Israel) for their continuous collaboration.

During the past three years, I had the pleasure of working closely with excellent colleagues in the department, including Simone, Arindom, Haiwu, and Jin. They helped me a lot to perform the electromechanical experiment and analyzing the data. I am also thankful to Sofie and Rana for their assistance in TEM and EIS experiments, respectively. Additionally, I express special thanks to Prof. Sebastian Molin for the endless discussion about defects chemistry and impedance analysis, constructive criticism, and proofreading for publications. Finally, I also thank all the technicians (especially Ebtisam) in the chemistry lab for their support in helping with the experiments. Last but not least, my parents and my wife (AYESHA) who always showed endless encouragement that inspired me to work further firmer to complete the thesis efficiently.

# Abstract

---

Electromechanically active materials, including piezoelectrics and electrostrictors, have a broad range of actuating and sensing applications from daily-life electronics to biomedical devices. The state-of-the-art ceramic materials of this kind contain the hazardous element, *i.e.*, lead (Pb), whose usage is restricted by the European Union RoHS directive and to be banned in the near future. Thus, it is of utmost interest to seek out substitutive materials with comparable performances. Most recently, a large electromechanical response has been discovered in highly oxygen defective Gd-doped cerium oxides (GDC) thin films. This compound is biocompatible, environment-friendly, economically cheap, and even more abundant in nature than lead. The observed electromechanical strain is in gigantic character, with electrostrictive strain coefficient  $M_{33} \sim 10^{-17}$ - $10^{-18}$  (m/V)<sup>2</sup> several orders of magnitudes higher than the best-performing commercial relaxor electrostrictors. Somewhat surprising, the material develops a compressive strain parallel to the field direction, which is opposite to classical behavior. The atomistic mechanism of such action is understood to be governed by the lability of local atomic bonds, as directed by the presence of oxygen vacancies. This concept is fundamentally unique compared to the existing classical theory of electrostriction. Owing to this peculiar behavior, the electromechanical response in cerium oxide does not obey Newnham's empirical relationship for the classical electrostrictors. Against these backgrounds, ceria based compound can be considered as a new family of next-generation electromechanical material.

Up to the present time, the non-classical electrostriction (ES) for the ceria-based compound is mostly reported in pure ceria and GDC thin films. Experimental outcomes show that electrostriction indeed requires a certain amount of oxygen vacancies. Moreover, the correlation between the electrostriction strain coefficient ( $M_{33}$ ) with oxygen vacancy concentration is found to be very complex. Taking into account that the thin-film is constrained to a substrate, thus subjected to a different level of stress depending on various factors, which

could affect/alter the electrostrictive response of the material. Thin films are tiny by definition (below 1  $\mu\text{m}$ ).

Consequently, their actuation and processing require more complicated, time-intensive, and financially expensive steps than for traditional ceramic processing technology. In this context, it would be rational to investigate ES in force-free conditions, *i.e.*, macroscale bulk materials, and shed some light on the current status of the ES properties in cerium oxides. Anyhow, for technical and industrial-scale applications, ES response ought to be introduced in bulk components. Considering such facts, the thesis is concentrated to achieve several objectives:

- i. To disclose the relationship in the electro-chemo-mechanical coupling, comprising defects chemistry, ionic migration, mechanical properties, and electromechanical strain.
- ii. To figure out the role of the different types of dopants and their associated oxygen vacancy on the ES response.
- iii. Investigate the effect of microstructure on the ES properties.
- iv. To verify whether the frequency-related electrostriction response in Gd-doped ceria represents the entire doped ceria system.

Firstly, the thesis work focuses on investigating the model material  $\text{Ce}_{1-x}\text{Gd}_x\text{O}_{2-\delta}$  (GDC). Among all ceria compounds, GDC is enriched with more literature data, including ionic conductivity, defects association, local crystal structure, mechanical as well as electromechanical properties. To investigate the role of microstructure, high-density bulk Gd-doped ceria (GDC) with a fixed Gd concentration are fabricated by different thermal treatments, including field-assisted spark plasma sintering (SPS), cold sintering process (CSP), fast-firing and conventional sintering. Such methods lead to developing different microstructures from nanocrystalline to microcrystalline grains with tuned oxygen vacancy configurations at the ion-blocking barriers. In common with thin films, the electrostrictive response in GDC bulk illustrates a non-Debye type frequency-dependent strain relaxation. The most striking finding is that electrostriction at low-frequency regime follows neither grain size nor bulk conductivity

dependency. Instead, it shows a strict relation with the oxygen vacancy configuration. Whereas, the high-frequency region is mostly unaffected by any governing factors. To verify such a result, microcrystalline Gd-doped ceria and Sm/Nd co-doped ceria with various dopant concentrations from low-to-high are also explored. Even though it shows a dependency on the nominal vacancy concentration, the configuration effect at the ion-blocking barrier holds a similar conclusion. The material with a high ion-blocking factor presents a large  $M_{33}$  value at the low-frequency regime, whereas the high-frequency, is shown to be almost untunable for these dopants. Interestingly, it is found that the electrode material can also influence electromechanical strain, particularly at the lower applied frequencies.

The frequency-dependent electrostriction relaxation disappears when the dopant is too different than of host  $Ce^{4+}$ . For a divalent dopant such as  $Ca^{2+}$ , a steady electromechanical strain with little fluctuation is noticed up to 1 kHz. No dramatic effect on dopant concentration, configuration, and microstructure is observed. Undersized dopant such as  $Sc^{3+}$  and  $Mg^{2+}$  also demonstrates an analogous response like calcium-doped ceria. Such implications highlight that enhanced dopant-defect interaction in the lattice as induced by the combination of electrostatic and elastic interaction plays an emerging impact on the frequency-controlled strain relaxation mechanism. In addition to that, the mechanical properties, comprising elastic modulus, hardness, creep, are examined by the nanoindentation method at room temperatures. No strong correlation between such properties and the electrostriction coefficient is identified. The choice of dopant, concentration variation, and sintering protocol were selected in such a way that direct comparison between measured and literature available data is possible.

# Scientific Approach

---

Electrostriction in defective cerium oxide is a room temperature effect that develops due to the rearrangement of Ce- $V_{\text{O}}^{\bullet\bullet}$  pairs under an external electric field. Emphasize the fact that this mechanism requires no oxygen vacancy migration rather an oscillation. The oxygen vacancies reside in both free and isolated forms (ordered clusters) in the crystal lattice, and a complex arrangement at the crystallographic defects structures. In practice, the configuration of the oxygen vacancies can be analyzed by various methods, including transmission electron microscopy (TEM), X-ray absorption spectroscopy (XAS), X-Ray photoelectron spectroscopy (XPS), X-ray diffraction (XRD), complex electrochemical impedance spectroscopy (EIS), *etc.* Moreover, an unambiguous characterization of oxygen defects and their association is still under debate.

Some technique provides too local information (TEM) and does not have enough resolution (XRD). Others operate in reducing conditions or under vacuum (XAS, XPS, and TEM). The high-energy XAS experiment is costly, and data extraction is complicated, requiring multi-step calculation and modeling. Thus, the estimation of the oxygen vacancy configuration in these methods is not rational.

On the other side, EIS is a powerful tool that can qualitatively analyze the local status of the oxygen vacancies. This technique allows separating the dielectric and resistive properties of the material from low to high temperatures. As dielectric properties in ceria do not change much with concentration/processing routes, an attempt is made to interlink resistive part to the electrostriction coefficient. As a descriptor of the configuration of the oxygen vacancy ( $V_{\text{O}}^{\bullet\bullet}$ /Ce- $V_{\text{O}}^{\bullet\bullet}$ ), a macroscopic parameter ( $\alpha_{\text{gb}}$ ) defined by EIS is employed. However, due to instrumental limitation and very large room-temperature resistivity of ceria,  $\alpha_{\text{gb}}$  is considered at a temperature of 300 °C and correlates with the  $M_{33}$ , measured at room temperatures.

# Thesis Outline

---

The thesis is structured in five chapters, which follow:

- i.** Chapter 1 describes the underlying theory of classical electromechanical effect followed by the atomistic concept of non-classical electrostriction mechanism in ceria. The fundamental properties such as defects chemistry, ionic migration mechanism, solid-state mass-diffusion, and mechanical properties are also outlined.
- ii.** Chapter 2 briefly explains the synthesis and fabrication method of bulk ceramics for doped ceria. The physical characterization techniques, such as x-ray diffraction method (XRD), electron microscope (EM), as well as electrochemical, electromechanical, and mechanical characterization method, is described. Besides, the description of the process and measurement parameters are highlighted.
- iii.** Chapter 3 provides a comprehensive analysis of the role of microstructure and ion-blocking effect on the ES properties of bulk GDC. The impact of the electrode material is also summarized.
- iv.** Chapter 4 demonstrates the role of dopant types, associating with their strength of lattice dopant-defect interaction on tuning ES response.
- v.** Chapter 5 presents a summary of the thesis and points out a few open suggestions for future work.

# Table of Content

---

Chapter 1: Introduction .....	1
1.1 Electromechanical Effect .....	1
1.1.1 Piezoelectric Effect .....	2
1.1.2 Electrostrictive Effect .....	3
1.2 Electrostriction in Cerium Oxides .....	6
1.3 Defect Chemistry of Ceria .....	9
1.4 Ionic migration in Cerium Oxides .....	12
1.5 Ion-blocking Effect in Cerium Oxides .....	15
1.6 Sintering and Solid-state Mass Diffusion (Endogenic of the Ion-blocking Factor) ...	20
1.7 Mechanical Properties of Ceria .....	23
Chapter 2: Experimental Procedure .....	29
2.1 Selection of Materials .....	29
2.2 Powder Synthesis .....	29
2.3 Pellet Fabrication .....	32
2.3.1 Free Sintering .....	32
2.3.2 Field-assisted Spark Plasma Sintering (SPS) .....	33
2.3.3 Cold Sintering Process (CSP) .....	35
2.4 Physical Characterization .....	36
2.4.1 Density Measurement .....	36
2.4.2 X-Ray Diffraction (XRD) .....	36
2.4.3 Scanning Electron Microscopy (SEM) .....	38
2.4.4 Transmission Electron Microscopy (TEM) .....	40
2.5 Electrochemical Characterization .....	41
2.6 Mechanical Characterization (Nanoindentation) .....	45
2.7 Electromechanical Characterization .....	47

Chapter 3: The Role of Microstructure and Ion-blocking Factors on Electrostriction .....	52
3.1 Motivation.....	52
3.2 Effect of Microstructure on 10 mol% Gd-doped Ceria.....	52
3.2.1 Structural and Microstructural Design by Sintering Methods.....	54
3.2.2 Electro-chemo-mechanical Characterization .....	56
3.3 Grain Boundary Engineering by Fast Diffusion/Cold Sintering.....	64
3.3.1 Structural and Microstructural Analysis by Designed Grain Boundary .....	65
3.3.2 Electro-chemo-mechanical Characterization .....	67
3.4 Tuning the Ion-blocking Factor by Gd Concentration.....	73
3.4.1 Structural and Microstructural Characterization of Various Doped GDC .....	73
3.4.2 Electro-chemo-mechanical Characterization .....	75
3.5 Concluding Remarks .....	79
Chapter 4: Tuning of Ion-blocking Barriers via Various Dopant.....	83
4.1 Motivation.....	83
4.2 Effect of Sintering on the Ion-blocking Barriers for CDC .....	85
4.2.1 Structural and Microstructural Design by Sintering Methods.....	86
4.2.2 Electro-chemo-mechanical Characterization .....	88
4.3 Effect of Ca Concentration on the Ion-blocking Barriers for CDC.....	92
4.3.1 Structural and Microstructural Characterization of Various Doped CDC.....	93
4.3.2 Electro-chemo-mechanical Characterization of Various Doped CDC .....	94
4.4 The Effect of Enhanced Dopant-Defect Interaction.....	100
4.4.1 Structural and Microstructural Characterization .....	101
4.4.2 Electro-chemo-mechanical Characterization .....	102
4.5 Effect of Co-doping Strategy .....	106
4.5.1 Structural and Microstructural Characterization .....	107
4.5.2 Electro-chemo-mechanical Characterization .....	109
4.6 Concluding Remarks .....	112
Chapter 5: Summary and Future Work .....	116

5.1	Summary.....	116
5.2	Future Outlook .....	119
5.2.1	Single Crystal.....	119
5.2.2	Computational Modelling.....	120
5.2.3	Alternative Defective Oxides .....	120
5.2.4	Sintering and Characterization .....	121
5.2.5	Effect of Electrode.....	122
5.2.6	High-frequency Characterization .....	122
	Appendices .....	123
	List of Figures.....	125
	List of Tables.....	133



# Chapter 1: Introduction

---

In the following chapter, the mechanism and application of classical electromechanical materials are briefly underlined. Besides, the status of the non-classical electrostrictive response in cerium-based compounds is systematically explained, emphasizing its physical origin and limitation. The defects chemistry of ceria and the role of oxygen defects on intrinsic properties such as ionic conduction, mass-diffusion, and creep deformation are also elucidated.

Few sections of the introduction were published in a chapter named "mass diffusion phenomena in cerium oxides", [Ahsanul Kabir](#), Haiwu Zhang, and Vincenzo Esposito. Metal-oxide book series (Elsevier): Cerium Oxide (CeO<sub>2</sub>): Synthesis, Properties, and Applications, Eds: Salvatore Scire and Leonardo Palmisano.

## 1.1 Electromechanical Effect

Simply stated, the interaction between an external electrical field and a rigid body results in a mechanical deformation known as the electromechanical effect. The interaction may be time-dependent or -independent [1]. The electromechanically active materials, *i.e.*, both artificial and natural materials, have been widely used for a variety of technological applications, ranging from artificial muscles to mechanical actuators and sonars [2][3]. These kinds of materials can be divided into two categories as (i) organic (polymers) and (ii) inorganic (ceramics). Electroactive polymers (EAPs) can generate large electromechanical strain that is 1-2 orders of magnitude higher than electroactive ceramics (EACs) [4]. However, the former possess a lower power efficiency (actuation force) than the latter due to a very low elastic modulus (< 1 GPa). Thus for industrial applications, electroactive ceramics have taken

significant attention over recent years. **Table 1.1** briefly summarized the electromechanical properties of these two types of material [4][5].

**Table 1.1:** A general comparison of electromechanical properties between polymers and ceramics.

Electromechanical Property	Polymers	Ceramics
Strain	> 10%	0.1-0.3%
Force (MPa)	0.1-3	30-40
Reaction speed	$\mu$ sec-min	$\mu$ sec-sec
Drive voltage	$\sim$ 100 MV/m	$\sim$ 0.1-5 MV/m
Power consumption	m-Watts	Watts

Based on the fundamental mechanism, the electromechanical effect is divided mainly into two classes, such as piezoelectric and electrostrictive.

### 1.1.1 Piezoelectric Effect

In solid-state theory, piezoelectricity is a primary electromechanical effect resulting from a linear coupling between the mechanical and electrical force on a crystalline material [6][7]. The name piezo is derived from the Greek word 'piezien' means pressure, reflecting the generation of an electric field under applied mechanical load. This effect is nevertheless reversible: materials indeed develop mechanical strain under an electric field. The first effect is called the direct piezoelectric effect, while the second one is termed as converse piezoelectricity. Various types of materials exhibit piezoelectric properties, including polymers, ceramics, biological materials such as bone and wood. They have a wide range of technical applications, for instance, electromechanical transducers, ultrasonic generators, radiofrequency filters, sensors, microbalances, mechanical watches, etc. [7][8]. The atomistic origin of the piezoelectric effect is based on the asymmetric charge distribution of different ions constituting the material, requiring a material to have electric dipoles. Such dipole is naturally present in many materials or manually induced by external stimuli. Thus, materials with no center of symmetry mostly display piezoelectricity [9]. Due to the pure lattice effect of ionic displacement, the piezoelectric response can stay steady up to GHz ranges of applied field frequency. The piezoelectric coefficient ( $d_{ijk}$ ) is a third-ranked tensor, expressed as:

$$x_{ij} = d_{ijk}E_k \quad (1.1)$$

Where  $x$  and  $E$  are the component of mechanical strain and applied electric field, respectively.

### 1.1.2 Electrostrictive Effect

Electrostriction is the basis of the second-order electromechanical coupling shown in all-dielectric materials irrespective of crystal symmetry, which means strain develops at twice the frequency of the applied electric field [10][11]. Despite quadratic, this effect is usually weaker than of piezoelectric. For example, a typical piezoelectric and electrostrictive displacement is in the order of  $\sim 10^{-9}$  m and  $\sim 10^{-12}$  m, respectively, if a 1 mm thick sample experiences an external voltage of 1 kV [12]. However, the latter offers other noteworthy advantages over the former, including low hysteresis, no walk-off strain, small creep, and aging effects [10][13]. Electrostrictive materials operate at a relatively lower electric field with high reproducibility. They have a wide range of sensing and actuating applications such as consumer electronics, ultrasonic transducers, tunable capacitors, micro-pumps, sonar, *etc.* [10][12][14]. The fundamental mechanism of this effect is explained in a schematic diagram in **Fig. 1.1**.

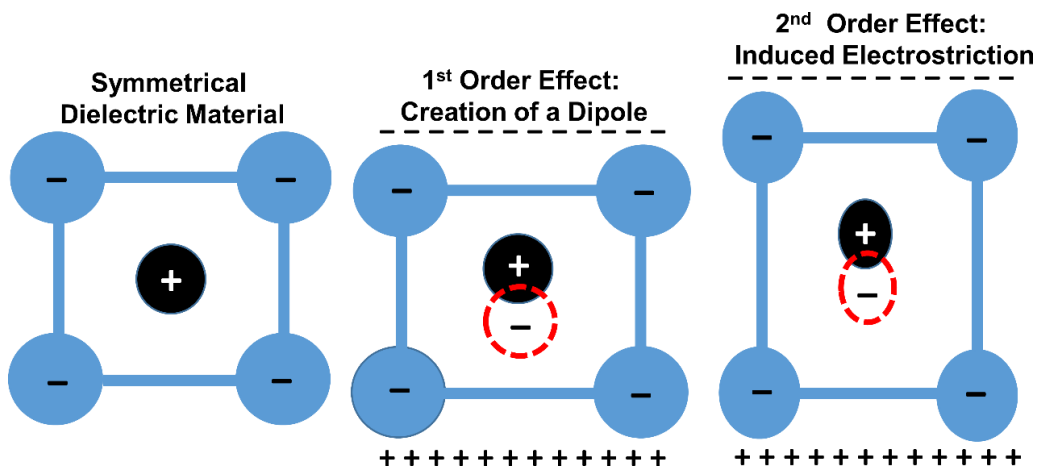


**Figure 1.1:** Schematic illustration of the atomistic mechanism of classical electrostriction in insulators. The image is adapted from Ref. [15].

As can be seen from **Fig. 1.1**, under an external electric field ( $E$ ), a dielectric material creates a dipole moment due to the attraction of opposite charges. This field converts into a mechanical strain ( $S$ ) on a planar charge distribution ( $\sigma$ ). Hence, it can be written that:

$$S = \frac{\sigma E}{Y} \quad (1.2)$$

Where  $Y$  is the elastic modulus. Assuming no quasi-permanent charges, the charge density ( $\sigma$ ) on the electrode is developed, resulting from the applied voltage where,  $\sigma = \epsilon_0 \epsilon E$ . **Eqn 1.2** then becomes:

$$S = \epsilon_0 \epsilon \frac{E^2}{Y} \quad (1.3)$$

**Eqn 1.3** clearly states that the electric field is required twice for the development of electrostriction [16]. The first step leads to induce polarization (non-centrosymmetry) and to maintain voltage conditions on the electrode. In the second step, the material expands parallel to the field direction. In summary, the quadratic effect is obtained through the cooperative combination of two direct outcomes: formation of the electric dipole and induced piezoelectric effect [16]. Changing the sign of voltage would create a reversed dipole moment. Nevertheless, an identical strain will be generated. Characteristically, inorganic electrostrictive ceramics elongate parallel to field direction, but polymers, *e.g.*, PVDF, extends perpendicularly [13]. Moreover, the phenomenological description of the electrostrictive effect is expressed in the following equation [17][18]:

$$x_{ij} = Q_{ijmn} P_m P_n = M_{ijmn} E_m E_n \quad (1.4)$$

Where  $x_{ij}$  is the electromechanical strain tensor at constant stress and temperature.  $Q_{ijmn}$  and  $M_{ijmn}$  are the fourth-ranked polarization- and electric-field related- electrostriction coefficient, respectively. These coefficients are identical in linear dielectric materials. Remarkably, electrostriction is not often quadratic with the electric field, especially for ferroelectrics or other high permittivity materials [10]. Therefore, Newnham *et al.* formalized the effect using polarization related electrostriction coefficient ( $Q_{ijmn}$ ) that shows a better representation of quadratic nature for electrostriction [10][19]. The  $Q_{ijmn}$  ranges from  $\sim 10^{-3} \text{ m}^4/\text{C}^2$  in relaxor ferroelectrics to  $\sim 10^3 \text{ m}^4/\text{C}^2$  for polymeric materials. Moreover,  $M_{ijmn}$  varies oppositely from  $\sim 10^{-24} (\text{m}/\text{V})^2$  in polymers to  $\sim 10^{-16} (\text{m}/\text{V})^2$  in relaxor ceramics, for example, lead magnesium niobate (PMN) [10]. Furthermore, to compare electrostrictive materials with different crystallographic symmetry, a universal hydrostatic electrostriction polarization coefficient ( $Q_h$ ) has been defined and commonly used. For a cubic or isotropic material,  $Q_h$  is written as:

$$Q_h = Q_{xxxx} + 2Q_{xyyy} \quad (1.5)$$

Where  $Q_{xxxx}$  and  $Q_{xyyy}$  are the longitudinal and transverse polarization coefficient, respectively. As mentioned above, an external field relocates the cation and anion in a lattice in the opposite direction. Such a small displacement ( $\Delta r$ ) is the driving force for the electrical polarization, dielectric constant ( $\epsilon$ ), and electrostrictive strain. To a first approximation, this relationship can be expressed as:

$$Q_h = \frac{x}{p^2} \sim \frac{\Delta r}{(\Delta r)^2} = \frac{1}{\Delta r} = \frac{1}{\Delta r} \sim \frac{1}{\epsilon_0 \epsilon} \quad (1.6)$$

In reality, linear dielectric materials with high compliances and small permittivity do not follow this trend. In another term, electrostrictive strain acts against the elastic forces within the material and is proportional to the ratio of dielectric change ( $\Delta\beta$ ) and stress ( $X$ ), which follows:

$$Q_h \sim \frac{\Delta\beta}{(X)} \sim \frac{x}{\left(\frac{x}{S}\right)} \sim S \quad (1.7)$$

From **Eqn 1.6** and **1.7**, it can be seen that  $Q_h$  is proportional to  $\sim \frac{1}{\epsilon_0 \epsilon} S$ . The value of  $Q_h$  for different electrostrictive materials as a function of the ratio of ( $S/\epsilon$ ) is plotted in **Fig. 1.2**. As observed,  $Q_h$  shows a linear relation with ( $S/\epsilon$ ) on a log scale and empirically it follows [20]:

$$|Q_h| \approx 2.37 \cdot (S/\epsilon\epsilon_0)^{0.59} \quad (1.8)$$

In summary, the combined effect of dielectric and elastic properties predicts the electrostrictive behavior in all insulators.

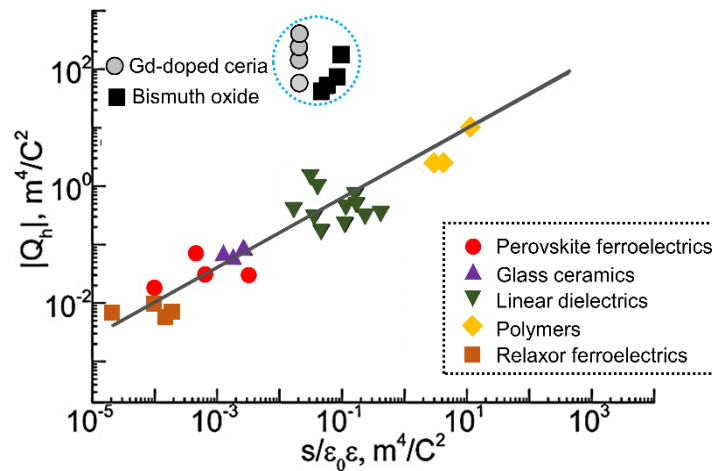


**Figure 1.2:** The empirical correlation between hydrostatic electrostriction polarization coefficient ( $Q_h$ ) and the ratio of elastic compliance and dielectric constant. The image is adapted from Ref. [10] with permission from John Wiley & Sons.

## 1.2 Electrostriction in Cerium Oxides

Recently, it has been demonstrated that thin films of oxygen defective cerium oxides exhibit giant electromechanical response at room temperatures [21]. Despite being ceramics, ceria thin films in (111) orientation display an in-plane expansion perpendicular to applied field direction, with high compressive stress ( $\sim 500$  MPa). The electrostriction strain coefficient ( $M_e$ ) is reported to be  $6.47 \cdot 10^{-18} \text{ (m/V)}^2$  at 0.1 Hz for 20 mol% Gd-doped ceria (GDC),  $[V_O] = 5\%$  [21]. Such a value is significantly large for a material with low dielectric constant ( $\epsilon_r^{\text{GDC}} \approx 30$ ) [22], even higher compared to relaxor ceramics, e.g., Ca-doped PMN (Pb, Mg)NbO<sub>3</sub> ( $\epsilon_r^{\text{Ca-PMN}} \approx 4000$ ) [10]. The estimated  $Q_h$  value is about  $\sim 100 \text{ m}^4/\text{C}^2$  that is at least two orders of magnitude higher than **Eqn 1.8** prediction (see **Fig. 1.2**), particularly not complying with the classical trend. Such a result strongly suggests that a fundamentally different atomistic mechanism than of classical electrostriction (cooperative ionic displacement) is functioning this property.

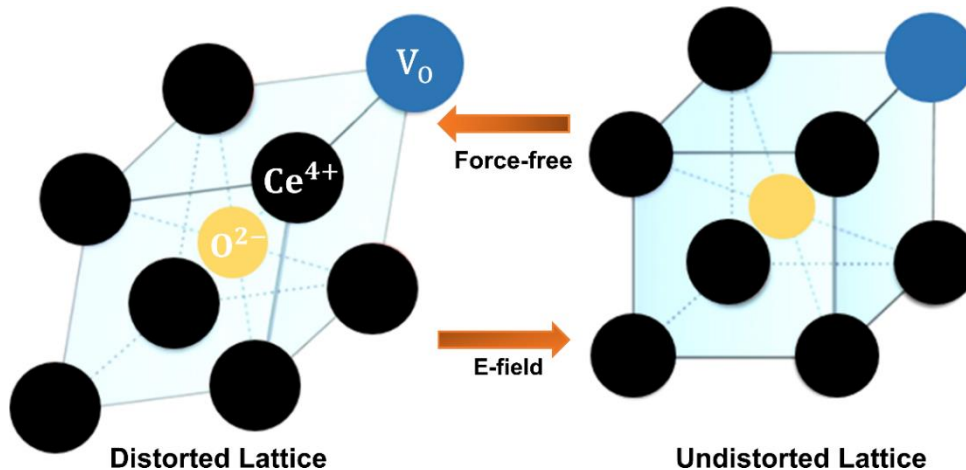


**Figure 1.3:** Schematic illustration of the atomistic mechanism of electrostriction in oxygen defective ceria. The image is adapted from Ref. [23] with permission from AIP publishing.

Based on X-ray absorption spectroscopy (XAS) measurements coupled with theoretical modeling Lubomirsky *et al.* explained that electrostriction in ceria (10 mol% Gd-doped ceria) is associated with the formation of electroactive elastic dipoles  $\text{Ce}_{\text{Ce}}-\text{V}_O$  [21][23]. The oxygen vacancy in the ceria lattice ( $\text{V}_O$ ) increases the  $\text{Ce}_{\text{Ce}}-\text{V}_O$  bond length due to columbic repulsion, resulting in reduced six anomalous  $\text{Ce}_{\text{Ce}}-\text{O}_O$  bonds, in comparison to the bond length of the undistorted fluorite structure. Accordingly, a distorted lattice complex ( $\text{Ce}_{\text{Ce}}-\text{7O}_O-\text{V}_O$ ) is formed,

with a uniaxial symmetrical dipole. Under an external electric field, each  $\text{Ce}_{\text{Ce}}-\text{V}_{\text{O}}^{\ddot{}}$  bond in the distorted lattice complex increases its bond length ( $\approx 4.6\%$ ) towards a bond of undistorted  $\text{Ce}_{\text{Ce}}-\text{V}_{\text{O}}^{\ddot{}}$  complex (see **Fig. 1.3**), inducing a local strain. These bonds consist of ca. 3.4% of the total  $\text{Ce}_{\text{Ce}}-\text{O}_{\text{O}}$  bond in the lattice. Thus, the development of the total macroscopic strain is the spatial average of the sparsely distributed local strain ( $10^{-3}$ - $10^{-4}$ ) [23]. The exclusion of the electrical field regenerates the distorted lattice environment. Unexpectedly, the oxygen vacancy next to Gd ion does not respond to the electric field [23]. Conclusively, oxygen defective ceria can be considered as the latest member of the high-performance electromechanically active materials. To verify the model experimentally, the electromechanical response was monitored as a function of time under a combined AC and DC voltage [21]. The results showed that the amplitude of the mechanical stress increases from  $\sim 5$  MPa to  $\sim 20$  MPa till 18 hours and then starts to saturate. In contrast to ferroelectricity, reversing the DC voltage polarity does not affect the response. However, the feedback vanishes by heating the sample at elevated temperature, e.g., 150-200 °C, and recovers it again at room temperature by applying voltage [21]. From this perspective, one may conclude that poling results in the rearrangement of distorted lattice to back towards more fluorite symmetry. In another experiment, Hadad *et al.* verified the electromechanical response in thin films of 20 mol% Gd-doped ceria [24]. This work claimed that additional oxygen vacancies than dopant-compensated are essential to enhance the electrostrictive performance. The reported electrostriction strain coefficient ( $M_e$ ) is  $\sim 0.9 \cdot 10^{-18} (\text{m/V})^2$  at 66 Hz which tends to decrease at higher frequencies. These authors emphasized that the electrostriction response depends on processing parameters, microstructures, as well as operating electrodes. Undoped oxygen defective ceria thin films *i.e.* reduced by chemical effect also generate electrostriction. But the effect is minimized when thin film is oxidized and the (intrinsic) oxygen vacancies come to be annihilated. Such a finding strongly supports the microscopic model that oxygen vacancy is a prerequisite for the development of electrostriction in ceria. However, the oxygen vacancies do not necessarily scale up the magnitude of electrostriction in Gd-doped ceria thin films, rather show a complex trend (see **Fig.1.4**).

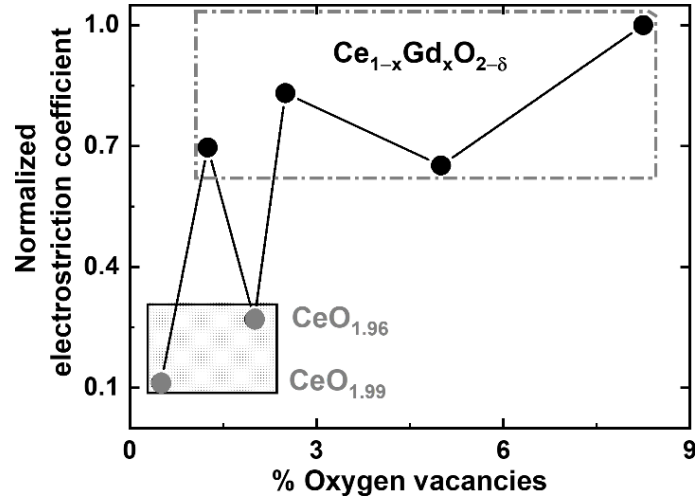


**Figure 1.4:** The normalized electrostrictive coefficient (stress) as a function of the fraction of oxygen vacancies in the thin films of undoped and Gd-doped ceria. The value at 33 mol% Gd-doped ceria is taken as 100%. The data is obtained from Ref. [23][25] with permission from AIP publishing, and John Wiley & Sons.

For the case of bulk ceria ceramics, one can logically expect that the response would be significantly low due to the lack of preferred orientation and the presence of grain boundaries. The grain boundary is the primary source of potential drop resulting from the space charge layer that also distributes potential non-uniformly [26][27]. Residual porosity, impurity segregation, nanodomains are another source of reduction of voltage in the samples. Remarkably, literature reports demonstrated that the bulk form of GDC and another defective fluorite ( $\text{Bi}_2\text{O}_{3-\delta}$ ) show an electromechanical response, even with a larger magnitude  $\sim 10^{-16}$ - $10^{-17} \text{ (m/V)}^2$  [28][29]. However, similar fluorite structured 8 mol% yttria-stabilized zirconia (single crystal) exhibits considerably lower  $M_{33}$  of  $\sim 10^{-21} \text{ (m/V)}^2$ . In  $\text{Bi}_2\text{O}_{3-\delta}$ , the value of  $M_{33}$  was found to increase monotonically with nominal oxygen vacancy concentration [28]. Moreover, electrostriction in GDC was reported only for 10 mol% Gd content and surprisingly, the electrostriction strain efficient  $M_{33}$  did not correlate either with grain size or sample thickness [29]. The GDC samples display a large electrostrictive coefficient ( $M_{33}$ ) between  $2 \cdot 10^{-17} \text{ (m/V)}^2$  at lower applied frequency regime that tends to relax (non-Debye type) with increasing frequencies, follow as [29]:

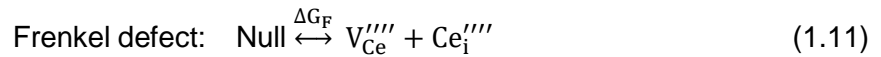
$$M_{33}(f) = \frac{M_{33}^0}{\sqrt{1+(\tau f)^{2+\alpha}}} + M_{33}^\infty \quad (1.9)$$

Where  $M_{33}^0$  and  $M_{33}^\infty$  are the electrostriction coefficient at lower and higher frequencies, respectively.  $\tau$  is the relaxation time, and  $\alpha$  is denoted as a non-ideality factor. The time-delaying response in a time-varying electric field supports the atomistic origin of the hypothesis that field-assisted bond reorientation is driven by the vacancy [24]. Yavo *et al.* suggested that scattered  $M_{33}$  below the relaxation time derives from the electronically conductive grain boundaries that could trap charges under electric-field [29]. Whatever the reason is, such a time-delaying response would probably limit the high frequency (MHz-GHz) technical application of Gd-doped ceria. Finally, not even any rough relationship between oxygen vacancy concentrations, types of dopant, microstructures, processing protocols on the electrostriction properties of bulk ceria ceramics was made up until now. Therefore, the current work aims to build a fundamental relationship between electrostriction and these factors on the bulk ceria component. Apart from this, an effort will be given to design a strategy to maximize and steady electrostriction at least up to the kHz level. As already mentioned that electrostriction is mastered by the presence of oxygen vacancy in the lattice, thus in the following sections, a brief explanation will be addressed in what way oxygen vacancies are presented in dense bulk ceramics and how these defects can tune other functionality, for example, ionic conductivity, creep, *etc.* and how can it be related to electrostriction.

### 1.3 Defect Chemistry of Ceria

Intending to understand the mechanism of electrostriction and other properties in ceria, its defects chemistry needs to be outlined. Ceria has a stable cubic fluorite structure (space group Fm-3m) from room temperature up to the melting point. Purely stoichiometric ceria (undoped CeO<sub>2</sub>) consists of equivalent point charges of opposite sign, *i.e.*, cation (Ce<sup>4+</sup>) and anion (O<sup>2-</sup>). At low temperatures, regular sites of these ions are fully occupied, whereas interstitial sites are empty. However, small energy fluctuations between two sublattices of regular and interstitial sites of identical ion can create partial occupation. The ion can dislocate from its natural position and reside in an interstitial site. Successively, it will lead to form a self-interstitial vacancy pair, a defect named Frenkel defect. Alternatively, both ions can leave their lattice

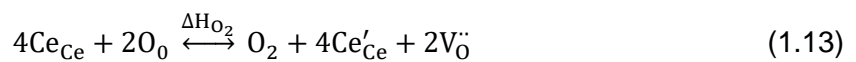
sites by creating identical vacancies. This type of defect is called a Schottky defect. The formation of these two types of intrinsic defect is a thermally activated process in which the degree of defect formation is increased with temperature [30]. In the ionic balance, the sum of the defects must be electroneutral. The following equation expresses the equilibrium of intrinsic defect formation in Kröger-Vink notation:



Defects can also be generated extrinsically when ceria is doped with aliovalent cations such as  $\text{Gd}^{3+}$ . The following defect equation then follows:



For the charge neutrality,  $[\text{M}'_{\text{Ce}}] = 2[V_{\text{O}}'']$ , showing that an increase of dopant concentration linearly maximizes the oxygen vacancy content. The **Eqn 1.12** is valid for all trivalent dopants. Thus, dopant with different chemical identity ( $\text{Gd}^{3+} \rightarrow \text{Sm}^{3+}$ ) will not change neutrality equilibrium [31]. Alternatively, similar defects can be introduced by a direct chemical reaction with the atmosphere, e.g., by chemical reduction at low  $p\text{O}_2$  or/and in the presence of reducing species such as  $\text{H}_2$  and  $\text{CO}$  at a moderate temperature around 600-800 °C. Defect equation then becomes:



The formation of different types of defects in ceria is schematically illustrated in **Fig. 1.5**. As shown in section 1.2, that high electrostriction is observed at a relatively higher doping concentration. Therefore, the current study will focus exclusively on the dopant compensated extrinsic defects. The oxygen vacancies tend to interact with cations due to a strong columbic interaction, resulting in defect association as well as defect clusters [33]. Such an effect is pronounced at relatively high defect concentrations. As a result, vacancies turn out to be isolated, and their true (free) concentration is drastically reduced. The possible defect equations for the formation of defect association follows:

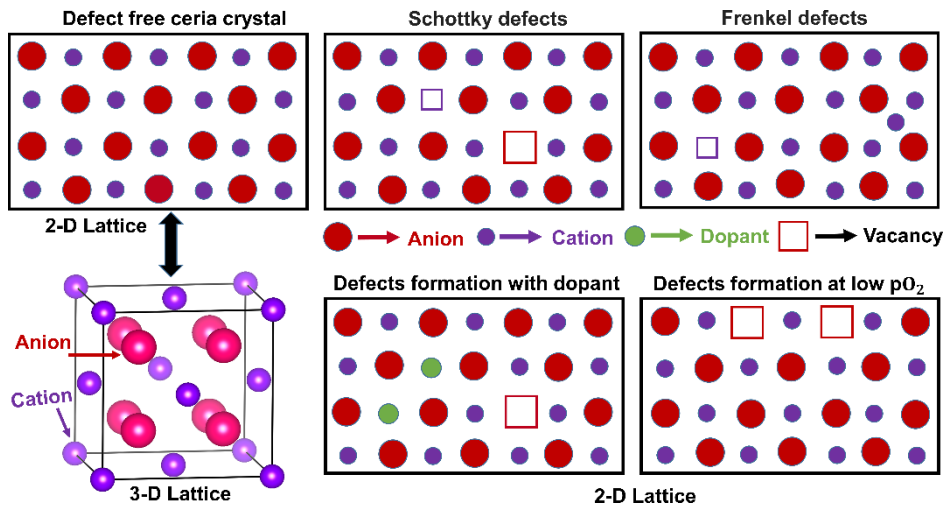
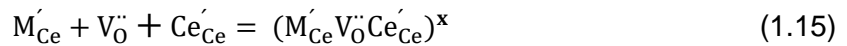


**Figure 1.5:** Schematic illustration of the type of defects formation in cerium oxides. The image is adapted from Ref. [32] with permission from Elsevier.

**Fig. 1.6a** schematically demonstrates the formation of defect association. Strictly speaking, the defect association is mainly dependent on two factors, namely: (i) dopant charge and (ii) dopant ionic radius. As illustrated in **Fig. 1.6b**, the binding energy of dopant-defect interaction differs significantly when these two aspects are too different than  $\text{Ce}^{4+}$ . Small binding energy favors the affinity of dopant towards oxygen vacancies, *i.e.*, more attraction interaction. As observed, the divalent dopant has lower binding energy than of trivalent dopant due to the higher effective charge. Additionally, a significant difference between cation size mismatch also decreases the binding energy. Thermodynamically, for a large ionic radius dopant ( $\text{La}^{2+}$ ), the extra lattice strain energy is reduced through forming an association. On the other hand, for a small cation size ( $\text{Sc}^{3+}$ ), the dopant relaxes towards the oxygen vacancy, increasing the stability of the association [34]. Considering these mismatch effects,  $\text{Gd}^{3+}$  holds maximum binding energy as it has a similar ionic radius of the host  $\text{Ce}^{4+}$ . From this plot, one can postulate that the configuration of oxygen vacancy in the ceria lattice is strongly related to the dopant. To correlate the role of oxygen vacancy configuration in electrostriction response, dopant with various types and/or different concentrations is used in this study.

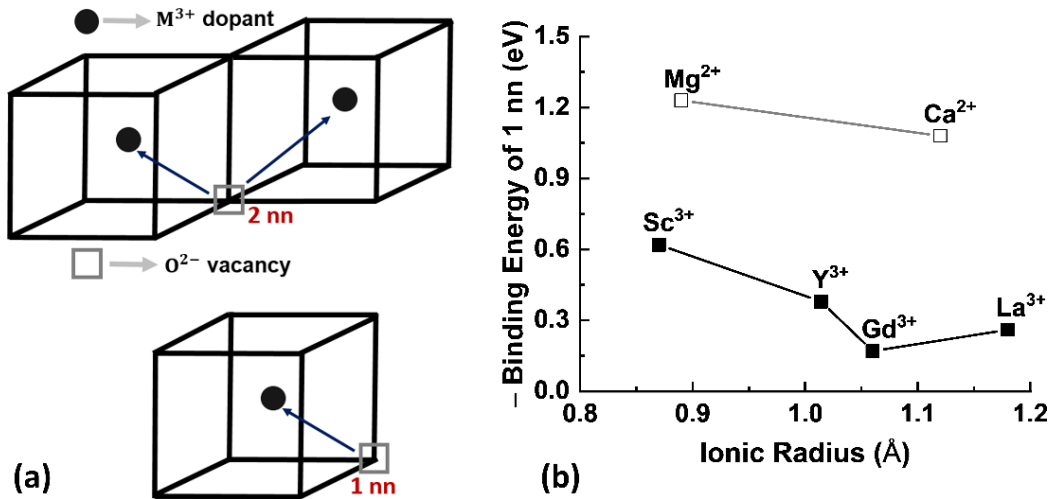


**Figure 1.6:** (a) Schematic illustration of the formation of typical defect association where an oxygen vacancy sits with one/two nearest neighbors substitutional cation ( $M^{3+}$ ). (b) The experimental binding energy of dopant-vacancy association as a function of ionic radius. The data is taken from Butler *et al.* [34] with permission from Elsevier.

#### 1.4 Ionic migration in Cerium Oxides

Doped ceria is an excellent ionic conductor and applied as an electrolyte material for intermediate-temperature solid oxide fuel cells (IT-SOFCs) over the years [31]. Ionic conductivity is a measure of migration of an ion from one lattice site to another under an external electric field [35]. In the case of cerium oxides, the ionic migration/hopping mechanism is driven through point defects, *i.e.*, mainly oxygen vacancies ( $V_O$ ) [36]. The  $V_O$  in ceria typically do not move at low temperatures, require sufficient thermal energy for migration. Point to note that electrostriction occurs at room temperatures but an extremely high electric field  $\sim 3$ -10 kV/cm. The electric field might lead to generating some heat by Joule heating and probably result in ion migration. Hence, the electromechanical response in ceria might encounter competition from the ionic conduction. Above all, by measuring the ionic conductivity (AC) the local environment of oxygen vacancies inside a material can be predicted. It is then so important to understand which factors controlling its ionic conductivity. The mathematical relation of ionic conductivity ( $\sigma$ ) is expressed below:

$$\sigma = nq\mu \quad (1.16)$$

Here,  $n$  is the number of mobile charge carriers,  $q$  the elementary charge, and  $\mu$  the charge mobility. Consider a crystal in a given volume with  $N$  equivalent sites per unit volume. The occupied and unoccupied lattice site fraction is termed as  $c$  and  $(1-c)$ , respectively. For the conduction, the charge must move from one lattice site to another. For doing so, the charge must overcome the energy barrier ( $\Delta G_m$ ). According to Einstein formula, the mobility of charge ( $\mu$ ) is related to the ionic self-diffusion coefficient ( $D$ ), expressed as:

$$\mu = \frac{qD}{kT} \quad (1.17)$$

Where  $k$  is the Boltzmann constant and  $T$  the absolute temperature in kelvin. In the view of random walk theory in a three-dimensional lattice, the self-diffusion coefficient is written as:

$$D = \frac{z}{6} f(1-c) a_0^2 v_0 \exp \left\{ -\frac{\Delta G_m}{kT} \right\} \quad (1.18)$$

$$D = \frac{z}{6} f(1-c) a_0^2 v_0 \exp \left\{ -\frac{\Delta H_m - T\Delta S_m}{kT} \right\} \quad (1.19)$$

Where  $z$  is the number of equivalents near neighbor sites,  $f$  the correlation factor,  $a_0$  the distance between equivalent sites,  $v_0$  is characteristic lattice frequency,  $\Delta H_m$  the migration enthalpy, and  $\Delta S_m$  the migration entropy. **Eqn 1.17** can be written as:

$$\mu = \frac{q}{kT} \gamma(1-c) a_0^2 v_0 \exp \left\{ -\frac{\Delta H_m}{kT} \right\} \quad (1.20)$$

Where  $\gamma = \frac{z}{6} f \exp \left\{ \frac{\Delta S_m}{kT} \right\}$ .

After putting the value of mobility ( $\mu$ ) in **Eqn 1.16** and rewritten as:

$$\sigma = Nc q \frac{q}{kT} \gamma(1-c) a_0^2 v_0 \exp \left\{ -\frac{\Delta H_m}{kT} \right\} \quad (1.21)$$

$$\sigma = N[V_0^{\bullet\bullet}] \frac{q^2}{kT} \gamma(1-[V_0^{\bullet\bullet}]) a_0^2 v_0 \exp \left\{ -\frac{\Delta H_m}{kT} \right\} \quad (1.22)$$

$$\sigma = \frac{\sigma_0}{T} \exp \left\{ -\frac{E_a}{kT} \right\} \quad (1.23)$$

Where  $\sigma_0 = N[V_0^{\bullet\bullet}] \frac{q^2}{k} \gamma(1-[V_0^{\bullet\bullet}]) a_0^2 v_0$ , the pre-exponent constant and  $E_a$  is the activation energy/enthalpy. The **Eqn 1.23** is commonly known Arrhenius equation, which highlights that the conductivity value can be maximized by increasing the pre-exponent factor or/and decreasing the activation enthalpy value [37]. However, the concentration-dependent pre-exponent constant ( $\sigma_0 \propto V_0^{\bullet\bullet}$ ) does not follow a linear relation at high dopant concentration, as

thermodynamically favored defect interaction occurs between the dopant and oxygen vacancies, forming associates (pairs, dimers, clusters, *etc.*) [38]. Thus, the activation energy ( $E_a$ ) includes not only the thermal migration energy but also the extra contribution arisen from defect association energy (see **Fig. 1.7**). At a given temperature, the equilibrium concentration of mobile and bound oxygen vacancies then depend on the magnitude of  $\Delta H_{\text{asso}}$ . For this defect association, the ionic conductivity does not increase monotonically with nominal oxygen vacancy concentration as it should be, instead shows bell-shaped relation, *i.e.*, a maximum at a doping level of around 15-20 mol% [38]. Moreover, experimentally it has been observed that activation energy shows a minimum with increasing dopant concentration [39]. Faber *et al.* claimed that this minimum is weakly connected to the maximum in conductivity owing to the concentration dependence of the pre-exponent factor [40]. Considering an interaction radius ( $r_c$ ), these authors described that the minimum activation energy is attributed to the changes in the energy of oxygen sites nearby cation. With increasing dopant concentration, the overlapping of the spheres of the dopant would form interconnected pathways with a lowered energy barrier, resulting in a reduction of activation energy [31][40]. Hence, it can be concluded that at low doping concentration, *i.e.*, 0-20%, conductivity is controlled by dopant concentration. Conversely, at higher doping (20-30%), conductivity value is dominated by the activation energy value. Activation energy term also depends on the ionic size of the dopant, generally showing a minimum value when the dopant and host cation are similar in size so that elastic strain is minimized [40]. The dopant-defect associates are more prominent at low temperatures and start to dissociate at elevated temperatures typically above 400 °C [41]. Owing to the fact of defect association, it is highly probable that high dopant concentration would not lead any positive impact on electrostriction somewhat might decrease it. Accordingly, most of the experiment in this study is carried out in a dopant concentration ranging from 1-20 mol%.

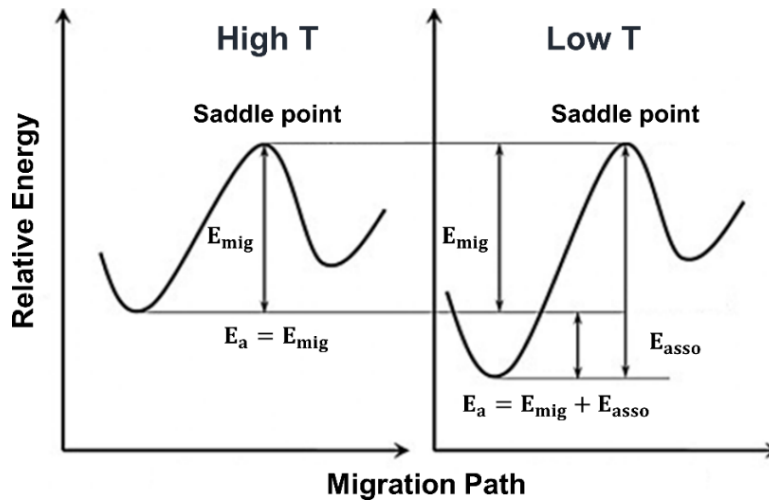


**Figure 1.7:** Schematic illustration of the activation energy-dependent ionic migration in ceria at high and low temperatures. Here,  $E_{\text{mig}}$  and  $E_{\text{asso}}$  represents the activation energy of ion migration and dopant-defect association, respectively. The image is adapted from Ref. [42] with permission from Elsevier.

### 1.5 Ion-blocking Effect in Cerium Oxides

In the interest of reaching thermodynamic equilibrium, a crystal never has perfect lattice arrangement, showing crystallographic defects, *e.g.*, dislocations and grain boundaries. Other process-related defects include pore, voids, cracks, inclusion, *etc.* are also pretty much inevitable in bulk ceramics. For oxide materials such as ceria, these defects areas usually have nonstoichiometry. The oxygen vacancies reside not freely in this structure but various specific configurations. Recalling that such effects on the electrostriction properties of ceria were not even highlighted yet. Hence, the present work seeks an attempt to correlate these effects. In general, oxygen vacancies are sluggish in these particular features, generally act as barriers to ionic migration [43]. The below paragraphs explain the configuration of oxygen vacancies on the major ion-blocking mechanism.

In a polycrystalline system, the interfacial region between two distinct grains is called grain boundary [44]. It is a structural discontinuity of a crystalline structure that has a reduced average coordination number of the atoms and modified bond lengths compared to the lattice [45]. Due to these variations, the grain boundary is not electronically neutral and has excess free energy leading to introduce an obstacle to the grain-to-grain ionic migration [46]. As grain boundary has a different misorientation, therefore the charge transport properties within the

grain boundaries would be highly anisotropic. This effect is expected to become more dominant when the density of grain boundary is significant, *i.e.*, in nanostructured materials [47]. In general, the resistivity of the grain boundary is around two-seven orders of magnitude larger than the bulk, depending on certain conditions, such as dopant concentration, microstructure, applied temperature and oxygen partial pressure [27]. The presence of an impurity, for example, the intergranular siliceous phase, is defined as the most common blocking mechanism denoted by the grain boundaries [48][49]. Such aspects block the conduction pathway of charge carriers as well as the current line. However, it has become apparent that even high purity materials do exhibit significantly larger resistivity, understanding that grain-to-grain contact creates indeed an "intrinsic" blocking effect [46][50]. In a solid-state ionic conductor, a grain boundary consists of a grain boundary core and two neighboring space charge layers (SCLs) [51][52]. The width of the SCL ( $\lambda^*$ ) is associated with Debye length ( $\lambda$ ).

$$\delta_{g.b.} = 2\lambda^* + \delta_{g.b.}^{core} \quad (1.24)$$

Under equilibrium conditions, the grain boundary core is enriched with specific charge carriers of a particular polarity. However, for the sake of following coulomb's law, *i.e.*, preserving charge neutrality, opposite charge carriers are encountered in the space charge layers [21].

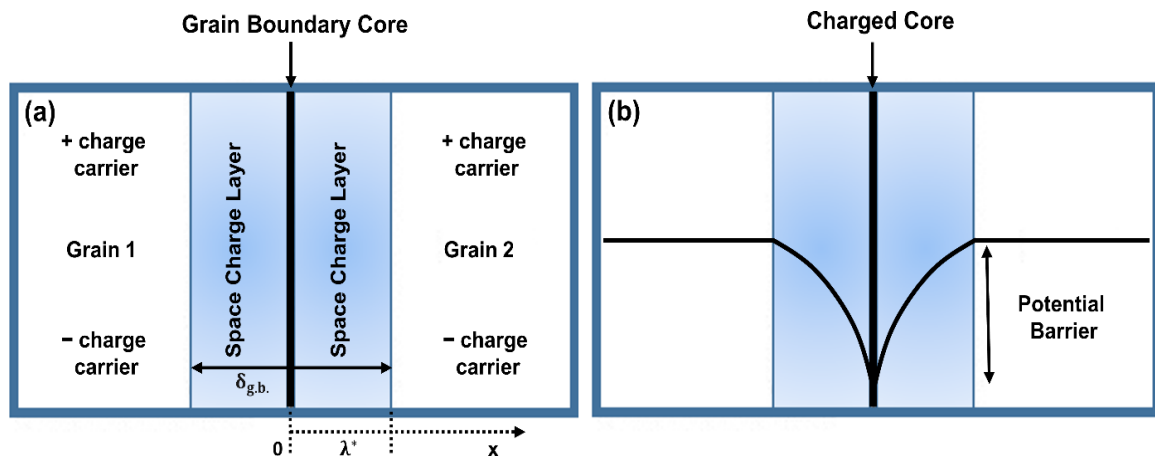


**Figure 1.8:** (a) Schematic diagram of an electrical grain boundary, consisting of grain boundary core and adjacent space charge layer. (b) The configuration profile of charge carriers, *i.e.*, oxygen vacancies in the grain boundaries. The image is adapted from Ref. [26] with permission from Elsevier.

Experimentally, it has been observed that an excessive amount of oxygen vacancies ( $V_O^{\bullet\bullet}$ ) and/or acceptor dopants are enriched at the grain boundary core for doped ceria and zirconia

ceramics [26][52]. However, Guo *et al.* have claimed that the dopant segregation is not adequate to balance the charge of the oxygen vacancy segregation, ultimately resulting in a positively charged grain boundary core [26]. Furthermore, this will lead to a depletion of  $V_{\text{O}}^{\bullet\bullet}$  in the adjacent SCL [21][26]. As  $V_{\text{O}}^{\bullet\bullet}$  is the main charge carrier in an ionic conductor, the depletion of  $V_{\text{O}}^{\bullet\bullet}$  in the SCL is the decisive factor causing the ion-blocking effect in an electrical grain boundary. Besides, numerous experimental studies demonstrate that the accumulation of dopant (effective negative charge) is more pronounced in the space charge region [26], indicating a partial compensation of the positive charge of the grain boundary core. The distribution of oxygen vacancies in an electrically structured grain boundary is schematically represented in **Fig. 1.8**. Mathematically the profile is governed by Poisson equation and is written as follows:

$$\frac{C_j(x)}{C_j(\infty)} = \exp\left(-\frac{ze\Delta\varphi(x)}{kT}\right) \quad (1.25)$$

Where  $C_j(x)$  and  $C_j(\infty)$  are the defect concentration at location  $x$  (see **Fig. 1.8**) and bulk, respectively.  $\Delta\varphi(x)$  is the potential barrier, and  $e$ ,  $z$ ,  $k$ , and  $T$  have their common meaning. It is worth mentioning that due to charged-core and depletion of  $V_{\text{O}}^{\bullet\bullet}$  the dopant-defect association is negligible in the space charge region. In general, the charge density at the SCL is directed by the effective charge of the dopant, showing a deviation with respect to bulk concentration [26]. The height of the potential barrier (Schottky barrier) is related to the conductivity of both bulk and grain boundary and is expressed in the following equation:

$$\frac{\sigma_{\text{g.b.}}}{\sigma_{\text{bulk}}} \cong \frac{4e\Delta\varphi(0)/kT}{\exp(2e\Delta\varphi(0)/kT)} \quad (1.26)$$

Where  $\Delta\varphi(0) = \varphi(0) - \varphi(\infty)$  is the potential barrier at the grain boundary core regarding the bulk. The **Eqn 1.26** assumed a Mott-Schottky approximation in which dopant is constant from bulk to the grain boundary core [53]. For the details analysis, see sections 3 and 4 in Ref. [26].

The thickness of the space charge ( $\lambda^*$ ) and Debye length ( $\lambda$ ) follows:

$$\lambda^* = \lambda \sqrt{\frac{4e}{kT}} \Delta\varphi(0) \quad (1.27)$$

$$\lambda = \sqrt{\frac{kT\epsilon}{4e^2C_{\infty}}} \quad (1.28)$$

According to **Eqn 1.27**, SCL is proportional to Debye length, so does inversely related to dopant concentration. Consequently, the ion-blocking effect generated from the grain boundaries would reduce as the dopant concentration increases, considering the core is dopant insensitive in doped ceria [54].

Another ion-blocking feature is the formation of nanodomains in doped ceria. Experimentally it has been observed that aggregation and segregation of dopant-defect association with a more highly ordered structure leads to form nanodomains and thus decreases free oxygen vacancy concentration [55]. Merely saying, nanodomain is dopant and oxygen vacancy enriched structures. The computational simulation results further confirm this outcome for bulk grain, illustrating the formation of an ordered dumbbell structure [56]. This kind of arrangement is considered as a seed for nanodomain formation as well as phase transformation (F- to C-type structure) [56][57]. Nanodomain results in lattice distortion/reorientation in the ceria lattice (**Fig. 1.9**) and is characteristically guided by dislocations [58].

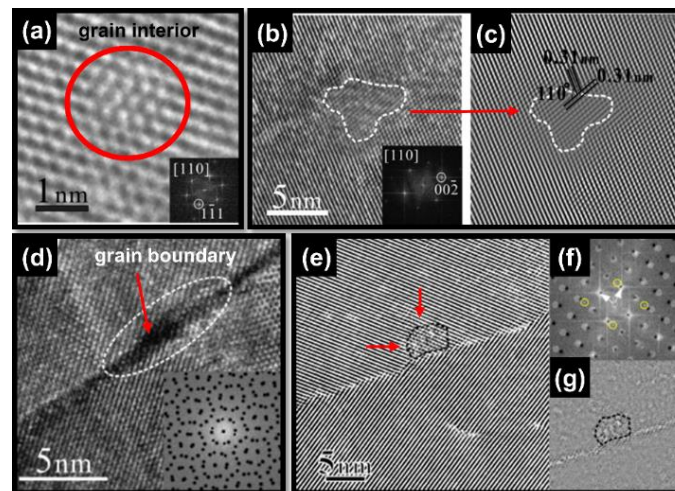


**Figure 1.9:** Evidence of nanodomain in defective cerium oxides. (a)-(c) Nanodomain formation in grain interior leads to lattice distortion and reorganization, (d)-(g) Nanodomain in the grain boundary. SAED pattern illustrates an additional curve diffuse scattering. The image is taken from Ref. [55] with permission from Elsevier.

Recent investigations also illustrate the presence of ordered nanodomains in the grain boundary zone [56]. The extent of nanodomain increases sharply with dopant concentration and can be characterized by HR-TEM image, diffuse scattering and/or extra spots in SAED

patterns. For example, the average volume ratio of domains measured by Mori *et al.* is approximately ~10.6% and ~19.1% for 10 and 20 mol% Gd-doped ceria, respectively [56].

Most of the experiments to investigate the ion-blocking effect were performed on a dense sample and ignored the effect of residual porosity. Typically, the presence of pore increases and decreases the effective length and area of the sample, respectively. Thus the brick layer model, as well as the conductivity equation needs to consider the factor of porosity ( $f_{por}$ ) [59].

An experimental study by Perez-Coll *et al.* shows that the ion-blocking effect is less sensitive for porosity between 5-8%. In contrast, the grain boundary conductance value decreased dramatically when the porosity is above 10% [59]. A preliminary study of electrostriction measurement on a porous Ca-doped ceria bulk sample illustrates a reduced coefficient at a higher applied voltage (see **Fig. 1.10**). Such a result is not reliable because high porosity does cause internal charging, and it is hard to say what the distribution of the voltage in the samples is. Because of this outcome, a highly dense sample was considered for all experiments.

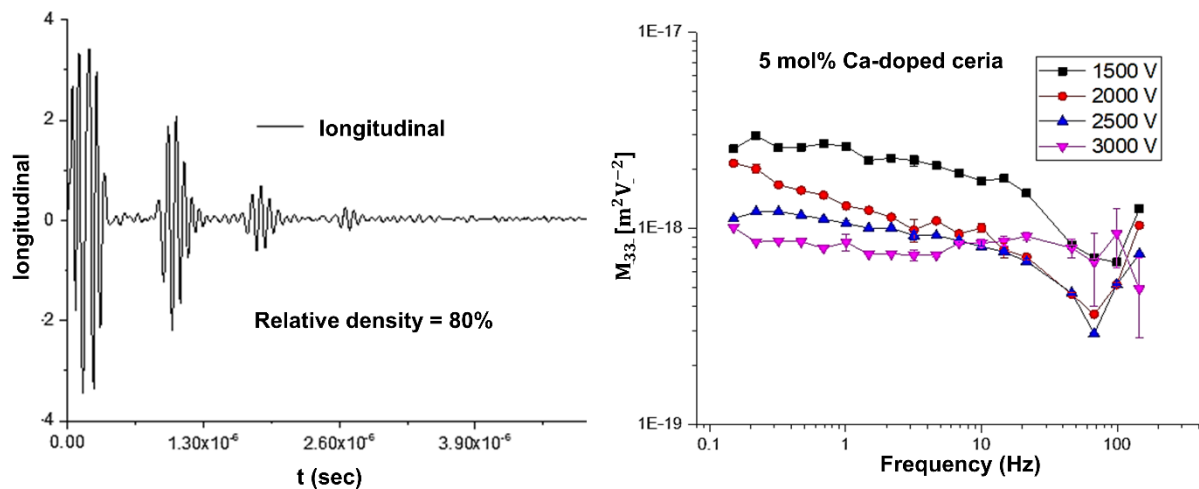


**Figure 1.10:** A preliminary study of electromechanical behavior (right) of a partially dense 5 mol% Ca-doped ceria ceramics, sintered at 1450 °C for 10 hours. The ultrasound bouncing (left) is very low compared to highly dense samples (15-20 bounces), indicating the presence of porosity.

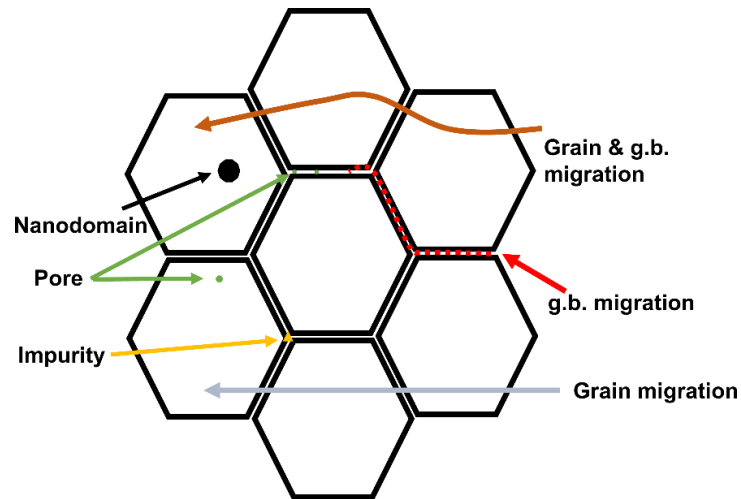


**Figure 1.11:** Schematic diagram of the ion-migration and ion-blocking effect in doped ceria. The image is adapted from Ref. [60] with permission from Elsevier.

Though not investigated for all mechanisms on the electrostriction, this preliminary analysis implies that other ion-blocking features might introduce a negative effect. The ion-migration and ion-blocking effects are schematically illustrated in **Fig. 1.11**.

## 1.6 Sintering and Solid-state Mass Diffusion (Endogenic of the Ion-blocking Factor)

There is an orthodox understanding that large grain size, *i.e.*, less grain boundary area, decreases the blocking effect for ionic solids, and many experiments indeed affirmed it [61]. However, a study on 20 mol% Sm-doped ceria/Gd-doped ceria shows the opposite behavior, *i.e.*, a sample of smaller grain size illustrates lower blocking effect than of larger grain size [62]. Hence, it can be emphasized that the ion-blocking effect is not necessarily a mere geometrical factor of microstructure. As reported, it depends on the nature of the blocking barrier electrical properties that are attributed to the thermal history of the materials [62][63]. The configuration of oxygen vacancies can be manipulated during the mass-diffusion process in sintering together with the sintering atmosphere (air/reducing). Sintering is one of a materials processing technique that consolidates a compact green body employing thermal energy with/without the assistance of external factors such as additives, pressure, electric-field, plasma, *etc.* [64][65]. The mass transport occurs due to the concentration and pressure gradient resulting from the difference of radius of curvature of the particles [66]. Thermodynamically, the driving force for

sintering is the reduction of the surface energy associated with compact particles [67]. The trajectory of the atomic migration follows two competitive paths, such as densification and grain growth, since various diffusion mechanisms are activated concerning temperature [62]. **Fig. 1.12** schematically explains different atomic migration pathways in sintering and as well as their dominance concerning temperature. The surface diffusion and lattice diffusion from the surface to the neck favors grain coarsening. In contrast, densification is dominated by grain boundary diffusion, lattice diffusion from the grain boundary, and viscous flow [68]. The atomic migration is a thermally activated process, and the solid-state mass diffusion equation for a polycrystalline ceramics follows an Arrhenius-type relationship:

$$D_i = D_0 \exp[-\Sigma Q_i/RT] \quad (1.29)$$

where  $\Sigma Q_i$  is the sum of the activation energies for the diffusive atoms, mainly including surface-, grain boundary-, and lattice- diffusion.  $D$  is the diffusion coefficient,  $R$  the universal gas constant, and  $T$  the absolute temperature. As different element participates in the diffusion process, the  $D_i$  also relies on self-diffusion and mass concentration. The activation energy of the diffusion is lower in crystalline defects than bulk lattice following  $D_l > D_{gb} > D_s$ .

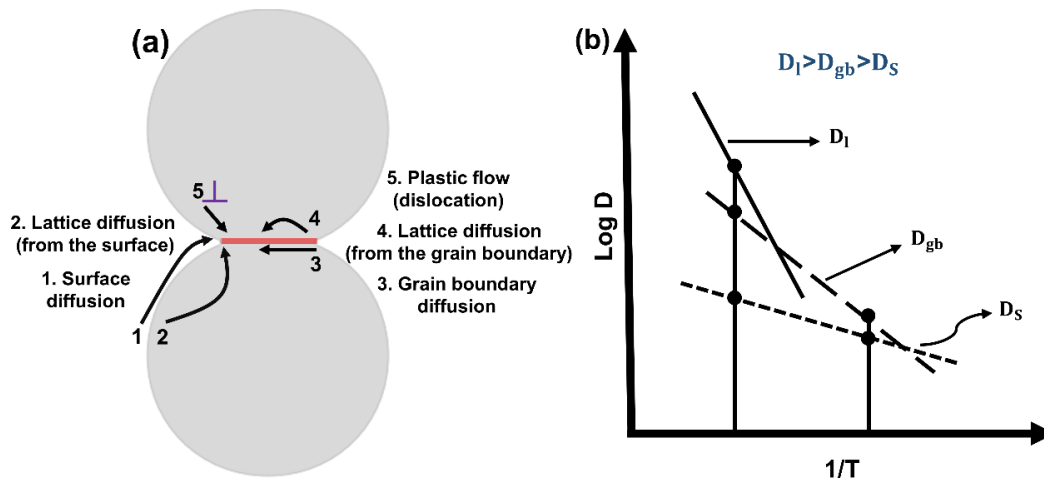


**Figure 1.12:** Schematic illustration of the (a) mass transport mechanism during sintering, (b) dependence of diffusion mechanism as a function of sintering temperature, adapted from Ref. [62][69] with permission from Elsevier.

As notably mentioned in section 1.3 that ceria is an ion-conducting ceramics, which contains not only  $Ce^{4+}$  and  $O^{2-}$  but also dopant ( $M^{2+/3+}$ ) and associated oxygen vacancies  $V_O^{\bullet}$ . In general,

the velocity of the anion is faster than cation in ceria, *e.g.*, at  $\sim 1000$  °C in air, the estimated diffusion coefficient is around  $D_{\text{O}} \sim 10^{-6} - 10^{-7} \text{ cm}^2\text{s}^{-1}$  and  $D_{\text{Ce}} \sim 10^{-13} \text{ cm}^2\text{s}^{-1}$  [70]. In the highly-doped system, Dopant migration is further slowed down if the cation size/charge mismatch becomes too dissimilar than host  $\text{Ce}^{4+}$ . In the diffusional process, ion moves across the grain boundaries, *i.e.*, from higher curvature towards the lower. Due to slow cation movement, interaction potential is generated between the boundary and solute, leading to exert a drag force on the boundary. Such a mechanism is called solute drag that causes solute segregation at the grain boundary [71][72]. The rate-limiting step in the diffusion mechanism is thus solute diffusion at the grain boundary [73]. The solute drag effect is more pronounced at a high dopant concentration. The grain boundary mobility ( $M_b$ ) is expressed as:

$$M_b = \frac{D_{\text{solute}}\Omega}{2\delta kT (C_{\text{solute}} e^{U/RT})} \quad (1.30)$$

where  $U$  is the interaction energy between solute and grain boundary,  $\Omega$  the atomic volume,  $\delta$  the grain boundary thickness, and  $D_b$  the grain boundary diffusion coefficient [73]. Experimentally, it was reported that grain boundary mobility of undoped ceria is mostly higher than of acceptor doped ceria ( $> 1$  mol% dopant) [74]. **Fig. 1.13a** shows that mobility is hindered owing to the solute drag effect, which is strengthened with the reciprocal lattice diffusivity of the solute [70]. Moreover, the plot emphasizes that mobility data does not follow the simple relation as per **Eqn 1.30** because of an additional dependence on the interaction (elastic and electrostatic) between the solute and grain boundary. For this reason, the mobility first decreases from  $\text{Ca}^{2+}$  to  $\text{Y}^{3+}$  (less available  $V_{\text{O}}^{\bullet\bullet}$ ) and again rises for tetravalent  $\text{Zr}^{4+}$  (less interaction). The effect of elastic interaction can be better visualized from **Fig. 1.13b**. The results demonstrate that dopants, *e.g.*,  $\text{Y}^{3+}$  that are less associated with oxygen vacancies generate minimum grain boundary mobility.  $\text{Sc}^{3+}$  shows a different scenario as it has a strong oxygen vacancy scavenging effect by trapping  $V_{\text{O}}^{\bullet\bullet}$  at every cation site. In this situation, not enough  $V_{\text{O}}^{\bullet\bullet}$  is available, resulting in greater mobility [74]. In conclusion, the grain boundary mobility ( $M_b$ ) in ceria strongly depends on the sense of balance between electrostatic and elastic interaction of dopant and host  $\text{Ce}^{4+}$ [70][74].

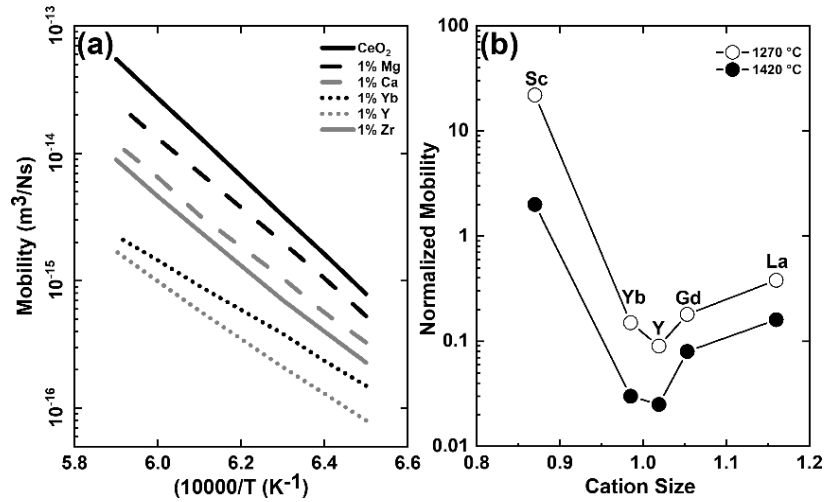


**Figure 1.13:** (a) Grain boundary mobility of pure and 1 mol% doped ceria, with dopants of different effective charges. (b) Normalized grain boundary mobility of 1 mol% doped ceria, with dopants of different cation size. The data is taken from Ref. [70][74] with permission from John Wiley & Sons.

## 1.7 Mechanical Properties of Ceria

In ceramics oxides, the mechanical deformation at room temperature is mainly elastic, which follows the typical Hook's law as the applied stress ( $\sigma$ ) is proportional to mechanical strain ( $\epsilon$ ). The elastic deformation in such a case is instant, entirely reversible, and time-independent [75]. Moreover, time-variant strain relaxation known as anelasticity, is very uncommon for ceramics but typical for polymeric materials. Due to anelasticity, materials illustrate time-dependent non-linear deformation under constant mechanical load called creep [76]. In ceramics materials, creep tends to occur at a moderately high temperature when materials start to show some ductility with a low strain rate [77]. **Fig. 1.14** illustrates a typical creep curve, showing different stages of creep under constant load. The creep deformation follows an empirical equation:

$$(u - u_0) = A (t - t_0)^m + kt \quad (1.31)$$

Where  $A$  is termed as creep rate constant,  $m$  and  $k$  are the fitting parameters that reflect primary and steady-state creep.

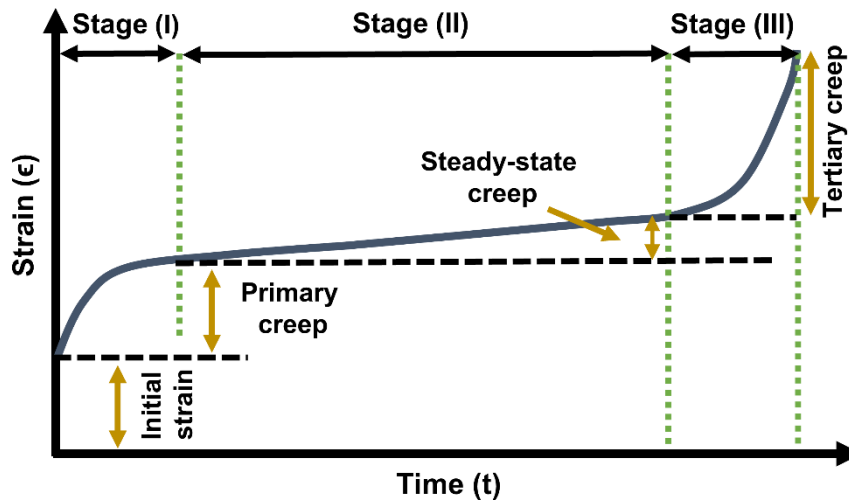


**Figure 1.14:** Schematic diagram of the stages of deformation during creep in ceramics materials.

It has been observed experimentally that the ceria-based compound develops noticeable creep (transient) deformation at room temperature under fast loading in the nanoindentation technique [76]. These findings are much unexpected for ceramics, especially for a high-melting-point material like ceria. Analogical to electrostriction model, it has been proposed that creep in ceria is attributed to the rearrangement of elastic dipoles  $Ce_{Ce}-V_{O}^{\bullet\bullet}$  to anisotropic mechanical stress [28][78]. Lubomirsky and co-workers have claimed that grain boundaries unlikely participate in this creep mechanism, as the applied indentation depth was smaller than the grain size [78]. An indentation load of 150 mN on a bulk grain ( $\sim 3 \mu\text{m}$ ) can generate stress of about 10 GPa, which is roughly 5% of the elastic modulus. Concerning this fact, grain boundary can not produce sufficient deformation (10-40 nm) in such a short time (8-20 s) [25]. Cation migration is active at a high temperature above 1000 °C with typical creep time like hours. The deformation through dislocation might not be possible since dislocation density and its migration are very low in ceria at room temperature. Accordingly, it inevitable accepts that creep in ceria is derived from the lability of  $Ce_{Ce}-7O_{o}-V_{O}^{\bullet\bullet}$ . This assumption supported by the fact that creep constant is drastically reduced under slow loading, *i.e.*, the time-scale of loading is more substantial than the time-scale of lattice reorganization [79]. Additionally, it is shown that creep tends to suppress at higher dopant concentrations due to local-scale phase transformation to double fluorite structure [25][78].

## References:

- [1] <https://www.comsol.dk/multiphysics/electromechanical-effects> (accessed on 04-04-2020).
- [2] Y. Bar-Cohen and I. A. Anderson, "Electroactive polymer (EAP) actuators—background review," *Mech. Soft Mater.* (2019) 1:5.
- [3] R. Korobko, "Control of Elastic Properties of Ceramics by External Electric Field, PhD Thesis, Jan 2013.
- [4] Yoseph Bar-Cohen, "Electroactive Polymer (EAP) Actuators as Artificial Muscles: Reality, Potential, and Challenges," Second Edition 2004.
- [5] Yoseph Bar-Cohen, "<https://ntrs.nasa.gov/archive/nasa/casi.ntrs.nasa.gov/20010067234.pdf>." (accessed on 04-04-2020).
- [6] A. L. Kholkin, N. A. Pertsev, and A. V. Goltsev, "Piezoelectricity and crystal symmetry," in *Piezoelectric and Acoustic Materials for Transducer Applications*, 2008, Springer Boston MA.
- [7] P. Muralt, "Stress Coupled Phenomena: Piezoelectric Effect," in *Encyclopedia of Materials: Science and Technology*, 2001.
- [8] J. F. Tressler, S. Alkoy, and R. E. Newnham, "Piezoelectric sensors and sensor materials," *J. Electroceramics*, 2(4) (1998) 257–272.
- [9] A. Arnau and D. Soares, "Fundamentals of piezoelectricity," in *Piezoelectric Transducers and Applications*, 2008 Springer.
- [10] R. E. Newnham, V. Sundar, R. Yimnirun, J. Su, and Q. M. Zhang, "Electrostriction: Nonlinear electromechanical coupling in solid dielectrics," *J. Phys. Chem. B*, 101 (1997) 10141–10150.
- [11] R. Yimnirun, S. M.-L. Eury, V. Sundar, P. J. Moses, S.-J. Jang, and R. E. Newnham, "Electrostriction measurements on low permittivity dielectric materials," *J. Eur. Ceram. Soc.*, 19 (1999) 1269–1273.
- [12] A. Kvasov, and A. K. Tagantsev, "Positive effective  $Q_{12}$  electrostrictive coefficient in perovskites," *J. Appl. Phys.*, 112 (2012) 094106.
- [13] A. Dogan, J. Tressler, and R. E. Newnham, "Solid-state ceramic actuator designs," *AIAA J.*, 39 (2001) 1354–1362.
- [14] A. Volatier, B. Ivira, C. Zinck, N. Ben Hassine, and E. Defaÿ, "Electrostrictive Resonators," in *Integration of Ferroelectric and Piezoelectric Thin Films: Concepts and Applications for Microsystems*, 2013.
- [15] E. Defaÿ, "Integration of Ferroelectric and Piezoelectric Thin Films," 2011.
- [16] F. Carpi, "Electromechanically Active Polymers," *Polymer International*, 2010.
- [17] A. F. Devonshire, "Theory of ferroelectrics," *Adv. Phys.*, 3 (1954) 85–130.
- [18] R. Yimnirun, P. J. Moses, R. E. Newnham, and R. J. Meyer, "Electrostrictive strain in low-permittivity dielectrics," *J. Electroceramics*, 8 (2002) 87–98.
- [19] V. Sundar and R. E. Newnham, "Electrostriction and polarization," *Ferroelectrics*, 135 (1992) 431–446.
- [20] S. Eury, R. Yimnirun, V. Sundar, P. J. Moses, S. J. Jang, and R. E. Newnham, "Converse electrostriction in polymers and composites," *Mater. Chem. Phys.*, 61 (1999) 18–23.
- [21] R. Korobko et al., "Giant electrostriction in Gd-doped ceria," *Adv. Mater.*, 24 (2012) 5857–5861.
- [22] V. Shelukhin, I. Zon, E. Wachtel, Y. Feldman, and I. Lubomirsky, "Low temperature dielectric properties of  $Ce_{0.8}Gd_{0.2}O_{1.9}$  films," *Solid State Ionics*, 211 (2012) 12–19.
- [23] R. Korobko, A. Lerner, Y. Li, E. Wachtel, A. I. Frenkel, and I. Lubomirsky, "In-situ extended X-ray absorption fine structure study of electrostriction in Gd doped ceria," *Appl. Phys. Lett.*, 106 (2015) 042904.
- [24] M. Hadad, H. Ashraf, G. Mohanty, C. Sandu, and P. Muralt, "Key-features in processing and

- microstructure for achieving giant electrostriction in gadolinium doped ceria thin films,” *Acta Mater.*, 118 (2016) 1–7.
- [25] E. Wachtel, A. I. Frenkel, and I. Lubomirsky, “Anelastic and Electromechanical Properties of Doped and Reduced Ceria,” *Advanced Materials*, 30 (2018) 1707455.
- [26] X. Guo and R. Waser, “Electrical properties of the grain boundaries of oxygen ion conductors: Acceptor-doped zirconia and ceria,” *Prog. Mater. Sci.*, 51 (2006) 151–210.
- [27] X. Guo, W. Sigle, and J. Maier, “Blocking grain boundaries in yttria-doped and undoped ceria ceramics of high purity,” *J. Am. Ceram. Soc.*, 86 (2003) 77–87.
- [28] Y. Nimrod et al., “Large Nonclassical Electrostriction in (Y, Nb)-Stabilized  $\delta$ -Bi<sub>2</sub>O<sub>3</sub>,” *Adv. Funct. Mater.*, 26 (2016) 1138–1142.
- [29] N. Yavo, O. Yeheskel, E. Wachtel, D. Ehre, A. I. Frenkel, and I. Lubomirsky, “Relaxation and saturation of electrostriction in 10 mol% Gd-doped ceria ceramics,” *Acta Mater.*, 144 (2018) 411–418.
- [30] J. R. Schrieffer, “Theory of super conductivity,” 2018.
- [31] J. A. Kilner, “Fast oxygen transport in acceptor doped oxides,” *Solid State Ionics*, 129 (2000) 13–23.
- [32] A. Kabir, H. Zhang, and V. Esposito, “Mass diffusion phenomena in cerium oxide,” in *Cerium Oxide (CeO<sub>2</sub>): Synthesis, Properties and Applications*, 2020.
- [33] S. R. Bishop, K. L. Duncan, and E. D. Wachsman, “Defect equilibria and chemical expansion in non-stoichiometric undoped and gadolinium-doped cerium oxide,” *Electrochim. Acta*, 54 (2009) 1436–1443.
- [34] V. Butler, C. R. A. Catlow, B. E. F. Fender, and J. H. Harding, “Dopant ion radius and ionic conductivity in cerium dioxide,” *Solid State Ionics*, 8 (1983) 109–113.
- [35] I. A. Abrikosov, S. I. Simak, D. A. Andersson, N. V. Skorodumova, and B. Johansson, “Optimization of ionic conductivity in doped ceria,” *Proc. Natl. Acad. Sci.*, 103 (2006) 3518–3521.
- [36] S. Wang, T. Kobayashi, M. Dokiya, and T. Hashimoto, “Electrical and Ionic Conductivity of Gd-Doped Ceria,” *J. Electrochem. Soc.*, 19 (1999) 193–200.
- [37] J. A. Kilner and R. J. Brook, “A study of oxygen ion conductivity in doped non-stoichiometric oxides,” *Solid State Ionics*, 6 (1982) 237–252.
- [38] J. Koettgen, S. Grieshammer, P. Hein, B. O. H. Grope, M. Nakayama, and M. Martin, “Understanding the ionic conductivity maximum in doped ceria: Trapping and blocking,” *Physical Chemistry Chemical Physics*, 20 (2018) 14291–14321.
- [39] D. Y. Wang, D. S. Park, J. Griffith, and A. S. Nowick, “Oxygen-ion conductivity and defect interactions in yttria-doped ceria,” *Solid State Ionics*, 2 (1981) 95–105.
- [40] J. Faber, C. Geoffroy, A. Roux, A. Sylvestre, and P. Abélard, “A Systematic investigation of the dc electrical conductivity of rare-earth doped ceria,” *Appl. Phys. A Solids Surfaces*, 49 (1989) 225–232.
- [41] S. Omar, E. D. Wachsman, and J. C. Nino, “Higher ionic conductive ceria-based electrolytes for solid oxide fuel cells,” *Appl. Phys. Lett.*, 91 (2007) 144106.
- [42] X. Wei, W. Pan, L. Cheng, and B. Li, “Atomistic calculation of association energy in doped ceria,” *Solid State Ionics*, 180 (2009) 13–17.
- [43] X. Guo and J. Maier, “Grain Boundary Blocking Effect in Zirconia: A Schottky Barrier Analysis,” *J. Electrochem. Soc.*, 148 (2001) E121.
- [44] W. E. Lee, “Ceramic processing and sintering,” *Int. Mater. Rev.*, 2012.
- [45] R. Waser and R. Hagenbeck, “Overview No. 137: grain boundaries in dielectric and mixed-conducting ceramics,” *Acta Materialia*. 48 (2000) 797–825.
- [46] X. Guo and J. Maier, “Grain boundary blocking effect in zirconia: A schottky barrier analysis,” *J. Electrochem. Soc.*, 148 (2001) E121.

## Introduction

- [47] H. Hojo et al., "Atomic structure of a CeO<sub>2</sub> grain boundary: The role of oxygen vacancies," *Nano Lett.*, 10 (2010) 4668-4672.
- [48] D. Y. Wang and A. S. Nowick, "The grain-boundary effect in doped ceria solid electrolytes," *J. Solid State Chem.*, 35 (1980) 325-333.
- [49] S. P. S. Badwal and J. Drennan, "Evaluation of conducting properties of yttria-zirconia wafers," *Solid State Ionics*, 40-41 (1990) 869-873.
- [50] X. Guo, W. Sigle, J. U. Fleig, and J. Maier, "Role of space charge in the grain boundary blocking effect in doped zirconia," *Solid State Ionics*, 154-155 (2002) 555-561.
- [51] X. Guo and Y. Ding, "Grain Boundary Space Charge Effect in Zirconia," *J. Electrochem. Soc.*, (151) 2004 J1-J7.
- [52] S. Kim and J. Maier, "On the Conductivity Mechanism of Nanocrystalline Ceria," *J. Electrochem. Soc.*, 149 (2002) J73.
- [53] M. C. Göbel, G. Gregori, and J. Maier, "Numerical calculations of space charge layer effects in nanocrystalline ceria. Part II: Detailed analysis of the space charge layer properties," *Phys. Chem. Chem. Phys.*, 16 (2014) 10214-10231.
- [54] H. J. Avila-Paredes, K. Choi, C.-T. Chen, and S. Kim, "Dopant-concentration dependence of grain-boundary conductivity in ceria: A space-charge analysis," *J. Mater. Chem.*, 19 (2009) 4837.
- [55] Z. P. Li, T. Mori, G. J. Auchterlonie, J. Zou, and J. Drennan, "Nanodomain formation and distribution in Gd-doped ceria," *Mater. Res. Bull.*, 47 (2012) 763-767.
- [56] Z. P. Li, T. Mori, F. Ye, D. R. Ou, J. Zou, and J. Drennan, "Structural phase transformation through defect cluster growth in Gd-doped ceria," *Phys. Rev. B - Condens. Matter Mater. Phys.*, 84 (2011) 180201.
- [57] D. R. Ou, F. Ye, and T. Mori, "Defect clustering and local ordering in rare earth co-doped ceria," *Phys. Chem. Chem. Phys.*, 13 (2011) 9554-9560.
- [58] P. Yan et al., "Microstructural and chemical characterization of ordered structure in yttrium doped ceria," *Microsc. Microanal.*, 19 (2013) 102-110.
- [59] D. Pérez-Coll, E. Sánchez-López, and G. C. Mather, "Influence of porosity on the bulk and grain-boundary electrical properties of Gd-doped ceria," *Solid State Ionics*, 181 (2010) 1033-1042.
- [60] M. Han, X. Tang, H. Yin, and S. Peng, "Fabrication, microstructure and properties of a YSZ electrolyte for SOFCs," *J. Power Sources*, 165 (2007) 757-763.
- [61] F. S. Baumann, J. Fleig, H. U. Habermeier, and J. Maier, "Impedance spectroscopic study on well-defined (La,Sr)(Co,Fe)O<sub>3-δ</sub> model electrodes," *Solid State Ionics*, 177 (2006) 1071-1081.
- [62] V. Esposito and E. Traversa, "Design of electroceramics for solid oxides fuel cell applications: Playing with ceria," *J. Am. Ceram. Soc.*, 91, (2008) 1037-1051.
- [63] V. Esposito et al., "Enhanced mass diffusion phenomena in highly defective doped ceria," *Acta Mater.*, 61 (2013) 6290-6300.
- [64] L. C. De Jonghe and M. N. Rahaman, "Sintering of Ceramics," in *Handbook of Advanced Ceramics: Materials, Applications, Processing and Properties*, 1-2 (2003) 187-264.
- [65] H. Inaba, "Ceria-based solid electrolytes," *Solid State Ionics*, 83 (1996) 1-16.
- [66] S.-J. L. Kang, "INITIAL STAGE SINTERING," in *Sintering*, 2005.
- [67] R. M. German, "Coarsening in sintering: Grain shape distribution, grain size distribution, and grain growth kinetics in solid-pore systems," *Crit. Rev. Solid State Mater. Sci.*, 35 (2010) 263-305.
- [68] S.-J. L. Kang, "Sintering: densification, grain growth, and microstructure," 1st Edition, 2005.
- [69] H. Djohari and J. J. Derby, "Transport mechanisms and densification during sintering: II. Grain boundaries," *Chem. Eng. Sci.*, 64 (2009) 3810-3816.
- [70] P. L. Chen and I. W. Chen, "Grain growth in CeO<sub>2</sub>: Dopant effects, defect mechanism, and solute drag," *J. Am. Ceram. Soc.*, 79 (1996) 1793-1800.

## Introduction

- [71] J. W. Cahn, "The impurity-drag effect in grain boundary motion," *Acta Metall.*, 10 (1962) 789–798.
- [72] K. Ishizaki, K. Niihara, M. Isotani and R.G. Ford, "Grain Boundary Controlled Properties of Fine Ceramics," 2011.
- [73] J. D. Powers and A. M. Glaeser, "Grain Boundary Migration in Ceramics," *Interface Sci.*, 6 (1998) 23–39.
- [74] P. -L Chen and I. -W Chen, "Role of Defect Interaction in Boundary Mobility and Cation Diffusivity of CeO<sub>2</sub>," *J. Am. Ceram. Soc.*, 77 (1994) 2289–2297.
- [75] G. M. L. Gladwell, "Solid mechanics and its applications," *Solid Mech. its Appl.*, 2014.
- [76] R. Korobko et al., "Influence of Gd content on the room temperature mechanical properties of Gd-doped ceria," *Scr. Mater.*, 66 (2012) 155–158.
- [77] J. P. Poirier, "Creep of crystals: high-temperature deformation processes in metals, ceramics and minerals.," *Creep Cryst. high-temperature Deform. Process. Met. Ceram. Miner.*, 1985.
- [78] R. Korobko, S. K. Kim, S. Kim, S. R. Cohen, E. Wachtel, and I. Lubomirsky, "The role of point defects in the mechanical behavior of doped ceria probed by nanoindentation," *Adv. Funct. Mater.*, 23 (2013) 6076–6081.
- [79] M. Varenik, S. Cohen, E. Wachtel, A. I. Frenkel, J. C. Nino, and I. Lubomirsky, "Oxygen vacancy ordering and viscoelastic mechanical properties of doped ceria ceramics," *Scr. Mater.*, 163 (2019) 19–23.

## Chapter 2: Experimental Procedure

---

This chapter briefly explains the synthesis procedure of starting powder, pellet fabrication methods, including different sintering mechanisms as well as physical, electrochemical, mechanical, and electromechanical characterization techniques used in this work.

### 2.1 Selection of Materials

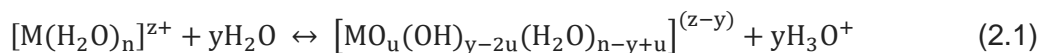
In chapter 1, it has been described that a large number of oxygen vacancies and their local configuration are the two most important factors for the development of electrostriction in cerium oxides. The defects chemistry of ceria underlines the formation of thermodynamic defect association (short- and long-range) through elastic and electrostatic interaction, controlling oxygen vacancy configuration in the lattice. With the purpose of understanding the role of oxygen vacancy and their local environment, several dopant types, comprising trivalent and divalent dopants with various sizes and different sintering protocols is followed in the current study.

### 2.2 Powder Synthesis

Oxide ceramics, such as ceria, can be synthesized from many different routes. Some standard methods are solid-state reaction, hydrothermal synthesis, sol-gel, solution combustion, and co-precipitation [1]. In this work, the co-precipitation synthesis route is mostly used because it allows obtaining homogeneous powders with well-controlled stoichiometry and designed morphology [2]. Co-precipitation is a wet-chemical synthesis process that separates the phase of solid dissolved in an aqueous solution comprising different ionic species [3][4]. In general, the reaction mechanism of co-precipitation of the metal oxide is quite complicated, and it is explained briefly in the following sections. The metal salt dissolves typically in the aqueous solution at room temperature. During the dissolution process, it undergoes hydrolysis and

## Experimental Procedure

condensation type reactions, leading to form molecular combinations of different kinds. The hydrolysis reaction can be described by the "particle charge model," illustrating that the water molecule solvates the metal cation (M). Subsequently, it will trigger to form a metal complex  $[M(H_2O)_n]^{z+}$  (assuming only one cation) which has an affinity to release protons. The reaction then becomes [5]:



Based on the degree of hydrolysis, the cation is associated with three types of ligands, namely: aquo ( $H_2O$ ), hydroxo ( $OH^-$ ), and oxo ( $O^{2-}$ ), as illustrated in **Fig. 2.1**. The formation of such ligands strongly depends on cation charge (Z) and solution pH, which can be estimated from the so-called "charge-pH" diagram. An increment of pH assists forward reaction. The diagram in **Fig. 2.1** shows that lower and higher valence cation typically forms aquo and oxo ligand, respectively, in pH below 10. Multiple associations are possible for tetravalent cation, such as aquo-hydroxo, hydroxo, and hydroxo-oxo.

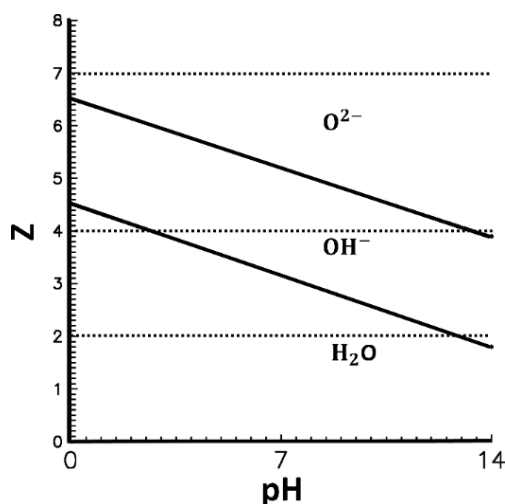
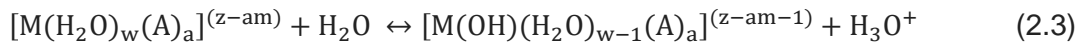
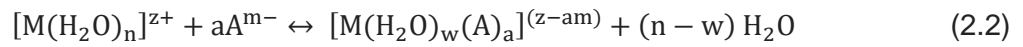


**Figure 2.1:** Illustration of the charge-pH diagram. The figure is adapted from Ref. [5] with permission from Springer Nature.

Furthermore, these hydrolyzed molecular species experience condensation reactions *via* "olation" or "oxalation". The former typically occurs with hydroxo-aquo complex  $[M(OH)_x(H_2O)_{n-x}]^{(z-x)+}$  ( $x < n$ ) and forms a hydroxo bridge M-OH-M. Whereas the latter follows with oxo-hydroxo complex  $[MO_x(OH)_{n-x}]^{(n+x-z)+}$  ( $x < n$ ), resulting in an oxo

## Experimental Procedure

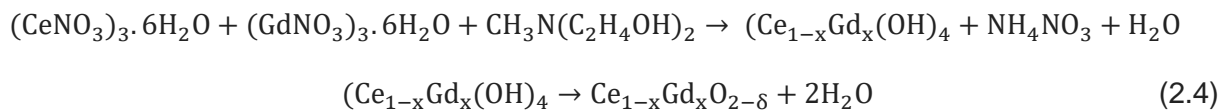
connection M-O-M. These condensation reactions subsequently pursue other association reactions, eventually resulting in the evolution of gel. One condition of gel formation is that the reaction kinetics of both hydrolysis and condensation should not be too fast. Otherwise, unwanted complexes might form e.g.  $[M(OH)_z]/MO_{z/2}$ . Alternatively, the formed precipitates would be inhomogeneous with a compositional fluctuation in each particle. However, to control the reaction kinetics organic complexants, e.g., diamine organic metal chelating agents are typically added. In this case, the hydrolysis reaction is slowed down by a deprotonation mechanism:



For example, the equilibrium rate constant of hydrolysis of ion is reduced by a factor of  $10^{22}$  with the presence of an EDTA (ethylene diamine tetraacetic acid) [5].

In this work, N-methyl diethanolamine (MDEA) is used as a ligand that can slowly release ammonia within the solution. Stoichiometric amounts of cerium nitrate hexahydrate (Sigma-Aldrich, USA) and particular dopant nitrate hydrate (Sigma-Aldrich, USA) salts are dissolved in deionized water to prepare 0.1 M solution. After that, 0.3 M MDEA (N-methyl-diethanolamine) is slowly added into it. The solutions are then kept overnight under mild stirring. The resulting precipitates are centrifuged and washed several times with ethanol and deionized water. Then the subsequent solid gel is oven-dried and calcined at 500 °C for 2 hours. After the calcination, hard agglomerated powders are ball-milled in ethanol/water medium with 2 mm zirconia balls for 5-10 hours, followed by drying at 120 °C for 10 hours. Finally, the powders are softly crushed, e.g., with a mortar and pestle, sieved using a 150 µm mesh, and stored in a plastic bottle. The flow-chart of the powder synthesis method is explained in **Fig. 2.2**.

For a 10 mol% Gd-doped ceria powder, the final reaction can be written as:



## Experimental Procedure

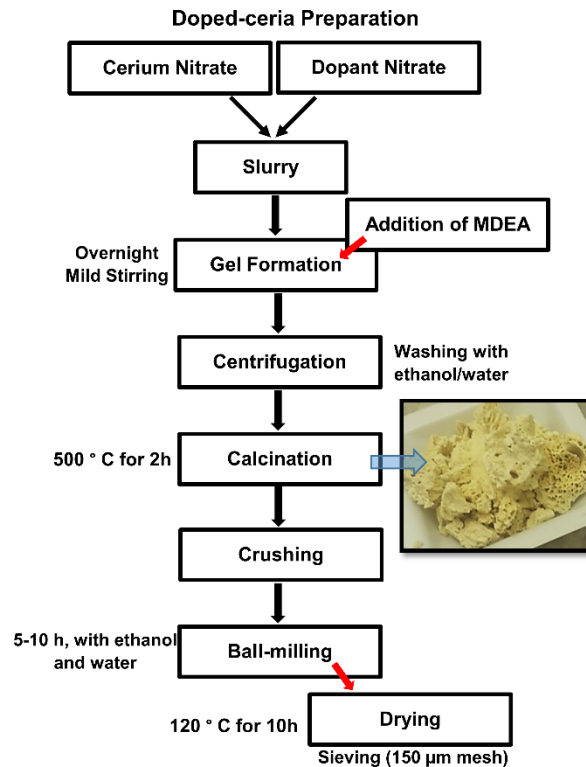


**Figure 2.2:** Schematic flow-diagram of co-precipitation synthesis method of doped-ceria powder.

## 2.3 Pellet Fabrication

### 2.3.1 Free Sintering

The conventional sintering, *i.e.*, free sintering, is the most common sintering practice for the fabrication of ceria. The typical sintering mechanism in ceria is the so-called solid-state sintering, where no additive or liquid phase is introduced [6]. As for this and other functional ceramics, the composition must be highly controlled both at the bulk and the boundary. In the free sintering, such conditions are generally fulfilled by pressing the starting powders and activating the mass diffusion mechanisms leading to the consolidation of the polycrystalline body as the temperature is raised smoothly to the sintering temperature ( $\sim 1300\text{-}1500\text{ }^{\circ}\text{C}$ ) for a few hours. In general, a mild ramping of  $\sim 2\text{-}5\text{ }^{\circ}\text{C}/\text{min}$  is used. In the case of electrostrictive ceria, high density is desired because porosity can decrease the elastic modulus and impair the mechanical response of the ceramic body. To obtain high density *via* the free sintering procedure, it is crucial to start with well-packed powders, *i.e.*, high green density [7]. Due to high temperature and long dwelling time, thermodynamically equilibrium relaxed microstructure with significant grain growth are achieved [8]. Conversely, it is possible to obtain

## Experimental Procedure

a dense sample with non-relaxed nanostructure if sintering is performed at rapid ramping rates ( $\sim 20$  °C/min) for a short dwelling time like 5-10 minutes. One most important requirement of such a process is to use nanoscale starting powder ( $\sim 5$ -20 nm) [8][9], especially from the wet-synthesis method. This process is called rapid sintering or fast firing. **Fig. 2.3** displays typical thermal treatments and microstructure obtained for 10% Gd-doped ceria.

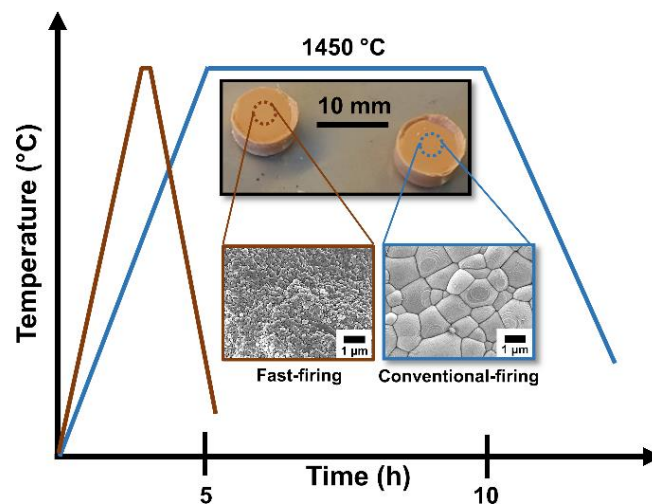


**Figure 2.3:** Illustration of the free-sintering profile for doped ceria, and respective microstructure.

To prepare the green sample with excellent packing, the powder is uniaxially cold-pressed in a 12 mm die (3-4 mm thick) under an external pressure of  $\sim 150$ -200 MPa for 30 sec. No additional binder is used. Afterward, the green pellet is put into a rubber balloon, air-evacuated, and firmly knotted up. Then the sample is isostatically cold-pressed in water medium at 500 MPa for 20 sec, followed by conventional sintering at 1450 °C for 10 hours with a heating and cooling ramp rate of 3 and 5 °C/min, respectively. For the fast-firing, the sample is sintered at 1450 °C for 0.1 hours with an identical heating and cooling cycle of 20 °C/min to avoid thermal shock.

### 2.3.2 Field-assisted Spark Plasma Sintering (SPS)

In the last few years, electric field-assisted sintering, for example, spark plasma sintering (SPS), has been applied to various kinds of ion-conducting electroceramics, including ceria and zirconia [10][11]. The SPS process is considerably different from conventional sintering, which uses both electric-field (DC) and simultaneous pressure to densify the green compact

## Experimental Procedure

[12][13]. On the other hand, the latter sinters through radiation from the furnace [14]. In SPS, a current is passed through the die as well as the sample, resulting in a direct way of heating, *i.e.*, Joule heating [12][15]. The heat is dissipated at the interfacial contact between the particles leading to form high local current densities [16]. As a result, fast heating (up to 1000 °C/min) is reached that facilitates densification over grain coarsening, eventually forms a homogeneous nanostructure [10][17]. The schematic illustration of the SPS apparatus and the typical sintering profile is shown in **Fig. 2.4**.

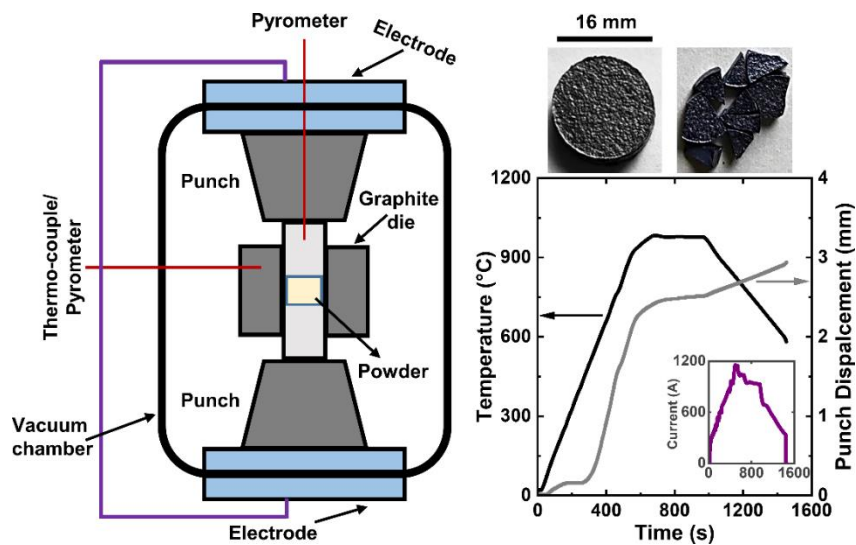


**Figure 2.4:** Schematic diagram of the SPS set-up (left). The image is adapted from Ref. [12] with permission from John Wiley & Sons. Example of a typical temperature and displacement profile in the SPS process (right).

In this work, an optimized SPS procedure is followed. A graphite die (16 mm diameter) is chosen due to its high electrical conductivity. To avoid direct contact between the die and the powder, a graphite paper is rolled into the die. Then the powder is discharged into it. Additionally, a couple of graphite spacers are positioned between the punch and the powders. After that, the powder is uniaxially cold-pressed at 50 MPa for 5 sec. Next, it is placed into the SPS chamber (Dr. Sinter Lab 515S, Japan) and held between two graphite electrodes. The sample is consolidated under a high vacuum ( $\leq 6 \cdot 10^{-6}$  Torr) at 850-1050 °C, uniaxial pressure of 50/70 MPa with a heating rate of 100 °/min, and 5 min dwelling. The sintering temperature is monitored by a thermocouple injected in the die. The resultant SPS sample undergoes

## Experimental Procedure

coloration as it turns into dark black, whereas the powder has a yellowish-white color, confirming the occasion of chemical reduction [15].

Interestingly, the coloration is highly heterogeneous, often showing more dark color at the edge than of the center. As SPS is performed with graphite tooling under vacuum, a localized reduction around the sample is typically expected in this temperature range [18]. The reduction effect ( $\text{Ce}^{4+} \rightarrow \text{Ce}^{3+}$ ) leads to the release of oxygen ions and creates oxygen vacancies in the ceria lattice. Subsequently, a local phase transformation from  $\text{CeO}_2$  to  $\text{Ce}_2\text{O}_3$  and an evident chemical expansion take place [19]. Such an event can cause the development of microscale and/or macroscopic cracks in the material. Due to these cracks, samples are frequently broken after the sintering process (see **Fig. 2.4**). Therefore, the sample is then subjected to post-annealing, *i.e.*, the re-oxidation process at 700-800 °C for 1-10 hours to preserve equilibrium oxygen vacancy concentration.

### 2.3.3 Cold Sintering Process (CSP)

In recent times, a low-temperature (< 300 °C) sintering process named cold sintering process (CSP) has been developed by Randall and co-workers at the Pennsylvania State University [20][21]. The CSP is a non-equilibrium pressure-assisted liquid phase sintering process. In this method, the powders are mixed with a liquid solvent (commonly water or  $-\text{OH}$ ), resulting in the partial dissolution of the powder and subsequently reduce the interfacial area. Under external heat (> 150-200 °C) and mechanical pressure (50-500 MPa), the liquid phase redistributes into the particle-to-particle contacts and ultimately activates the rapid mass flow as the liquid starts evaporating [22]. This stage creates a supersaturated solution and precipitation, finally form a dense body [23][24]. The densification takes place within 1-60 minutes, reaching nearly ~80-98% of the theoretical density [25]. However, for high-temperature ionic conductors such as zirconia and ceria, it is required to perform an additional post-annealing to complete densification and achieve equilibrium [26]. The basic steps in the CSP are shown diagrammatically in **Fig. 2.5**.

## Experimental Procedure

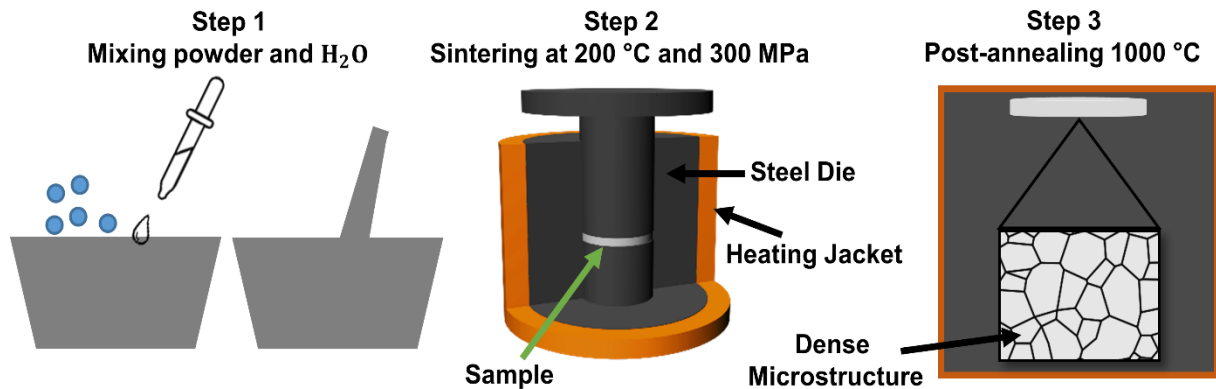


**Figure 2.5:** Schematic representation of the steps in the cold sintering process for ceria compounds.

The engineering design of the CSP is straightforward, needs a steel die, press, and heat controller [27]. In this thesis, only one sample (GDC10) is fabricated through the cold sintering process and prepared in the lab of Salvatore Grasso (Southwest Jiaotong University, China). To start with, 1 g high purity GDC powder (Rhodia, France) and 0.4 g deionized water are mixed in a centrifuge tube using a vortex mixer. The mixed paste is then loaded into a steel die (15 mm inner dia) and uniaxially pressed at a pressure of ~300 MPa. Then, the sample is sintered at 200 °C for 0.5 hours. The measured relative density of the as-CSP sample is about 70%. Therefore, it is additionally post-annealed at 1000 °C for 1 hour with a heating rate of 10 °C/min.

## 2.4 Physical Characterization

### 2.4.1 Density Measurement

The experimental density of the sample was measured by the Archimedes principle in the water medium. The density of the water is estimated, according to DIN 623-2 (1993) using the following formula:

$$\frac{\rho_{\text{sample}}}{\rho_{\text{water}}} = \frac{W_{\text{sample (air)}}}{W_{\text{sample (air)}} - W_{\text{sample (water)}}} \quad (2.5)$$

Where  $\rho$  and  $W$  denote the density and weight.

### 2.4.2 X-Ray Diffraction (XRD)

X-ray powder diffraction (XRD) is a widely used technique to characterize the structural features of crystalline materials [28]. This method allows determining unit cell parameters,

## Experimental Procedure

crystallite size, microstrain, residual stress, *etc.* [29][30]. The investigated material is usually a finely ground powder. However, other forms, such as thin films, solid pellets, as well as biological fluids, are also characterized. Inside a crystal, the atoms are arranged in a highly ordered 3-dimensional periodic structure. When an X-ray beam impinges on a sample, it energetically interacts with the electron cloud of the specimen atom and subsequently scatters in different directions. Such a mechanism is known as elastic scattering, where the electron is called the scatter [31]. The resultant scattered (diffracted) waves interfere with each other and might cancel out in most directions by forming a destructive interface. Moreover, a constructive interface might also originate in some directions if the condition of Bragg's law is satisfied [32].

$$n\lambda = 2d\sin\theta \quad (2.6)$$

Where  $d$  is the lattice spacing between two diffracting planes,  $\theta$  the incident angle,  $n$  the positive integer, and  $\lambda$  the wavelength of the X-ray beam. **Fig. 2.6** schematically illustrates the Bragg's diffraction behavior of crystalline material.

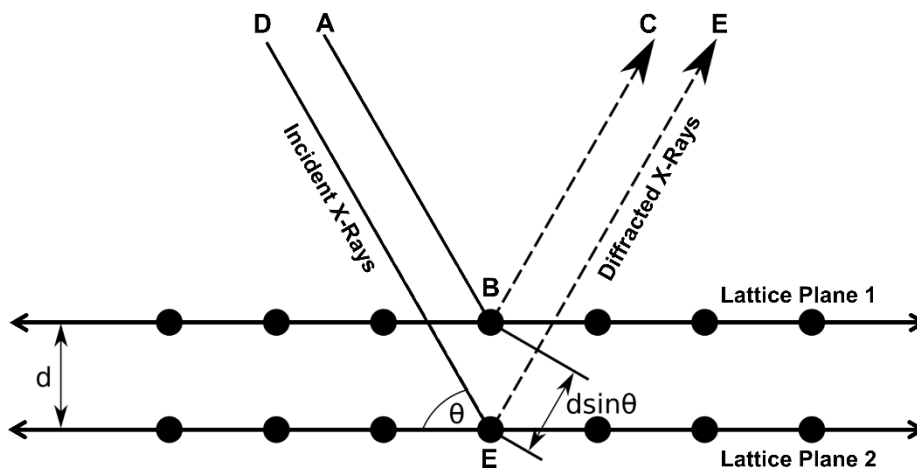


**Figure 2.6:** Schematic representation of the X-ray diffraction method, showing constructive interference when the distance between paths ABC and DEF differs by an integer number of wavelength ( $\lambda$ ). The image is adapted from Ref. [33] with permission from Elsevier.

Counting the intensity of the constructive interface and measuring the angles it occurs, a diffraction pattern can be produced for a wide range of  $2\theta$  angles [34]. In general, each crystalline material represents a specific diffractogram and is regarded as the proof of identity of the material crystal structure. From the diffraction peak, the crystallite size of the particles can be measured from the Scherrer equation [35], as given by:

## Experimental Procedure

$$\tau = \frac{K\lambda}{\beta \cos\theta} \quad (2.7)$$

Here,  $\tau$  is the mean size of the crystallite,  $K$  the dimensionless shape factor having a typical value of 0.9 and  $\beta$  the line broadening at full-width half maximum (FWHM). The value of  $\lambda$  in CuK $\alpha$  radiation is about  $\sim 0.15406$  nm. Addition to that from the lattice spacing, the unit cell parameter of the crystalline lattice can be evaluated, following the equation for cubic crystal structure:

$$\frac{1}{d^2} = \frac{h^2+k^2+l^2}{a^2} \quad (2.8)$$

Where  $a$  is the unit cell parameter or lattice constant and  $h, k, l$  are the integers in miller indices. The significant advantage of the XRD technique is that it requires minimal sample preparation, straightforward data interpretation, and availability of literature data. However, the detection limit of this method is inadequate, *i.e.*, below 3-10 % for the case of multiphase material, depending on the x-rays absorption coefficient of the elements in the compounds. The depth resolution is between 20 Å to 30  $\mu\text{m}$ , subjected to other factors such as material properties, incident angle, and experimental parameters [29]. Therefore, it is challenging to detect the minor secondary phase from this technique.

In this XRD diffraction measurement, a Bruker D8 (Germany) diffractometer is used to examine the structural phase purity of both powders and sintered pellets. The diffraction pattern is acquired using Cu K $\alpha$  radiation and scanned over a  $2\theta$  of 20-90° with a scan speed of 2°/min. The background noise of the pattern is subtracted using DIFFRAC.EVA software.

### 2.4.3 Scanning Electron Microscopy (SEM)

The scanning electron microscope (SEM) is an electron microscope that creates an image by scanning the surface of the specimen in a raster scan pattern with focused beams of high-energy electrons [36]. An SEM produces a high-resolution black and white 3-D image that further offers topographical, morphological, and chemical compositional information of the investigated material. SEM has an image magnification from about 10 to 100,000 times and a resolution limit between 50 nm to 100 nm. The spatial resolution of the SEM depends on the

## Experimental Procedure

electron beam spot and the size of the interaction volume [37]. The interaction volume is defined as the volume of the interaction between the specimen and incoming electron beams [38]. When an inbound electron beam hits the sample, numerous signals are generated, including secondary electron (SE), backscatter electron (BSE), characteristics X-rays, *etc.* (see **Fig. 2.7**). Each signal carries different types of an electron, for example, SE is low-energy electrons (50 eV) that emerge from the top few nanometers of the sample surface due to the inelastic interactions between the sample atom and the e-beam [39]. Instead, BSE is originated from a much larger depth as a result of elastic interactions [39][40]. Therefore, the image resolution of BSE is significantly lower than of the SE. Furthermore, the BSE image illustrates more information about the chemical composition of the sample, as the BSE signal is strongly sensitive to the atomic number ( $Z$ ). The lower the atomic number, the darker is the physical appearance.

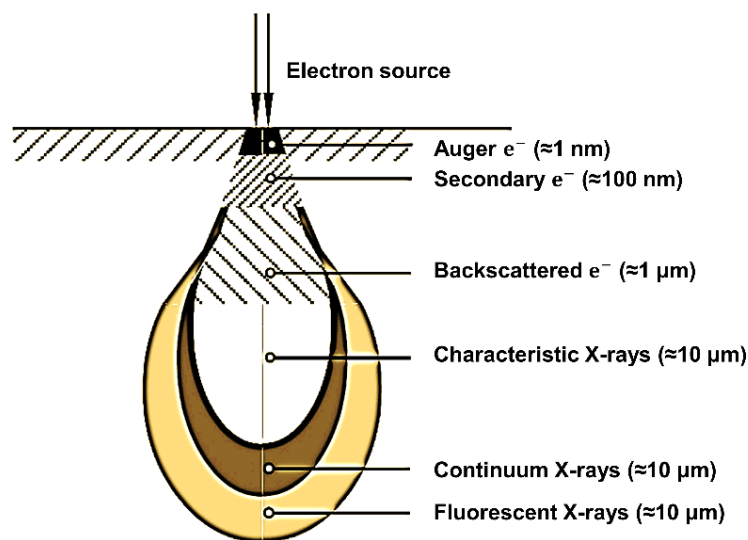


**Figure 2.7:** Depth range of different types of scattered electrons in an interaction volume. The image is slightly modified from the original [41].

The investigated sample in SEM has to be in solid form and can be directly placed onto the operating chamber. Point to note the sample is required to be electrically conductive. If not, measuring a sharp image will be difficult because the non-conducting sample would accumulate charge under the electron beams, a process named as charging [42]. To avoid charging, a thin layer of a conductive metal coating such as Au, Pt is typically sputtered onto

## Experimental Procedure

the specimen. In this work, the dense pellet is broken by a hammer, and the resultant cold-fractured cross-section is inspected by a high-resolution SEM (Zeiss Merlin, Germany). For analyzing polished cross-section, the sample is dispersed into epoxy and mechanically mirror-polished using different alumina grinding discs in the water medium. Afterward, the sample is cleaned with deionized water and/or ethanol under sonication for 15-30 min, followed by degassing in a vacuum. Before measurement, both categories of the samples are coated with carbon. The average grain sizes are calculated by the linear intercept method using a minimum of 100 grains, multiplying with correction factor 1.57 [43].

### 2.4.4 Transmission Electron Microscopy (TEM)

The transmission electron microscope (TEM) is also a type of electron microscope in which a high-energy electron beam typically above 100 kV is passed through the sample. The transmitted high-energy electrons are enlarged onto an imaging device to create an image [44][45]. The magnification up to 1,000,000 times is also possible in TEM that allows providing sub-micrometer information about the sample, such as atomic structure and configuration, the interatomic spacing, element identification, and distribution of different phases [46]. Due to the electron's high energy, it is considered as a wave rather than a particle. When the electron moves through the specimen, it interacts with the atoms through a strong electrostatic columbic force leading to scattering (diffraction) as well as the transfer of electron energy. The underlying mechanism of TEM imaging is represented in **Fig. 2.8**. The diagram shows that transmitted beams (both diffracted and non-diffracted) are refocused by an objective lens to the image plane of the microscope, creating a conventional image. Furthermore, by placing an extra aperture underneath the sample beam-column, a selected area electron diffraction (SAED) spot can be produced in the TEM experiment. SAED is identical to the X-ray diffraction technique, but it can investigate nanometers in size, as the wavelength of the electron is much smaller than the X-rays. Every crystal corresponds to individual diffraction spot, a pattern, *i.e.*, the fingerprint of sample crystal structure and lattice parameter. In TEM, the examined sample has to be in ultrathin form, *i.e.*, below 100 nm thin or a suspension on a grid. The sample

## Experimental Procedure

preparation of TEM is extensive, and small area detection limits the usage of the technique. To characterize crystal structure and morphology of the starting powders, a convention TEM (JEOL 2100, USA) is used. The image is taken in bright-field contrast mode. The particle size is calculated discretely in both lateral and transverse directions and then averaged.

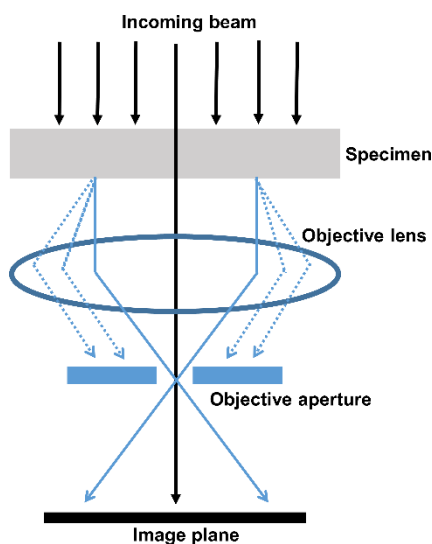


**Figure 2.8:** A general layout of image formation in TEM. Dashed lines are reflected electrons. The image is redrawn from Ref. [47].

### 2.5 Electrochemical Characterization

Electrochemical impedance spectroscopy (EIS) is a powerful tool for investigating the electrochemical reactions mechanism, dielectric, and charge transport properties in ionic solids. In common with electrical resistance, impedance is also a measure of the ability of a circuit to resist electrical current. However, impedance does not follow the simple concept of resistance, *i.e.*, one ideal resistor. In reality, especially ionic materials contain many complex circuits. Impedance is measured by exerting a small amplitude of AC (sinusoidal) voltage on an electrochemical cell and the resultant behavior of the electrical current [48]. The excited and responded signal can be expressed as a function of time in the following equation:

$$E_t = E_0 \sin(\omega t) \quad (2.9)$$

$$I_t = I_0 \sin(\omega t + \Phi) \quad (2.10)$$

## Experimental Procedure

Where  $\omega$  is the angular frequency in radians ( $\omega = 2\pi f$ ),  $E_t$  and  $I_t$  are the potential and current at time  $t$ ,  $E_0$  and  $I_0$  the amplitude of the potential and current,  $\Phi$  the phase shift. Similar to Ohm's law, the impedance is estimated by:

$$Z = \frac{E_t}{I_t} = \frac{E_0 \sin(\omega t)}{I_0 \sin(\omega t + \Phi)} = Z_0 \frac{\sin(\omega t)}{\sin(\omega t + \Phi)} \quad (2.11)$$

With Euler relationship,

$$Z = Z_0(\cos \Phi + j \sin \Phi) \quad (2.12)$$

$$\text{Re}(Z) = Z' = |Z| \cos(\Phi) \quad (2.13)$$

$$\text{Im}(Z) = Z'' = |Z| \sin(\Phi) \quad (2.14)$$

Where phase angle  $\Phi = \tan^{-1}\left(\frac{Z''}{Z'}\right)$  and  $|Z| = \sqrt{(Z')^2 + (Z'')^2}$ . From **Eqn 2.12**, it is evident that impedance ( $Z$ ) comprised of one real and one imaginary part. By plotting the real part on the x-axis and imaginary part on the y-axis, a typical impedance plot named Nyquist plot is obtained (see **Fig. 2.9a**). It illustrates a semicircle in which the frequency is decreased from the right side of the plot to the left.

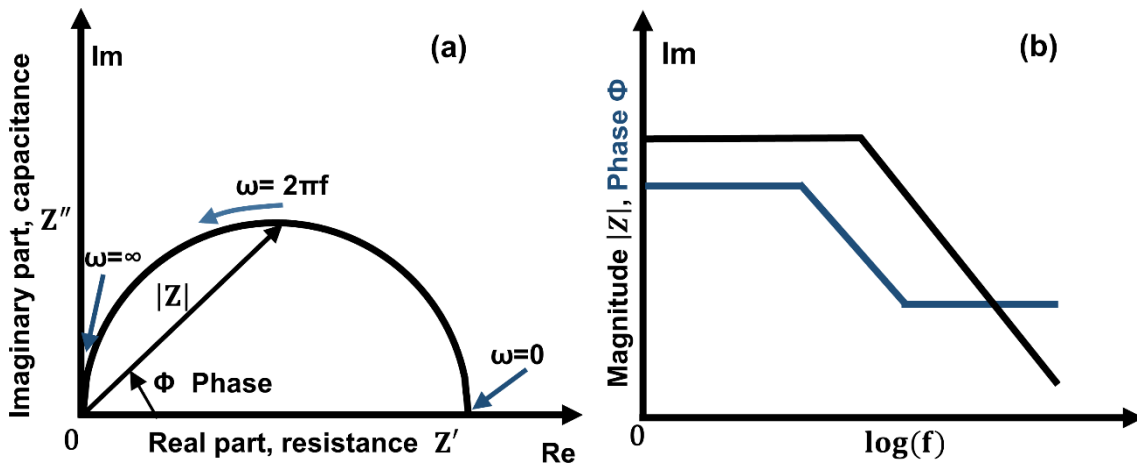


**Figure 2.9:** Schematic demonstration of (a) an impedance plot ( $Z$ ) and (b) a Bode plot. The image is adapted from Ref. [49] with permission from John Wiley & Sons.

Alternatively, a Bode plot is used to present the impedance data. In this plot, the absolute impedance or phase angle is plotted against the log frequency (see **Fig. 2.9b**), representing a maximum at a frequency called relaxation frequency ( $\omega_r$ ), given by:

$$\omega_r = \frac{1}{RC} \quad (2.15)$$

## Experimental Procedure

Where R and C are the resistor and capacitor, representing the faraday current and dielectric displacement current, respectively, in a simple RC circuit. In the relaxation frequency, the current thru the R and C are equal [50]. Solid-state oxides can contain multiple circuits, even with different relaxation frequencies. Depending on the absolute value of R and C, such relaxation frequencies might lead to evolving several semicircles in the Z plane in which each arch is representative of one circuit [51]. This type of behavior is generally observed for ion-conducting ceramics such as ceria, zirconia, *etc.* and can be easily analyzed by considering the so-called brick layer model [52][53]. Assume a polycrystalline system of cubic grains, laterally homogeneous grain boundaries, and parallel homogenous electrodes (see **Fig. 2.10a**). The migration of charge along the highly resistive grain boundary is expected to be very small and can be ignored. Accordingly, only the migration across the grain boundary is considered [54]. The flow of current in each contribution (bulk, grain boundary, electrode) is represented by individual RC-element. The n number of grains can be added together to form a single RC element with n-fold resistance and 1/n-fold capacitance of a single grain. Similarly, the n-1 of grain boundaries, as well as two-electrode impedances, can be combined, respectively, and the model resembles a series combination of three RC elements with (**Fig. 2.10b**).

$$R_{\text{bulk}} = \frac{L}{\sigma_{\text{bulk}} A} \quad (2.16)$$

$$C_{\text{bulk}} = \frac{\varepsilon_{\text{bulk}} A}{L} \quad (2.17)$$

$$R_{\text{g.b.}} = \frac{g}{\sigma_{\text{g.b.}} A} \left( \frac{L}{G-1} \right) \quad (2.18)$$

$$C_{\text{g.b.}} = \frac{\varepsilon_{\text{g.b.}} A}{g} \frac{1}{\left( \frac{L}{G-1} \right)} \quad (2.19)$$

$$R_{\text{el}} = \frac{2w_{\text{el}}}{\sigma_{\text{el}} A} \quad (2.20)$$

$$C_{\text{el}} = \frac{\varepsilon_{\text{el}} A}{2w_{\text{el}}} \quad (2.21)$$

Here L and A are the sample length and area, respectively.  $\varepsilon$  is the dielectric constant, G represents the grain size, g and w are the grain boundary and electrode thickness, respectively. Combing **Eqn 2.16** and **2.17**, the relaxation frequency then becomes,

## Experimental Procedure

$$\omega_r = \frac{\sigma}{\varepsilon} \quad (2.22)$$

and thus independent of geometry. In most common cases, polycrystalline ionic conductors generate a different relaxation frequency for grains, grain boundaries, and electrodes. Accordingly, three semicircles are created in the impedance plot (**Fig. 2.10c**).

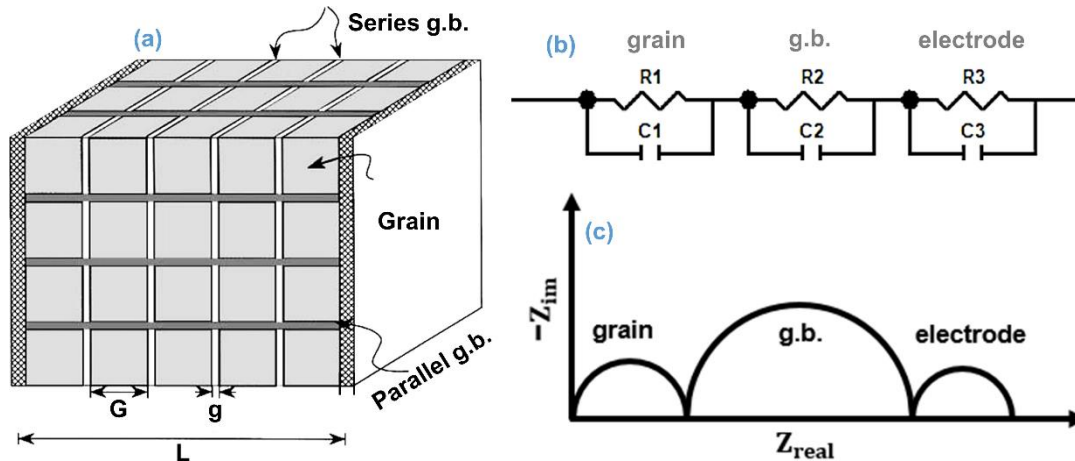


**Figure 2.10:** (a) Brick-layer model: a polycrystal consists of cubic grains, laterally homogeneous resistive grain boundaries and electrodes, respectively, (b) Typical equivalent circuits of RC elements, and (c) resulting characteristic impedance spectra. The image is adapted from Ref. [55] with permission from Cambridge University Press.

The bricklayer model frequently unfit many cases: heterogeneous current flow, spatially varying grain boundary properties or irregular electrodes, *etc.* are the typical problem in solid-state dielectrics [51]. For example, the bulk relaxation frequency is sometimes above the measurement range of the impedance set-up (10 MHz) for a highly conductive material ( $\sigma > 10^{-3}$  S/cm) and non-blocking grain boundaries. The relaxation frequency of the electrode is often too low to separate from the grain boundary. Semicircles sometime overlap due to the development of similar relaxation frequency, especially for nanocrystalline materials [56].

In this experiment, a two-point probe, symmetric cell configuration, electrochemical complex impedance analyzer (Solatron 1260, UK), is used. The sample in the form of a rectangular bar is parallelly coated by silver paste and then dried at 500-600 °C for 1 hour. The sample is sandwiched between two platinum plates in a quartz sample holder. The platinum plates work as current leads. In some experiments, a platinum wire is attached to the sample, which is connected to gold wires and coupled to the platinum wire of the sample holder. The sample

## Experimental Procedure

holder is sealed by a quartz tube and placed inside a tube furnace. The impedance is recorded at a temperature between 250-600 °C at 25 °C interval in a frequency range between  $10^7$ - $10^{-1}$  Hz with an AC voltage of 100 mV in ambient air. The data are fitted by the RC equivalent circuit model and analyzed using ZView software. **Fig. 2.11** shows the impedance spectroscopy set-up for the measurement of bulk ceria ceramics.

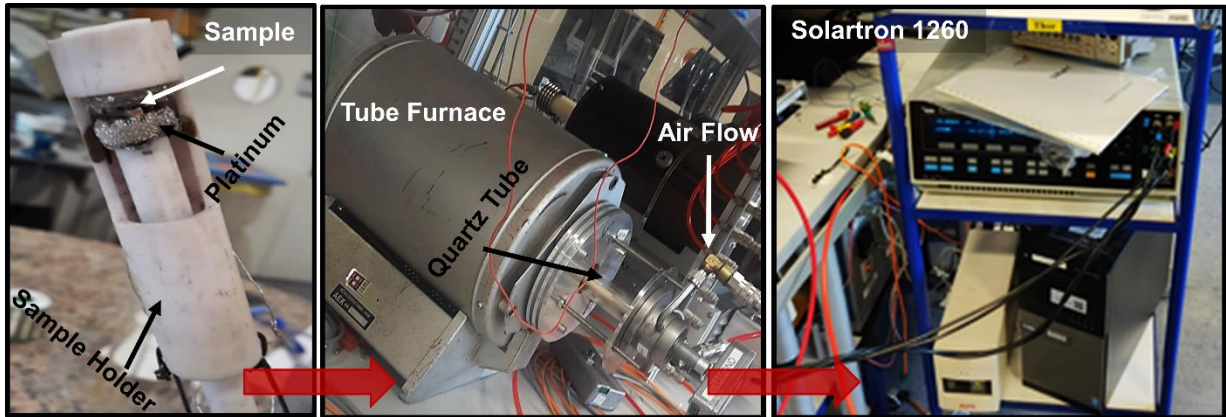


**Figure 2.11:** The instrumental set-up of impedance spectroscopy measurement for bulk pellets. Photo courtesy: Rana-al-Tahan and DTU Energy.

### 2.6 Mechanical Characterization (Nanoindentation)

The mechanical properties of a material are most frequently characterized, employing the indentation method. Nanoindentation is a standard depth-sensing indentation technique applied to small-scale volume to material, allowing to characterize properties such as elastic modulus, hardness, scratch resistance, creep deformation, *etc.* [57][58]. The foundation of this technique is based on the load-displacement profile. For an indentation test, a hard indenter typically diamond with known geometry and properties is pressed onto the top surface of the investigated specimen [59]. The load is then increased progressively to the designed maximum value, might hold constant for some duration, and then unloads (see **Fig 2.12**). The hardness ( $H$ ) is measured from the residual penetration depth of the indenter, which follows the relation [60]:

$$H = \frac{P_{\max}}{A_r} \quad (2.23)$$

## Experimental Procedure

Where  $P_{\max}$  is the maximum load and  $A_r$  is the residual indentation area. The slope of the unloading load-displacement curve is a measure of the stiffness ( $S$ ) of the contact and is used to estimate the elastic modulus  $E_r$ ,

$$E_r = \frac{1}{\beta} \frac{\sqrt{\pi}}{2} \frac{S}{\sqrt{A_p(h_c)}} \quad (2.24)$$

Where  $A_p(h_c)$  is the area of the indentation at contact depth  $h_c$  and  $\beta$  is a geometrical constant. Typically, the depth of nm resolution and load in the  $\mu\text{N}$  range is applied.

The mechanical properties of the samples are investigated by the nanoindentation technique (KLA G200, USA) with a Berkovich indenter at room temperature. The measurement is carried out based on the typical trapezoidal load-hold-unload scheme, as shown in **Fig. 2.12** [58]. The sample is loaded at a rate of 15 mN/s (fast loading) and 1.5 mN/s (slow loading) until the maximum load (150 mN) or maximum depth (1000 nm) is obtained. The load is held constant for 20 sec for both protocols. During dwelling, the progressive creep displacement of the sample is monitored. The creep data is analyzed according to **Eqn 1.31**. The unloading rate is kept the same as loading. The elastic modulus and hardness are measured from the unloading curve using **Eqn 2.23** and **2.24**, as explained by the Oliver-Pharr method [60]. The experimental values reported for each sample are based on measurements at  $> 8$  different locations.

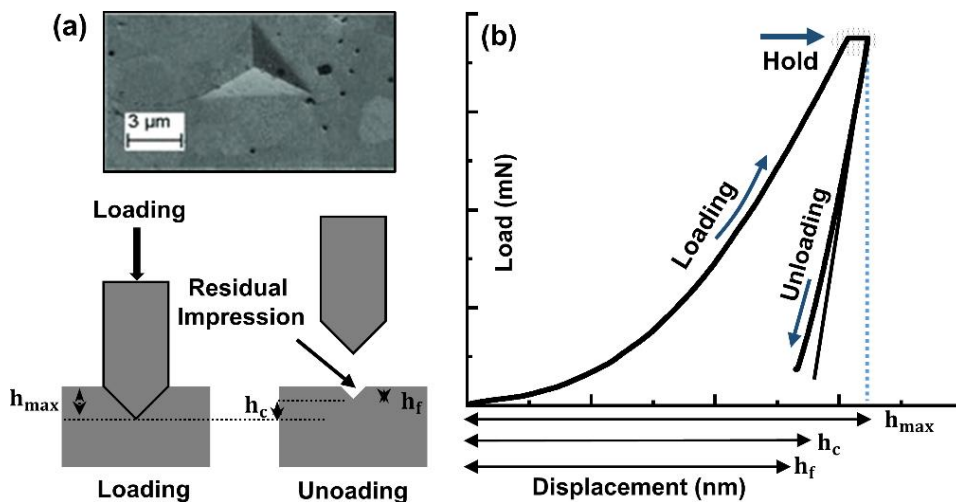


**Figure 2.12:** (a) Schematic drawing of the nanoindentation working principle, the top SEM image shows a typical indenter mark. The image is adapted from Ref. [61][62] with permission from John Wiley & Sons. (b) A representative load-displacement curve in the nanoindentation method.

### 2.7 Electromechanical Characterization

The electromechanical measurement is performed jointly in two different set-ups at Weizmann Institute of Science (WIS) and Technical University of Denmark (DTU), respectively. For the analysis in WIS, the electromechanical strain is measured by a proximity sensor-based system of the capacitance type (Lion) with lock-in detection, as described in detail elsewhere [62]. The sensor measures the absolute displacement of a pushrod (sample), which is connected to the sample surface through a spring. It is essential to have an accurate alignment between the sensor and pushrod, and more than  $2^\circ$  is preferred. The radius of the sensor is 1.5 mm and has a sensitivity of 1.9 mV/nm displacement. The system has an absolute sensitivity of  $\sim 0.05$  nm, equivalent to 0.05 ppm strain for a 1 mm thick sample. It is worth emphasizing that the sample is not subjected to any kind of sputtered coating, whereas two metal electrodes made of aluminum (top) and brass (bottom) are used. The sample is glued (silver paste) to the bottom electrode under a uniaxial force of  $\sim 10$  N. The top electrode is connected to the sample with an applied force around 1 N during the measurement. The AC voltage is applied with changing frequencies, and the sensor measures the subsequent longitudinal electromechanical displacement.

The instrumental set-up in DTU is based on a single-beam laser interferometer of Michelson type. It consists of a beamsplitter, mirrors M1 and M2 (see **Fig. 2.13**). A beam of light from a laser source hits the beamsplitter. Due to its partial reflectiveness, some light is transmitted through the beam splitter to Mirror M1, while some are reflected towards M2. Both of these bounces back the mirrors and are recombined, leading to produce an interference fringe pattern on the detector screen [63]. A gravity wave changes the distance between the mirrors, so it does change the peaks and valleys of incoming beams. Consequently will result in the formation of a constructive pattern with the intensity depending on the difference of mirror distance. Following this intensity, actual displacement is measured.

## Experimental Procedure

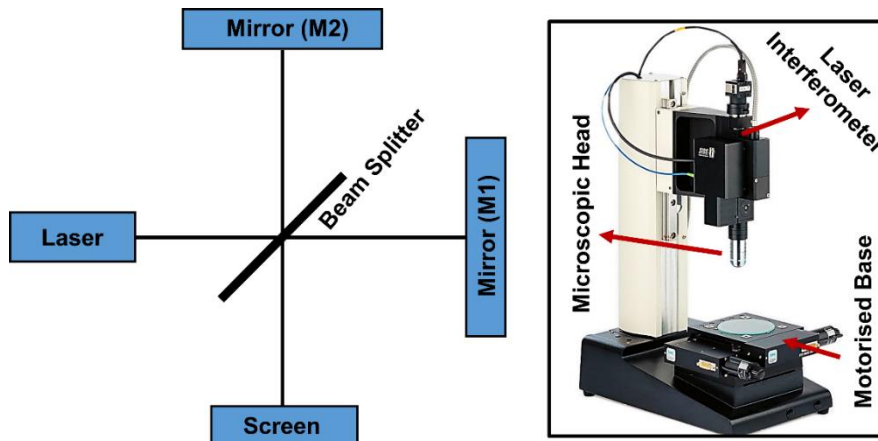


**Figure 2.13:** Schematic drawing of a Michelson laser interferometer (left). Nanovibration analyzer (right). Image courtesy: SIOS (Germany).

The schematic diagram of the set-up is illustrated in **Fig. 2.14**. A laser interferometric vibrometer (SIOS Nanovibration Analyser, Germany) is placed on an optical table to reduce the environmental vibration to the minimum. This instrument can measure with a frequency range of 0-1 kHz with an amplitude resolution of 5 pm. The investigated sample is finely polished (6  $\mu\text{m}$ ) on both sides, and then the gold electrode was sputtered onto it. A single crystal of silicon is glued on the top surface of the sample to increase the optical signal from the laser. Then the sample is fixed by a silver paste onto the specimen holder. The top and bottom electrodes are then connected by two platinum rods. By using a function generator (Aim-TTI TGP 3100), the electric field is applied in a sinusoidal form. The resultant vertical displacement/strain is calculated as a function of electrical fields and frequencies.

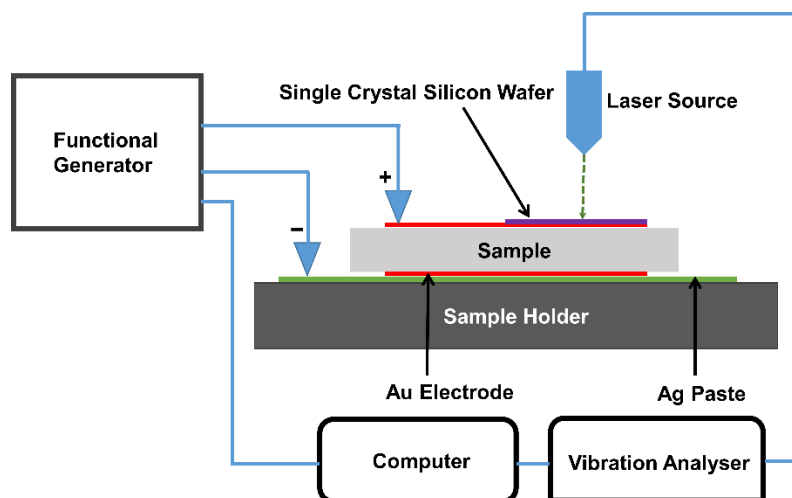


**Figure 2.14:** Schematic representation of the set-up of electromechanical characterization.

## Experimental Procedure

### References:

- [1] B. Matović et al., "Synthesis, calcination and characterization of Nanosized ceria powders by self-propagating room temperature method," *Ceram. Int.*, 39 (2013) 5007–5012.
- [2] M. J. Godinho, R. F. Gonçalves, L. P. S Santos, J. A. Varela, E. Longo, and E. R. Leite, "Room temperature co-precipitation of nanocrystalline CeO<sub>2</sub> and Ce<sub>0.8</sub>Gd<sub>0.2</sub>O<sub>1.9-δ</sub> powder," *Mater. Lett.*, 61 (2007) 1904–1907.
- [3] A. Townshend and E. Jackwerth, "Precipitation of major constituents for trace preconcentration : Potential and problems," *Pure Appl. Chem.*, 61 (1989) 1643–1656.
- [4] I. M. Kolthoff, "'Theory of Coprecipitation.' The formation and properties of crystalline precipitates," *J. Phys. Chem.*, 36 (1932) 860–881.
- [5] M. Kakihana, "'Sol-Gel' preparation of high temperature superconducting oxides," *J. Sol-Gel Sci. Technol.*, 6 (1996) 7–55.
- [6] H. Inaba, "Sintering behaviors of ceria and gadolinia-doped ceria," *Solid State Ionics*, 106 (2002) 263–268.
- [7] J. A. Glasscock et al., "The effect of forming stresses on the sintering of ultra-fine Ce<sub>0.9</sub>Gd<sub>0.1</sub>O<sub>2-δ</sub> powders," *J. Eur. Ceram. Soc.*, 33 (2013) 1289–1296.
- [8] V. Esposito and E. Traversa, "Design of electroceramics for solid oxides fuel cell applications: Playing with ceria," *J. Am. Ceram. Soc.*, 91 (2008) 1037–1051.
- [9] M. Biesuz, L. Spiridigliozzi, M. Frasnelli, G. Dell'Agli, and V. M. Sglavo, "Rapid densification of Samarium-doped Ceria ceramic with nanometric grain size at 900–1100 °C," *Mater. Lett.*, 190 (2017) 17–19.
- [10] U. Anselmi-Tamburini, J. E. Garay, and Z. A. Munir, "Fast low-temperature consolidation of bulk nanometric ceramic materials," *Scr. Mater.*, 54 (2006) 823–828.
- [11] U. Anselmi-Tamburini et al., "Nanoscale effects on the ionic conductivity of highly doped bulk nanometric cerium oxide," *Adv. Funct. Mater.*, 16 (2006) 2363–2368.
- [12] O. Guillon et al., "Field-assisted sintering technology/spark plasma sintering: Mechanisms, materials, and technology developments," *Advanced Engineering Materials*, 16 (2014) 830–849.
- [13] T. Mori and J. Drennan, "Influence of microstructure on oxide ionic conductivity in doped CeO<sub>2</sub> electrolytes," in *Journal of Electroceramics*, 17 (2006) 749–757.
- [14] M. S. M. Ghazali, M. S. Shaifudin, W. R. W. Abdullah, W. M. I. W. M. Kamaruzzaman, M. F. M. Fekeri, and M. A. Zulkifli, "Conventional Sintering Effects on the Microstructure and Electrical Characteristics of Low-Voltage Ceramic Varistor," in *Sintering Technology - Method and Application*, 2018.
- [15] A. Prasad, L. Malakkal, L. Bichler, and J. Szpunar, "Challenges in spark plasma sintering of cerium (Iv) oxide," *Ceram. Trans.*, 261 (2018) 217–224.
- [16] J. Narayan, "A new mechanism for field-assisted processing and flash sintering of materials," *Scr. Mater.*, 69 (2013) 107–111.
- [17] C. Plapcianu, C. Valsangiacom, J. E. Schaffer, A. Wieg, J. Garay, and L. Stanciu, "Spark plasma sintering studies of nanosize lanthanidedoped ceria obtained by sol-gel method," *J. Optoelectron. Adv. Mater.*, 13 (2011) 1101–1108.
- [18] S. K. Sistla, T. Mishra, Y. Deng, A. Kaletsch, M. Bram, and C. Broeckmann, "Electric Field-Assisted Sintering of Gadolinium-Doped Ceria: Sintering and Grain Growth Kinetics," *J. Ceram. Sci. Technol.*, (1–10) 2019.
- [19] D. Marrocchelli, S. R. Bishop, H. L. Tuller, and B. Yildiz, "Understanding chemical expansion in non-stoichiometric oxides: Ceria and zirconia case studies," *Adv. Funct. Mater.*, 22 (2012) 1958–1965.
- [20] J. Guo et al., "Cold Sintering: A Paradigm Shift for Processing and Integration of Ceramics," *Angew. Chemie - Int. Ed.*, 55 (2016) 11457–11461.

## Experimental Procedure

- [21] H. Guo, A. Baker, J. Guo, and C. A. Randall, "Cold Sintering Process: A Novel Technique for Low-Temperature Ceramic Processing of Ferroelectrics," *J. Am. Ceram. Soc.*, 99 (2016) 3489–3507.
- [22] M. Biesuz et al., "A theoretical analysis of cold sintering," *Adv. Appl. Ceram.*, 119 (2019) 75–89.
- [23] J. Guo, S. S. Berbano, H. Guo, A. L. Baker, M. T. Lanagan, and C. A. Randall, "Cold Sintering Process of Composites: Bridging the Processing Temperature Gap of Ceramic and Polymer Materials," *Adv. Funct. Mater.*, 26 (2016) 7115–7121.
- [24] S. Funahashi et al., "Demonstration of the cold sintering process study for the densification and grain growth of ZnO ceramics," *J. Am. Ceram. Soc.*, 100 (2017) 546–553.
- [25] A. Baker, H. Guo, J. Guo, C. Randall, and D. J. Green, "Utilizing the Cold Sintering Process for Flexible-Printable Electroceramic Device Fabrication," *J. Am. Ceram. Soc.*, 99 (2016) 3202–3204.
- [26] H. Guo, T. J. M. Bayer, J. Guo, A. Baker, and C. A. Randall, "Current progress and perspectives of applying cold sintering process to ZrO<sub>2</sub>-based ceramics," *Scr. Mater.*, 136 (2017) 141–148.
- [27] J. Guo, A. L. Baker, H. Guo, M. Lanagan, and C. A. Randall, "Cold sintering process: A new era for ceramic packaging and microwave device development," *J. Am. Ceram. Soc.*, 2017.
- [28] M. Leoni, R. Di Maggio, S. Polizzi, and P. Scardi, "X-ray diffraction methodology for the microstructural analysis of nanocrystalline powders: Application to cerium oxide," *J. Am. Ceram. Soc.*, 87 (2004) 1133–1140.
- [29] R. Heimann and R. Heimann, "X-Ray Powder Diffraction (XRPD)," in *The Oxford Handbook of Archaeological Ceramic Analysis*, 2016.
- [30] "Principles of X-ray Diffraction," in *Thin Film Analysis by X-Ray Scattering*, 2006.
- [31] H. Stanjek and W. Häusler, "Basics of X-ray diffraction," *Hyperfine Interact.*, 2004.
- [32] H. A. Wilson, "The reflexion of x-rays by crystals," *Phys. Rev.*, 18 (1921) 396.
- [33] J. Epp, "X-Ray Diffraction (XRD) Techniques for Materials Characterization," in *Materials Characterization Using Nondestructive Evaluation (NDE) Methods*, (2016) 81–124.
- [34] W. L. Bragg, "The diffraction of short electromagnetic waves by a crystal," *Proc. Camb. Philol. Soc.*, 17 (1913) 43–57.
- [35] A. L. Patterson, "The Scherrer formula for X-ray particle size determination," *Phys. Rev.*, 56 (1939) 978.
- [36] K. C. A. Smith and C. W. Oatley, "The scanning electron microscope and its fields of application," *Br. J. Appl. Phys.*, 6 (1955) 391.
- [37] J. I. Goldstein, D. E. Newbury, J. R. Michael, N. W. M. Ritchie, J. H. J. Scott, and D. C. Joy, *Scanning electron microscopy and x-ray microanalysis*. 2017.
- [38] D. C. Joy, "Introduction to the Scanning Electron Microscope," *Microsc. Microanal.*, 9 (2003) 1556–1557.
- [39] L. Reimer, "Scanning Electron Microscopy: Physics of Image Formation and Microanalysis, Second Edition," *Meas. Sci. Technol.*, 2000.
- [40] C. Scheu and W. D. Kaplan, "Introduction to Scanning Electron Microscopy," *In-Situ Electron Microscopy: Applications in Physics, Chemistry and Materials Science*, 2012.
- [41] "W. Werner," <https://sites.ualberta.ca/~ccwj/teaching/microscopy/#XWerner2012>. (accessed on 04-04-2020).
- [42] K. H. Kim, Z. Akase, T. Suzuki, and D. Shindo, "Charging effects on SEM/SIM contrast of metal/insulator system in various metallic coating conditions," *Mater. Trans.*, 51 (2010) 1080–1083.
- [43] M. I. MENDELSON, "Average Grain Size in Polycrystalline Ceramics," *J. Am. Ceram. Soc.*, 52, (1969) 443–446.
- [44] B. J. Inkson, "Scanning Electron Microscopy (SEM) and Transmission Electron Microscopy

## Experimental Procedure

- (TEM) for Materials Characterization,” in *Materials Characterization Using Nondestructive Evaluation (NDE) Methods*, 2016.
- [45] D. B. Williams and C. B. Carter, *Transmission electron microscopy: A textbook for materials science*. 2009.
- [46] R. Lin, J. Zheng, and J. X. Ma, “Transmission electron microscopy,” in *PEM Fuel Cell Diagnostic Tools*, 2011.
- [47] M. Reza, E. Kontturi, A. S. Jääskeläinen, T. Vuorinen, and J. Ruokolainen, “Transmission electron microscopy for wood and fiber analysis-A review,” *BioResources*. 2015.
- [48] J. R. Macdonald, “Impedance spectroscopy,” *Ann. Biomed. Eng.*, 1992.
- [49] J. R. Macdonald and W. B. Johnson, “Fundamentals of Impedance Spectroscopy,” in *Impedance Spectroscopy: Theory, Experiment, and Applications*, Second Edition, 2005.
- [50] J. Fleig, “Microelectrodes in solid state ionics,” *Solid State Ionics*, 20 (2003) 289–305.
- [51] J. Fleig, “Influence of non-ideal microstructures on the analysis of grain boundary impedances,” *Solid State Ionics*, 131 (2000) 117–127.
- [52] J. Fleig and J. Maier, “The impedance of ceramics with highly resistive grain boundaries: Validity and limits of the brick layer model,” *J. Eur. Ceram. Soc.*, 19 (1999) 693–697.
- [53] X. Guo and R. Waser, “Electrical properties of the grain boundaries of oxygen ion conductors: Acceptor-doped zirconia and ceria,” *Prog. Mater. Sci.*, 51 (2006) 151–210.
- [54] J. H. Hwang, D. S. Mclachlan, and T. O. Mason, “Brick layer model analysis of nanoscale-to-microscale cerium dioxide,” *J. Electroceramics*, 3 (1999) 7–16.
- [55] S. M. Haile, D. L. West, and J. Campbell, “The role of microstructure and processing on the proton conducting properties of gadolinium-doped barium cerate,” *J. Mater. Res.*, 13 (1998) 1576–1595.
- [56] H. L. Tuller, “Ionic conduction in nanocrystalline materials,” *Solid State Ionics*, 131 (2000) 143–157.
- [57] S. P. Baker, “Between nanoindentation and scanning force microscopy: Measuring mechanical properties in the nanometer regime,” *Thin Solid Films*, 308–309 (1997) 289–296.
- [58] V. Maier, B. Merle, M. Göken, and K. Durst, “An improved long-term nanoindentation creep testing approach for studying the local deformation processes in nanocrystalline metals at room and elevated temperatures,” *J. Mater. Res.*, 28 (2013) 1177–1188.
- [59] X. Li and B. Bhushan, “A review of nanoindentation continuous stiffness measurement technique and its applications,” *Mater. Charact.*, 48 (2002) 11–36.
- [60] W.C. Oliver and G. M. Pharr, “An improved technique for determining hardness and elastic modulus using load and displacement sensing indentation experiments,” *J. Mater. Res.*, 7 (1992) 1564–1583.
- [61] R. He et al., “Studies on mechanical properties of thermoelectric materials by nanoindentation,” *Phys. Status Solidi Appl. Mater. Sci.*, 212 (2015) 2191–2195.
- [62] Y. Nimrod et al., “Large Nonclassical Electrostriction in (Y, Nb)-Stabilized  $\delta$ -Bi<sub>2</sub>O<sub>3</sub>,” *Adv. Funct. Mater.*, 26 (2016) 1138–1142.
- [63] P. Giacomo, “The Michelson interferometer,” *Mikrochim. Acta*, 93 (1987) 19–31.

## Chapter 3: The Role of Microstructure and Ion-blocking Factors on Electrostriction

---

### 3.1 Motivation

The existence of electrostriction response in bulk cerium oxides, *i.e.*, 10 mol% Gd-doped ceria (GDC), was first verified by Nivo *et al.* [1]. These authors have characterized more than ten dense (> 97%) samples having a different thickness (0.8-3 mm) with grain size ranging between ~0.5-5  $\mu\text{m}$  for a wide range of applied frequencies. The electrostriction strain coefficient ( $M_{33}$ ) was found to be extremely high ( $\sim 2\text{-}20 \cdot 10^{-17} (\text{m/V})^2$ ), but only for frequency < 10 Hz. The  $M_{33}$  function revealed unexpected frequency-dependent relaxation behavior. Despite such intriguing findings, no correlation between the microstructure, grain size, ionic conductivity, and ion-blocking effect on the electrostriction has been underlined. In this context, the experimental studies described in this chapter seek to address which factor dominates the electrostriction response in bulk GDC.

### 3.2 Effect of Microstructure on 10 mol% Gd-doped Ceria

The following work has been published as "Effect of oxygen defects blocking barriers on gadolinium doped ceria (GDC) electro-chemo-mechanical properties", [A. Kabir](#), S. Santucci, N.V. Nong, M. Varenik, I. Lubomirsky, R. Nigon, P. Muralt and V. Esposito, *Acta Materialia* 174 (2019) 53–60.

The primary goal of this work is to investigate the role of microstructural effect on the electro-chemo-mechanical properties of Gd-doped ceria (GDC). As microstructure evolution strongly depends on the thermal history of the ceramic processing steps, different sintering method is applied. To obtain microstructure of varying grain sizes, nanoscale powders of 10 mol% Gd-doped ceria ( $\text{Ce}_{0.9}\text{Gd}_{0.1}\text{O}_{1.95}$ ,  $\delta = 0.05$ ) with an average size of ~12 nm is consolidated and

thermally treated in different conditions, including field-assisted spark plasma sintering (SPS), fast firing, and conventional free sintering method. Such methodologies govern not only different microstructures but also activate unlikely solute-drag mechanisms and Gd-diffusion, eventually resulting in a different distribution of dopants and oxygen vacancies in the material. Therefore, oxygen vacancy configuration at the ion-blocking barriers, comprising grain boundary, defects association, segregation, *etc.* would not be the same for the different sintering methods. It is recognized that ion-blocking barriers affect the electrochemical properties in the materials. In this work, we emphasize that the same features can control the electromechanical properties of GDC at room temperature.

Nanosize gadolinium doped ceria (GDC10) powder is prepared by the co-precipitation method, as described in section 2.2. The as-synthesized powder is calcined at 500 °C for 2 hours. Two different types of microstructures covering nanocrystalline and microcrystalline are produced, in which each type includes two different samples, as explained in **Table 3.1**.

**Table 3.1:** Sintering protocol of GDC ceramics.

	<b>GDC-10 bulk ceramics</b>			
<b>Type of Microstructure</b>	<b>Nanocrystalline</b>		<b>Microcrystalline</b>	
<b>Sample ID</b>	GDC-SPS	GDC-0.1h	GDC-10h	GDC-2.5h
<b>Sintering Parameter</b>	980 °C-70 MPa	1450 °C-0.1h	1450 °C-10h	1450 °C-2.5h

With the purpose of producing nanostructured GDC, the starting powder is rapidly consolidated in SPS method with a heating rate of 100 °C/min at 980 °C for 5 min under a uniaxial pressure of 70 MPa. The resultant pellet achieves a density above 96% of the theoretical density. As the as-fabricated SPS sample is highly reduced (see chapter 2, section 2.3.2), re-oxidation is performed in the atmospheric air at 700 °C for 1 hour. Another nanostructured material, namely by the fast-firing method, is fabricated by two steps. At first, GDC powder is pre-sintered *via* the SPS at 900 °C for 5 min with 70 MPa and then rapidly heated at 1450 °C for 0.1 hours with a 20 °C/min ramping. For the case of the microcrystalline samples, a conventional heating protocol is followed. The powder is uniaxially and isostatically

cold-pressed, and then sintered at 1450 °C for 10 hours. Another sample is thermally treated at 1450 °C for 2.5 hours. It is worth mentioning that this sample is prepared by a tape casting method and provided by a commercial manufacturer (Kerafol, Germany). Kerafol did not disclose any information about the starting powders, microstructural features, and tape casting parameters, *e.g.*, binders, additives, *etc.*

### 3.2.1 Structural and Microstructural Design by Sintering Methods

**Fig. 3.1a** illustrates the TEM analysis of morphology and crystallographic phase purity of the starting powders. As can be seen, the particles are small and loosely agglomerated, having a so-close spherical shape. The size distribution of the particle is very narrow, with an average size of around 12 nm. The inset image of **Fig. 3.1a** illustrates the corresponding selected area electron diffraction (SAED) pattern, revealing continuous ring patterns of cubic fluorite structure. No additional diffraction spots or rings are observed. This result confirms that powders are highly crystalline and randomly oriented. **Fig. 3.1b** presents a TEM image of a sintered sample in crushed powder form, *i.e.*, pre-sintered sample of GDC-0.1h (SPS at 900 °C). The estimated average particle size is about 70-80 nm, highlighting a limited grain growth in the SPS method. The observation of discrete rings in the SAED pattern (see inset **Fig. 3.1b**) indeed confirms the thermally activated particle coarsening. The most important observation is that a sharp grain-to-grain contact and, in a few cases, a cleavage fracture exists.

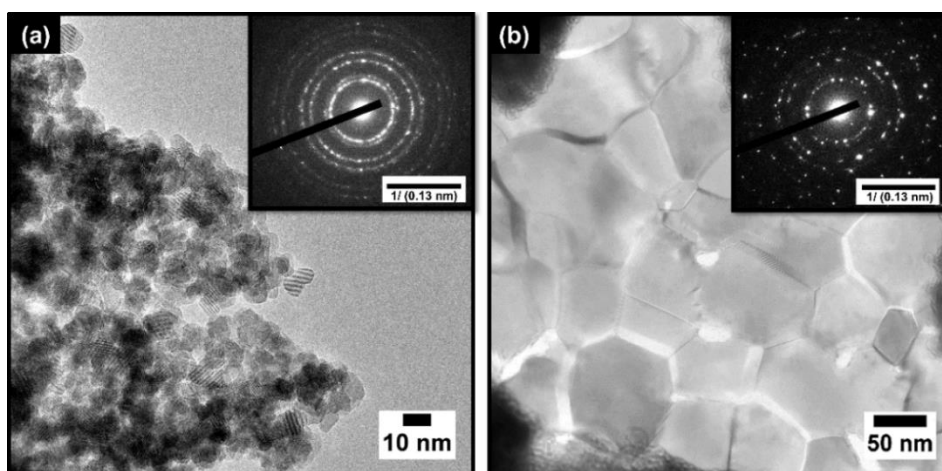


**Figure 3.1:** The conventional TEM image (bright-field) of the (a) GDC powder and (b) pre-sintered GDC-0.1h pellet, SPS at 900 °C. Inset: Respective selective area electron diffraction (SAED) pattern.

The structural phase crystallinity is further verified by the X-ray powder diffraction (XRD) method for both powders and pellets, as demonstrated in **Fig. 3.2**. The diffraction pattern for all samples accord with the theoretic profile of reference undoped ceria sample (ICSD # 251473), representing a cubic fluorite structure (Fm-3m). Within the detection resolution of the XRD technique, no other phases are observed. The estimated lattice parameter and crystallite size for the GDC powder is  $\sim 0.540$  nm and  $\sim 12$  nm, respectively. The crystallite size is measured using the Scherrer formula on the (111) peak. As expected, the diffraction peak becomes more narrow and sharp for the sintered samples, due to the thermally activated particle coarsening [2].

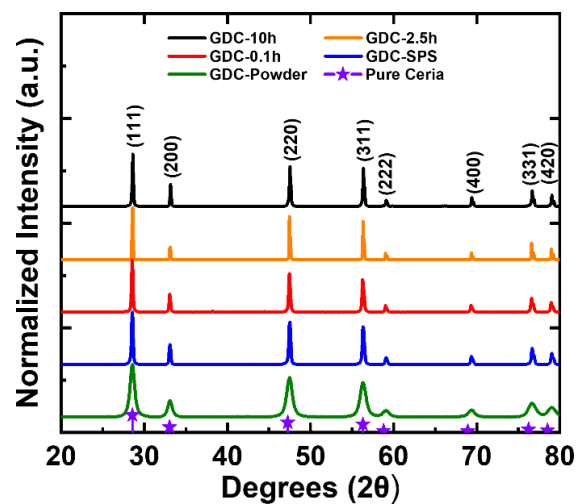


**Figure 3.2:** The X-ray powder diffraction (XRD) pattern of GDC powder and sintered pellets.

The microstructure of the sintered samples is analyzed by a high-resolution scanning electron microscope (SEM) and presented in **Fig. 3.3**. The microstructure appears to be highly dense, which is consistent with the calculated relative density, *i.e.*,  $\geq 96\%$  for all samples. The grain size analysis shows that both the SPS and fast-fired samples (GDC-SPS and GDC-0.1h) have a narrow size distribution, with an average size ranging between  $\sim 150$ - $200$  nm. These grains have a polygonal shape with no surface relaxation at the grain boundary. The limited grain growth in these samples is due to non-conventional thermal treatment, *i.e.*, fast heating rates, which avoids surface-diffusion associated grain-coarsening [3]. On the other hand, conventionally sintered samples exhibit significant grain growth, illustrating a less

homogeneous size distribution. The assessed average grain size of the GDC-10h and GDC-2.5h sample is roughly  $2.0 \pm 0.3 \mu\text{m}$  and  $1.5 \pm 0.2 \mu\text{m}$ , respectively. Moreover, few of these grains are thermodynamically relaxed (see black arrows in **Fig. 3.3**) with a residual small grain boundary curvature as well as having an equilibrium shape at the triple point (see red lines in **Fig. 3.3**). In brief, non-conventional and conventional sintering results in nanocrystalline and microcrystalline microstructure, respectively.

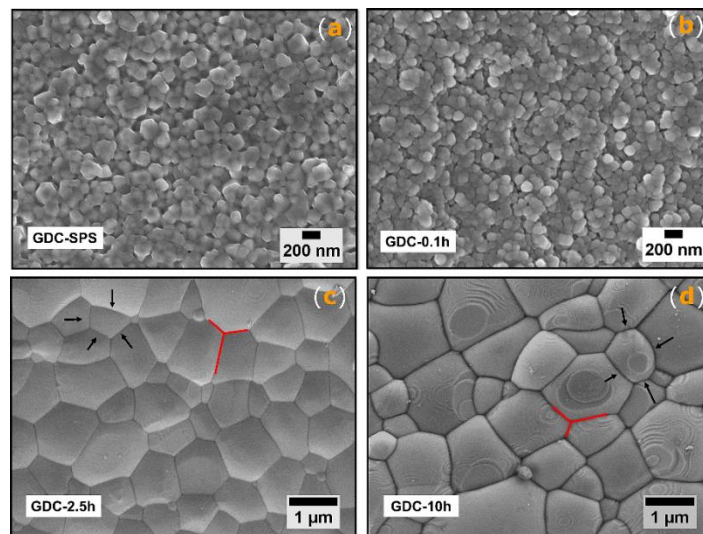


**Figure 3.3:** The scanning electron microscope (SEM) images of four different GDC samples, sintered in (a) SPS at 980 °C, 70 MPa (b) air at 1450 °C, for 0.1h (c) air at 1450 °C, for 2.5h (d) air at 1450 °C, for 10h.

### 3.2.2 Electro-chemo-mechanical Characterization

The state of play of the local environment of oxygen vacancies is measured by electrochemical impedance spectroscopy (EIS). The EIS is carried out from low to high temperatures (~250-575 °C) in atmospheric air with a frequency ranging from  $10^{-1}$ - $10^6$  Hz applying 100 mV alternative potential. Silver is used for the electrodes in the symmetric configuration. The electrical impedance is analyzed in the form of geometry normalized Nyquist and Bode-like plot and is represented in **Fig. 3.4a**, and **Fig. 3.4b** for the measurement at 300 °C. The geometry normalization accounts for the total volume of the sample and does not include the actual volume fraction of the grain boundary. The plots are fitted using an equivalent circuit

model of RQ element where R and Q are denoted as the resistor and constant phase element, respectively. The capacitance (C) is estimated from the following equation:

$$C = (R^{1-n}Q)^{1/n} \quad (3.1)$$

Where n is the fitting parameter. The nanocrystalline samples (GDC-SPS and GDC-0.1h) displays a single semicircle in the Nyquist plot, as evident in **Fig. 3.4a**, which corresponds to superimposed bulk and grain boundary contribution. Such a feature can arise because nanocrystalline materials have a similar order of magnitude in the space charge layer width and the grain size [4]. Due to a comparable size effect, bulk and grain boundary might also have close similarities in relaxation times [5]. Above all, the relatively higher resistance value in these materials points out that the overlapped semicircle should be dominated by the overwhelming contribution of the grain boundary resulted from its high density. This consequence also affects the capacitance value as one order smaller magnitude is reported than typical grain boundary capacity (see **Table 3.2**).

In contrast, microcrystalline samples (GDC-10h and GDC-2.5h) exhibit two well-defined semicircles that resemble bulk and grain boundary contribution according to the bricklayer model. The resistivity of the bulk between these samples is identical. However, a significant difference in the grain boundary arises. The effect of the ion blocking properties is characterized employing the grain boundary blocking factor ( $\alpha_{gb}$ ), which is defined as the ratio of grain boundary resistance to the total resistance ( $\alpha_{gb} = \frac{R_{gb}}{R_{bulk} + R_{gb}}$ ) [6]. One should note that the ion-blocking effect ( $\alpha_{gb}$ ) not only includes the contribution from the grain boundary but also other blocking sources such as defect-dopant association, nanodomains, segregation, residual pore, *etc.* [7][8]. For simplicity, the grain boundary is accounted as the origin of the second semicircle in the Nyquist plot, as stated in the bricklayer model. The estimated  $\alpha_{gb}$  for the GDC-10h and GDC-2.5h is about 0.9 and 0.65, respectively, at 300 °C. The observed grain size in the former is larger than the latter, further validating the experimental hypothesis that the ion-blocking factor is not a mere geometrical effect [9]. The nature of the Gd-diffusion

drives the highly different oxygen vacancy configuration between the samples, associated with the solute drag effect owing to different thermal treatments, *i.e.*, diffusion kinetics.

The low-frequency arc in the Nyquist plot attributes to the electrode/material interface polarization mechanisms and is not relevant for this discussion [10]. The distribution of oxygen vacancies is estimated through the relaxation frequency illustrated in a Bode-like plot in **Fig. 3.4c**. Due to identical bulk resistivity, both the GDC-10h and GDC-2.5 samples expose a similar bulk relaxation frequency ( $\sim 200$  kHz). However, dissimilar grain boundary relaxation occurs due to their different grain boundary resistivity. In general, high bulk and low grain boundary relaxation frequency represent a substantial ion-blocking effect, as observed in the GDC-10 sample. The nanocrystalline sample reveals a single relaxation frequency, for example,  $\sim 1.2$  kHz and  $\sim 5$  kHz for GDC-SPS and GDC-0.1h sample, respectively.

Additionally, a closer look in **Fig. 3.4c** indicates that the GDC-0.1h sample does respond similarly to the microcrystalline samples at the high-frequency regime, whereas GDC-SPS exhibits a feeble response. The impedance data, including capacitance, dielectric constant, and relaxation frequency of the samples, as well as the grain size, are summarized in **Table 3.2**.

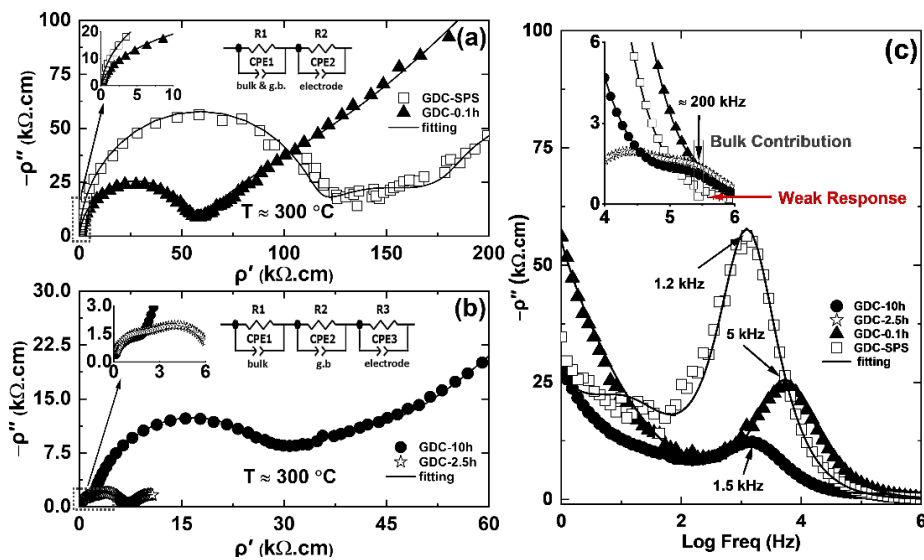


**Figure 3.4:** Geometry normalized (a) Nyquist plot ( $\rho'$  vs  $\rho''$ ) of GDC-SPS and GDC-0.1h sample, (b) Nyquist plot ( $\rho'$  vs  $\rho''$ ) of GDC-10h and GDC-2.5h sample, (c) Bode-type plot (imaginary  $\rho''$  vs log frequency) of all GDC compounds.

**Table 3.2:** The summary of impedance analysis at 300 °C together with the average grain size.

Sample ID	$C_{\text{total}}$ (F)		$f_{\text{total}}$ (Hz)		Dielectric Constant ( $\epsilon$ )	Grain Size (nm)
GDC-SPS	$2.0 \cdot 10^{-11}$		$1.2 \cdot 10^3$		130	$200 \pm 25$
GDC-0.1h	$3.5 \cdot 10^{-11}$		$5.0 \cdot 10^3$		150	$170 \pm 20$
	$C_{\text{bulk}}$ (F)	$C_{\text{gb}}$ (F)	$f_{\text{bulk}}$ (Hz)	$f_{\text{gb}}$ (Hz)	Dielectric Constant ( $\epsilon$ )	Grain Size ( $\mu\text{m}$ )
GDC-10h	$1.2 \cdot 10^{-11}$	$3.0 \cdot 10^{-10}$	$2.0 \cdot 10^5$	$1.5 \cdot 10^3$	450	$2.0 \pm 0.3$
GDC-2.5h	$2.9 \cdot 10^{-11}$	$4.0 \cdot 10^{-10}$	$2.0 \cdot 10^5$	$2.0 \cdot 10^4$	750	$1.5 \pm 0.2$

The Arrhenius type temperature-dependent electrical conductivity of the samples are shown in **Fig. 3.5**. The conductivity is measured separately for total, bulk, and grain boundaries. It is worth mentioning that electronic contribution is negligible at atmospheric pressure for a highly doped compound such as 10 mol% GDC [11]. Accordingly, it is assumed that electrical conductivity is merely dominated by the mobility of oxygen vacancies ( $V_{\text{O}}$ ). As shown in **Fig. 3.5a**, the total electrical conductivity ( $\sigma = 1/\rho'$ ) of the conventionally sintered microcrystalline samples (GDC-2.5h and GDC-10h) exhibit a higher value than nanocrystalline samples (GDC-SPS and GDC-0.1h). Amongst all samples, the GDC-2.5h records maximum conductivity, and it also contains relatively low activation energy for charge migration. Other specimens have a relatively higher activation energy value of  $\sim 0.9$ - $1.0$  eV. Additionally, **Fig. 3.5b** distinguishes bulk and grain boundary (specific) conductivity of the GDC-10h and GDC-2.5h samples. The bulk and grain boundary resistivity are normalized by the actual volume of each component, as reported in Ref. [12]. Both materials show a similar bulk conductivity. However, a noteworthy difference in grain boundary conductivity is noticed which is not surprising as they contain a different degree of ion-blocking factor ( $\alpha_{\text{gb}}$ ). Moreover, they reveal comparable activation energy for both bulk and grain boundaries. The total electrical conductivity of the nanocrystalline sample is also plotted in **Fig. 3.5b**, assuming that grain boundary and/or other blocking sources control the charge transport in these samples.

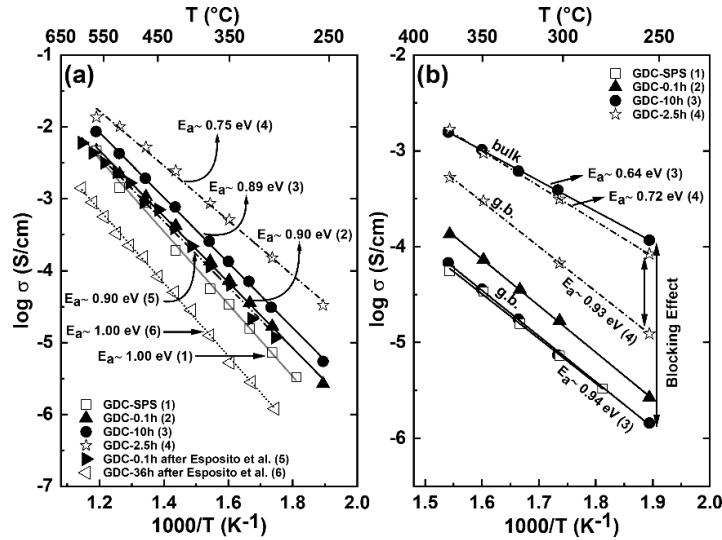


**Figure 3.5:** The Arrhenius plot for the estimation of (a) total electrical conductivity of the GDC samples, in comparison with data from the literature [9], (b) bulk and (specific) grain boundary electrical conductivity of conventionally sintered GDC-10h and GDC-2.5h samples.

The electromechanical characterization of these samples has been conducted in collaboration with Professor Igor Lubomirsky at Weizmann Institute of Science. A proximity sensor of capacitance-type with lock-in detection is used to measure the atomic-scale displacement. The sample is placed in between two metal electrodes, namely aluminum (top) and brass (bottom). The electromechanical strain with the response to the external electrical field at given frequencies is represented in **Fig. 3.6**. All of the compounds respond at the second harmonic of the applied field frequency, verifying the existence of electrostriction behavior. Notably, a negative longitudinal strain is observed that agrees with the previous reports of GDC thin films and bulk materials [1][13]. The strain value starts to saturate at a particular electric field, and a more marked effect is detected at low applied frequency. In addition to that, the strain values get relaxed at higher frequencies. The strain saturation of the GDC samples is fitted with the following empirical equation:

$$u(E^2) = M_{33} \cdot E_{\text{sat}}^2 \cdot \left[ 1 - \exp\left(-\frac{E^2}{E_{\text{sat}}^2}\right) \right] \quad (3.2)$$

Where  $M_{33}$  is the electrostriction strain coefficient (3-3), and  $E_{\text{sat}}$  is the saturation electric field. The classical relationship (electromechanical strain  $\propto E^2$ ) is no more valid above the saturation point. Comparing results among the samples, the GDC-10h displays a maximum strain at any

given field and frequency (see **Fig. 3.6**). Interestingly, the GDC-2.5h illustrates a significantly lower strain than GDC-10h, especially under the small electric field. The former does not reveal any strain saturation, even experiencing up to  $\sim 9$  kV/cm electric field. However, the latter starts to saturate at an electric field around  $\sim 5$  kV/cm. Such a significant change in the electromechanical response is unexpected, as both these samples have a very similar microstructure and grain size. Furthermore, the most unanticipated result is observed with the GDC-SPS material. This sample does not respond at all below 5 kV/cm, and it requires a large electric field to exhibit reasonable strain. The GDC-0.1h sample displays an identical trend, like the GDC-10h. Nonetheless, it registers a slightly smaller strain than the latter.

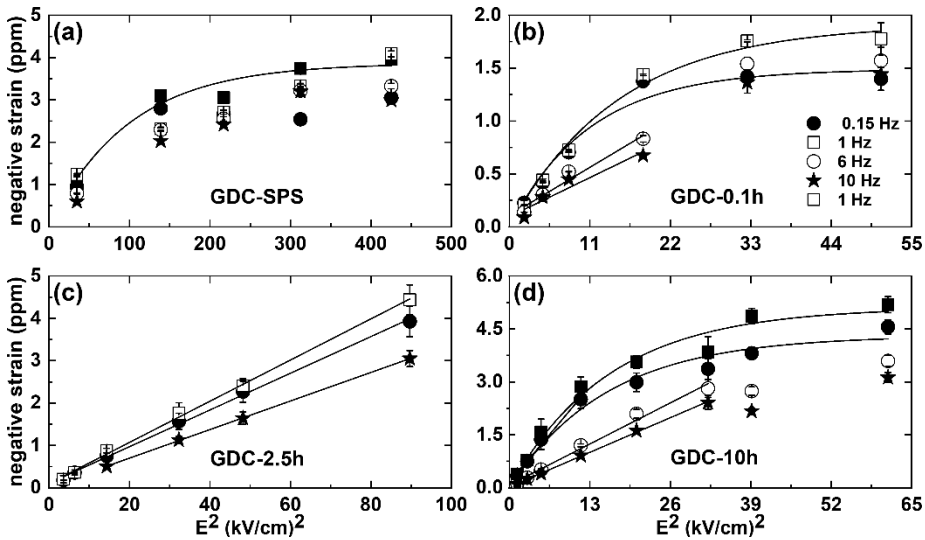


**Figure 3.6:** (a)-(d) The electrostrictive negative strain with the response to the external electric field square at frequencies between 0.15-10 Hz.

The electrostrictive strain coefficient ( $M_{33}$ ) is measured as a function of frequency up to 100 Hz and is represented in **Fig. 3.7**. As can be seen, all materials decrease their  $M_{33}$  value with increasing frequencies. More precisely, such relaxation occurs in the frequency range of 1-20 Hz. The relaxation of frequency-dependent  $M_{33}$  is empirically fitted by (non-ideal-Debye) following equation:

$$M_{33}(f) = \frac{M_{33}^0}{\sqrt{1+(\tau.f)^{2+\alpha}}} + M_{33}^\infty \quad (3.3)$$

Here,  $M_{33}^0$  and  $M_{33}^\infty$  are the frequency-related electrostriction coefficient.  $\tau$  is the relaxation frequency, and  $\alpha$  is the non-ideality factor. The measured fitting parameters are summarized

in **Table 3.3**. All samples illustrate a proper fit except GDC-0.1h, as it includes only a few measurements at the low-frequency range.

**Table 3.3:** Summary of the fitted parameter of Eqn 3.3 for GDC pellets.

Sample ID	$M_{33}^0$	$M_{33}^\infty$	$\tau$	$\alpha$
GDC-SPS	$0.3 \pm 0.01$	$0.07 \pm 0.01$	$0.25 \pm 0.02$	$-0.55 \pm 0.15$
GDC-0.1h	$2.3 \pm 1.8$	$-0.50 \pm 0.8$	$3.10 \pm 10$	$-1.65 \pm 0.3$
GDC-10h	$3.2 \pm 0.2$	$0.18 \pm 0.01$	$0.80 \pm 0.12$	$-0.5 \pm 0.08$
GDC-2.5h	$0.4 \pm 0.02$	$0.2 \pm 0.01$	$0.2 \pm 0.03$	$-0.15 \pm 0.03$

At lower-frequency, the GDC-10h sample demonstrates the maximum  $M_{33}$  value with an order of magnitude larger than GDC-SPS and GDC-2.5h sample. However, at higher-frequency (> 10 Hz) the value of  $M_{33}$  is almost identical for all compounds and in order of  $\sim 10^{-18}$  (m/V<sup>2</sup>). Such a magnitude is still one order greater than the prediction of the classical Newnham model. The recent report of Yavo *et al.* also demonstrated strain saturation and frequency associated relaxation for bulk GDC ceramics [1]. By considering such an outcome, the current work concludes that strain saturation and relaxation effects are an intuitive hallmark of the electromechanical properties of bulk Gd-doped ceria. Comparative analysis of grain boundary resistivity, ion-blocking factor, and electrostriction strain coefficient is described in **Table 3.4**.

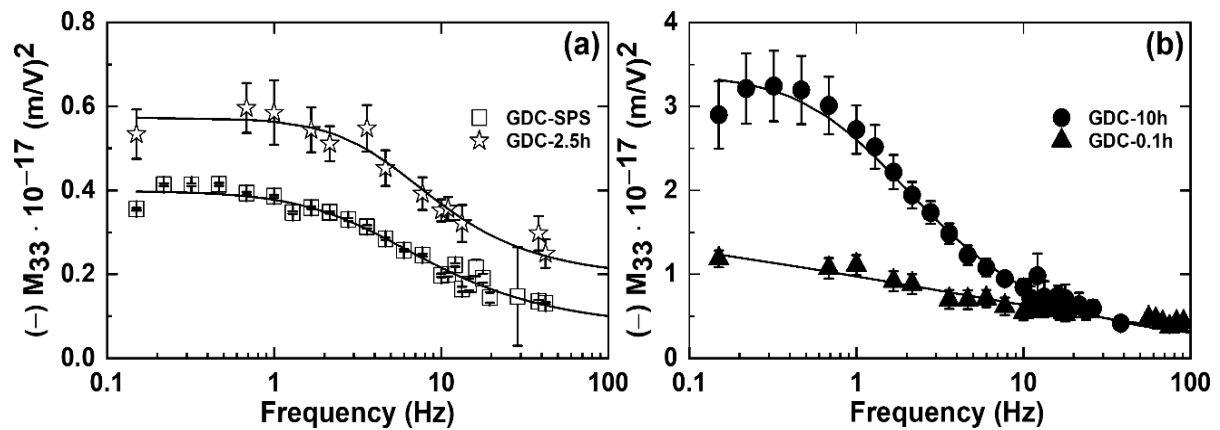


**Figure 3.7:** (a)-(b) The electrostrictive strain coefficient ( $M_{33}$ ) of the GDC samples as a function of applied frequency, up to 100 Hz.

## The Role of Microstructure and Ion-blocking Factors on Electrostriction

**Table 3.4:** The comparative analysis of the grain boundary resistivity, ion-blocking factor, and electrostriction strain coefficient ( $M_{33}$ ) of the GDC samples.

Material Properties	Nanocrystalline		Microcrystalline	
	GDC-SPS	GDC-0.1h	GDC-10h	GDC-2.5h
<b>G.B. Resistivity</b> ( $\approx 300^\circ\text{C}$ ) [ $\Omega\cdot\text{cm}$ ]	~100000	~50000	~30000	~3500
<b>Electrostriction</b> ( $\approx 1\text{ Hz}$ ) ( $\text{m/V}$ ) <sup>2</sup>	$0.4 \cdot 10^{-17}$	$1.0 \cdot 10^{-17}$	$2.8 \cdot 10^{-17}$	$0.6 \cdot 10^{-17}$
<b>Ion-blocking Factor</b> ( $\approx 300^\circ\text{C}$ )	~1	~0.65-0.9	0.9	0.65

By correlating these experimental findings, a conclusion can be drawn. All these samples contain the same oxygen vacancy concentration. However, they represent a somewhat different electromechanical response. Such results resolutely emphasize that oxygen vacancy concentration is not an accurate parameter controlling the electrostriction mechanism. Another clear evidence is that microstructure does not play any significant role in assessing the electrostriction in GDC. Surprisingly, the resistivity at the grain boundary, more precisely the ion-blocking factors acts a dominant role in controlling electrostriction at the low-frequency regime. Despite having a small density of ion-blocking barriers, the GDC-10h sample displays higher electrostriction than the GDC-0.1h and GDC-SPS samples of large blocking barrier density. Such an effect highlights the dominant role of oxygen vacancy configuration on the electromechanical properties in GDC. The electrostriction strain coefficient is scaled up with increasing ion-blocking factors up to a limit and then falls off significantly for an extensive blocking zone (see **Fig. 3.8**). This kind of region can be termed as a super blocking zone where a drastic voltage drop would occur (GDC-SPS).

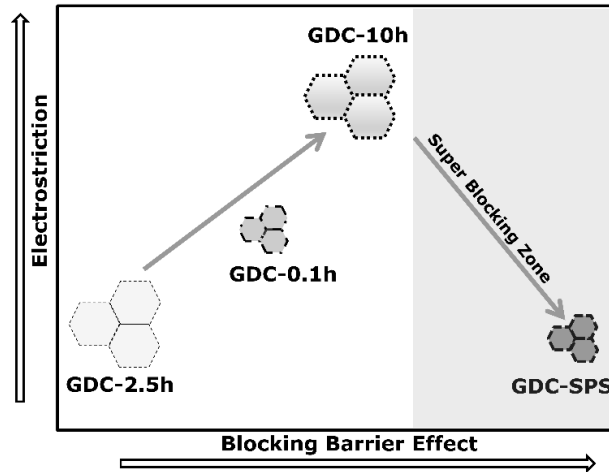


**Figure 3.8:** A schematic correlation of the electrostriction strain coefficient ( $M_{33}$ ) at the low-frequency regime with ion-blocking barriers for polycrystalline Gd-doped ceria ceramics.

### 3.3 Grain Boundary Engineering by Fast Diffusion/Cold Sintering

The following work has been submitted as "Effect of Cold Sintering Process (CSP) on the Electro-Chemo-Mechanical Properties of Gd-doped Ceria (GDC)", [A. Kabir](#), D. Ke, S. Grasso, B. Merle and V. Esposito, Journal of European Ceramics Society (under review).

The previous section elucidates that the grain size does not have any dominant contribution to the electrostrictive properties for bulk Gd-doped ceria (GDC). Surprisingly, the diffusion-controlled ion-blocking barriers built in the materials act as a central parameter to tune the electrostriction properties. To authenticate this hypothesis by reproducing similar results, we carried out additional experiments aiming to control the chemistry of the grain boundary in GDC. The electromechanical characterization is performed at a different set-up at DTU, which will further confirm the accuracy of the result since such a nanoscale range displacement technique might include measurement uncertainties or environmental errors.

The current study includes the same material composition as the previous one, *i.e.*, 10 mol% Gd-doped ceria (GDC) but with a different starting powder. The ion-blocking barriers,

particularly grain boundaries, are intended to be modified by a liquid mediated surface diffusion mechanism, applying a novel low-temperature cold sintering process (CSP). The effect of CSP on the electrochemical and mechanical properties are also a matter of interest.

A high-purity commercial 10 mol% Gd-doped ceria powders (Rhodia, France) with specific BET surface area  $\approx 35 \text{ m}^2/\text{g}$  are used in this experiment. To fabricate the sample through the CSP process, 1 g of GDC powder is mixed with 0.4 ml of distilled water in a centrifuge tube using a vortex mixer. The resultant paste is then put into a 15 mm steel die and uniaxially pressed at 300 MPa. Afterward, the temperature is applied and increased slowly from room temperature up to 200 °C and held for 0.5 hours. Moreover, the observed relative density of the sample is nearly 70%, which is not suitable for the desired properties. Thus, a second step thermal treatment is done at 1000 °C for 1 hour with a heating rate of 10 °C/min. The resultant macroscopic density of around 90%, as measured *via* the Archimedes method in the water medium. For a direct property comparison, two reference samples are produced. One material is conventionally sintered at 1450 °C for 1 hour in the air. The other sample is prepared through the SPS process at 1100 °C with a constant uniaxial pressure of 50 MPa for 5 min dwelling. The SPS sample is then re-oxidized at 800 °C for 10 hours. Compared to the previous SPS experiment, as shown in section 3.2, 100 °C higher re-oxidation temperature and longer times are applied to ensure that the sample is oxidized entirely from the surface to the inner core.

### 3.3.1 Structural and Microstructural Analysis by Designed Grain Boundary

**Fig. 3.9** shows the XRD diffraction pattern of the GDC powders and sintered pellets. As noted, the reflection peaks of all samples correspond to the general pattern of pure ceria (ICSD # 251473), indicating a single-phase cubic fluorite structure. The evaluated crystallite size from the (111) peak is about 10 nm.

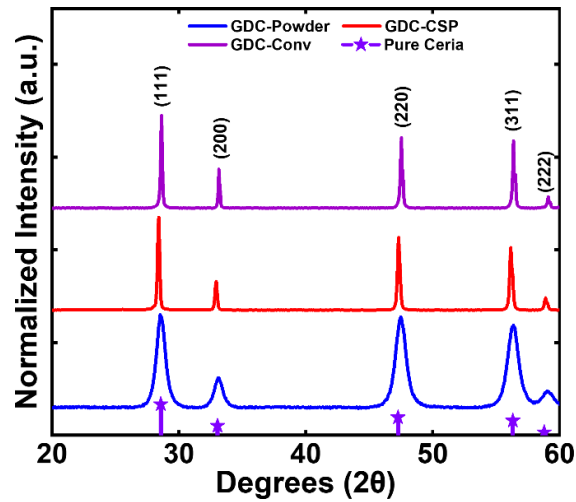


**Figure 3.9:** The X-ray diffraction (XRD) pattern of commercial 10 mol% gadolinium doped ceria (GDC) powder and sintered pellets.

The micrographs of the sintered samples are taken in a high-resolution electron microscope (SEM) and presented in **Fig. 3.10**. The reference GDC-SPS and GDC-Conv samples illustrate a microstructure comparable to the previous experiment (see **Fig. 3.3**). Moreover, the GDC-CSP sample shows a unique microstructure. This sample is relatively less dense and consists of 10-15% of residual open porosity, as measured with the ImageJ tool [14]. The grains are highly homogeneous, extremely non-relaxed, and small. They have typical spherical shapes with an average grain size of around  $80 \pm 20$  nm.

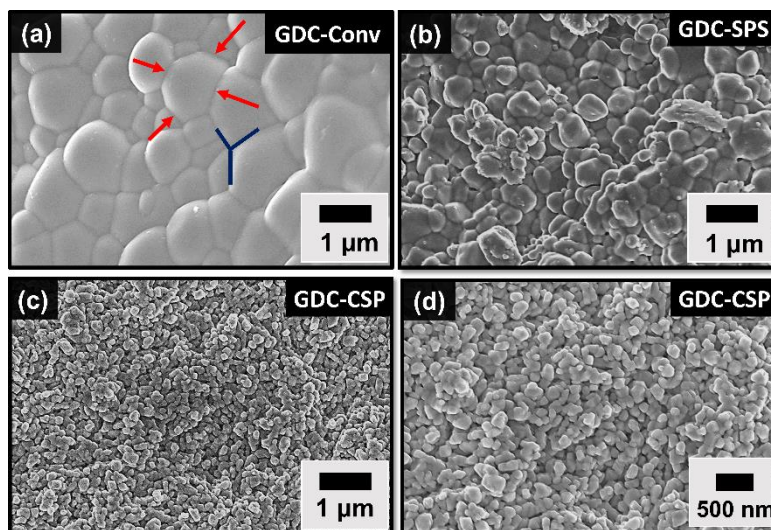


**Figure 3.10:** Scanning electron microscope (SEM) images of the GDC pellets, sintered in (a) conventional firing at 1450 °C for 1 hour, (b) SPS at 1100 °C for 5 min with 50 MPa, (c)-(d) CSP at 200 °C for 0.1h with 300 MPa, post-annealing at 1000 °C for 1 hour.

More detailed information about the microstructure of the GDC-CSP is obtained from the TEM image shown in **Fig. 3.11**. The analysis at low magnification illustrates the presence of residual pore. A rough estimation of pore diameter size is between 10-15 nm. It also shows that grain-to-grain contact is flat, and no visual evidence of impurity segregation is noted. The high magnification image indicates the presence of grain boundaries. The measured thickness of the grain boundary is around 0.5 nm.

The formation of such a microstructure with a large density of grain boundaries without the possible dopant segregation lies in the diffusion mechanism of the cold sintering process. From a kinetic point of view, mass transport during sintering is faster in the CSP than conventional solid-state diffusion due to the introduction of the aqueous phase, as described more in detail in chapter 2.

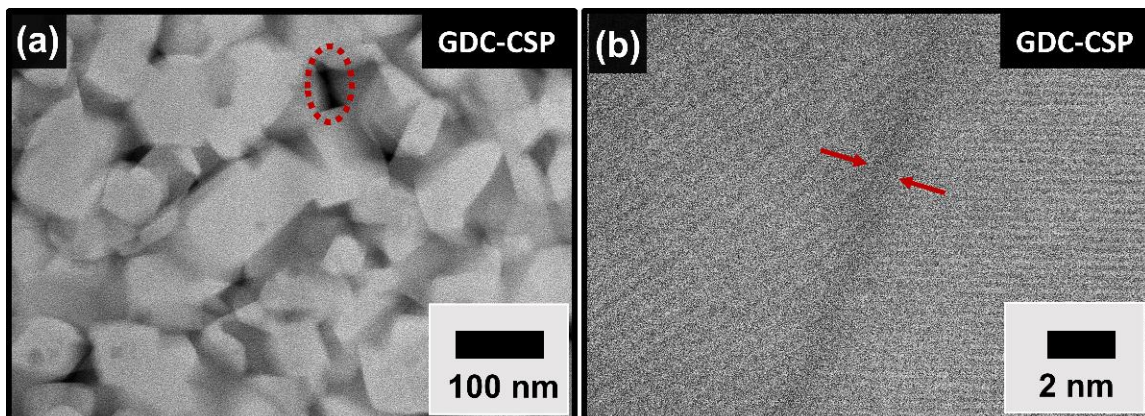


**Figure 3.11:** (a)-(b) High-resolution transmission electron microscopy (TEM) image of the GDC-CSP sample at low and high magnification (HAADF mode).

### 3.3.2 Electro-chemo-mechanical Characterization

The electrochemical properties are analyzed by the electrochemical impedance spectroscopy (EIS) in a temperature range of  $\sim 250$ - $500$  °C, with frequencies between  $\sim 10^{-1}$ - $10^7$  Hz under air. The impedance data at  $300$  °C is represented in **Fig. 3.12** as a geometry corrected Nyquist plot. The plots are fitted with an equivalent circuit according to the bricklayer model. The GDC-Conv and GDC-SPS samples display two well-defined semicircles, referring to the high and intermediate frequency associated with bulk and grain boundary impedance, respectively [15]. However, one semicircle is visible in the GDC-CSP sample that is attributed to the overlapped

bulk, grain boundary, and reduced grains contact due to porosity impedance. As mentioned in the previous section, such kind of response is typical for highly nanocrystalline ceria having a similar space charge width and grain size [4]. Moreover, a closer look at the high-frequency region of the impedance plot shows a discontinuity, indicating a probable bulk contribution. Assuming such a feature, ion-blocking factor ( $\alpha_{gb}$ ) is estimated to be above 0.96. As mentioned in section 3.2,  $\alpha_{gb}$  combines all blocking sources such as grain boundary, defects association, impurity segregation, nanodomains, residual pore, etc. The assessed  $\alpha_{gb}$  is much larger in the GDC-Conv ( $\alpha_{gb} \sim 0.85$ ) sample than of GDC-SPS ( $\alpha_{gb} \sim 0.60$ ). Comparing SPS results with the previous experiment, it is noticed that the use of high purity powder,  $\sim 100^\circ\text{C}$  higher sintering and reoxidation temperature, long re-oxidation time all combined reduces the ion-blocking effects. The measured total resistivity of the GDC-CSP is roughly 5-fold larger than the GDC-Conv sample.

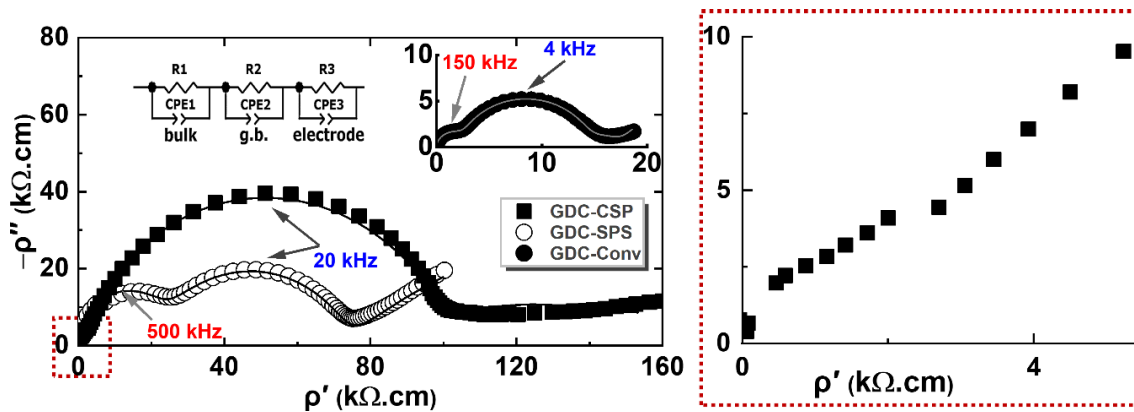


**Figure 3.12:** Typical geometry normalized Nyquist plots ( $\rho'$  vs  $\rho''$ ) as characterized by frequencies, recorded at  $300^\circ\text{C}$  for the GDC pellets. The red box shows impedance at the high-frequency regime.

The temperature dependence total electrical conductivity of the samples is demonstrated in **Fig. 3.13**. The plot shows that the GDC-SPS and GDC-CSP have identical electrical conductivity at low temperatures ( $< 350^\circ\text{C}$ ), but at least an order of magnitude smaller than the GDC-Conv sample. On the other hand, at a higher temperature ( $> 400^\circ\text{C}$ ), the GDC-CSP sample matches the conductivity of the GDC-Conv sample. The activation energy for charge migration is maximum in the GDC-CSP sample that is mainly related to the residual porosity as well as a high density of grain boundaries.

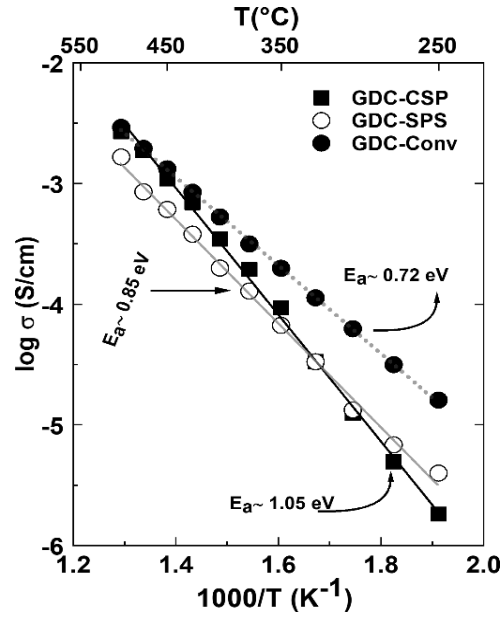


**Figure 3.13:** The temperature-dependent total electrical conductivity of the GDC samples, measured between 250-500  $^{\circ}C$ .

The mechanical properties of the GDC samples are carried out by the nanoindentation (NI) technique using continuous stiff measurement (CSM) mode at room temperature. The load is applied at a rate of 15 mN/s (fast loading) until a value of load 150 mN or depth of 1000 nm is reached. The load is then held constant for 20 sec. During this segment, progressive deformation (creep) of the sample as a function of time is measured. The same unloading rate is applied, like loading. The elastic modulus and hardness are measured from the unloading curve using the Oliver-Pharr method [16]. The experiment is taken at 12 different locations, and results are reported on averaging more than eight data points. **Fig. 3.14** represents a characteristic load/displacement-time curve in a nanoindentation measurement. All three samples illustrate a continuous deformation during the hold segment of the loading, indicating a creep behavior (see inset **Fig. 3.14**). The creep deformation is expressed with the following formula:

$$(u - u_0) = A (t - t_0)^m \quad (3.4)$$

Where  $u_0$  is the initial displacement at the commencement of hold stage  $t_0$ ,  $A$  the creep constant and  $m$  the fitting exponent. At room temperature, creep is very unlikely for ceramics, especially for ceria, which has a high melting point. It has been demonstrated that such an

unusual property is governed by the rearrangement of distorted lattice complex under external anisotropic stress [17][18]. The values of these parameters are listed in **Table 3.5**. The results highlight that A value is constant regardless of reaching 100 mN load or 1000 nm depth. It is comparatively higher in the GDC-CSP sample than counterparts and can be attributed to the super-fine grains and residual porosity. The pore can assist the lattice rearrangement by decreasing the grain-to-grain contact areas, resulting in less constraint and residual stress. The creep fitting parameter m varies between 0.3-0.4 and inversely correlates with the experimental A values. The estimated elastic modulus and hardness are also reported in **Table 3.5**. Interestingly, both these values scale down with decreasing grain sizes in which ~35-40% reduced values are obtained in the GDC-CSP sample compared to the GDC-Conv.

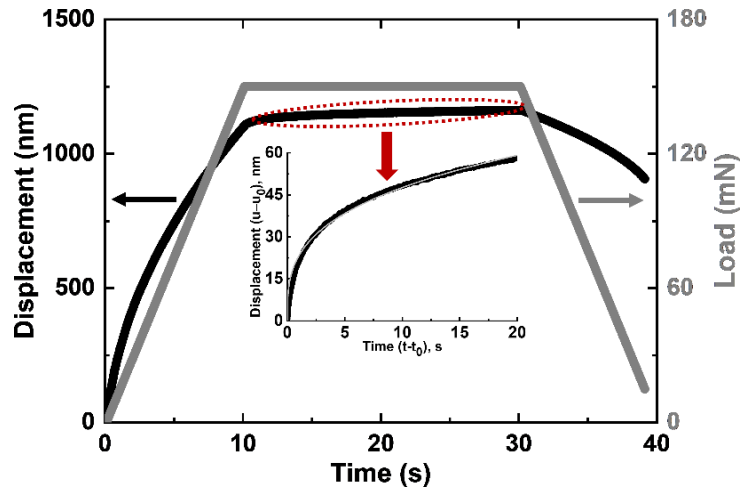


**Figure 3.14:** A typical displacement/load–time curve in the nanoindentation measurement for the GDC-CSP sample (fast loading mode). The inset plot illustrates the deformation under the constant load as a function of holding time, indicating a primary creep response.

**Table 3.5:** The experimental creep property, elastic constant, and hardness of the GDC pellets, measured in the nanoindentation measurement.

Parameter	Sample ID	Creep Constant, A (nm · s <sup>-m</sup> )	Creep Fitting Parameter, m	Elastic Modulus, E (GPa)	Hardness, H (GPa)
1000 nm (Fast)	GDC-Conv	14.3 ± 1.8	0.40 ± 0.015	230 ± 11.5	8.4 ± 0.8
	GDC-SPS	15.9 ± 0.6	0.35 ± 0.015	195 ± 8.9	7.2 ± 0.5
	GDC-CSP	19.0 ± 1.3	0.30 ± 0.01	135 ± 1.8	5.4 ± 0.1
150 mN (Fast)	GDC-Conv	16.9 ± 2.5	0.34 ± 0.012	225 ± 12.3	8.3 ± 0.7
	GDC-SPS	18.4 ± 1.1	0.34 ± 0.012	195 ± 4.9	7.3 ± 0.2
	GDC-CSP	21.9 ± 0.6	0.30 ± 0.004	135 ± 2.4	5.3 ± 0.1

The electromechanical measurement is accomplished at DTU using a Nanovibration analyzer (SIOS NA, Germany) coupled with a lock-in amplifier and an optical microscope. The sample is parallel coated using DC sputtering (Bal-tec SCD 005) with gold (Au) electrode of thickness ~50-80 nm at room temperature. The measurement duration is about 5 minutes and repeated a few times to screen out possible noise that arises from the surroundings, *i.e.*, external vibration or instrumental mechanical drift. The electrostrictive properties of the GDC pellets are demonstrated in **Fig. 3.15**. As expected, all samples respond at the second harmonic of the applied electric field and develop a negative strain parallel to the applied field direction. Analogous action is reported in the previous experiment (see section 3.2) as well as in the literature [1]. As observed, the measured electromechanical strain is minimum for the GDC-SPS sample. However, a comparable performance is noted for both GDC-CSP and GDC-Conv samples at the given conditions. For example, the strain value of the former and the latter is ~0.60 and ~0.45 ppm at 6 kV/cm and 5 Hz, respectively. In line with the earlier reports, the strain value reduces at higher frequencies, and it starts to saturate at the higher electric field [1][19]. The CSP shows saturation at around ~8 kV/cm electric field. The electrostriction strain coefficient ( $M_{33}$ ) as a function of applied field frequency is reported in **Fig. 3.15d**. The result demonstrates that  $M_{33}$  values gradually decrease with increasing frequencies for all investigated samples. The  $M_{33}$  of the GDC-CSP sample is in the order of  $10^{-18}$  (m/V)<sup>2</sup> and identical to the GDC-Conv. The evolution of quite different microstructures in these samples underlines the fact that grain size does not contribute to the electrostriction response for GDC bulk ceramics.  $M_{33}$  value of the GDC-SPS sample is one order of magnitude lower compare to counterparts. Recalling that the GDC-CSP and GDC-Conv sample develops high blocking factor > 0.8, whereas the GDC-SPS possesses a low blocking factor ~0.60. By correlating the electrostriction coefficient with the ion-blocking factor, it can be concluded that the large blocking factor indeed increases the electrostriction response, whereas the low-blocking effect significantly reduces it. Such an outcome validates our previous hypothesis that the oxygen vacancy configuration at the ion-blocking barriers tunes the electrostriction coefficient. The

most interesting finding is that the measured  $M_{33}$  in the GDC-Conv sample is one order smaller than the previous experiment. Even though both materials have a similar microstructure and ion-blocking factor.

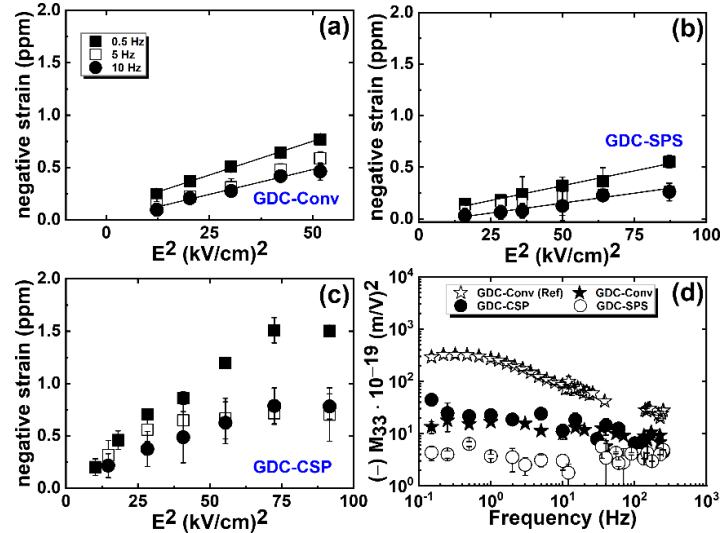


**Figure 3.15:** (a–c) The electromechanical strain of the GDC samples under external electric field at frequencies between 0.5-10 Hz. (d) The electrostriction strain coefficient ( $M_{33}$ ) as a function of applied frequencies ranging from 0.5-250 Hz. Electrode material: gold (Au). The results are compared with the GDC-10 (conventionally sintered 1450 °C for 10 hours) sample from Ref. [19].

An early report shows that the TiN (titanium nitride) electrode governs a better electrostriction performance in thin films of GDC compared to metal electrodes [20]. To optimize the electrostrictive response, TiN is applied in one of the samples (GDC-CSP). TiN has very stable chemical stability like Au, but it has half as much low electrical conductivity than the latter. According to Ref. [21], the conductivity of Au and TiN is reported as  $\sim 4.1 \times 10^7$  and  $9.2 \times 10^6$  S/m at 20 °C, respectively. The observed result is entirely unanticipated, as **Fig. 3.16** illustrates that the TiN sputtered GDC-CSP sample produced at least three times less electromechanical strain than of the sample with an Au electrode. The former reports one small order magnitude of  $M_{33}$  value than the latter. Although not conclusive, it might be possible that TiN reacts with oxygen impurity from the vacuum chamber and forms  $\text{TiO}_2$  or other undesired reactions. However, no microscopic image and chemical analysis of the interface between the electrode-material is performed.

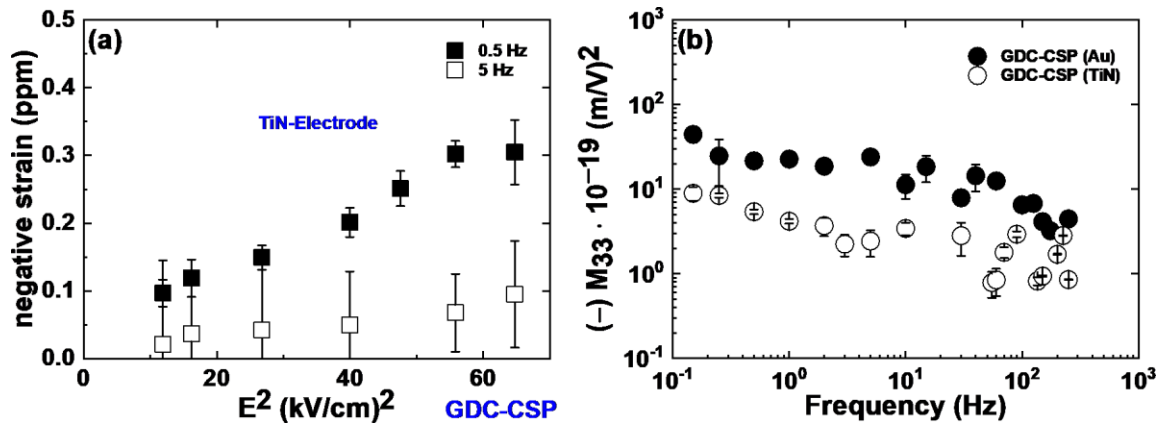


**Figure 3.16:** (a) The electromechanical strain and (b) The electrostriction strain coefficient ( $M_{33}$ ), of the GDC-CSP sample. Electrode material: TiN.

### 3.4 Tuning the Ion-blocking Factor by Gd Concentration

The following work has been published as "The Role of Oxygen Defects on the Electro-Chemo-Mechanical Properties of Highly Defective Gadolinium Doped Ceria", [A. Kabir](#), J. K. Han, B. Merle, and V. Esposito, *Materials Letter* 266 (2020) 127490.

The previous two experiments establish the postulation that electrostriction strain coefficient ( $M_{33}$ ) at the low-frequency regime for GDC bulk is not associated with microstructure evolution rather than the ion-blocking barrier effect. In view of understanding how dopant concentration relates to the ion-blocking barrier, we examine the influence of Gd-dopant concentration ( $x = 0.05-0.3$ ) on the electro-chemo-mechanical properties in GDC ( $\text{Ce}_{1-x}\text{Gd}_x\text{O}_{2-\delta}$ ). The nanoscale powders are synthesized by the co-precipitation method, as described in section 2.2. The powders are uniaxially cold pressed at 200 MPa without any binder and then conventionally sintered at 1450 °C for 10 hours.

#### 3.4.1 Structural and Microstructural Characterization of Various Doped GDC

The X-ray diffraction pattern for the GDC powders is indexed with pure ceria (ICSD # 251473). As expected, the pattern shows the characteristic cubic fluorite structure (Fm-3m), confirming

the formation of a single-phase solid solution without any secondary phases (see **Fig. 3.17a**). The lattice parameter of the GDC materials as a function of Gd concentration is shown in **Fig. 3.17b**. As can be seen that the lattice parameters do not increase linearly according to Vegard rule instead follows a quadratic increment. Bevan *et al.* have claimed that the second-order term in the quadratic relation is related to the dopant-defect attraction interaction, which is more favorable at a high dopant concentration [22]. A similar trend was previously noticed for GDC and other compositions such as Nd/Y- doped ceria [23][24].

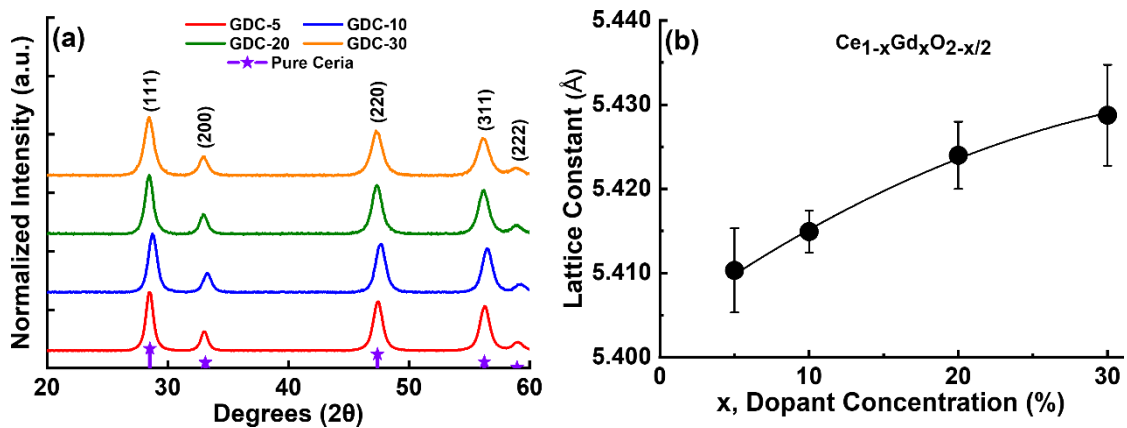


**Figure 3.17:** (a) The X-ray diffraction (XRD) pattern and (b) The estimated lattice parameter, of GDC powders with composition  $Ce_{1-x}Gd_xO_{2-\delta}$  where  $x = 0.05-0.3$ .

The SEM images of the cold-fractured surfaces of the GDC pellets are represented in **Fig. 3.18**. As observed, the microstructure is highly dense, agreeing with the measured experimental density, *i.e.*, above 95% of theoretical density. The grains are significantly large ( $> \mu m$ ), decreasing in size with increasing dopant concentration. The low-doped samples (GDC-5 and GDC-10) demonstrate more relaxed grains compare to highly doped GDC-20 and GDC-30 compounds, underlining that dopant-induced solute drag effect is more noticeable at a higher Gd concentration.

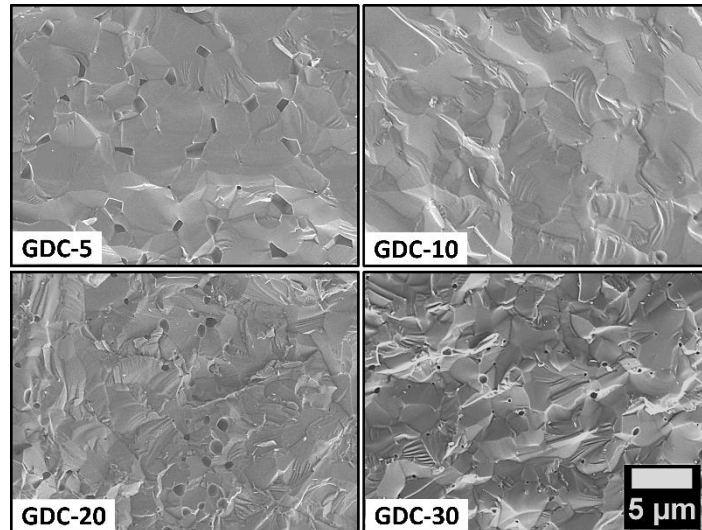


**Figure 3.18:** The cold-fractured SEM images of the GDC pellets with composition  $Ce_{1-x}Gd_xO_{2-\delta}$  where  $x = 0.05-0.3$ . The pellets are conventionally sintered at 1450 °C for 10 hours.

### 3.4.2 Electro-chemo-mechanical Characterization

The electrochemical impedance spectroscopy (EIS) is measured at a temperature range of 300-450 °C, with frequencies between  $10^{-1}$ - $10^7$  Hz under air. The impedance data is analyzed as explained by the bricklayer model and represented as a Nyquist plot in **Fig. 3.19** for a GDC-10 sample. The semicircle at the high, intermediate, and low frequency refers to bulk, grain boundary, and electrode-electrolyte impedance, respectively. The plot exhibits a dominant impedance contribution from the grain boundary semicircle. The ion-blocking effect is characterized namely by the grain boundary blocking factor ( $\alpha_{gb}$ ), which is the ratio of grain boundary resistance over the total resistance. The inset plot in **Fig. 3.19** shows that the ion-blocking factor scales down with dopant concentration. Note that the ion-blocking effect solely determines by the way oxygen vacancy is configured at the blocking barriers and not a true geometrical or concentration-dependent parameter [9]. The ion-blocking factor and the relaxation frequency of the samples measured at 300 °C are reported in **Table 3.6**.

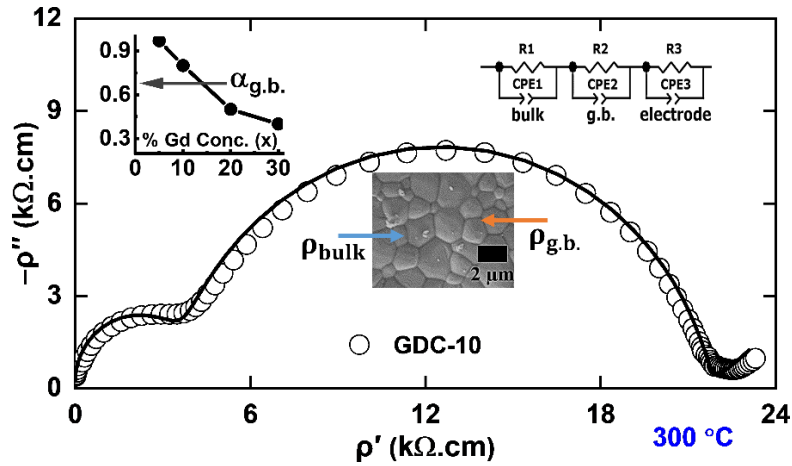


**Figure 3.19:** Characteristic Nyquist plot examined in the air at 300 °C for the GDC-10 sample. The inset shows the declining trend of an ion-blocking factor concerning dopant concentration.

**Table 3.6:** The ion-blocking factor and relaxation frequency of the GDC pellets at 300 °C.

Gd Fraction	$\sim f_{\text{grain}}$ (Hz)	$\sim f_{\text{gb}}$ (Hz)	$\alpha_{\text{gb}}$ (300 °C)
0.05	$2 \times 10^6$	80	0.98
0.10	$2 \times 10^5$	$4 \times 10^3$	0.8
0.20	$6 \times 10^5$	$4 \times 10^3$	0.5
0.30	$1 \times 10^5$	650	0.4

The temperature-dependent electrical conductivity of the samples, including bulk, grain boundary, and total, are illustrated in **Fig. 3.20**. As noticed, the bulk conductivity decreases as well as the related activation energy for migration increases for higher dopant concentration. Such an outcome is in line with theoretical and experimental predictions as the increment of dopant increases the formation of small and large scale oxygen vacancy ordering/associations, resulting in a reduction of bulk conductivity [9][25]. Moreover, grain boundary conductivity increases from GDC-5 to GDC-10 but then decreases for higher dopant samples. Avila *et al.* report that the enhancement of grain boundary conductivity with dopant concentration is due to the reduction of the space charge potential [12]. The grain boundary conductivity mainly depends on several factors, comprising grain boundary thickness, disorder, space charge potential at the grain boundaries. The grain boundary activation energy is reported as  $\sim 1.3\text{-}1.4$  eV for all samples, excluding GDC-5. The total conductivity is affected by the co-operative contribution from both bulk and grain boundary [9][26]. The GDC-10 and GDC-20 illustrate the maximum overall electrical conductivity among the samples, whereas

low conductivity is observed in GDC-5 and GDC-30 samples, ascribing to substantial ion-blocking factors and dopant-defect association, respectively.

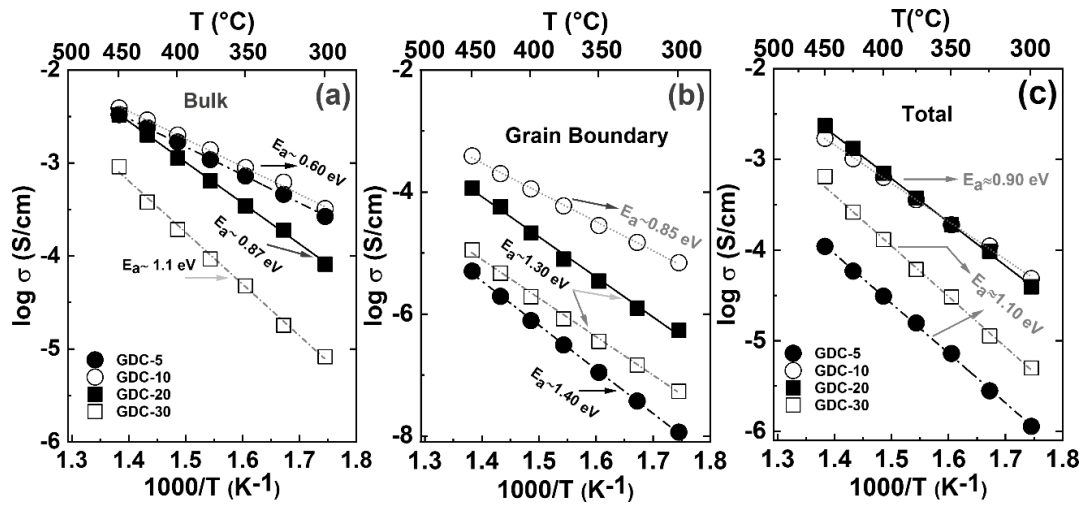


**Figure 3.20:** The temperature-dependent Arrhenius plots of (a) bulk, (b) (specific) grain boundaries and (c) total electrical conductivity of the GDC pellets with composition  $Ce_{1-x}Gd_xO_{2-\delta}$  where  $x = 0.05-0.3$ .

The mechanical properties of the samples, containing elastic modulus, hardness, and creep relaxation, are measured in the nanoindentation (NI) technique at room temperatures. The measurement is taken in continuous stiff measurement (CSM) mode under fast loading/unloading of 15 mN/s. The load is held constant for 20 sec when a maximum load (150 mN) or maximum depth (1000 nm) is acquired. The resultant data is summarized in **Table 3.7**. As observed, the creep constant ( $A$ ) decreases linearly from GDC-5 to GDC-20 sample, which fits with early reports, claiming a decline of creep is due to the increased interaction between dopants and oxygen vacancies [17][18]. Such a hypothesis is also consistent with the impedance result where increasing dopant concentration decreases bulk conductivity. The further increase of  $A$  value for the GDC-30 sample is due to the possible phase transformation from fluorite to double fluorite structure [27]. The creep fitting exponent ( $m$ ) ranges in between  $\sim 0.3-0.4$   $nm \cdot s^{-m}$  and lowers with Gd-content. The elastic modulus also decreases with increasing Gd concentration. Moreover, a significantly low value is reported for the GDC-30 sample. Hardness upsurges with dopant concentration up to 20 mol% and then fall off for 30 mol% GDC.

**Table 3.7:** The experimental creep property, elastic constant, and hardness of the GDC pellets.

Parameter	Sample ID	Creep Constant, A ( $\text{nm} \cdot \text{s}^{-m}$ )	Creep Fitting Parameter, m	Elastic Modulus, E (GPa)	Hardness, H (GPa)
1000 nm (Fast)	GDC-5	$20.3 \pm 2.2$	$0.37 \pm 0.02$	$220 \pm 3.0$	$7.9 \pm 0.5$
	GDC-10	$17.0 \pm 1.4$	$0.38 \pm 0.01$	$210 \pm 8.8$	$7.9 \pm 0.5$
	GDC-20	$11.5 \pm 1.1$	$0.35 \pm 0.02$	$215 \pm 11.2$	$9.6 \pm 1.2$
	GDC-30	$14.2 \pm 2.0$	$0.32 \pm 0.01$	$175 \pm 7.0$	$7.0 \pm 0.9$
150 mN (Fast)	GDC-5	$21.6 \pm 2.4$	$0.35 \pm 0.01$	$215 \pm 4.7$	$7.5 \pm 0.5$
	GDC-10	$18.3 \pm 1.6$	$0.35 \pm 0.02$	$210 \pm 12.4$	$8.4 \pm 1.0$
	GDC-20	$14.4 \pm 1.2$	$0.31 \pm 0.03$	$220 \pm 11.0$	$10.0 \pm 1.4$
	GDC-30	$17.6 \pm 1.9$	$0.28 \pm 0.01$	$180 \pm 10.0$	$7.2 \pm 0.9$

The electromechanical measurement is performed at DTU using a laser interferometer based Nanovibration analyzer (SIOS NA, Germany). The electromechanical response as a function of the external electric field is displayed in **Fig. 3.21**. Following the typical electrostrictive response for ceria, all samples generate a negative strain at the second harmonic of the applied field frequency. Surprisingly, within the applied electric field, no strain saturation activities are observed. A considerably larger strain is recorded in low-doped materials, especially for GDC-10. The strain value indeed reduces at high field frequency (compare 0.5 Hz vs 10 Hz).

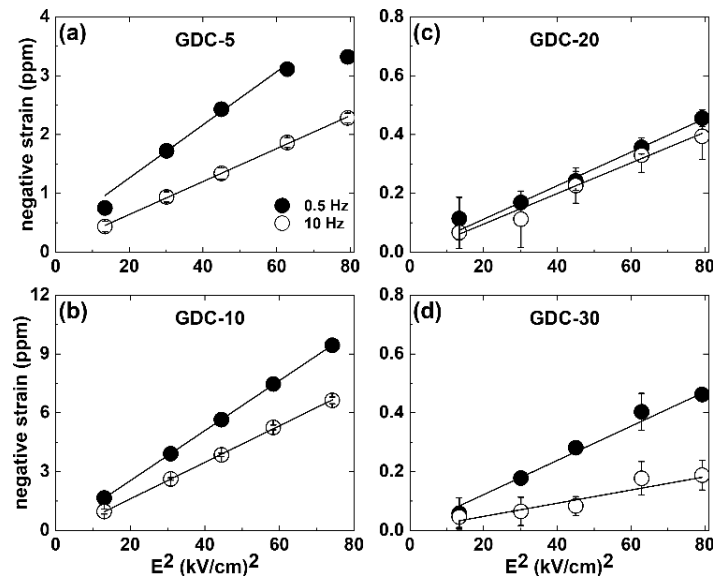


**Figure 3.21:** (a)-(d) The electrostrictive negative strain of the GDC samples as a function of the applied electric field at frequencies 0.5 and 10 Hz. Electrode material: Gold (Au).

**Fig. 3.22** illustrates the electrostrictive strain coefficient ( $M_{33}$ ) as a function of applied frequency. As expected, the value of  $M_{33}$  decreases with increasing frequencies. Considering all samples, GDC-10 yields the maximum  $M_{33}$  value. The GDC-5 possess similar order magnitude like GDC-10 with an order of  $10^{-18}$  (m/V)<sup>2</sup>. Conversely, highly doped GDC-20 and GDC-30 samples display comparatively a low  $M_{33}$ , at least one order of smaller than the GDC-10 sample.

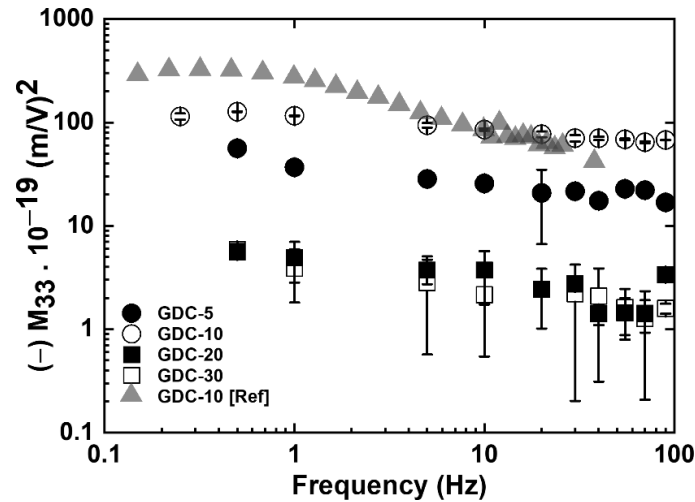


**Figure 3.22:** The electrostrictive strain coefficient ( $M_{33}$ ) as a function of frequencies ranging from 0.15-100 Hz. The result is compared with Ref. [19].

These samples contain noteworthy defect-dopant associations as well as a low-ion blocking factor. Based on previous results, a large blocking factor is required to optimize electrostriction for GDC samples, and the low-doped samples satisfy this condition. Additionally, comparing the result with Ref. sample [19], it can be emphasized that electrode material is another critical parameter influencing electrostrictive performance.

### 3.5 Concluding Remarks

Highly dense polycrystalline Gd-doped ceria displays non-classical electrostriction with a strong dependency on applied electric field and frequency. At the low-frequency regime, the electrostriction strain coefficient ( $M_{33}$ ) is high, showing a relaxation phenomenon from ~1 Hz to ~20 Hz. However, at the high-frequency regime (> 20 Hz)  $M_{33}$  value is independent of applied frequency. As the electrostriction mechanism in ceria is associated with the local lattice

rearrangement, the relaxation occurrences may be believed to an intrinsic electromechanical property for the GDC system. The experimental results also confirm that neither grain size nor nominal oxygen vacancy concentration is an actual parameter that can be associated with the electrostriction properties. The electrostrictive response is firmly related to the ion-blocking factor developed in the materials. Quite surprisingly, this effect is only practical at the low-frequency regime, while the high-frequency region is unaffected. Strictly speaking,  $M_{33}$  at higher frequencies does not depend on any parameter. The blocking effect is a resolution of the configuration of the oxygen vacancy at the blocking barrier and not a geometrical parameter. Such a feature is achieved by controlling diffusion kinetics, *i.e.*, Gd-diffusion during sintering as well as with dopant concentration. The purity and morphology of the starting powder is another parameter that can control it. The fundamental electrostriction equation is related to the material elastic modulus. Interestingly, it is observed that even a sample (GDC-CSP) with low modulus and hardness can develop considerable electrostriction if the creep parameter is sufficiently high. However, another material with a relatively high creep parameter (GDC-SPS) does not generate reasonable electrostriction. Although the creep mechanism is believed to be similar to electrostriction, such as rearrangement of lattice under the mechanical field, no meaningful correlation between creep and  $M_{33}$  is found. The  $M_{33}$  reports to be small for the materials with high dopant concentration while the sample with low Gd having a significant ion-blocking factor displays a high  $M_{33}$ . Last but not least, the electromechanical response is dependent on the contact resistance or the stability of the electrode. Surprisingly noncontact electrode display better performance than a sputtered ceramic one. Aiming to understand what causes such difference, the electrode-electrolyte interface reaction, such as possible reduction of  $Ce^{4+}$  to  $Ce^{3+}$  and the associated chemical expansion, is required to be comprehensively investigated. To sum up, more work is necessary to develop the best performing electrode and to define a methodology that can hinder the relaxation mechanism and put ceria as an alternative material for frequency insensitive electromechanical application.

## References:

- [1] N. Yavo, O. Yehekel, E. Wachtel, D. Ehre, A. I. Frenkel, and I. Lubomirsky, "Relaxation and saturation of electrostriction in 10 mol% Gd-doped ceria ceramics," *Acta Mater.*, 144 (2018) 411–418.
- [2] A. L. Patterson, "The scherrer formula for X-ray particle size determination," *Phys. Rev.*, 56 (1939) 978–982.
- [3] C. Plapcianu, C. Valsangiacom, J. E. Schaffer, A. Wieg, J. Garay, and L. Stanciu, "Spark plasma sintering studies of nanosize lanthanidedoped ceria obtained by sol-gel method," *J. Optoelectron. Adv. Mater.*, 13 (2011) 1101–1108.
- [4] H. L. Tuller, "Ionic conduction in nanocrystalline materials," *Solid State Ionics*, 131 (2000) 143–157.
- [5] F. Maglia, F. Farina, M. Dapiaggi, I. G. Tredici, and U. Anselmi-Tamburini, "Transport properties in bulk nanocrystalline Sm-doped ceria with doping content between 2 and 30 at.%, " in *Solid State Ionics*, 255 (2012) 412–415.
- [6] K. Neuhaus, R. Dolle, and H.-D. Wiemhöfer, "Assessment of the effect of transition metal oxide addition on the conductivity of commercial Gd-Doped Ceria," *J. Electrochem. Soc.*, 165 (2018) F533–F542.
- [7] V. Esposito, M. Zunic, and E. Traversa, "Improved total conductivity of nanometric samaria-doped ceria powders sintered with molten  $\text{LiNO}_3$  additive," *Solid State Ionics*, 180 (2009) 1069–1075.
- [8] Z. P. Li, T. Mori, G. J. Auchterlonie, J. Zou, and J. Drennan, "Direct evidence of dopant segregation in Gd-doped ceria," *Appl. Phys. Lett.*, 98 (2011) 093104.
- [9] V. Esposito and E. Traversa, "Design of electroceramics for solid oxides fuel cell applications: Playing with ceria," *J. Am. Ceram. Soc.*, 91 (2008) 1037–1051.
- [10] D. Z. de Florio, R. Muccillo, V. Esposito, E. Di Bartolomeo, and E. Traversa, "Preparation and Electrochemical Characterization of Perovskite/YSZ Ceramic Films," *J. Electrochem. Soc.*, 152 (2004). A88.
- [11] M. G. Bellino, D. G. Lamas, and N. E. W. De Reça, "Enhanced ionic conductivity in nanostructured, heavily doped ceria ceramics," *Adv. Funct. Mater.*, 16 (2006) 107–113.
- [12] H. J. Avila-Paredes, K. Choi, C.-T. Chen, and S. Kim, "Dopant-concentration dependence of grain-boundary conductivity in ceria: A space-charge analysis," *J. Mater. Chem.*, 19 (2009) 4837.
- [13] R. Korobko et al., "Giant electrostriction in Gd-doped ceria," *Adv. Mater.*, 24 (2012) 5857–5861.
- [14] C. A. Schneider, W. S. Rasband, and K. W. Eliceiri, "NIH Image to ImageJ: 25 years of image analysis," *Nature Methods*, 7 (2012) 671–5.
- [15] X. Guo, S. Mi, and R. Waser, "Nonlinear Electrical Properties of Grain Boundaries in Oxygen Ion Conductors: Acceptor-Doped Ceria," *Electrochem. Solid-State Lett.*, 8 (2004) J1.
- [16] W.C. Oliver and G. M. Pharr, "An improved technique for determining hardness and elastic modulus using load and displacement sensing indentation experiments," *J. Mater. Res.*, 7 (1992) 1564–1583.
- [17] R. Korobko, S. K. Kim, S. Kim, S. R. Cohen, E. Wachtel, and I. Lubomirsky, "The role of point defects in the mechanical behavior of doped ceria probed by nanoindentation," *Adv. Funct. Mater.*, 23 (2013) 6076–6081.
- [18] R. Korobko et al., "Influence of Gd content on the room temperature mechanical properties of Gd-doped ceria," *Scr. Mater.*, 66 (2012) 155–158.
- [19] A. Kabir et al., "Effect of oxygen defects blocking barriers on gadolinium doped ceria (GDC) electro-chemo-mechanical properties," *Acta Mater.*, 174 (2019) 53–60.
- [20] S. Santucci, H. Zhang, S. Sanna, N. Pryds, and V. Esposito, "Enhanced electro-mechanical coupling of  $\text{TiN/Ce}_{0.8}\text{Gd}_{0.2}\text{O}_{1.9}$  thin film electrostrictor," *APL Mater.*, 7 (2019) 071104.

## The Role of Microstructure and Ion-blocking Factors on Electrostriction

- [21] S. Kasap, C. Koughia, and H. E. Ruda, "Electrical conduction in metals and semiconductors," in Springer Handbooks, 2017.
- [22] T. C. P. J.M. Bevan, W.W. Barker, "in: L. Eyring (Ed.), New York," Proc. Fourth Conf. Rare Earth Res. Gordon Breach, New York, (1965) 441.
- [23] S. Omar, E. D. Wachsman, and J. C. Nino, "Higher conductivity Sm<sup>3+</sup> and Nd<sup>3+</sup> co-doped ceria-based electrolyte materials," *Solid State Ionics*, 178 (2008) 1890–1897.
- [24] I. E. L. Stephens and J. A. Kilner, "Ionic conductivity of Ce<sub>1-x</sub>Nd<sub>x</sub>O<sub>2-x/2</sub>," *Solid State Ionics*, 177 (2006) 669–676.
- [25] J. Koettgen, S. Grieshammer, P. Hein, B. O. H. Grope, M. Nakayama, and M. Martin, "Understanding the ionic conductivity maximum in doped ceria: Trapping and blocking," *Physical Chemistry Chemical Physics*, 20 (2018) 14291–14321.
- [26] T. S. Zhang, J. Ma, L. B. Kong, S. H. Chan, and J. A. Kilner, "Aging behavior and ionic conductivity of ceria-based ceramics: A comparative study," *Solid State Ionics*, 170 (2004) 209–217.
- [27] M. Varenik, S. Cohen, E. Wachtel, A. I. Frenkel, J. C. Nino, and I. Lubomirsky, "Oxygen vacancy ordering and viscoelastic mechanical properties of doped ceria ceramics," *Scr. Mater.*, 163 (2019) 19–23.

# Chapter 4: Tuning of Ion-blocking Barriers via Various Dopant

---

## 4.1 Motivation

It has been shown that the electrostriction strain coefficient for bulk Gd-doped cerium oxides (GDC) strongly depends on the inherent oxygen vacancy configuration at the ion-blocking barriers. Moreover, numerous reports, including both computational and experimental studies, demonstrate that the oxygen vacancy adopts a different configuration if the dopant size and valence differ meaningfully than to the host cerium cation  $\text{Ce}^{4+}$  [1][2]. For example, incorporation of a divalent cation ( $\text{A}^{2+}$ ) in cerium oxide produces two times higher oxygen vacancy than of  $\text{Gd}^{3+}$ , as  $\text{A}^{2+}$  maintains a 1:1 charge ratio with the oxygen vacancy. Such ration eventually enhances the electrostatic interaction at the host lattice *via* a stronger  $\text{A}^{2+}\text{-V}_{\text{O}}^{\bullet\bullet}$  attraction. In addition to the valence, a very different ionic radius (Shannon) of the dopants introduces a high lattice distortion. Substitutional  $\text{Ca}^{2+}$  (1.12 Å) in octahedral coordination is larger than both  $\text{Gd}^{3+}$  (1.05) and  $\text{Ce}^{4+}$  (0.97 Å), resulting in approximately twice as high elastic strain in the lattice compared to  $\text{Gd}^{3+}$  doped ceria. Due to these intensified electrostatic (attractive) and elastic (repulsive) interactions, dopant tends to cluster more with the  $\text{V}_{\text{O}}^{\bullet\bullet}$  forming small or large scale dopant-defect associations and/or to segregate at the crystallographic disorder. As a result, typically a decreased ionic conductivity than of Gd-doped ceria is observed. **Fig. 4.1** schematically explains the effect of dopant charge/size on the defect interaction, highlighting that more similar dopant such as  $\text{Gd}^{3+}$  yields less dopant-defect interaction.

## Tuning of Ion-blocking Barriers via Various Dopant

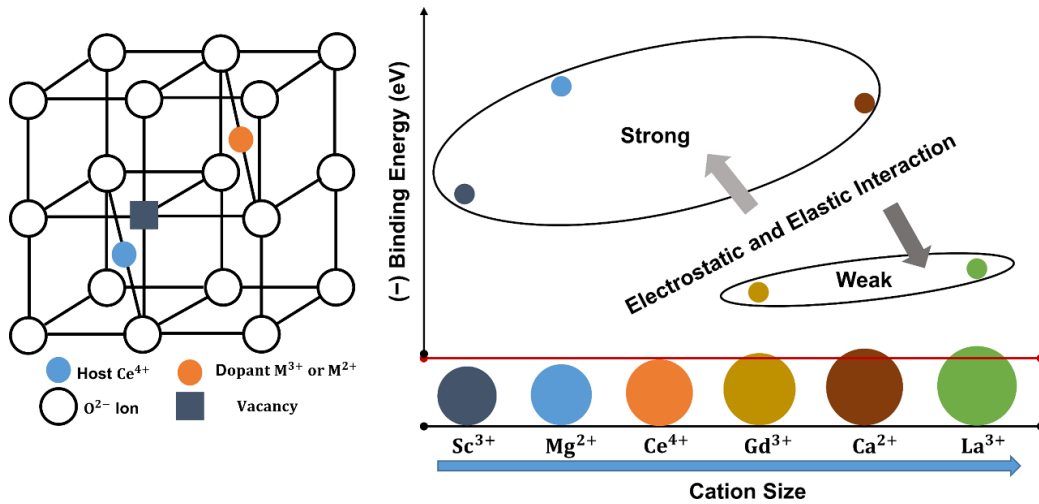


**Figure 4.1:** Schematic illustration of the (left) acceptor doped ceria lattice. The image is adapted from Ref. [3] with permission from Elsevier. The binding energy of dopant-defect interaction (1 NN) for different dopants in ceria (right). The data is taken from Butler *et al.* [4] with permission from John Wiley & Sons.

Aimed at a paramount ionic conductor, electrostatic, and elastic interaction should be in the sense of balance. Computational report of Andersson *et al.* claims that an ideal dopant should have an atomic number 61 (Pm) [5]. The dopant size larger than Pm, oxygen vacancy prefers sitting in the next neighbor (2NN) position. Whereas for smaller dopant size, it favors the nearest location (1NN) (see **Fig. 4.2**). The total interaction is governed by the cooperative strength of both electrostatic and elastic interaction deciding whether 1NN or 2NN site preferences dominate. It is found that dopant size between Sm and Pm, no site preferences of atomic configuration exists, which means a maximum number of oxygen sites are available. In this case, the electronic and elastic interaction is counterbalanced within the host lattice. However, Pm is radioactive. Thus, it has been suggested using an equimolar co-doping concept of Sm/Nd matching atomic number and radius of Pm. Omar *et al.* experimentally verified this hypothesis, presenting a 14% enhanced bulk conductivity for a 10 mol% Sm/Nd doped ceria compared to GDC-10 [6]. Moreover, no information on how oxygen vacancy configures at the ion-blocking barriers in these materials is outlined. In summary, it is of significant interest to investigate experimentally other types of dopants to figure out the correlation of dopant-defect interaction energy (strong or weak) on the ion-blocking barrier and eventually to the electromechanical properties.

## Tuning of Ion-blocking Barriers via Various Dopant

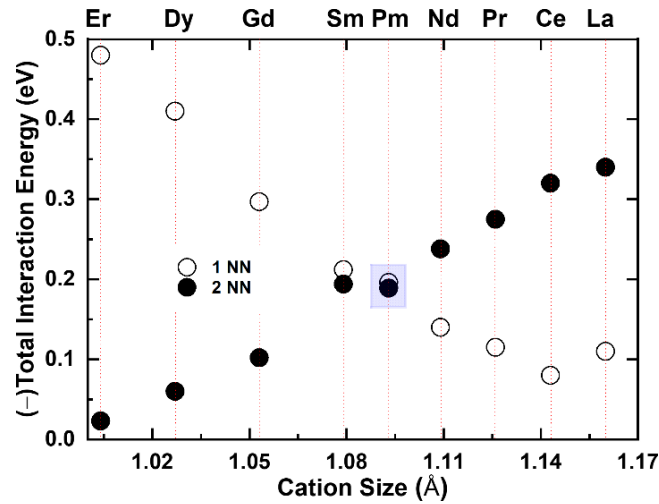


**Figure 4.2:** The total interaction energy between rare-earth dopant and oxygen vacancy occupying the next neighbor (1 NN) and next-nearest neighbor (2NN) position of the dopant. The figure is redrawn after Andersson *et al.* [5].

### 4.2 Effect of Sintering on the Ion-blocking Barriers for CDC

The following work has been submitted as "Electro-Chemo-Mechanical Properties in Nanostructured Ca-doped Ceria (CDC) by Field Assisted Sintering", [A. Kabir](#), H. Zhang, S. Colding-Jørgensen, S. Santucci, S. Molin, and V. Esposito, *Scripta Materialia* (under review).

Divalent dopants ( $A^{2+}$ ) such as calcium, magnesium, based ceria compound generally illustrates lower ionic conductivity than of trivalent Gd-doped ceria. Due to their low conduction, these compounds are less popular for the solid-state electrolyte application. Nevertheless, decreased conductivity might be favorable for the electromechanical response as it allows less electronic leakage in the material [7], leading to a decrease in the potential drop in the materials. More importantly, these elements are more abundant in nature, cost, and environment effective than of trivalent rare-earth dopants. Therefore, a divalent dopant based ceria system would be a more logical choice for electromechanical application if equivalent performance to GDC were obtained. In the following study, the role of  $Ca^{2+}$  dopant addition on the evolution of the ion-blocking barriers and the correlated electro-chemo-mechanical

properties is investigated. As experimentally illustrated in the previous chapter that the ion-blocking barrier is tuned by the thermally activated diffusion mechanism for GDC ceramics, hence a similar experimental concept is executed. For this purpose, nanosize powders of 5 mol% Ca-doped ceria ( $\text{Ce}_{0.95}\text{Ca}_{0.05}\text{O}_{1.95}$ ,  $\delta = 0.05$ ) with an average size of  $\sim 10$  nm is consolidated and sintered in two different methods, including field-assisted spark plasma sintering (SPS) and conventional method. It is highly anticipated that these two distinct thermal treatment would lead to developing different microstructure as well as ion-blocking barriers.

The calcium doped ceria (CDC-5) powders are prepared by the co-precipitation method, as described in section 2.2. The powders are consolidated by the SPS method at  $980^\circ\text{C}$ , with a uniaxial pressure of 50 MPa and 5 min dwelling. The as-sintered sample is found to be chemically reduced and thus re-oxidized at  $800^\circ\text{C}$  for 10 hours. The conventional sample is uniaxially cold-pressed at 200 MPa for 30 sec and sintered at  $1450^\circ\text{C}$  in the air for 10 hours. A 10 mol% GDC conventionally sintered at  $1450^\circ\text{C}$  for 10 hours considers as an equivalent reference in terms of oxygen defects concentration, as reported in Ref. [8].

#### 4.2.1 Structural and Microstructural Design by Sintering Methods

The starting CDC powder morphology and crystal structure are analyzed by a conventional TEM and illustrated in **Fig. 4.3**.

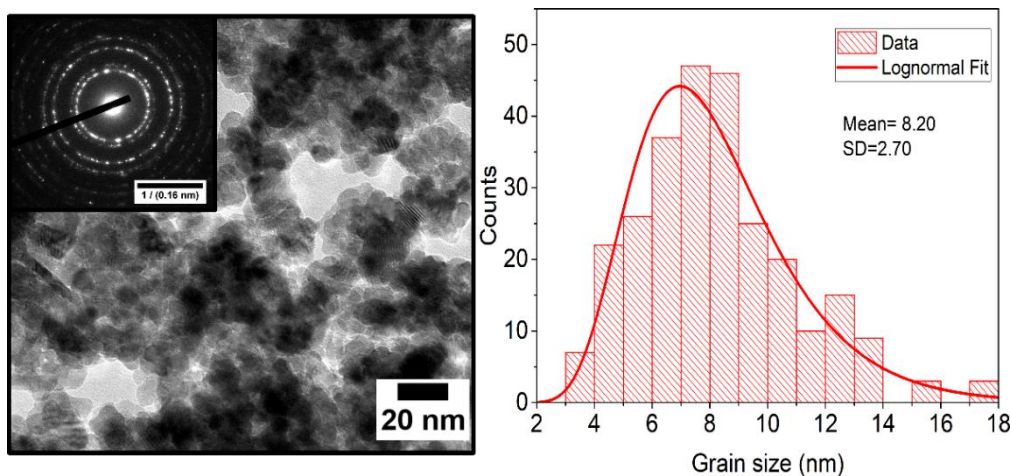


**Figure 4.3:** Bright-field TEM image of the CDC starting powders (left), Inset: SAED pattern. Estimation of the particle size distribution (right).

The particle size analysis shows that the particle has a very narrow size distribution, having an average size of  $8.20 \pm 2.70$  nm. The inset plot displays the corresponding selected area electron diffraction pattern, revealing a cubic fluorite structure of ceria. **Fig. 4.4** shows the X-ray diffraction (XRD) pattern of the CDC powder and sintered pellets. The resultant patterns are indexed according to the reference pattern of pure ceria powder (ICSD # 251473), representing a cubic fluorite structure (Fm-3m) having no other phases. The estimated lattice parameter and crystallite size (Scherrer) is around 0.540 nm and 0.13 nm, respectively.

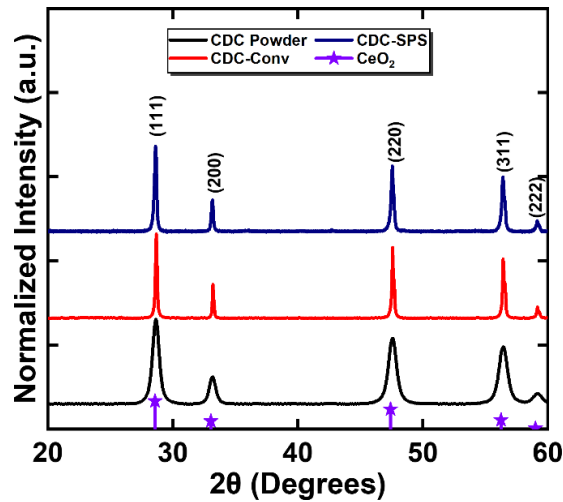


**Figure 4.4:** The X-ray powder diffraction (XRD) pattern of the CDC powders and sintered pellets.

The microstructures of the sintered CDC pellets are investigated by a high-resolution scanning electron microscope (SEM) and displayed in **Fig. 4.5**. As observed, the CDC-SPS sample presents nanoscale grains with an average size of  $150 \pm 20$  nm. These grains are non-relaxed, having a typical polygonal shape. Conversely, the CDC-Conv material experiences a considerable grain growth, having an average grain size of  $4.0 \pm 0.25$   $\mu$ m. Most of these grains are thermodynamically relaxed, *i.e.*, the curvature at the grain boundary is minimized. Furthermore, a visible thin layer at the grain boundary and triple point (red circle) indicate a likely enrichment of calcium segregation. It is worth mentioning that chemical analysis in these regions, as well as local lattice strain measurement, are not performed at this point.

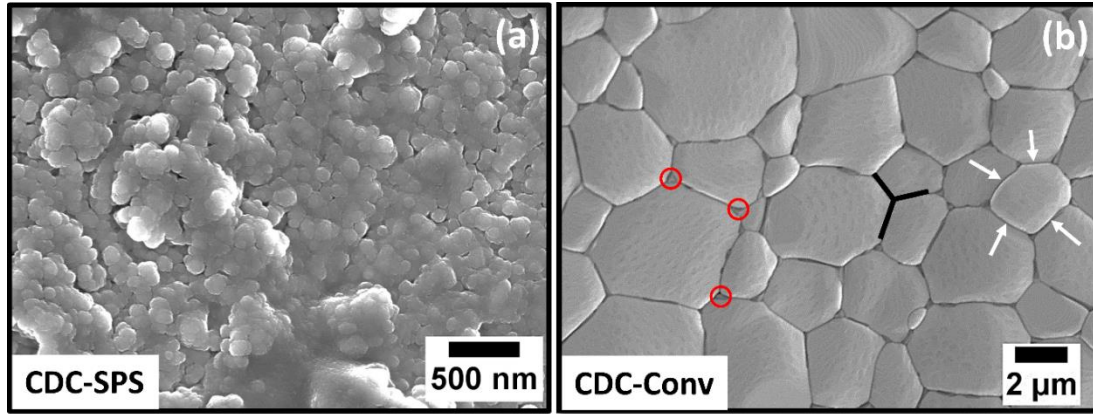


**Figure 4.5:** The high-resolution SEM images of the CDC pellets sintered in (a) SPS at 980 °C, 50 MPa for 5 min, (b) air at 1450 °C for 10 hours.

#### 4.2.2 Electro-chemo-mechanical Characterization

The electrochemical properties of the samples are examined using electrochemical impedance spectroscopy (EIS) in the temperature range of ~250-575 °C in ambient air using a frequency distribution of  $10^{-1}$  to  $10^7$  Hz. The electrical impedance is analyzed in the Nyquist plot formalism and represented in **Fig. 4.6** for the measurement at 300 °C. The plots are fitted using an equivalent circuit of RQ elements according to the bricklayer theory (see chapter 2 for details). As can be seen, the nanocrystalline CDC-SPS sample displays only one semicircle that attributes to overlapped bulk and grain boundary impedance. As already mentioned in chapter 3, such behavior is prevalent for nanostructured conductors due to a comparable order of length-scale of space charge region and grain size, leading to similar relaxation times for bulk and grain boundary conduction [9]. Thus, it is not possible to deconvolute each contribution, and only total resistivity is considered for the CDC-SPS sample. Whereas the two semicircles in the CDC-Conv sample is ascribed to high and intermediate frequency related bulk and grain boundary polarization, respectively. The GDC-Conv (Ref. sample) follows the same trend as CDC-Conv. For doped ceria, the ion-blocking effect is typically associated with the grain boundary and is characterized by the ion-blocking factor ( $\alpha_{gb}$ ) [10]. As noticed, the resistivity of the CDC-Conv sample is principally dominated by the grain (lattice), as it has at least four times larger resistivity than the grain boundary. This sample features half as much less total resistance compared to the GDC-Conv material. The

grain boundary resistivity of the former is around ten times small than the latter, despite macroscopic segregation of  $\text{CaO}_x$  at the grain boundary. The estimated  $\alpha_{\text{gb}}$  for the CDC-Conv and GDC-Conv is  $\sim 0.17$  and  $\sim 0.9$ , respectively, at  $300^\circ\text{C}$ . The bulk relaxation frequency of the GDC-Conv sample is extremely high ( $\sim 200$  kHz) compared to the CDC-Conv sample ( $\sim 30$  kHz), whereas both exhibits a similar grain boundary relaxation frequency  $\sim 1$  kHz. The overlapped relaxation frequency ( $\sim 20$  kHz) of the CDC-SPS is comparable to the bulk relaxation frequency ( $\sim 30$  kHz) of the CDC-Conv sample. However, the large resistivity value in the former suggests that the semicircle is dominated by the grain boundary. Although not conclusive, the ion-blocking barrier factor in this sample is high and indeed above 0.5.

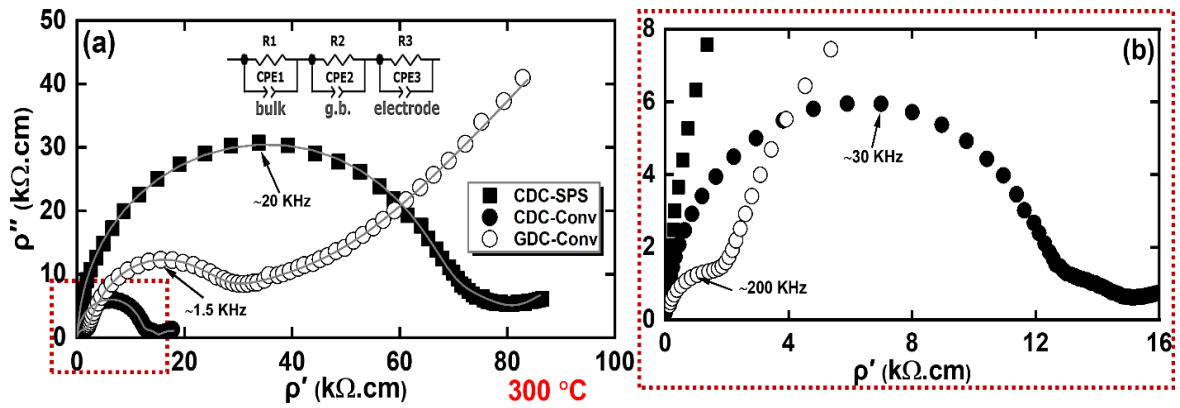


**Figure 4.6:** (a)-(b) Geometry corrected Nyquist plot ( $\rho'$  vs  $\rho''$ ) of the CDC pellets, measured at  $300^\circ\text{C}$ . The outcome is compared with the GDC-Conv sample, sintered at  $1450^\circ\text{C}$  for 10 hours [8]. Electrode: Silver (Ag).

The Arrhenius type temperature-dependent total electrical conductivity of the samples is demonstrated in **Fig. 4.7**. As observed, the CDC-SPS sample displays a minimum conductivity amongst the sample throughout the inspected temperature. The low conductivity value in this nanostructured material could be attributed to the formation of the dopant-defect association, as well as to the high blocking barrier density [11]. Moreover, these defects structures are getting relaxed at high-temperature sintering by forming local precipitates at the grain boundary [12]. In general, these kinds of precipitates contain a substantial amount of  $\text{Ca}^{2+}$ . Surprisingly, it is found that local enrichment of  $\text{Ca}^{2+}$  at the grain boundary facilitates ion migration with non-blocking grain boundary effects. At relatively low-temperatures, the CDC-

Conv sample exhibits a higher conductivity than of GDC-Conv. While at intermediate-high temperatures ( $> 400\text{ }^{\circ}\text{C}$ ), the conductivity value of the latter surplus the former. The observed activation energy value of the GDC sample is higher ( $\sim 0.9\text{ eV}$ ) compared to both CDC samples ( $\sim 0.65\text{ eV}$ ). Such difference in the activation energy values can be attributed to change of ionic migration mechanisms that may also involve transfer of oxygen vacancies in the CaO-rich structures at the grain boundary or even to other charge carriers, e.g. polarons and  $\text{Ca}^{2+}$  [13].

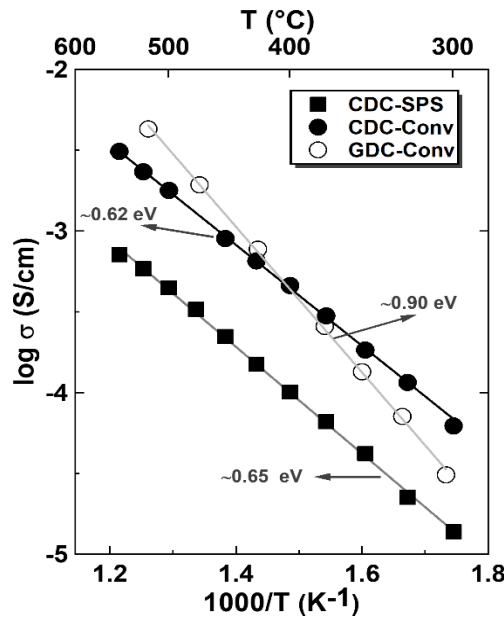


**Figure 4.7:** The temperature-dependent Arrhenius plot for the estimation of total electrical conductivity of the CDC samples, measured between 300-550  $^{\circ}\text{C}$ . The results are compared with GDC-Conv [8].

The electromechanical characterization is performed using a laser interferometer based Nanovibration analyzer. The sample is coated with a gold (Au) electrode with a thickness of  $\sim 50\text{-}80\text{ nm}$ . The electromechanical response of the CDC samples as a function of the external electric field is represented in **Fig. 4.8**. The results confirm that CDC samples also respond at the second harmonic of the applied field frequency, validating the occurrence of electrostriction in the materials. Within the investigated field, no strain saturation is observed. Opposite to GDC compounds, the strain value did not fall off radically with increasing frequencies rather presenting a slightly scattered response. For a given field frequency, CDC-SPS develops a higher strain than the CDC-Conv sample.

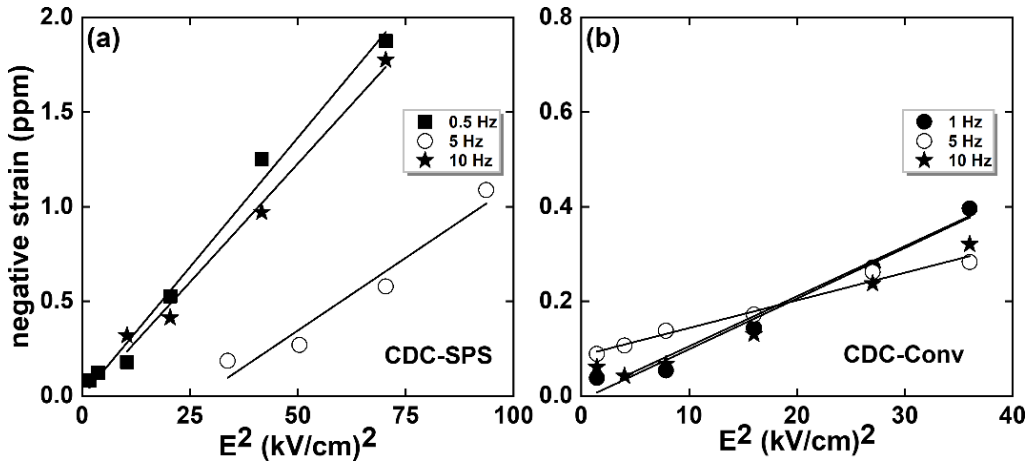


**Figure 4.8:** (a)-(b) The electrostrictive negative strain of the CDC samples as a function of the applied electric field at frequencies between 0.5-10 Hz.

The electrostrictive strain coefficient ( $M_{33}$ ) as a function of applied frequency is reported in **Fig. 4.9**. As can be seen that both the CDC samples display a lower  $M_{33}$  value than GDC-Conv at the low-frequency regime. Characteristically bulk GDC shows a high magnitude at the low-frequency region followed by relaxation with increasing frequency. However, such behavior is not observed in the CDC materials. Surprisingly both CDC samples exhibit an identical  $M_{33}$  value in the order of  $\sim 10^{-18} (\text{m}/\text{V})^2$  with a little fluctuation (shaded box). Although, the microstructure and the electrical properties, *i.e.*, ion-blocking effect in these materials, are significantly different. Accounting such results, it can be suggested that neither grain size nor blocking factor carries any role in governing a frequency-insensitive electrostriction response in CDC. It might be possible that the presence of local lattice distortion (enhanced electrostatic and elastic interaction) as induced by dopant  $\text{Ca}^{2+}$  plays a leading role. Furthermore, to resolve the local lattice distortion effect on electrostriction, additional analysis, including strong or weak interaction effect, is explained in the following sections.

## Tuning of Ion-blocking Barriers via Various Dopant

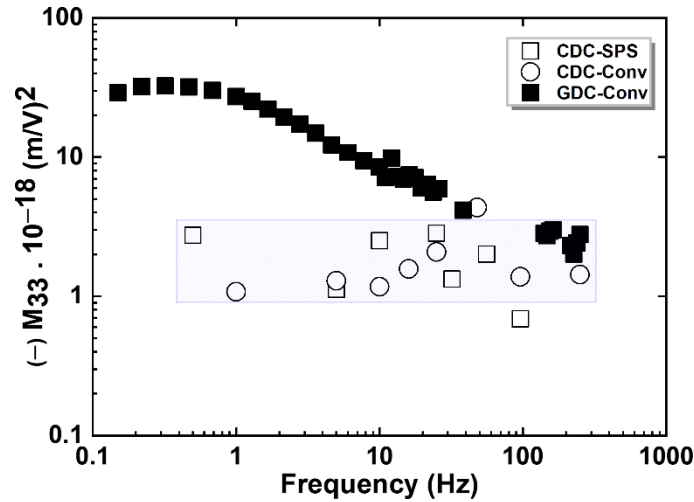


**Figure 4.9:** The electrostriction strain coefficient ( $M_{33}$ ) as a function of applied frequencies ranging from 0.1-250 Hz.

### 4.3 Effect of Ca Concentration on the Ion-blocking Barriers for CDC

The following work will be submitted to a peer-review journal as "Steady Electrostriction Properties in Calcium Doped Cerium Oxide", [A. Kabir](#), S. Santucci, K. T. S. Thyden, E. Paris, M. Varenik, I. Lubomirsky, and V. Esposito.

The preliminary results of the 5 mol%  $\text{Ca}^{2+}$  incorporated cerium oxides do confirm the development of non-classical electrostriction activities. Remarkably, CDC material illustrates a steady electrostriction performance from low to high frequencies. To shed some light on this performance, the current work aims to understand how the nominal  $\text{Ca}^{2+}$  concentration shows a relationship with the ion-blocking barrier and associated with the electro-chemo-mechanical properties.

Nano-size CDC powders with compositions  $\text{Ce}_{1-x}\text{Ca}_x\text{O}_{2-\delta}$  where,  $x = 0.025, 0.05, 0.1$  and  $0.15$  named as CDC-2.5, CDC-5, CDC-10 and CDC-15, respectively are synthesized by solution combustion method. At first, the stoichiometric proportion of cerium nitrate hexahydrate (Sigma-Aldrich, USA) and calcium nitrate tetrahydrate (Sigma-Aldrich, USA) salts are dissolved in deionized water to produce a 0.2 M solution. Afterward, 0.3 M citric acid and 0.1

## Tuning of Ion-blocking Barriers via Various Dopant

M ethylene glycol are added into it. The solution is then heated at 200 °C on a hot plate for several hours until foamy powders formed. The powders are then calcined at 500 °C for 2 hours, followed by overnight ball milling in ethanol, oven-dried, grounded and sieved (150 µm). The powders are uni-axially cold-pressed without any binder under a force of 200 MPa for 30 sec. The green pellet is sintered in air at 1450 °C for 10 hours.

### 4.3.1 Structural and Microstructural Characterization of Variously Doped CDC

The experimental density of the samples is observed to be above 95% of theoretical density. The XRD patterns in **Fig. 4.10** illustrates the characteristic cubic fluorite structure for ceria. No impurity phases of  $\text{CaO}_x$  based compounds are observed. At this stage, the local lattice strain measurement is lacking and due to be performed.

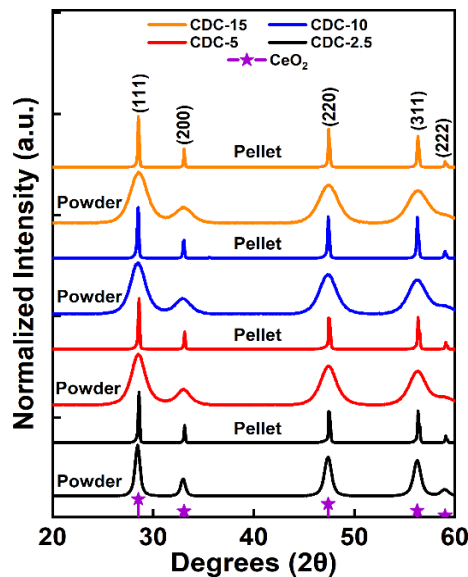


**Figure 4.10:** The X-ray diffraction (XRD) pattern of variously doped calcium doped ceria powders and pellets,  $\text{Ca}^{2+} = 2.5\text{-}15\text{ mol}\%$ . The results are indexed with undoped ceria (ICSD # 251473).

**Fig. 4.11** demonstrates the SEM images of cold-fractured and polished surfaces of the CDC samples. The observed microstructure is highly dense. However, a few residual porosities are found in the CDC-2.5 sample. The grains are in the micron range, with a size between ~3-5 µm. The grain growth is inhibited in the CDC-5 and CDC-15 samples, whereas CDC-10 possesses a relatively larger grain. At high dopant concentration, local segregation of  $\text{Ca}^{2+}$

(red circle) is visible at the grain boundaries and as secondary phases, in agreement with the previous reports [7][12].

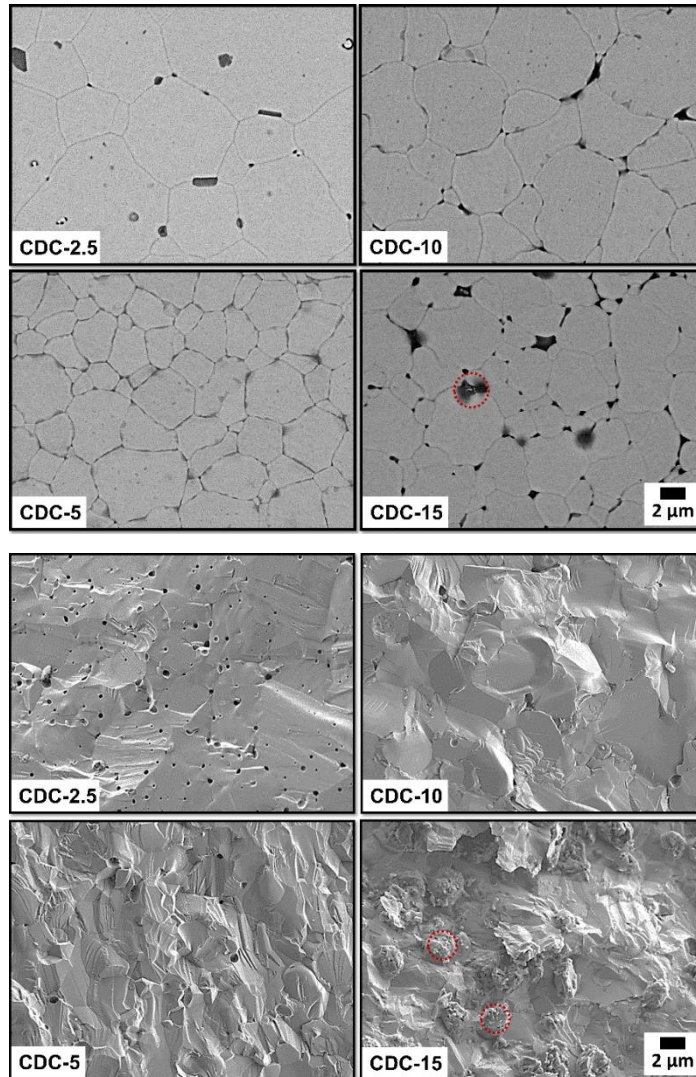


**Figure 4.11:** The high-resolution SEM images of the cold-fractured cross-section (bottom) and polished cross-section (top) of the CDC samples. The polished samples are thermally etched at 1250 °C for 0.5 hours.

#### 4.3.2 Electro-chemo-mechanical Characterization of Variously Doped CDC

The electrochemical properties are characterized at a temperature range of ~250-500 °C in atmospheric air. The impedance data is represented as Nyquist and Bode-like plots for a given temperature of 300 °C in **Fig. 4.12**. As noticed, all CDC samples excluding CDC-2.5 reveal two well-resolved semicircles at a high and intermediate frequency associated bulk (grain) and grain boundary polarization. Although having large grains of around 5 μm, the CDC-2.5

compound surprisingly displays a single semicircle (see **Fig. 4.12.a**). Thus, the only total resistance is considered for further analysis. The bulk resistivity of the samples increases with calcium concentration. For example, the CDC-15 sample develops twice as large resistivity than of CDC-5. Such an outcome is expected as more  $\text{Ca}^{2+}$  concentration increases the degree of the dopant-defect interaction, subsequently leading to a decrease of the “true” oxygen vacancy concentration in bulk [1]. Moreover, grain boundary resistivity, to some extent, increases from CDC-5 to CDC-10 and then falls off for the CDC-15 sample. Although microstructural analysis indicates large segregation of  $\text{Ca}^{2+}$  at the grain boundary in CDC-15. Such a result simply illustrates that high enrichment of  $\text{Ca}^{2+}$  at the grain boundary decreases its resistivity, which is in line with the recent work of Bowman and co-workers [7]. These authors presented that the grain boundary resistivity in the CDC compound is primarily controlled by the local  $\text{Ca}^{2+}$  concentration rather than the microscopic grain boundary character. Additionally, it has been claimed that the local concentration of  $\text{Ca}^{2+}$  exceeds the bulk solubility limit, *i.e.*, below 20 mol% [12], as a result of this forms a Ca-super saturated phase at the grain boundary. Moreover, the detailed analysis of calcium concentration at the grain boundary by an HRTEM is ongoing and will be reported elsewhere. The estimated blocking factor in CDC-10 ( $\alpha_{\text{gb}} \sim 0.35$ ) sample is near twice as large as CDC-5 and CDC-15 samples ( $\alpha_{\text{gb}} \sim 0.2$ ). Nevertheless, such low  $\alpha_{\text{gb}}$  value highlights that the total resistivity of oxygen vacancy migration in the CDC compounds is controlled by bulk, *i.e.*, by the high-frequency mechanisms. The characteristic frequency response of the charge transport is demonstrated in a Bode-like plot in **Fig. 4.12b**. These three samples expose an identical bulk relaxation frequency around  $\sim 400$  kHz whereas grain boundary relaxation differs from  $\sim 3$ -10 kHz depending on the ion-blocking effect. The CDC-2.5 shows a superimposed relaxation frequency at  $\sim 3$  kHz. The impedance result at 300 °C is summarized in **Table 4.1**.

## Tuning of Ion-blocking Barriers via Various Dopant

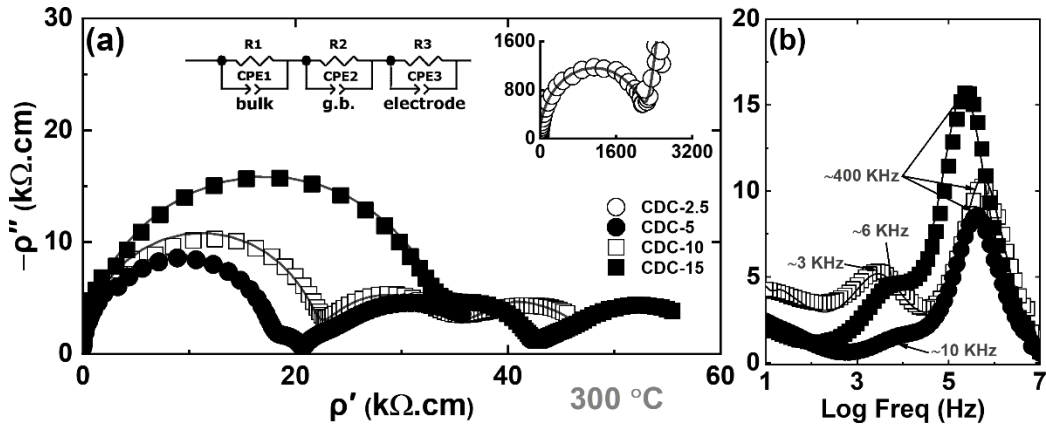


**Figure 4.12:** The geometry normalized (a) Nyquist plots ( $\rho'$  vs  $\rho''$ ) and (b) Bode-like plots ( $\rho''$  vs frequency), of the sintered CDC pellets at 300 °C.

**Table 4.1:** The grain size, capacitance and relaxation frequency of the CDC pellets at 300 °C.

Sample ID	$C_{\text{bulk}}$ (F)	$C_{\text{gb}}$ (F)	$f_{\text{bulk}}$ (Hz)	$f_{\text{gb}}$ (Hz)	Grain Size ( $\mu\text{m}$ )
CDC-2.5	$1.5 \cdot 10^{-11}$			$3.0 \cdot 10^3$	$4.8 \pm 0.3$
CDC-5	$2.8 \cdot 10^{-11}$	$5.5 \cdot 10^{-09}$	$40 \cdot 10^4$	$10 \cdot 10^3$	$3.5 \pm 0.3$
CDC-10	$3.0 \cdot 10^{-11}$	$2.2 \cdot 10^{-08}$	$50 \cdot 10^4$	$3.0 \cdot 10^3$	$4.5 \pm 0.4$
CDC-15	$2.5 \cdot 10^{-11}$	$4.5 \cdot 10^{-09}$	$25 \cdot 10^4$	$5.5 \cdot 10^3$	$3.0 \pm 0.4$

The Arrhenius type temperature-dependent bulk, grain boundary (specific), and total electrical conductivity of the CDC samples are illustrated in **Fig. 4.13**. The CDC-2.5 sample is plotted only for total conductivity. As can be seen, the bulk conductivity decreases to some extent, with increasing  $\text{Ca}^{2+}$  addition. On the other side, grain boundary conductivity is quite similar in CDC-5 and CDC-15 samples, but a reduced value is obtained for the CDC-10 sample. The activation energy for bulk and grain boundary conductivity is reported as  $\sim 0.85$  and  $\sim 1.10$  eV, respectively, for all compounds. The total conductivity value is minimum in the CDC-2-5, though other materials illustrate equivalent value to each other. The total activation energy is estimated at around  $\sim 0.80$ - $0.90$  eV, a typical value for ceria ceramics.

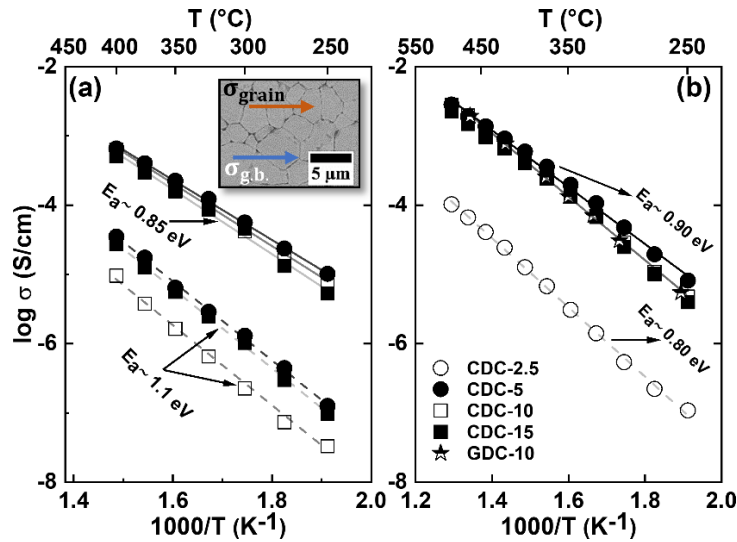


**Figure 4.13:** The temperature-dependent Arrhenius plots for the estimation of (a) bulk (solid line), specific grain boundary (dashed line), and (b) total electrical conductivity of the CDC ceramics. The data of the GDC-10 sample is taken from Ref. [8].

The electromechanical characterization is carried out at room temperature using a proximity sensor-based system with lock-in detection. This method uses a physically contacting electrode made of aluminum (top) and brass (bottom) metal plate. The electromechanical response of the CDC pellets under the application of the electric field is demonstrated in **Fig. 4.14**. As expected, all investigated samples develop a negative strain parallel to the field direction. Within the applied electric field, for example, below 7 kV/cm, no strain saturation is detected in any of those samples. Remarkably, the magnitude of strain is unaffected by applied frequency. The observed strain value of the CDC-5 and CDC-10 is slightly larger than of CDC-2.5 and CDC-15 samples. For example, the former generates a strain value of approximately  $\sim 0.5$  ppm, whereas the latter shows  $\sim 0.25$  ppm with an applied electric field square and frequency of 20 (kV/cm)<sup>2</sup> and 1 Hz, respectively.

## Tuning of Ion-blocking Barriers via Various Dopant

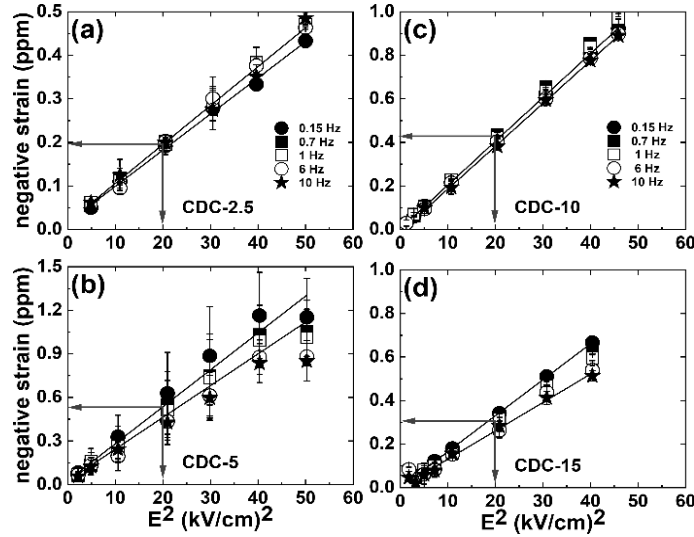


**Figure 4.14:** (a)-(d) The electrostrictive negative strain of the CDC pellets as a function of applied electric field amplitude at frequencies between 0.15-10 Hz.

The electrostrictive strain coefficient ( $M_{33}$ ) is plotted in **Fig. 4.15** as a function of applied frequency. The  $M_{33}$  value is also summarized for selected frequencies in **Table 4.2**. All CDC samples display a frequency-independent  $M_{33}$  value throughout the examined frequency range that complies with the previous findings. The observed  $M_{33}$  value has the same order of magnitude  $10^{-18}$  (m/V)<sup>2</sup> for all CDC samples, fluctuating minimally with nominal Ca<sup>2+</sup> concentration. For instance, the difference of electrostriction strain coefficient ( $\Delta M_{33}$ ) between the CDC-1 and CDC-5 sample is around  $\sim 1-2 \cdot 10^{-18}$  (m/V)<sup>2</sup>. Amongst the samples, the CDC-5 composition illustrates the maximum  $M_{33}$  at any given frequency. The  $M_{33}$  value is compared with a reference GDC-10 pellet fabricated in the identical condition as CDC. Similar to the result obtained in section 4.2.2, all CDC samples display one order lower electrostriction coefficient than GDC material at low operating frequencies. In contrast, at the high-frequency regime, the  $M_{33}$  for CDC samples are comparable to the GDC-10 sample. It is understood that the large ion-blocking barrier factor assists in increasing the electrostriction response at the low-frequency regime. However, CDC materials do not develop such a large ion-blocking factor around 0.8-0.9, rather illustrates a non-blocking barrier ( $\alpha_{gb} < 0.4$ ). In consideration of previous findings, the current result emphasizes that the reflection of steady electrostriction in the CDC is not directly associated with the ion-blocking effect.

## Tuning of Ion-blocking Barriers via Various Dopant

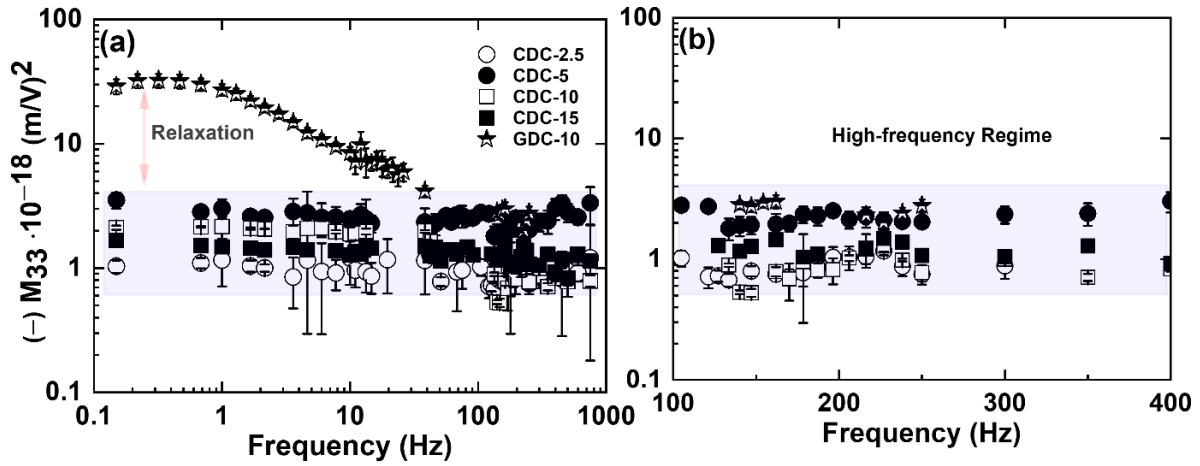


**Figure 4.15:** The electrostriction strain coefficient ( $M_{33}$ ) of the CDC samples with applied frequencies between  $0.1 < f < 1000$  Hz. The data of GDC-10 is taken from Ref. [8].

**Table 4.2:** The electrostrictive strain coefficient ( $M_{33}$ ) of the sintered CDC pellets at selected frequencies, in comparison with reference GDC-10 sample.

~Frequency (Hz)	~Electrostrictive strain coefficient ( $M_{33}$ ) $10^{-18} \text{ (m/V)}^2$				
	CDC-2.5	CDC-5	CDC-10	CDC-15	GDC-10
0.15	1.0	3.5	2.1	1.7	28
1	1.2	3	2.2	1.5	27
6	1.0	2.5	2.1	1.4	10
15	0.9	2.3	2.0	1.5	7
45	1.3	2.3	1.4	1.5	4.1
90		2.5		1.3	
150	0.8	1.9	0.5	1.3	2.7
250	0.8	2.0	0.8	1.0	2.7
400		3.0	0.8	1.0	
500	1.0	2.8	0.8	0.9	

#### 4.4 The Effect of Enhanced Dopant-Defect Interaction

The following work will be submitted to a peer-review journal as "The effect of enhanced dopant-defect interaction on the electromechanical properties of bulk ceria," [A. Kabir](#), M. Varenik, I. Lubomirsky, and V. Esposito.

The electrostrictive response of calcium-doped ceria shows intriguing performance, illustrating no dependency on applied frequencies up to 1 kHz. A direct comparison with the GDC compound might suggest that such behavior can arise due to the development of a non-ion-blocking effect in the CDC. However, intrinsic dopant-defect attraction due to columbic and elastic interaction is significantly larger in the latter than the former. Thus, it is not surprising to expect that such enhanced interaction plays an essential role in controlling the electrostriction response. In this view, the subsequent study aims to figure out the effect of lattice dopant-defect interaction on the electrostriction properties in bulk ceria. For this purpose, the doped ceria compound is prepared with various dopants, comprising Sc, Mg, Gd, and La. According to **Fig. 4.1**, Sc- and Mg-doped ceria would create a much stronger interaction than of Gd- and La-doped ceria.

The doped ceria powder with a composition of  $Ce_{1-x}M_xO_{2-\delta}$  where  $x = 0.10$  and  $0.05$  for trivalent ( $M= Sc, Gd, La$ ) and divalent ( $M= Mg$ ) dopant, respectively is prepared by the core-shell method following the nitrate route [14]. The stoichiometric proportion of respective metal salts is dissolved in boiling 5 N nitric acid and then cooled. The nanoscale pure ceria powder, as synthesized by the co-precipitation method, is dispersed in ethanol, and the metal nitrate solution is poured into it. The dispersed suspension is then ball-milled overnight in a PE bottle, oven-dried at  $100\text{ }^\circ\text{C}$  and calcined at  $500\text{ }^\circ\text{C}$  for 2 hours. The powder is then softly grounded and sieved ( $150\text{ }\mu\text{m}$ ). The powders are uniaxially cold-pressed with a pressure of 200 MPa for 30 sec and then sintered at  $1450\text{ }^\circ\text{C}$  for 10 hours. In core-shell powder, the dopant remains on the outer shell of the pure ceria powder. As sintering is performed at high temperatures for a long time, dopant would migrate from the outer shell of the powder to the inner core (grain).

However, the cation migration is always the rate-limiting step for the diffusion mechanism for ceria, and it is highly probable that a considerable amount of dopant remains locally isolated at the grain boundaries. Such a methodology might impose a large ion-blocking effect on the materials.

#### 4.4.1 Structural and Microstructural Characterization

**Fig. 4.16** illustrates the characteristics of the X-ray diffraction (XRD) pattern of the sintered samples. As expected, all XRD patterns are in agreement with the reference pure ceria powder (ICSD # 251473), showing a cubic fluorite structure.

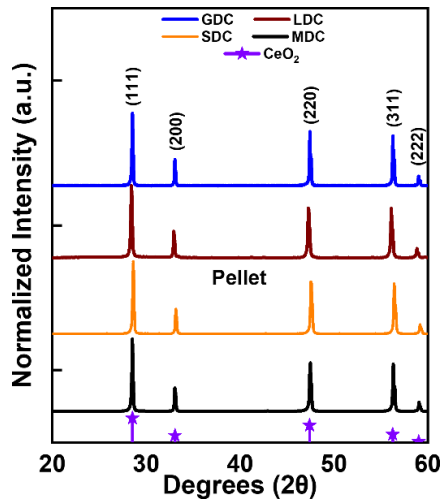


**Figure 4.16:** The X-ray diffraction (XRD) pattern of variously doped ceria pellets sintered at 1450 °C for 10 hours.

Although the powder processing and sintering method remains the same for all samples, the SDC material shows a relative density of around 92%. In contrast, other compounds reveal above 96% of the theoretical density. The low-density value in SDC could be attributed to the possible experimental errors. It might happen that the die and pressure punch was not appropriately aligned during uniaxial pressing, resulting in a relatively low-green density in the sample. The microstructure of the pellets is illustrated in **Fig. 4.17**. All samples develop considerable grain growth with size in the range of microns.

## Tuning of Ion-blocking Barriers via Various Dopant

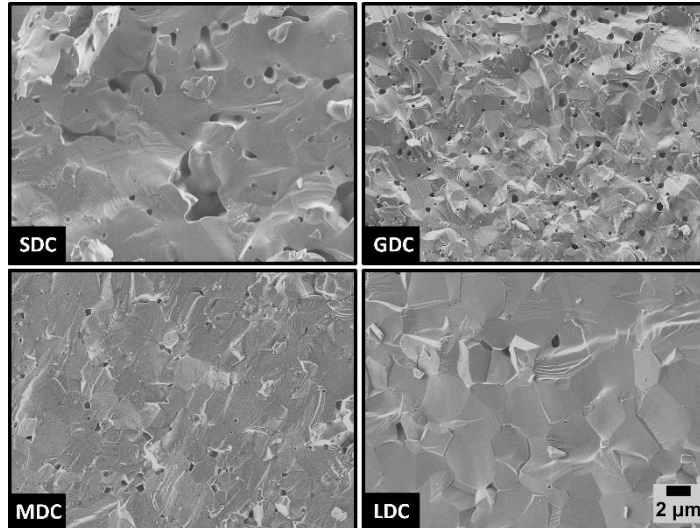


**Figure 4.17:** The high-resolution scanning electron microscope (SEM) images of the cold-fractured ceria pellets. All samples contain an equivalent 2.5 mol%  $V_2O_5$ .

### 4.4.2 Electro-chemo-mechanical Characterization

The electrochemical properties are characterized by the impedance spectroscopy with a frequency range of 10 MHz to 0.1 Hz at the temperature distribution of  $\sim 250$ -450 °C. **Fig. 4.18** represents the typical Nyquist plot ( $\rho'$  vs  $\rho''$ ) for the measurement at 300 °C for the LDC and GDC samples. Interestingly, both samples illustrate a very different bulk and grain boundary resistivity. The GDC sample develops one order higher grain boundary resistivity than the LDC compound. The ion-blocking factor ( $\alpha_{gb}$ ) in the former and latter is estimated at around 0.99 and 0.9 eV, respectively.

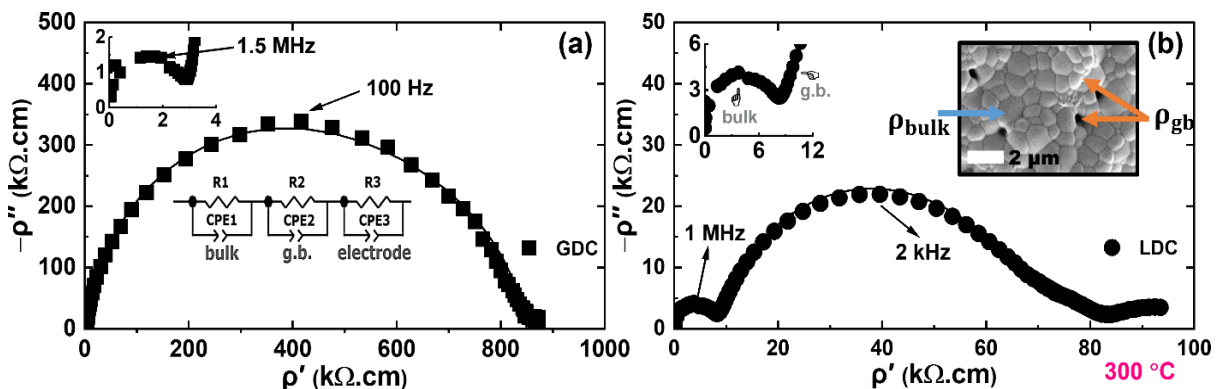


**Figure 4.18:** The geometry normalized Nyquist plot ( $\rho'$  vs  $\rho''$ ) of the (a) GDC and (b) LDC sample, examined at 300 °C in ambient air.

The impedance data of the MDC and SDC samples below 350 °C are found quite noisy at the low-frequency regime. Hence, it is highly recommended to use a sample with a large geometrical ratio (> 2-3) or use a set-up capable of measuring resistance in the GΩ-TΩ range.

**Fig. 4.19** shows the Nyquist plot at 350 °C, displaying a single semicircle for both samples. Taking into account the characteristic frequency response and the resistivity value, it is to be expected that this semicircle is dominated by grain boundary impedance.

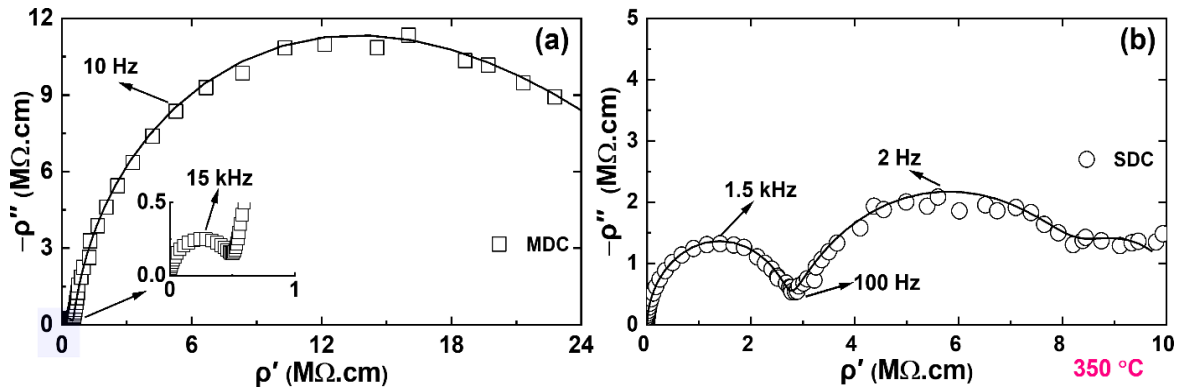


**Figure 4.19:** The geometry normalized Nyquist plot ( $\rho'$  vs  $\rho''$ ) of the (a) MDC and (b) SDC sample, examined at 350 °C in ambient air.

The temperature-dependent total electrical conductivity of the sample presented in an Arrhenius plot in **Fig. 4.20**. As anticipated, the conductivity value maintains a considerable difference between the samples, despite having equivalent oxygen vacancy concentration. This result highlights the governing role of the configuration of oxygen vacancies on controlling charge migration properties. The LDC sample illustrates a maximum electrical conductivity, whereas the SDC shows a minimum. The conductivity value of the SDC and MDC sample is one-two orders of magnitude lower the reported literature value [15]. The activation energy of all materials is between ~0.95-1.05 eV, a typical value for ceria based compound.

## Tuning of Ion-blocking Barriers via Various Dopant

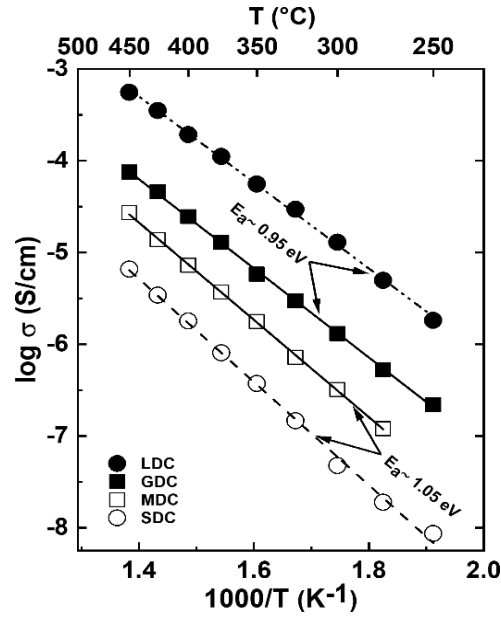


**Figure 4.20:** The temperature-dependent Arrhenius plot for the estimation of total electrical conductivity of variously doped ceria compounds.

The electromechanical characterization is performed using a proximity sensor based on lock-in detection. The sample is pressed between two metal electrodes, namely aluminum (top) and brass (bottom). The measured electromechanical strain as a function of the external AC electric field is represented in **Fig. 4.21**. As observed, the strain value increases proportionally to the field square throughout the examined ranges for the MDC and SDC samples, illustrating no significant dependency on the applied frequency. For the case of the LDC and GDC materials, the strain value starts saturating under an electric field of ~5-7 kV/cm. The strain saturation is fitted with the following empirical equation:

$$u(E^2) = M_{33} \cdot E_{\text{sat}}^2 \cdot \left[ 1 - \exp\left(-\frac{E^2}{E_{\text{sat}}^2}\right) \right] \quad (4.1)$$

Where  $M_{33}$  is the electrostriction strain coefficient, and  $E_{\text{sat}}$  is the saturation electric field. These samples include a dramatic reduction of strain at a higher applied frequency.

## Tuning of Ion-blocking Barriers via Various Dopant

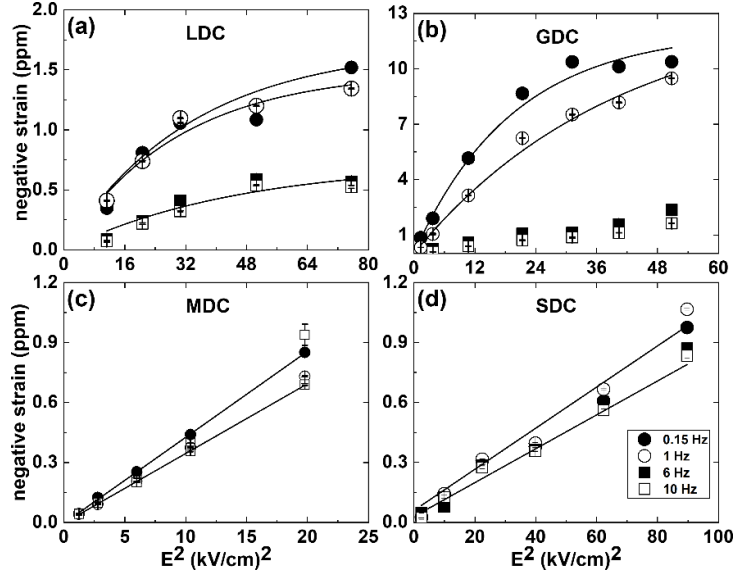


**Figure 4.21:** (a)-(d) Illustration of the electrostrictive strain response under applied electric field square at frequencies between  $\sim 0.15$ -10 Hz.

**Fig. 4.22** displays the correlation of the electrostrictive strain coefficient ( $M_{33}$ ) as a function of applied frequency. At lower frequencies, the GDC sample demonstrates one order of magnitude greater  $M_{33}$  compared to counterparts. The  $M_{33}$  starts relaxing at frequencies between 0.15-10 Hz. Similar to GDC, the LDC sample also shows a relaxation mechanism. The relaxation is empirically fit with the following equation:

$$M_{33}(f) = \frac{M_{33}^0}{\sqrt{1+(\tau \cdot f)^{2+\alpha}}} + M_{33}^\infty \quad (4.2)$$

Where  $M_{33}^0$  and  $M_{33}^\infty$  are the electrostriction coefficient value at low and high frequencies, respectively.  $\tau$  is the relaxation time, and  $\alpha$  is the non-ideality factor. Remarkably, no frequency related electrostriction reduction is observed for the SDC and MDC samples. These samples demonstrate comparable  $M_{33}$  value around  $\sim 1\text{-}3 \cdot 10^{-18} (\text{m/V})^2$  throughout the investigated frequencies. These findings support the hypothesis assumed for the CDC compound that steady electrostriction behavior is associated with the enhanced dopant-defect interaction. Moreover, at the high-frequency regime ( $> 10$  Hz), GDC sample displays similar  $M_{33}$  value to these samples. Whereas the LDC sample shows the minimum coefficient of  $\sim 3 \cdot 10^{-19} (\text{m/V})^2$ .

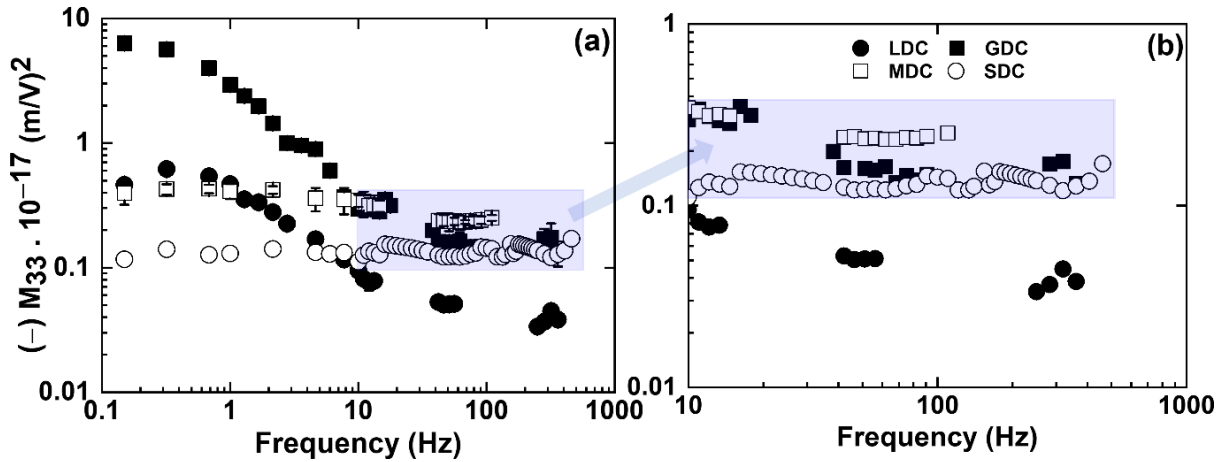


**Figure 4.22:** (a)-(b) The electrostrictive strain coefficient ( $M_{33}$ ) of all samples with a response to an applied frequency ranging between 0.15-700 Hz.

#### 4.5 Effect of Co-doping Strategy

The following work has been submitted as "Enhanced Electromechanical Response in Defective Sm and Nd Co-doped Ceria", [A. Kabir](#), J. Bowen, M. Varenik, I. Lubomirsky, and V. Esposito, *Materialia* (under review).

It is well understood that the minimization of binding energy (negative) for dopant-defect interaction maximizes the configuration of oxygen vacancy in the ceria lattice, leading to increase the bulk ionic conductivity. As explained in section 4.1, equimolar co-doped ceria with effective atomic number 61 (ionic radius 1.094 Å) exerts less dopant-defect interaction than to singly doped ceria. However, the ionic properties depend on not only the lattice but also the ion-blocking barriers. From that perspective, the current work investigates the effect of the co-doping strategy for  $\text{Sm}^{3+}$  and  $\text{Nd}^{3+}$  pair (equivalent ionic radius 1.093 Å) on the oxygen vacancy configuration at the ion-blocking barriers and its correlation with electromechanical properties. The nanometric Sm and Nd co-doped ceria (CoDC) powders with a composition of  $\text{Ce}_{1-x}\text{Sm}_{x/2}\text{Nd}_{x/2}\text{O}_{2-x/2}$  where  $x = 0.01-0.15$  is synthesized by the co-precipitation method as

described in Ref. [16]. The powders are cold-pressed at 200 MPa and sintered at 1450 °C for 10 hours.

#### 4.5.1 Structural and Microstructural Characterization

The X-ray diffraction (XRD) patterns of the starting powders and respective pellets are illustrated in **Fig. 4.23**. All resultant patterns are indexed with the reference pattern of pure ceria (ICSD # 251473), showing a single-phase cubic fluorite structure. As can be seen, with increasing dopant concentration, the featured peaks of the patterns are slightly shifted towards low  $2\theta$  angles, validating the expansion of host lattice.

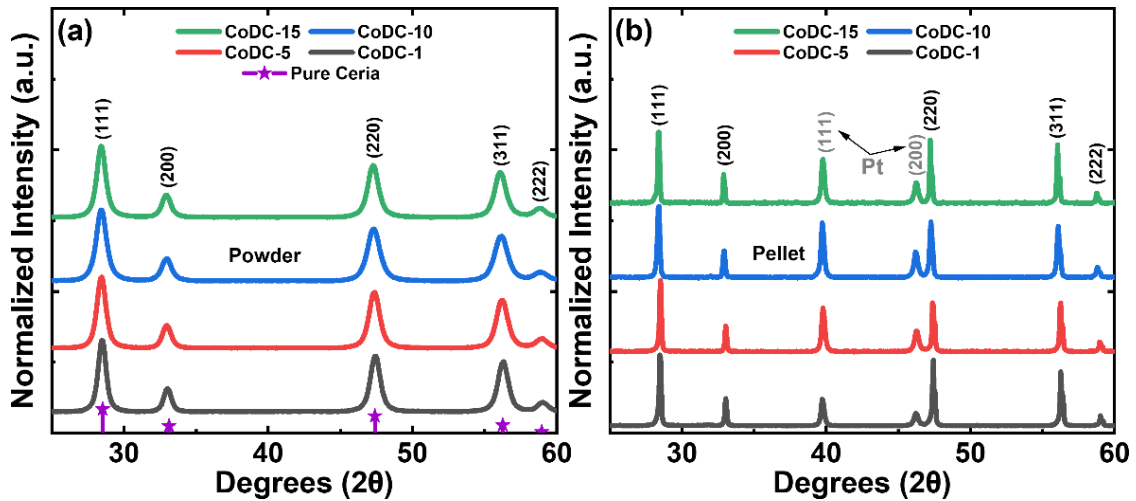


**Figure 4.23:** The X-ray diffraction (XRD) pattern of the starting powders and sintered pellets of co-doped ceria, with composition  $Ce_{1-x}Sm_{x/2}Nd_{x/2}O_{2-x/2}$  where  $x = 0.01-0.15$ . Platinum is used as an internal reference.

The estimated lattice constant of both powder and pellet samples are illustrated in **Fig. 4.24**, following a linear trend with dopant concentration, opines the Vegard's rule [17]. A previous report by Omar *et al.* also demonstrates a comparable manner for Sm/Nd-co-doped ceria system [6]. Numerous study claims that the lattice parameter of the singly doped ceria pursues a quadratic expression with dopant content where the coefficient of the second-order is defined as oxygen vacancy ordering [18][19]. The non-existence of a second-order term addresses that the dopant-defect association is relatively less in these compounds in comparison with singly-doped ceria [6]. Besides, the lattice constant is found to be small for

## Tuning of Ion-blocking Barriers via Various Dopant

the sintered pellet, ascribing to the high-temperature and long-time thermal treatment that relaxes the lattice defect during the mass diffusion process.

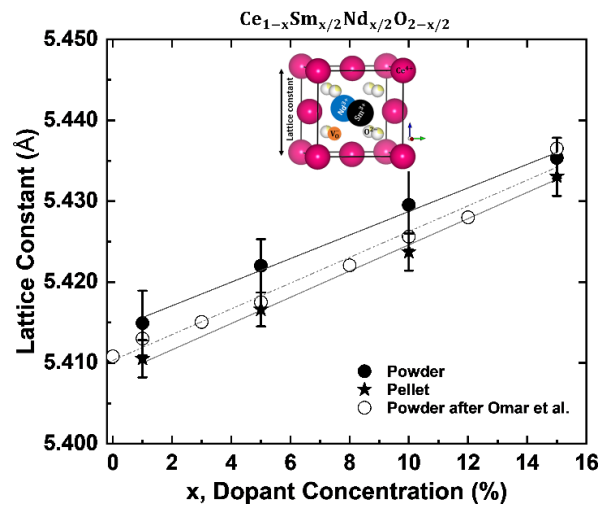


**Figure 4.24:** The lattice constant of the CoDC samples as a function of dopant concentration, where  $x = 1-15$  mol%. The outcome is compared with the experimental data of Omar *et al.* [6].

The microstructure is highly dense, containing a negligible amount of residual pores, which agrees with the measured relative density (> 95%), as shown in **Fig. 4.25**. The observed grains are mostly thermodynamically relaxed, with the average size is in the micron range (~3-6  $\mu\text{m}$ ).

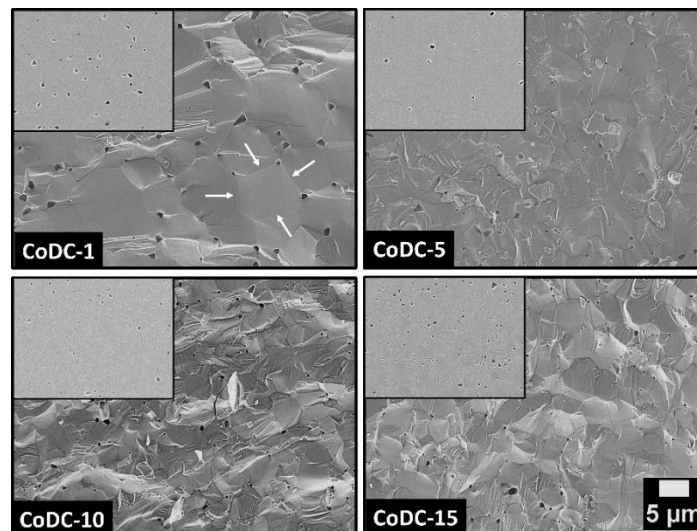


**Figure 4.25:** The high-resolution scanning electron microscope (SEM) micrographs of the fractured and polished cross-sectional face of the CoDC samples.

#### 4.5.2 Electro-chemo-mechanical Characterization

The electrochemical properties of the samples are investigated using complex impedance spectroscopy from low to intermediate temperatures (~250-550 °C). The result is analyzed by the method described in preceding sections and represented as Nyquist plots in **Fig. 4.26**. As evident at 300 °C, the bulk resistivity differs moderately between the materials. Conversely, these samples observe a significant difference in grain boundary resistivity. More specifically, a large resistivity is noticed for the CoDC-1 compound. The CoDC-5 material develops three-four times larger grain boundary resistivity than highly doped CoDC-10 and CoDC-15 samples. The ion-blocking factor ( $\alpha_{gb}$ ), as well as the characteristic grain boundary frequency response of the samples, are found to be decreasing with increasing dopant concentration (see **Table 4.3**).

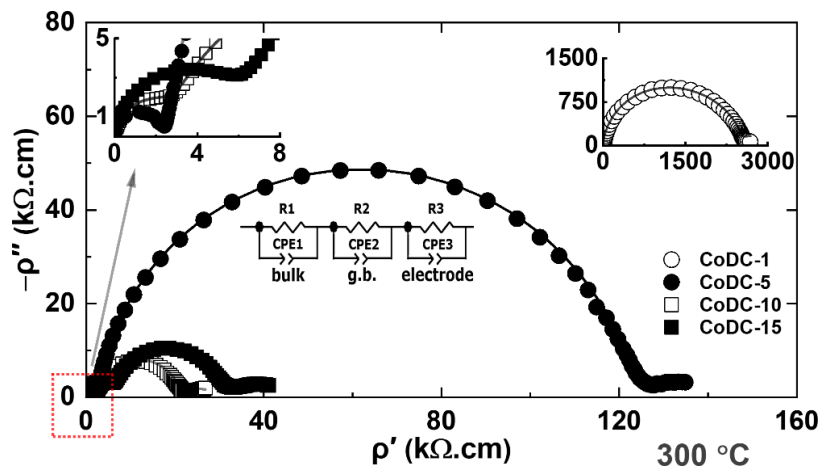


**Figure 4.26:** The geometry corrected Nyquist plots ( $\rho'$  vs  $\rho''$ ) of the CoDC samples, measured at 300 °C in atmospheric air.

The temperature-dependent electrical conductivity of samples, counting bulk, grain boundary, and total are plotted in an Arrhenius relationship in **Fig. 4.27**. As reported, the bulk conductivity increases for low doping concentration, *i.e.*, from CoDC-1 to CoDC-5 sample and then decreases slightly for the highly-doped material throughout the investigated temperature. Such an outcome underlines that for large dopant concentration (CoDC-10 and CoDC-15), a strong oxygen defect-dopant association is inevitable. Although the XRD data for the lattice constant trend indicates a less probable association. The evolution of defect associates

magnifies the formation of high migration energy barriers [5][20], eventually increases activation energy for bulk conduction. This kind of behavior is previously reported by Omar and co-workers for the bulk ionic conductivity of Sm/Nd co-doped ceria [6]. The grain boundary conductivity increases with dopant concentration until 10 mol% and falls off for the CoDC-15 sample. The combination of bulk and grain boundary affects the total conductivity, and as observed, it increases with dopant concentration. Both the CoDC-10 and CoDC-15 samples have identical total electrical conductivity, particularly one order larger than the CoDC-5 sample at the low-temperature regime ( $< 375$  °C). The activation energy for total conductivity is relatively large for low-doped samples, which has a weak vacancy ordering but a significant blocking barrier factor. The impedance results are summarized in **Table 4.3**.

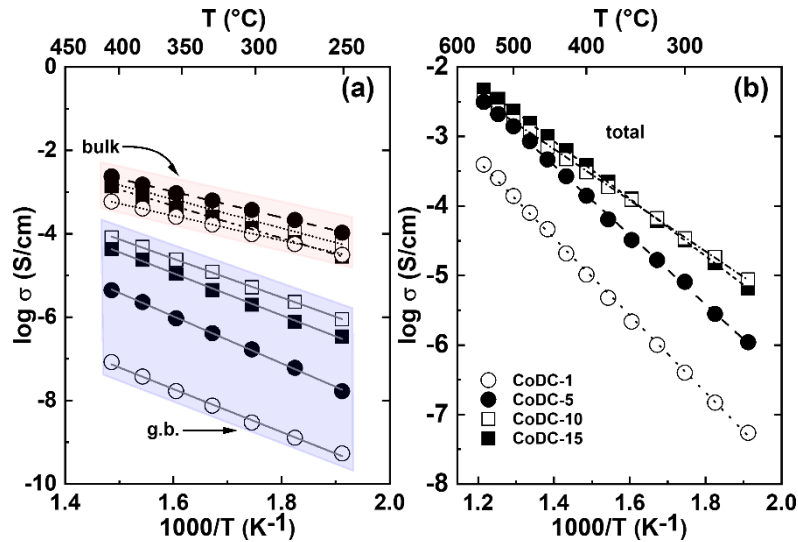


**Figure 4.27:** The temperature-dependent Arrhenius plot for the estimation of (a) bulk, grain boundary, and (b) total electrical conductivity of the CoDC samples.

**Table 4.3:** Summary of the impedance analysis, comprising activation energy for charge migration, relaxation frequency, and ion-blocking factors.

Sample ID	$E_{\text{total}}$ (eV)	$E_{\text{grain}}$ (eV)	$E_{\text{gb}}$ (eV)	$\sim f_{\text{grain}}$ (Hz), 300 °C	$\sim f_{\text{g.b.}}$ (Hz), 300 °C	$\alpha_{\text{gb}}$ , 300 °C
CoDC-1	1.1	0.58	1.0	$1 \times 10^6$	$1.5 \times 10^1$	0.99
CoDC-5	1.0	0.60	1.10	$2 \times 10^6$	$3 \times 10^2$	0.98
CoDC-10	0.7	0.68	0.90	$1 \times 10^5$	$1 \times 10^3$	0.80
CoDC-15	0.8	0.76	1.0	$8 \times 10^4$	$1 \times 10^3$	0.75

The electromechanical strain of the samples with a response to electric field and frequency is illustrated in **Fig. 4.28**. The strains are compressive in parallel to field direction, following the typical behavior for the ceria compound [8][21]. As noted, the strain starts saturating in all samples at a particular electric field, with a strong dependence on the operating frequency. Surprisingly, in a few cases, strain value declines at higher electric fields for low-applied frequency (red arrows). Interestingly, the CoDC-10 and CoDC-15 samples demonstrate an ideal linear response for 6 and 10 Hz.

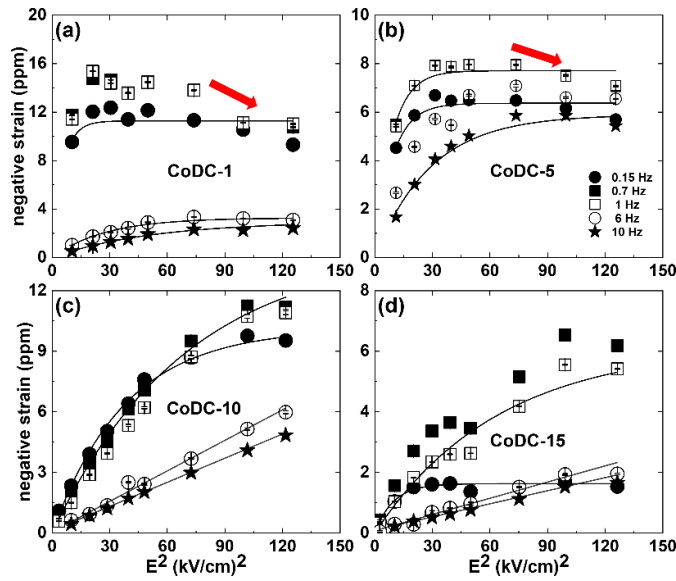


**Figure 4.28:** (a)-(d) The electromechanical strain with a response to the external electric field square at frequencies ranging from 0.15-10 Hz. The symbol size is larger than the error bar.

The electrostriction strain coefficient ( $M_{33}$ ) in connection with the applied frequency is demonstrated in **Fig. 4.29**. As can be seen, the  $M_{33}$  values tend to decrease with increasing frequency for all samples. Such type of reduction is fitted with the empirical expression (**Eqn 4.2**) and summarized in **Table 4.4**. At low-frequency regime ( $< 10$  Hz), CoDC-1 and CoDC-5 samples exhibit significantly greater  $M_{33}$  value than of CoDC-10 and CoDC-15 samples. The former develops relatively less oxygen vacancy ordering and a large ion-blocking factor than of the latter. Notwithstanding, at a higher frequency ( $> 50$  Hz), the magnitude of  $M_{33}$  is reasonably constant (box region in **Fig. 4.29**) in each sample. The value of  $M_{33}$  at high-frequency regimes ranges between  $\sim 0.1-0.3 \cdot 10^{-17} (\text{m/V})^2$ , suggesting that electrostriction response at the high-frequency region does not depend on either oxygen vacancy

concentration or its configuration at the ion-blocking barriers. Most importantly, high frequency  $M_{33}$  value is still one order of magnitude larger than classical electrostriction expectation.

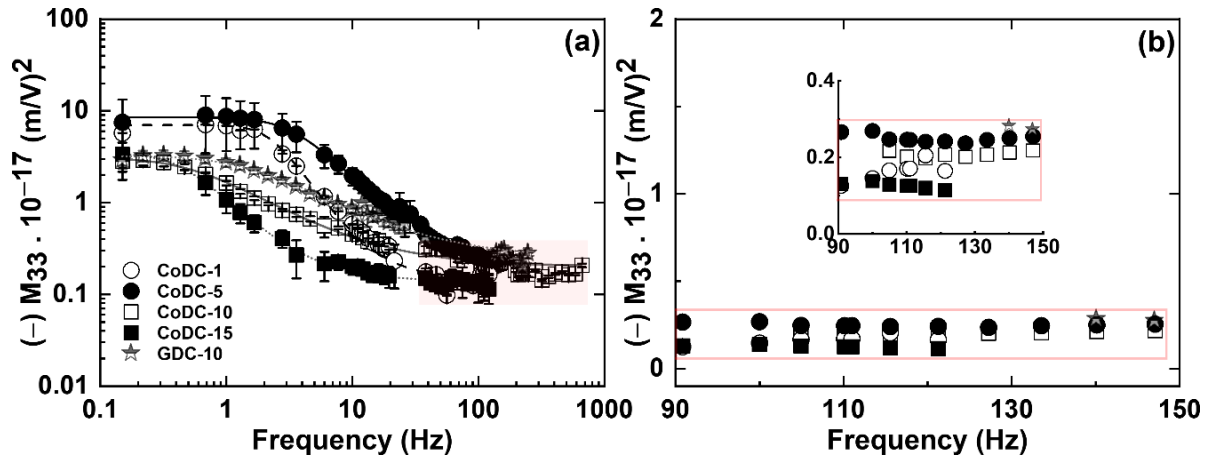


**Figure 4.29:** The electrostriction strain coefficient ( $M_{33}$ ) of the CoDC samples as a function of applied field frequencies from 0.15 Hz to 700 Hz, in comparison with a GDC-10 sample, sintered at 1450 °C for 10 hours [8].

**Table 4.4:** Fitting parameters of Eqn 4.2.

Sample ID	$(-M_{33}^0, 10^{-17} \text{ (m/V)}^2)$	$(-M_{33}^\infty, 10^{-17} \text{ (m/V)}^2)$	$\tau, \text{ S}$	$\alpha$
CoDC-1	$6.9 \pm 0.23$	$0.15 \pm 0.02$	$0.45 \pm 0.03$	$2.0 \pm 0.3$
CoDC-5	$8.3 \pm 1.3$	$0.20 \pm 0.06$	$0.30 \pm 0.01$	$0.70 \pm 0.1$
CoDC-10	$2.9 \pm 0.05$	$0.19 \pm 0.01$	$1.8 \pm 0.1$	$-0.3 \pm 0.1$
CoDC-15	$3.3 \pm 0.2$	$0.13 \pm 0.01$	$2.4 \pm 0.05$	$0.8 \pm 0.06$
GDC-10	$3.0 \pm 0.1$	$0.20 \pm 0.04$	$0.7 \pm 0.05$	$-0.3 \pm 0.1$

#### 4.6 Concluding Remarks

Irrespective of dopant type or atomistic configuration, all investigated ceria samples illustrate non-classical electrostriction. Most of the composition has a  $M_{33}$  value of at least one order larger than classical Newnham scaling law. The experimental result confirms that the magnitude of the electrostriction strain coefficient ( $M_{33}$ ) is insensitive to grain size as well as residual porosity (below 10%). For the case of calcium doped ceria (CDC), a very nearly constant electrostriction coefficient with no dependency on applied field frequency is noticed. Even undergoing an electric field of  $\sim 7\text{-}9 \text{ kV/cm}$ , no field associated strain saturation occurs. The  $M_{33}$  is found to be less influenced by nominal calcium concentration. However, the

observed results suggest that 5-10 mol% Ca concentration illustrates a somewhat larger coefficient. Additionally, no effect on the local calcium segregation is evidenced. The ion-blocking factor ( $\alpha_{gb}$ ) of the CDC does not maintain any correlation with a nominal dopant concentration as GDC. The measured  $\alpha_{gb}$  is ranging between  $\sim 0.2-0.4$ , highlighting that the blocking barrier has a non-ion-blocking property that favors more charge migration than of the bulk. In addition to that, the nanocrystalline CDC-SPS sample also develops a similar electromechanical response. Recalling from chapter 3 that highly doped GDC-20 and GDC-30 samples having a low ion-blocking factor below 0.5 demonstrates frequency-dependent electrostriction relaxation. Accounting such outcomes, one can suggest that steady electrostriction in CDC is not associated with the low ion blocking factor. Likewise, the CDC compound, SDC, and MDC materials introduce an intensified dopant-defect interaction in the lattice. These samples also reveal no electromechanical strain relaxation with a response to applied frequency, despite having one-two orders of magnitude small ionic conductivity than of CDC samples. The reported  $M_{33}$  values in these samples are equivalent to CDC compounds. On the other side, GDC and LDC samples illustrate one-two order larger electrostriction coefficients than of the CDC, SDC, and MDC sample at the low-frequency regime. However, at the higher-frequency regime, the difference in  $M_{33}$  between the samples reduces considerably. Excluding LDC, the counterparts illustrate  $M_{33}$  value in the order of  $\sim 10^{-18}$  (m/V)<sup>2</sup> at frequencies above 10 Hz. It is worth to remind that the GDC and LDC compounds have smaller dopant defect interactions than of the CDC, SDC, and MDC (see **Fig. 4.1**). Due to low interaction, the electrostriction mechanism in GDC and LDC compound is controlled by the ion-blocking factors developed in the materials. Such a statement is supported by the electromechanical result obtained in Sm and Nd co-doped ceria. According to computational calculation, these compounds possess the smallest interactions. The reported  $M_{33}$  value at the low-frequency regime is controlled by the ion-blocking factor in these materials, showing above  $5 \cdot 10^{-17}$  (m/V)<sup>2</sup> for  $\alpha_{gb} > 0.98$ . Interestingly, such high  $\alpha_{gb}$  is noticed for a sample with a low dopant concentration below 5 mol%. This finding additionally supports

our previous hypothesis made for the GDC compound that electrostriction does not necessarily need high dopant concentration. All co-doped samples illustrate similar relaxation activities like GDC and LDC. When the dopant-defect interaction is sufficiently weak, for instance, GDC, LDC, or CoDC sample, the electrostriction strain coefficient follows a frequency-dependent non-Debye type relaxation. As noticed, the large ion-blocking barrier factor assists in increasing the electrostriction response at the low-frequency regime. Whereas the high-frequency regime is not dependent on any factor rather displaying a flat  $M_{33}$  value in the order of  $\sim 10^{-18}$  (m/V)<sup>2</sup> for most of the compositions. In contrast, when the dopant defect interaction is extremely strong, the electrostriction strain coefficient demonstrates relatively an order of small magnitude. The resultant  $M_{33}$  follows no frequency-dependent relaxation, rather showing a steady response from low-high frequency until 700 Hz. Thus, it can be suggested that either calcium or scandium doped ceria can be used to replace the model GDC material for the potential electromechanical application due to its frequency insensitive electromechanical response.

### References:

- [1] J. Koettgen, S. Grieshammer, P. Hein, B. O. H. Grope, M. Nakayama, and M. Martin, "Understanding the ionic conductivity maximum in doped ceria: Trapping and blocking," *Physical Chemistry Chemical Physics*, 20 (2018) 14291–14321.
- [2] Z. P. Li, T. Mori, J. Zou, and J. Drennan, "Defects clustering and ordering in di- and trivalently doped ceria," *Mater. Res. Bull.*, 48 (2013) 807–812.
- [3] D. Y. Wang and A. S. Nowick, "Dielectric relaxation from a network of charged defects in dilute CeO<sub>2</sub>:Y<sub>2</sub>O<sub>3</sub> solid solutions," *Solid State Ionics*, 5 (1981) 551–554.
- [4] V. Butler, C. R. A. Catlow, B. E. F. Fender, and J. H. Harding, "Dopant ion radius and ionic conductivity in cerium dioxide," *Solid State Ionics*, 8 (1983) 109–113.
- [5] I. A. Abrikosov, S. I. Simak, D. A. Andersson, N. V. Skorodumova, and B. Johansson, "Optimization of ionic conductivity in doped ceria," *Proc. Natl. Acad. Sci.*, 103 (2006) 3518–3521.
- [6] S. Omar, E. D. Wachsman, and J. C. Nino, "Higher conductivity Sm<sup>3+</sup> and Nd<sup>3+</sup> co-doped ceria-based electrolyte materials," *Solid State Ionics*, 178 (2008) 1890–1897.
- [7] W. J. Bowman, M. N. Kelly, G. S. Rohrer, C. A. Hernandez, and P. A. Crozier, "Enhanced ionic conductivity in electroceramics by nanoscale enrichment of grain boundaries with high solute concentration," *Nanoscale*, 9 (2017) 17293–17302.
- [8] A. Kabir et al., "Effect of oxygen defects blocking barriers on gadolinium doped ceria (GDC) electro-chemo-mechanical properties," *Acta Mater.*, 174 (2019) 53–60.
- [9] H. L. Tuller, "Ionic conduction in nanocrystalline materials," *Solid State Ionics*, 131 (2000) 143–157.

## Tuning of Ion-blocking Barriers via Various Dopant

- [10] K. Neuhaus, R. Dolle, and H.-D. Wiemhöfer, "Assessment of the Effect of Transition Metal Oxide Addition on the Conductivity of Commercial Gd-Doped Ceria," *J. Electrochem. Soc.*, 165 (2018) F533.
- [11] M. Yan, T. Mori, J. Zou, G. J. Auchterlonie, and J. Drennan, "Microstructural and chemical aspects of working-temperature aged Ca-doped CeO<sub>2</sub>," *J. Eur. Ceram. Soc.*, 30 (2010) 2505–2513.
- [12] M. Yan, T. Mori, F. Ye, D. R. Ou, J. Zou, and J. Drennan, "Effects of dopant concentration and calcination temperature on the microstructure of Ca-doped ceria nanopowders," *J. Eur. Ceram. Soc.*, 28 (2008) 2709–2716.
- [13] William John Bowman, "Correlating Nanoscale Grain Boundary Composition with Electrical Conductivity in Ceria," PhD Thesis, 2016.
- [14] F. Kern, R. Gadow, and A. Kabir, "Mechanical properties and low temperature degradation resistance of alumina-doped 3Y-TZP fabricated from stabilizer coated powders," *Ceram. Mater.*, 69 (2017) 279–285.
- [15] P. Ravi Chandran and T. V. Arjunan, "Investigation on Mg and Sc co-doped ceria electrolyte for IT-SOFC," *Int. J. Eng. Technol.*, 2014.
- [16] V. Esposito and E. Traversa, "Design of electroceramics for solid oxides fuel cell applications: Playing with ceria," *J. Am. Ceram. Soc.*, 91 (2008) 1037–1051.
- [17] L. Vegard, "Die Konstitution der Mischkristalle und die Raumfüllung der Atome," *Zeitschrift für Phys.*, 5 (1921) 17–26.
- [18] I. STEPHENS and J. KILNER, "Ionic conductivity of Ce<sub>1-x</sub>Nd<sub>x</sub>O<sub>2-x/2</sub>," *Solid State Ionics*, 177 (2006) 669–676.
- [19] R. D. Shannon, "Revised effective ionic radii and systematic studies of interatomic distances in halides and chalcogenides," *Acta Crystallogr. Sect. A32* (1976) 751.
- [20] R. Krishnamurthy, Y.-G. Yoon, D. J. Srolovitz, and R. Car, "Oxygen Diffusion in Yttria-Stabilized Zirconia: A New Simulation Model," *J. Am. Ceram. Soc.*, 87 (2005) 1821–1830.
- [21] N. Yavo, O. Yehekel, E. Wachtel, D. Ehre, A. I. Frenkel, and I. Lubomirsky, "Relaxation and saturation of electrostriction in 10 mol% Gd-doped ceria ceramics," *Acta Mater.*, 144 (2018) 411–418.

# Chapter 5: Summary and Future Work

---

## 5.1 Summary

This Ph.D. project focuses on the electro-chemo-mechanical properties of oxygen defective bulk cerium oxides. Owing to the recent discovery of gigantic non-classical electromechanical response, doped ceria materials have received significant interests for the high-performance electromechanical applications. When the project started, the electromechanical effect of ceria compound was only investigated in thin films of about 1  $\mu\text{m}$  for  $\text{Ce}_{1-x}\text{Gd}_x\text{O}_{2-\delta}$  (GDC) materials. Hence, the primary goal of this work was to optimize electrostrictive properties in bulk by tailoring microstructures and oxygen defects. Along with the project, both DTU and WIS have verified the existence of non-classical electrostriction (ES) in polycrystalline bulk cerium oxides. The first report from WIS points out the fundamental electrostriction properties of the GDC bulk ceramics, *i.e.*, the functional dependency of the electrostriction strain coefficient ( $M_{33}$ ) on applied electric field and frequency. This work aimed to explore the effect of different dopants and the evolution of microstructure on ES. The acceptor dopants were selected in such a way that the interaction among the host cation and the charge compensating oxygen vacancies created by the dopant become either stronger or weaker, modulating the configuration of oxygen of vacancies. The conceptual strategy used mainly to interlink the ionic mobility of oxygen defect in polycrystalline doped-ceria at high temperatures with the electromechanical properties at room temperature. Such an approach allows taking advantage of the well-developed experimental methodologies and theoretical models around ionic conductivity in defective oxides. Despite some limitations brought by the different thermal regimes of the electrochemical vs electromechanical properties, relevant connections are established.

According to the theoretical model, electromechanical mechanisms of ceria materials do not depend on crystalline symmetry but the presence of oxygen vacancy ( $V_{\text{O}}^{\bullet\bullet}$ ) in the lattice. On

## Summary and Future Work

comparing the electrostrictive properties in a classical composition ( $\text{Ce}_{0.9}\text{Gd}_{0.1}\text{O}_{2-\delta}$ ), having different microstructures from nano to micron size grains, it has been observed that the electrostrictive strain coefficient ( $M_{33}$ ) presents no correlation with microstructure. The  $M_{33}$  relies on both the applied (i) electric field and (ii) frequency, especially  $M_{33}$  displays a non-ideal Debye frequency dependency with a strong relaxation up to one order of magnitude from  $\sim 0.5$  Hz to  $\sim 10$  Hz. Such an analysis has allowed discriminating two domains of electromechanical response in doped-ceria.

At lower frequencies ( $< 10$  Hz), the magnitude of  $M_{33}$  fluctuates between  $\sim 0.5-5 \cdot 10^{-17} (\text{m/V})^2$ , despite having particular oxygen vacancy concentration. Moreover,  $M_{33}$  value in this regime strongly associates with the evolution of oxygen vacancy configurations at the ion-blocking barriers. The sample with a large ion-blocking factor demonstrates a high coefficient. The dopant-diffusion tailors the ion-blocking barrier through the thermally driven solute drag mechanism. On the other hand, at the high-frequency regime ( $> 10$  Hz),  $M_{33}$  value is turned out to be very much stable with minute variability  $\sim 0.1-0.4 \cdot 10^{-17} (\text{m/V})^2$ , highlighting no limitation from the ion-blocking barrier. Concisely, this result underlines the leading role of vacancy configurations in tuning ES expressly at the low-frequency domain, overcoming the predicted contribution from nominal vacancy concentration.

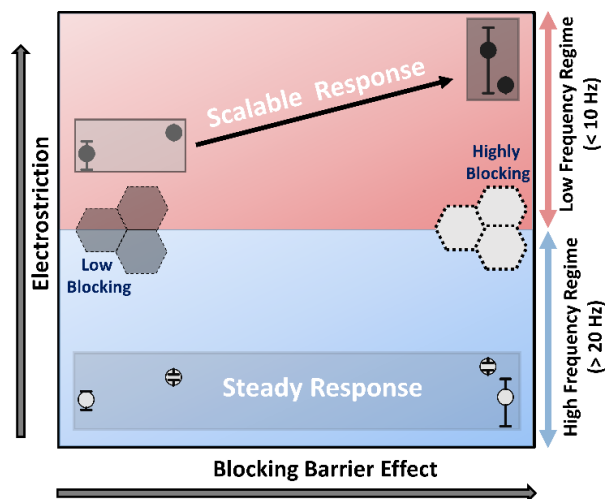
Following this result, the oxygen vacancy is varied in a wide range of concentrations in the GDC compounds in hopes of finding their configuration effect to the ES. As expected, the  $M_{33}$  illustrates a noticeable dependency on the applied frequency. It does not scale up with vacancy concentration rather the lightly doped GDC (Gd 5-10 mol%) samples display one order of magnitude larger  $M_{33}$  than of heavily doped GDC (Gd  $\geq 20$  mol%). The estimated ion-blocking factor in these samples follows a concentration dependency, which decreases with the oxygen vacancy content. Therefore, corresponding to the previous result, a high  $M_{33}$  obtained in the material is ascribed to the formation of a high ion-blocking factor.

In the same way as the GDC compound, La-doped ceria (LDC) develops similar electromechanical behavior. However, LDC demonstrates one order of magnitude lower  $M_{33}$

## Summary and Future Work

than of GDC from small to the high frequency up to ~500 Hz. Even though the former generates a significant blocking factor than the latter. This result indicates that not only the ion-blocking barrier but also the dopant character is a controlling factor that determines the magnitude of ES.

Numerous literature results on computational atomistic modeling demonstrate that dopant-defect interaction is weak in these compounds. Besides, the weakest interaction is reported for the radioactive Pm ( $Z = 61$ ) element. Accordingly, adopting a co-doping strategy using equimolar  $\text{Sm}^{3+}$  and  $\text{Nd}^{3+}$  dopant ( $Z \sim 61$ ), the electrostrictive response is investigated as a function of total dopant concentration. These materials report a higher electrostrictive strain coefficient ( $M_{33}$ ) even up to  $\sim 8 \cdot 10^{-17} (\text{m/V})^2$  at lower-frequencies and expected relaxation effects below 20 Hz. Similar to GDC materials, the ion-blocking factor is found to decrease with oxygen vacancy concentration. The sample with low-dopant level (1-5 mol%) having a large blocking factor presents a high  $M_{33}$  value. Such an outcome emphasizes that ES does not necessarily require a large number of oxygen vacancies. In contrast, the high-frequency  $M_{33}$  value is at least one order smaller than the low-frequency regime, steady and unaffected by both the vacancy concentration and configuration. Taking into account all these results, it can be concluded that the ES response does not attribute directly to the nominal oxygen vacancy concentration for the dopants yielding low dopant-defect interaction. The oxygen defects configuration indeed dominates it at the ion-blocking barriers built in the materials.



## Summary and Future Work

The dopant that introduces large dopant-defect interactions in the host ceria lattice, such as  $\text{Ca}^{2+}$ ,  $\text{Sc}^{3+}$ , and  $\text{Mg}^{2+}$ , illustrates a completely different electrostrictive response. A preliminary study of 5 mol% calcium-doped ceria (CDC) summarizes no dependency on either microstructure or ion-blocking barrier effect (non-blocking) to the ES. The observed  $M_{33}$  is one order of magnitude smaller than GDC or co-doped ceria. Remarkably, CDC develops no frequency-dependent relaxation rather sustains a steady response from low to high frequency. To understand the role of oxygen vacancies governing such behavior, oxygen vacancy content is changed from low to high concentration in CDC compounds. Opposite to GDC material, CDC illustrates a non-blocking barrier effect following no correlation with vacancy concentration. The observed  $M_{33}$  displays a firm value  $\sim 0.1\text{-}0.3 \cdot 10^{-17} (\text{m/V})^2$  over the investigated frequency up to  $\sim 1$  kHz. No marked influence from the microscopic secondary phases or calcium segregation is registered. This outcome highlights that electrostriction in CDC does not control either by vacancy concentration or configuration. Introduction of a smaller dopant such as Sc and Mg reveals the same ES response like CDC. Despite having a large blocking barrier effect, the reported  $M_{33}$  value is about  $\sim 0.1\text{-}0.3 \cdot 10^{-17} (\text{m/V})^2$  illustrating no frequency-variant relaxation. In conclusion, the steady ES mechanism in these compounds is attributed to the presence of enhanced local dopant-defect interaction. Last but not least, high-frequency  $M_{33}$  value is in the order of  $10^{-18} (\text{m/V})^2$  for most of the investigated samples, which is still one order of magnitude superior to Newnham's scaling law estimation.

## 5.2 Future Outlook

### 5.2.1 Single Crystal

The microscopic model of the ES mechanism is established based on experimental results from the x-ray absorption fine spectroscopy (XAS) for Gd-doped ceria thin films. Even though not considered in this study, additional XAS experiments, including other dopant types, especially single crystal form, are needed to support the hypothesis. Single crystal would be an ideal material as it is free from additional controlling factors such as substrate or grain boundaries. A comprehensive investigation of the high-purity single crystal would precisely

quantify the merits of the lattice model. It might also clarify the origin of frequency-dependent relaxation performance.

### 5.2.2 Computational Modelling

As demonstrated throughout the thesis that the magnitude and character of ES response are highly dependent on the dopant type. To figure out what other dopants or defective oxides could introduce non-classical ES, computational research precisely with DFT (density functional theory) is required.

### 5.2.3 Alternative Defective Oxides

The doped ceria ceramics investigated in the current research illustrate two limiting cases, *i.e.*, (i) electrostriction relaxation at high-frequency (ii) frequency insensitive electrostriction but with a low  $M_{33}$  value. Therefore, other compositions, especially multi-co-doping or dopant with  $M^{1+}$  ought to be examined in an attempt to optimize high electrostriction coefficient without relaxation effect. In comparison with ceria, a thorough study for the electromechanical properties of other defective fluorites is still mostly unexplored especially for bismuth oxides, since a report suggests that highly defective bismuth oxides illustrate comparable  $M_{33}$  response as GDC. Other oxides such as zirconia, hafnia also demonstrate similar ionic conduction as ceria. Thus, it would be worth investigating such compounds too.

A preliminary result from WIS indicate that partially hydrated Y-doped  $BaZrO_3$  and (Sr, Mg)-doped  $LaGaO_3$  reveals a high  $M_{33}$  inside the range of  $\sim 10^{-17}$ - $10^{-18}$  (m/V)<sup>2</sup> having a weak relaxation effect. These materials are a well-known protonic conductor ( $OH^+$ ), containing irrelevant content of oxygen vacancies at a hydrated state. Such findings suggest that a point defect of any kind could lead to developing electrocutation if it forms the electroactive elastic dipoles. Because of that, non-classical ES could be extended to acceptor doped perovskite materials. Furthermore, more effort is required to investigate in detail the role of interstitial point defects, dopant type, ion-blocking barrier, microstructure, *etc.* on the ES mechanism for different perovskite systems.

In recent times, high entropy fluorites have ascended significant interests for functional properties, such as ionic conductivity, hardness, and thermal properties. This type of material is mainly constructed by five or more elements in which the configuration entropy controls the intrinsic property. Due to the dominating role of configuration, it is highly projected that high entropy fluorites might develop interesting ES response. Thus, investigation of the state of the art composition consisting of the equimolar contribution of Zr, Hf, Ce, and acceptor dopants would be recommended.

### 5.2.4 Sintering and Characterization

As described, grain size does not play any crucial role in influencing electrostriction response. However, few reports showed that sintering *via* a reducing atmosphere radically enhances grain coarsening as well as minimizes the solute drag effect, leading to tuning oxygen vacancy configuration at the grain boundaries. More considerable attention is also requested for the cold sintering of ceria for various dopants. In this method, it would be possible to deliberately introduce a polymer or carbon-based nanomaterials, *e.g.*, graphene, nanotube at the grain boundary. By doing so, the dielectric and electrical properties of the grain boundary can be modified. It is highly anticipated that such significant changes in the grain boundary properties might bring supplementary or interesting outcomes to ES response. Even though a lot of work is published on the physical origin of the ion blocking effect, an in-depth analysis of space charge region, segregation, and nanodomains *via* TEM are indispensable, intending to obtain a complete understanding of why a blocking effect increases electrostriction. The experimental environment of TEM is highly reducing, and ceria changes its chemical state under such conditions. Thus, it is strongly suggested performing environment controlled ( $pO_2$ ) TEM experiments. Though relevant correlation is made between electrochemical against electromechanical response, a significant limitation lies in the fact that each technique accounts for specific experimental conditions. A meaningful way to improve the quality of the hypothesis is to measure impedance spectroscopy at low-temperature applying corresponding

electric field as for electrostriction. Mainly to see if any changes in the property of ion-blocking barriers occur with the response to the electric field.

### **5.2.5 Effect of Electrode**

For the electromechanical characterization, inclusive work needs to be carried out, finding the role of the electrode material. It is unknown why the non-sputter metal electrode performs better than the sputtered Au or ceramic (TiN) electrode. In turn, it suggests that the interface of the electrode-electrolyte can influence the overall performances. The result of TiN is found worst, although another study claims TiN is more stable and reliable. A precise elemental analysis of the electrode-electrolyte interface needs to be performed, as any form of impurity phases would be detrimental for the electrode performance. In conclusion, ideal electrode materials must be defined.

### **5.2.6 High-frequency Characterization**

Ultimately, characterization at high operating frequencies up to MHz ranges, particularly for Ca- or Mg-doped ceria, is desired. Such a study would allow recognizing whether these materials maintain stable ES response over the frequency range or demonstrate any frequency relaxation at super higher frequencies.

Considering all suggestions, the development of a prototype device offering a steady gigantic electromechanical response would be the highest priority. Such an outcome might lead to drawing industrial and scientific attention to motivate research on this topic.

# Appendices

---

## List of Publications:

- i. **Ahsanul Kabir**, Simone Santucci, Ngo Van Nong, Maxim Varenik, Igor Lubomirsky, Robin Nigon, Paul Muralt, Vincenzo Esposito, "Effect of Oxygen Defects Blocking Barriers on Gadolinium Doped Ceria (GDC) Electro-Chemo-Mechanical Properties," *Acta Materialia*, 53 (2019) 174.
- ii. **Ahsanul Kabir**, Jin Kyu Han, Benoit Merle, and Vincenzo Esposito, "The Role of Oxygen Defects on the Electro-Chemo-Mechanical Properties of Highly Defective Gadolinium Doped Ceria," *Materials Letter*, 266 (2020) 127490.
- iii. Vincenzo Esposito, **Ahsanul Kabir**, Massimo Rosa, Ngo Van Nong, Thenner S. Rodrigues, Lays N. Rodrigues, Marina F. S. Machado, Leticia P. R. Moraes, Debora Marani and Fabio Coral Fonseca, "Tuning diffusion paths in shaped ceria nanocrystals", *CrystEngComm*, 21 (2019) 4025.
- iv. **Ahsanul Kabir**, Jacob R. Bowen, Maxim Varenik, Igor Lubomirsky, Vincenzo Esposito, "Enhanced Electromechanical Response in Defective Sm and Nd Co-doped Ceria," *Materialia*, 2020 (under review).
- v. **Ahsanul Kabir**, Daoyao Ke, Salvatore Grasso, Benoit Merle, and Vincenzo Esposito "Effect of Cold Sintering Process (CSP) on the Electro-Chemo-Mechanical Properties of Gd-doped Ceria (GDC)," *Journal of European Ceramics Society*, 2020 (under review).
- vi. **Ahsanul Kabir**, Haiwu Zhang, Sofie Colding-Jørgensen, Simone Santucci, Sebastian Molin, and Vincenzo Esposito "Electro-Chemo-Mechanical Properties in Nanostructured Ca-doped Ceria (CDC) by Field Assisted Sintering," *Scripta Materialia*, 2020 (under review).

### List of Book Chapter:

- i. **Ahsanul Kabir**, Haiwu Zhang, and Vincenzo Esposito, "Mass diffusion phenomena in cerium oxide." Cerium Oxide (CeO<sub>2</sub>): Synthesis, Properties and Applications, Eds: Salvatore Scirè and Leonardo Palmisano, Elsevier.

### List of Conference Contributions:

- i. Oral Presentation: **Ahsanul Kabir**, Ngo Van Nong, and Vincenzo Esposito, "Effect of Field Assisted Sintering Technology (FAST) on GDC Electro-Chemo-Mechanical Properties," Electroceramics XVI, University of Hasselt, July 9-12<sup>th</sup>, 2018, Belgium.
- ii. Oral Presentation: **Ahsanul Kabir**, Ngo Van Nong, and Vincenzo Esposito, "Microstructure Forging of Electromechanically Active Bulk Ceria," Solid State Ionics-22, June 16-21<sup>st</sup>, 2019, South Korea.
- iii. Oral Presentation: **Ahsanul Kabir** and Vincenzo Esposito, (a) "Steady Non-classical Giant Electrostriction in Calcium Doped Cerium Oxide" and (b) "Tuning the electro-chemo-mechanical properties in defective cerium oxides," 44<sup>th</sup> International conference and exposition on advanced ceramics and composites, Jan 26-31<sup>st</sup>, 2020, Daytona, USA.

# List of Figures

---

<b>Figure 1.1:</b> Schematic illustration of the atomistic mechanism of classical electrostriction in insulators. The image is adapted from Ref. [15].	3
<b>Figure 1.2:</b> The empirical correlation between hydrostatic electrostriction polarization coefficient ( $Q_h$ ) and the ratio of elastic compliance and dielectric constant. The image is adapted from Ref. [10] with permission from John Wiley & Sons.	5
<b>Figure 1.3:</b> Schematic illustration of the atomistic mechanism of electrostriction in oxygen defective ceria. The image is adapted from Ref. [23] with permission from AIP publishing.	6
<b>Figure 1.4:</b> The normalized electrostrictive coefficient (stress) as a function of the fraction of oxygen vacancies in the thin films of undoped and Gd-doped ceria. The value at 33 mol% Gd-doped ceria is taken as 100%. The data is obtained from Ref. [23][25] with permission from AIP publishing, and John Wiley & Sons.	8
<b>Figure 1.5:</b> Schematic illustration of the type of defects formation in cerium oxides. The image is adapted from Ref. [32] with permission from Elsevier.	11
<b>Figure 1.6:</b> (a) Schematic illustration of the formation of typical defect association where an oxygen vacancy sits with one/two nearest neighbors substitutional cation ( $M^{3+}$ ). (b) The experimental binding energy of dopant-vacancy association as a function of ionic radius. The data is taken from Butler <i>et al.</i> [34] with permission from Elsevier.	12
<b>Figure 1.7:</b> Schematic illustration of the activation energy-dependent ionic migration in ceria at high and low temperatures. Here, $E_{mig}$ and $E_{asso}$ represents the activation energy of ion migration and dopant-defect association, respectively. The image is adapted from Ref. [42] with permission from Elsevier.	15
<b>Figure 1.8:</b> (a) Schematic diagram of an electrical grain boundary, consisting of grain boundary core and adjacent space charge layer. (b) The configuration profile of charge carriers, <i>i.e.</i> , oxygen vacancies in the grain boundaries. The image is adapted from Ref. [26] with permission from Elsevier.	16

## List of Figures

<b>Figure 1.9:</b> Evidence of nanodomain in defective cerium oxides. (a)-(c) Nanodomain formation in grain interior leads to lattice distortion and reorganization, (d)-(g) Nanodomain in the grain boundary. SAED pattern illustrates an additional curve diffuse scattering. The image is taken from Ref. [55] with permission from Elsevier. ....	18
<b>Figure 1.10:</b> A preliminary study of electromechanical behavior (right) of a partially dense 5 mol% Ca-doped ceria ceramics, sintered at 1450 °C for 10 hours. The ultrasound bouncing (left) is very low compared to highly dense samples (15-20 bounces), indicating the presence of porosity. ....	19
<b>Figure 1.11:</b> Schematic diagram of the ion-migration and ion-blocking effect in doped ceria. The image is adapted from Ref. [60] with permission from Elsevier. ....	20
<b>Figure 1.12:</b> Schematic illustration of the (a) mass transport mechanism during sintering, (b) dependence of diffusion mechanism as a function of sintering temperature, adapted from Ref. [62][69] with permission from Elsevier. ....	21
<b>Figure 1.13:</b> (a) Grain boundary mobility of pure and 1 mol% doped ceria, with dopants of different effective charges. (b) Normalized grain boundary mobility of 1 mol% doped ceria, with dopants of different cation size. The data is taken from Ref. [70][74] with permission from John Wiley & Sons.....	23
<b>Figure 1.14:</b> Schematic diagram of the stages of deformation during creep in ceramics materials. ....	24
<b>Figure 2.1:</b> Illustration of the charge-pH diagram. The figure is adapted from Ref. [5] with permission from Springer Nature. ....	30
<b>Figure 2.2:</b> Schematic flow-diagram of co-precipitation synthesis method of doped-ceria powder.....	32
<b>Figure 2.3:</b> Illustration of the free-sintering profile for doped ceria, and respective microstructure. ....	33
<b>Figure 2.4:</b> Schematic diagram of the SPS set-up (left). The image is adapted from Ref. [12] with permission from John Wiley & Sons. Example of a typical temperature and displacement profile in the SPS process (right).....	34

## List of Figures

<b>Figure 2.5:</b> Schematic representation of the steps in the cold sintering process for ceria compounds. ....	36
<b>Figure 2.6:</b> Schematic representation of the X-ray diffraction method, showing constructive interference when the distance between paths ABC and DEF differs by an integer number of wavelength ( $\lambda$ ). The image is adapted from Ref. [33] with permission from Elsevier. ....	37
<b>Figure 2.7:</b> Depth range of different types of scattered electrons in an interaction volume. The image is slightly modified from the original [41]. ....	39
<b>Figure 2.8:</b> A general layout of image formation in TEM. Dashed lines are reflected electrons. The image is redrawn from Ref. [47]. ....	41
<b>Figure 2.9:</b> Schematic demonstration of (a) an impedance plot ( $Z$ ) and (b) a Bode plot. The image is adapted from Ref. [49] with permission from John Wiley & Sons. ....	42
<b>Figure 2.10:</b> (a) Brick-layer model: a polycrystal consists of cubic grains, laterally homogeneous resistive grain boundaries and electrodes, respectively, (b) Typical equivalent circuits of RC elements, and (c) resulting characteristic impedance spectra. The image is adapted from Ref. [55] with permission from Cambridge University Press. ....	44
<b>Figure 2.11:</b> The instrumental set-up of impedance spectroscopy measurement for bulk pellets. Photo courtesy: Rana-al-Tahan and DTU Energy. ....	45
<b>Figure 2.12:</b> (a) Schematic drawing of the nanoindentation working principle, the top SEM image shows a typical indenter mark. The image is adapted from Ref. [61][62] with permission from John Wiley & Sons. (b) A representative load-displacement curve in the nanoindentation method. ....	46
<b>Figure 2.13:</b> Schematic drawing of a Michelson laser interferometer (left). Nanovibration analyzer (right). Image courtesy: SIOS (Germany). ....	48
<b>Figure 2.14:</b> Schematic representation of the set-up of electromechanical characterization. ....	48
<b>Figure 3.1:</b> The conventional TEM image (bright-field) of the (a) GDC powder and (b) pre-sintered GDC-0.1h pellet, SPS at 900 °C. Inset: Respective selective area electron diffraction (SAED) pattern. ....	54

## List of Figures

<b>Figure 3.2:</b> The X-ray powder diffraction (XRD) pattern of GDC powder and sintered pellets. .....	55
<b>Figure 3.3:</b> The scanning electron microscope (SEM) images of four different GDC samples, sintered in (a) SPS at 980 °C, 70 MPa (b) air at 1450 °C, for 0.1h (c) air at 1450 °C, for 2.5h (d) air at 1450 °C, for 10h.....	56
<b>Figure 3.4:</b> Geometry normalized (a) Nyquist plot ( $\rho'$ vs $\rho''$ ) of GDC-SPS and GDC-0.1h sample, (b) Nyquist plot ( $\rho'$ vs $\rho''$ ) of GDC-10h and GDC-2.5h sample, (c) Bode-type plot (imaginary $\rho''$ vs log frequency) of all GDC compounds.....	58
<b>Figure 3.5:</b> The Arrhenius plot for the estimation of (a) total electrical conductivity of the GDC samples, in comparison with data from the literature [9], (b) bulk and (specific) grain boundary electrical conductivity of conventionally sintered GDC-10h and GDC-2.5h samples.....	60
<b>Figure 3.6:</b> (a)-(d) The electrostrictive negative strain with the response to the external electric field square at frequencies between 0.15-10 Hz.....	61
<b>Figure 3.7:</b> (a)-(b) The electrostrictive strain coefficient ( $M_{33}$ ) of the GDC samples as a function of applied frequency, up to 100 Hz. ....	62
<b>Figure 3.8:</b> A schematic correlation of the electrostriction strain coefficient ( $M_{33}$ ) at the low-frequency regime with ion-blocking barriers for polycrystalline Gd-doped ceria ceramics....	64
<b>Figure 3.9:</b> The X-ray diffraction (XRD) pattern of commercial 10 mol% gadolinium doped ceria (GDC) powder and sintered pellets.....	66
<b>Figure 3.10:</b> Scanning electron microscope (SEM) images of the GDC pellets, sintered in (a) conventional firing at 1450 °C for 1 hour, (b) SPS at 1100 °C for 5 min with 50 MPa, (c)-(d) CSP at 200 °C for 0.1h with 300 MPa, post-annealing at 1000 °C for 1 hour. ....	66
<b>Figure 3.11:</b> (a)-(b) High-resolution transmission electron microscopy (TEM) image of the GDC-CSP sample at low and high magnification (HAADF mode). ....	67
<b>Figure 3.12:</b> Typical geometry normalized Nyquist plots ( $\rho'$ vs $\rho''$ ) as characterized by frequencies, recorded at 300 °C for the GDC pellets. The red box shows impedance at the high-frequency regime. ....	68

## List of Figures

- Figure 3.13:** The temperature-dependent total electrical conductivity of the GDC samples, measured between 250-500 °C..... 69
- Figure 3.14:** A typical displacement/load–time curve in the nanoindentation measurement for the GDC-CSP sample (fast loading mode). The inset plot illustrates the deformation under the constant load as a function of holding time, indicating a primary creep response..... 70
- Figure 3.15:** (a–c) The electromechanical strain of the GDC samples under external electric field at frequencies between 0.5-10 Hz. (d) The electrostriction strain coefficient ( $M_{33}$ ) as a function of applied frequencies ranging from 0.5-250 Hz. Electrode material: gold (Au). The results are compared with the GDC-10 (conventionally sintered 1450 °C for 10 hours) sample from Ref. [19]. ..... 72
- Figure 3.16:** (a) The electromechanical strain and (b) The electrostriction strain coefficient ( $M_{33}$ ), of the GDC-CSP sample. Electrode material: TiN. .... 73
- Figure 3.17:** (a) The X-ray diffraction (XRD) pattern and (b) The estimated lattice parameter, of GDC powders with composition  $Ce_{1-x}Gd_xO_{2-\delta}$  where  $x = 0.05-0.3$ . .... 74
- Figure 3.18:** The cold-fractured SEM images of the GDC pellets with composition  $Ce_{1-x}Gd_xO_{2-\delta}$  where  $x = 0.05-0.3$ . The pellets are conventionally sintered at 1450 °C for 10 hours..... 75
- Figure 3.19:** Characteristic Nyquist plot examined in the air at 300 °C for the GDC-10 sample. The inset shows the declining trend of an ion-blocking factor concerning dopant concentration. .... 76
- Figure 3.20:** The temperature-dependent Arrhenius plots of (a) bulk, (b) (specific) grain boundaries and (c) total electrical conductivity of the GDC pellets with composition  $Ce_{1-x}Gd_xO_{2-\delta}$  where  $x = 0.05-0.3$ . .... 77
- Figure 3.21:** (a)-(d) The electrostrictive negative strain of the GDC samples as a function of the applied electric field at frequencies 0.5 and 10 Hz. Electrode material: Gold (Au). ..... 78
- Figure 3.22:** The electrostrictive strain coefficient ( $M_{33}$ ) as a function of frequencies ranging from 0.15-100 Hz. The result is compared with Ref. [19]. ..... 79

## List of Figures

<b>Figure 4.1:</b> Schematic illustration of the (left) acceptor doped ceria lattice. The image is adapted from Ref. [3] with permission from Elsevier. The binding energy of dopant-defect interaction (1 NN) for different dopants in ceria (right). The data is taken from Butler <i>et al.</i> [4] with permission from John Wiley & Sons.....	84
<b>Figure 4.2:</b> The total interaction energy between rare-earth dopant and oxygen vacancy occupying the next neighbor (1 NN) and next-nearest neighbor (2NN) position of the dopant. The figure is redrawn after Andersson <i>et al.</i> [5]. .....	85
<b>Figure 4.3:</b> Bright-field TEM image of the CDC starting powders (left), Inset: SAED pattern. Estimation of the particle size distribution (right). .....	86
<b>Figure 4.4:</b> The X-ray powder diffraction (XRD) pattern of the CDC powders and sintered pellets. ....	87
<b>Figure 4.5:</b> The high-resolution SEM images of the CDC pellets sintered in (a) SPS at 980 °C, 50 MPa for 5 min, (b) air at 1450 °C for 10 hours. ....	88
<b>Figure 4.6:</b> (a)-(b) Geometry corrected Nyquist plot ( $\rho'$ vs $\rho''$ ) of the CDC pellets, measured at 300 °C. The outcome is compared with the GDC-Conv sample, sintered at 1450 °C for 10 hours [8]. Electrode: Silver (Ag). ....	89
<b>Figure 4.7:</b> The temperature-dependent Arrhenius plot for the estimation of total electrical conductivity of the CDC samples, measured between 300-550 °C. The results are compared with GDC-Conv [8]. .....	90
<b>Figure 4.8:</b> (a)-(b) The electrostrictive negative strain of the CDC samples as a function of the applied electric field at frequencies between 0.5-10 Hz. ....	91
<b>Figure 4.9:</b> The electrostriction strain coefficient ( $M_{33}$ ) as a function of applied frequencies ranging from 0.1-250 Hz. ....	92
<b>Figure 4.10:</b> The X-ray diffraction (XRD) pattern of variously doped calcium doped ceria powders and pellets, $\text{Ca}^{2+} = 2.5\text{-}15\text{ mol}\%$ . The results are indexed with undoped ceria (ICSD # 251473).....	93

## List of Figures

<b>Figure 4.11:</b> The high-resolution SEM images of the cold-fractured cross-section (bottom) and polished cross-section (top) of the CDC samples. The polished samples are thermally etched at 1250 °C for 0.5 hours. ....	94
<b>Figure 4.12:</b> The geometry normalized (a) Nyquist plots ( $\rho'$ vs $\rho''$ ) and (b) Bode-like plots ( $\rho''$ vs frequency), of the sintered CDC pellets at 300 °C. ....	96
<b>Figure 4.13:</b> The temperature-dependent Arrhenius plots for the estimation of (a) bulk (solid line), specific grain boundary (dashed line), and (b) total electrical conductivity of the CDC ceramics. The data of the GDC-10 sample is taken from Ref. [8]. ....	97
<b>Figure 4.14:</b> (a)-(d) The electrostrictive negative strain of the CDC pellets as a function of applied electric field amplitude at frequencies between 0.15-10 Hz. ....	98
<b>Figure 4.15:</b> The electrostriction strain coefficient ( $M_{33}$ ) of the CDC samples with applied frequencies between $0.1 < f < 1000$ Hz. The data of GDC-10 is taken from Ref. [8]. ....	99
<b>Figure 4.16:</b> The X-ray diffraction (XRD) pattern of variously doped ceria pellets sintered at 1450 °C for 10 hours. ....	101
<b>Figure 4.17:</b> The high-resolution scanning electron microscope (SEM) images of the cold-fractured ceria pellets. All samples contain an equivalent 2.5 mol% VO ..	102
<b>Figure 4.18:</b> The geometry normalized Nyquist plot ( $\rho'$ vs $\rho''$ ) of the (a) GDC and (b) LDC sample, examined at 300 °C in ambient air. ....	102
<b>Figure 4.19:</b> The geometry normalized Nyquist plot ( $\rho'$ vs $\rho''$ ) of the (a) MDC and (b) SDC sample, examined at 350 °C in ambient air. ....	103
<b>Figure 4.20:</b> The temperature-dependent Arrhenius plot for the estimation of total electrical conductivity of variously doped ceria compounds. ....	104
<b>Figure 4.21:</b> (a)-(d) Illustration of the electrostrictive strain response under applied electric field square at frequencies between ~0.15-10 Hz. ....	105
<b>Figure 4.22:</b> (a)-(b) The electrostrictive strain coefficient ( $M_{33}$ ) of all samples with a response to an applied frequency ranging between 0.15-700 Hz. ....	106

## List of Figures

<b>Figure 4.23:</b> The X-ray diffraction (XRD) pattern of the starting powders and sintered pellets of co-doped ceria, with composition $Ce_{1-x}Sm_x/2Nd_x/2O_{2-x/2}$ where $x = 0.01-0.15$ . Platinum is used as an internal reference.....	107
<b>Figure 4.24:</b> The lattice constant of the CoDC samples as a function of dopant concentration, where $x = 1-15$ mol%. The outcome is compared with the experimental data of Omar <i>et al.</i> [6]. .....	108
<b>Figure 4.25:</b> The high-resolution scanning electron microscope (SEM) micrographs of the fractured and polished cross-sectional face of the CoDC samples.....	108
<b>Figure 4.26:</b> The geometry corrected Nyquist plots ( $\rho'$ vs $\rho''$ ) of the CoDC samples, measured at 300 °C in atmospheric air.....	109
<b>Figure 4.27:</b> The temperature-dependent Arrhenius plot for the estimation of (a) bulk, grain boundary, and (b) total electrical conductivity of the CoDC samples. ....	110
<b>Figure 4.28:</b> (a)-(d) The electromechanical strain with a response to the external electric field square at frequencies ranging from 0.15-10 Hz. The symbol size is larger than the error bar. .....	111
<b>Figure 4.29:</b> The electrostriction strain coefficient ( $M_{33}$ ) of the CoDC samples as a function of applied field frequencies from 0.15 Hz to 700 Hz, in comparison with a GDC-10 sample, sintered at 1450 °C for 10 hours [8].....	112

## List of Tables

---

<b>Table 1.1:</b> A general comparison of electromechanical properties between polymers and ceramics. ....	2
<b>Table 3.1:</b> Sintering protocol of GDC ceramics. ....	53
<b>Table 3.2:</b> The summary of impedance analysis at 300 °C together with the average grain size. ....	59
<b>Table 3.3:</b> Summary of the fitted parameter of Eqn 3.3 for GDC pellets. ....	62
<b>Table 3.4:</b> The comparative analysis of the grain boundary resistivity, ion-blocking factor, and electrostriction strain coefficient (M33) of the GDC samples. ....	63
<b>Table 3.5:</b> The experimental creep property, elastic constant, and hardness of the GDC pellets, measured in the nanoindentation measurement. ....	70
<b>Table 3.6:</b> The ion-blocking factor and relaxation frequency of the GDC pellets at 300 °C. ....	76
<b>Table 3.7:</b> The experimental creep property, elastic constant, and hardness of the GDC pellets. ....	78
<b>Table 4.1:</b> The grain size, capacitance and relaxation frequency of the CDC pellets at 300 °C. ....	96
<b>Table 4.2:</b> The electrostrictive strain coefficient (M33) of the sintered CDC pellets at selected frequencies, in comparison with reference GDC-10 sample. ....	99
<b>Table 4.3:</b> Summary of the impedance analysis, comprising activation energy for charge migration, relaxation frequency, and ion-blocking factors. ....	110
<b>Table 4.4:</b> Fitting parameters of Eqn 4.2. ....	112



## Full length article

## Effect of oxygen defects blocking barriers on gadolinium doped ceria (GDC) electro-chemo-mechanical properties

Ahsanul Kabir<sup>a, c, \*</sup>, Simone Santucci<sup>a</sup>, Ngo Van Nong<sup>a</sup>, Maxim Varenik<sup>b</sup>, Igor Lubomirsky<sup>b</sup>, Robin Nigon<sup>c</sup>, Paul Murali<sup>c</sup>, Vincenzo Esposito<sup>a, \*\*</sup>

<sup>a</sup> Department of Energy Conversion and Storage, Technical University of Denmark, Frederiksborgvej 399, Roskilde, 4000, Denmark

<sup>b</sup> Department of Materials and Interfaces, Weizmann Institute of Science, Rehovot, 76100, Israel

<sup>c</sup> Ceramics Laboratory, Department of Materials, Swiss Federal Institute of Technology, Lausanne, 1015, Switzerland

## ARTICLE INFO

## Article history:

Received 15 February 2019

Received in revised form

24 April 2019

Accepted 5 May 2019

Available online 10 May 2019

## Keywords:

Electrostriction

Vacancies

Gadolinium-doped ceria

Sintering

## ABSTRACT

Some oxygen defective metal oxides, such as cerium and bismuth oxides, have recently shown exceptional electrostrictive properties that are even superior to the best performing lead-based electrostrictors, e.g. lead-magnesium-niobates (PMN). Compared to piezoelectric ceramics, electromechanical mechanisms of such materials do not depend on crystalline symmetry but on the concentration of oxygen vacancy ( $V_{\text{O}}^{\bullet\bullet}$ ) in the lattice. In this work, we investigate for the first time the role of oxygen defects configuration on the electro-chemo-mechanical properties. This is achieved by tuning the oxygen defects blocking barrier density in polycrystalline gadolinium doped ceria with known oxygen vacancy concentration,  $\text{Ce}_{0.9}\text{Gd}_{0.1}\text{O}_{2-\delta}$ ,  $\delta = 0.05$ . Nanometric starting powders of ca. ~12 nm are sintered in different conditions, including field assisted spark plasma sintering (SPS), fast firing and conventional method at high temperatures. These approaches allow controlling grain size and Gd-dopant diffusion, i.e. via thermally driven solute drag mechanism. By correlating the electro-chemo-mechanical properties, we show that oxygen vacancy distribution in the materials plays a key role in ceria electrostriction, overcoming the expected contributions from grain size and dopant concentration.

© 2019 Acta Materialia Inc. Published by Elsevier Ltd. All rights reserved.

## 1. Introduction

Cerium oxide ( $\text{CeO}_2$ ) has been comprehensively investigated in the last few decades due to its multifold applications, more specifically in electro-ceramics and catalysts [1–4]. It has a centrosymmetric fluorite structure with a pronounced oxygen defectivity, i.e. oxygen vacancies ( $V_{\text{O}}^{\bullet\bullet}$ ). This feature makes ceria an excellent ionic conductor, especially suitable for solid-state electrolytes at high temperatures [5], where acceptor dopants are used to enhance oxygen defects concentration,  $[V_{\text{O}}^{\bullet\bullet}]$ , in the lattice [6,7]. In cerium oxide,  $\text{Ce}^{4+}$  cation can also be reduced to  $\text{Ce}^{3+}$  under low oxygen partial pressure ( $P_{\text{O}_2}$ ) at high temperatures, creating both quasi-free localized electrons, i.e. small polarons and oxygen vacancies [8], resulting in mixed ionic-electronic

conductivity (MIEC) [5,9]. Besides these properties, ceria exhibits non-classical giant electrostriction at room temperatures [10–12], both in thin films and bulk materials. Remarkably, ceria thin film expands perpendicular to applied field direction, with large compressive stress ( $\approx 500$  MPa) [10]. The average electrostriction coefficient ( $M_e$ ) is reported as  $\approx 6.5 \cdot 10^{-18}$  (m/V)<sup>2</sup> for  $[V_{\text{O}}^{\bullet\bullet}] = 5\%$ , i.e. 20 mol% Gd-doped ceria [10]. Such value is high for a material with low dielectric constant ( $\epsilon_r^{\text{GDC}} \approx 30$ ) [13], even higher compared to relaxor ferroelectric metal oxides, e.g. Ca-doped PMN ( $\text{Pb,Mg,NbO}_3$  ( $\epsilon_r^{\text{Ca-PMN}} \approx 4000$ ) [14]. Yavo et al. also verified this type of electromechanical properties in bulk gadolinium doped ceria and another oxygen defective fluorite oxide ( $\text{Bi}_2\text{O}_3$ ), which exhibit similar results, thus representing to a new class of electroactive materials [12,15]. The atomistic model proposed by Lubomirsky et al. based on XANES/EXAFS measurements [16] comprehensively explains the underlying phenomena of this unusual behavior, further suggested that the presence of oxygen vacancy makes distorted  $\text{Ce}_{\text{Ce}}-7\text{O}-V_{\text{O}}^{\bullet\bullet}$  units: consisting of contracted Ce–O and expanded Ce– $V_{\text{O}}^{\bullet\bullet}$  bond, compared to Ce–O bond in Ce–8O unit [10,16]. As a result, asymmetric charge

\* Corresponding author. Department of Energy Conversion and Storage, Technical University of Denmark, Frederiksborgvej 399, Roskilde, 4000, Denmark.

\*\* Corresponding author.

E-mail addresses: [ahsk@dtu.dk](mailto:ahsk@dtu.dk) (A. Kabir), [vies@dtu.dk](mailto:vies@dtu.dk) (V. Esposito).

distribution and anisotropic local dipolar elastic field are developed in the fluorite lattice [17]. Under the applied electric field, distorted  $\text{Ce}_{\text{Ce}}-7\text{O}_0-\text{V}_\text{O}^\bullet$  complexes conform to more fluorite-like structure and subsequently, local atomic displacement produces giant electromechanical effect [16]. Despite intriguing, some questions about the role of oxygen vacancies and microstructure on electrostriction still remain unexplored [12]. Besides, Lubomirsky and co-workers suggested a power-law dependence of  $I-V$  relationship in grain boundary blocking behavior based on space charge mechanisms [18,19] and demonstrated that an increase of grain boundary resistance leads to a decrease in the portion of applied voltage drop in the bulk, decreasing electromechanical properties [20].

As ionic conductor at high temperatures, bulk properties of ceria-based compounds are controlled by process parameters, *i.e.* morphology of initial powders, sintering kinetics/thermal history, densification, final microstructure, *etc.* For sintering and consolidation, mass diffusion mechanisms are especially dominated by solute drag phenomena, which, depends on both dopant size and valence. These can influence ionic configurations at the grain boundary, for instance, by trapping vacancies in disorder and/or in vacancies-ions complexes with low mobility [21,22]. This is described by the so-called “brick model” that is observed for highly defective ceria where fast ionic migration mechanisms are activated, thus reducing cations trapping effects at the grain boundaries [23–26]. Solute drag phenomena create specific grain boundary configurations and non-stoichiometry, which acts as blocking barriers to migrate charge species in the material, significantly affect intrinsic properties [21]. Moreover, Shibata et al. experimentally showed that the long-range electric interaction is the governing factor in controlling the local charge distribution at the crystal interface [27].

Based on previously published reports, designing the microstructure at nano-scale is also expected to create more significant differences between oxygen migration effects, revealing dissimilar physical and chemical properties than a grain of micron sizes. In addition, decreasing the grain size leads to increase grain boundary effect on the material, as well as increasing the density of the blocking barrier [28]. On the other hand, Esposito et al. proposed that grain boundary blocking factor is not necessarily a geometrical factor [3]: at a fixed oxygen vacancy concentration, different grain boundary blocking effects are encountered, depending on the entity of solute drag effect, controlled by sintering conditions [3]. The grain boundary blocking effect is explained both theoretically and experimentally by the distribution of defects by space charge layer model [29–35]. Other techniques also can disrupt the solute drag effect, even maintaining the polycrystalline in the nanoscale. This occurs by field assisted sintering techniques (FASTs), such as spark plasma sintering (SPS) [36]. FASTs use three important parameters (i) pulsed electric field, (ii) high heating rates and (iii) high pressure to preserve ultra-fine grains [37,38].

In the present work, we use nanometric 10 mol % gadolinium doped ceria (GDC10) to produce polycrystalline samples with different oxygen vacancy configuration. This is done by sintering the nano-powders by field assisted (SPS), fast firing and conventional method, which yields dense polycrystalline samples with tuned oxygen ions blocking barriers. A commercial high-density tape cast sample with minimized grain boundary is also used for comparison. The influence of oxygen vacancy configuration on electro-chemo-mechanical properties of GDC was investigated, comparing the electrochemical properties from low to intermediate temperatures (*ca.* 300–575 °C) with the electromechanical properties at room temperatures, expecting unchanged oxygen vacancy configuration in the materials.

## 2. Experimental procedure

### 2.1. Powder synthesis

Nano size gadolinium doped ceria (GDC10) powders were prepared by co-precipitation method using diamine in aqueous solution [3]. Cerium nitrate hexahydrate (Sigma-Aldrich, USA) and gadolinium nitrate hexahydrate (Sigma-Aldrich, USA) salts were mixed together in stoichiometric proportions to prepare 0.1 M solution in deionized water. Then MDEA (N-methyl-diethanolamine) was added dropwise. The molar ratio between total cations and MDEA was 1:3. The resulting precipitates were kept overnight under mild stirring. Afterward, the precipitates were centrifuged and washed several times with ethanol. The resulting gel was dried at 120 °C followed by calcination at 500 °C for 2 h. After the calcination, hard agglomerated powders were ball-milled in ethanol with 2 mm zirconia balls for 10–12 h at 50 rpm, followed by drying at 120 °C for 10 h. Finally, the powders were softly crushed by mortar and pestle and sieved using a 150  $\mu\text{m}$  mesh.

### 2.2. Pellet preparation

The SPS sample was consolidated by field assisted spark plasma sintering (SPS) (Dr. Sinter Lab 515S, Japan) under high vacuum ( $\leq 6 \cdot 10^{-6}$  Torr) at 980 °C, uniaxial pressure of 70 MPa with 5 min dwelling. To minimize the chemical reduction that may occur by FAST treatments, the sample was re-oxidized by post-heating at 700 °C for 1 h. For the conventional sample, powders were uniaxially cold pressed at 200 MPa for 30 s, followed by sintering at 1450 °C in air for 10 h. To achieve high density in the pellets independently by the powders packing [39], the fast-fired sample was pre-densified by SPS at 900 °C and then thermally treated at 1450 °C for 0.1 h with 20 °C/min heating and cooling rate. Commercial tape (Kerafol Germany) was sintered at 1450 °C for 2.5 h.

### 2.3. Materials characterization

The density of the samples was measured in water using Archimedes method. The particle size and phase composition of the samples were analyzed by transmission electron microscope (TEM) (JEOL 2100, USA) and X-ray diffraction technique (XRD) (Bruker D8, Germany), respectively. The microstructure was investigated by a high-resolution scanning electron microscope (SEM) (Zeiss Merlin, Germany). The grain sizes were calculated by the linear intercept method using a minimum of 100 grains, multiplying with correction factor 1.57 [40]. The electrochemical impedance spectroscopy (EIS) was performed at 300–575 °C in air using Solartron 1260 (UK), in a frequency range of 0.01 Hz–1 MHz with a 100 mV alternate signal. The samples have bar-like geometry. Gold-silver mixture electrodes pastes were coated on top of the sample and dried at 600 °C for 15 min. Symmetric configuration using gold as electrodes, silver as current collectors and platinum wire as current leads were used. The EIS data were plotted using Real  $Z'$  and Imaginary  $Z''$  of the impedance normalized by the geometrical cell parameter  $k$  of each sample, where  $k = A/t$ ,  $A$  is the electrode area and  $t$  is the thickness. The resulting geometry normalized EIS plots are thus expressed as geometrically normalized Nyquist plots, *i.e.*  $\rho'$  vs  $\rho''$  (Cole-Cole plots), and as  $\rho''$  vs frequency plots (similar to Bode-plot). The latter related the relative dielectric constant,  $\epsilon_r = \frac{1}{-2 \cdot \pi \cdot f \cdot \rho''}$ , as a function of the AC electric field frequency ( $f$ ). The data were fitted by equivalent circuit and analyzed by ZView software shareware version. The electromechanical measurement was performed using a proximity sensor (Capacitance, Lion) based system with a lock-in detection, as previously reported in Refs. [12,15]. Prior to measurement, the system was calibrated with

PZT (Shenzhen Yuije Electronics Co. Ltd. China). The sample was pressed between two metal electrodes using a spring. A pushrod is used to transfer displacement from the electrodes to a proximity sensor. The signal from the proximity sensor is captured using a lock-in amplifier. Longitudinal electrostrictive strain (parallel to the applied electric field) is calculated as a ratio between the displacement and the original thickness of the ceramic pellets.

### 3. Results and discussion

Use of nano-powder in ceramic processing allows fine control of the microstructural features in final bulk materials. The morphology and structure of the starting nano-powder used in this work are shown in Fig. 1. TEM analysis revealed that particles have a spherical shape and are loosely agglomerated. The nano-powders have a narrow range of size distribution with an average particle size ranging between 10–15 nm. Electron diffraction pattern shows fluorite symmetry of ceria. Crystallography was further confirmed by X-Ray diffraction technique.

Fig. 2 illustrates the XRD pattern of GDC powder and sintered samples. Within the detection threshold of the technique, the patterns reveal no secondary phases. The reflection peaks of the pattern perfectly fit with the theoretical pattern (ICSD code 251473). Average crystallite size by Scherrer and lattice parameter for the starting powders are estimated as  $\approx 12$  nm and 0.540 nm, respectively. Results are consistent with the TEM analysis in Fig. 1. For the sintered samples, XRD patterns in Fig. 2 also display identical results. Narrow peaks imply an increase of particle size during sintering, according to the Scherrer formula [41].

The microstructures of sintered GDC samples are presented in Fig. 3. The micrographs indicate that grains are highly dense with negligible intra-granular porosity. The outcome is consistent with the experimental density of the pellets, which is above  $\geq 96\%$ , for all samples. Grain size analysis shows that both the SPS and fast firing sample have a significantly smaller grain size (around 150–200 nm) than conventionally sintered materials. They exhibit typical polygonal grains with nearly homogeneous size distribution. Furthermore, they show no surface relaxation at the grain boundary. Plapcianu et al. found similar results in SPS sintering of GDC [37]. These authors stated that restricted grain growth in this type of non-conventional sintering is attributed to fast heating rates especially in the initial stage of sintering, where grain-

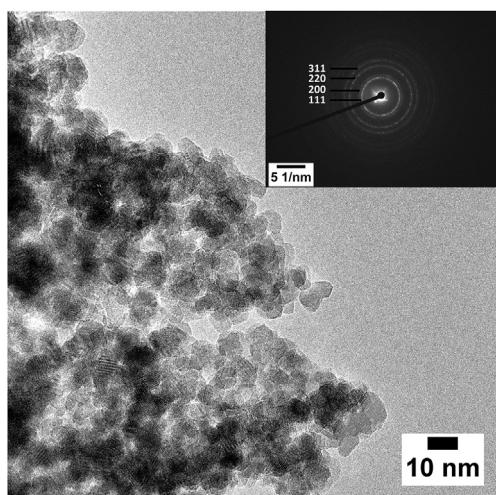


Fig. 1. Bright field TEM images of GDC powder, calcined at 500 °C for 2 h. Inset shows the selective area electron diffraction (SAED) pattern of it.

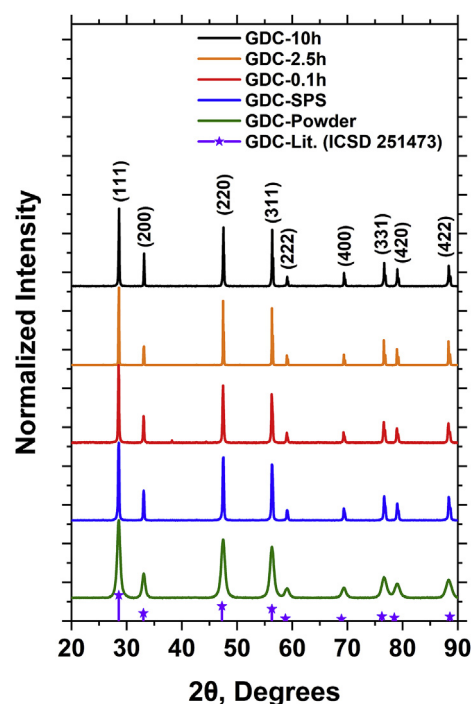


Fig. 2. XRD pattern of gadolinium doped ceria (GDC) powder and sintered pellets.

coarsening mechanism dominates. However, GDC-10 h and GDC-2.5 h materials show a high degree of grain growth with an average grain size of  $2.0 \pm 0.3 \mu\text{m}$  and  $1.5 \pm 0.2 \mu\text{m}$ , respectively. Nearly all grains have equilibrium shape at the triple point (red lines in Fig. 3c, 3d) with fully relaxed and residual small grain boundary curvature (see black arrows in Fig. 3c, 3d).

Fig. 4a and Fig. 4b illustrates the geometry normalized Nyquist plots ( $\rho'$  vs  $\rho''$ ) at 300 °C. The geometrical normalization is carried out for the total volume of the samples, to have a direct comparison between the materials, and it does not take into account the actual volume fraction of the grain boundary in the sample. These Nyquist spectra were fitted by using parallel equivalent circuits of RQ element. R is denoted as resistor and Q is termed as constant phase element, as  $C = (R^{1-n}Q)^{1/n}$ , where C is the capacitance and n is the fitting parameter. At this temperature, as evident from Fig. 4a, only one semicircle is observed in both the nanostructured GDC-SPS and GDC-0.1 h samples, which correspond to strongly overlapped bulk and grain boundary contribution, with capacitance representing the bulk value (see Table 1). Similar features were previously reported in other studies on nanocrystalline ceria materials, suggesting superimposed semicircle is predominated by grain boundary impedance [42,43]. Tuller et al. stated that such overlapping behavior is due to the similar order of magnitude between the space charge width and grain size [44]. Since deconvolution of bulk and grain boundary contribution from these samples is not possible and due to the typical frequency response, the single semicircle is attributed to the grain boundary. On the other hand, conventionally sintered microcrystalline GDC-10 h and GDC-2.5 h samples display two well-defined semi-circles (see Fig. 4b) that according to brick layer model, refer to the high and intermediate frequency associated bulk and grain boundary impedance, respectively [45]. The low frequency arc attributes to the electrode/material interface polarization mechanisms that are not relevant for this discussion [46]. Both GDC-10 h and GDC-2.5h samples exhibit a comparable bulk resistance, however, distinct grain boundary resistance is measured. The effect of grain boundary

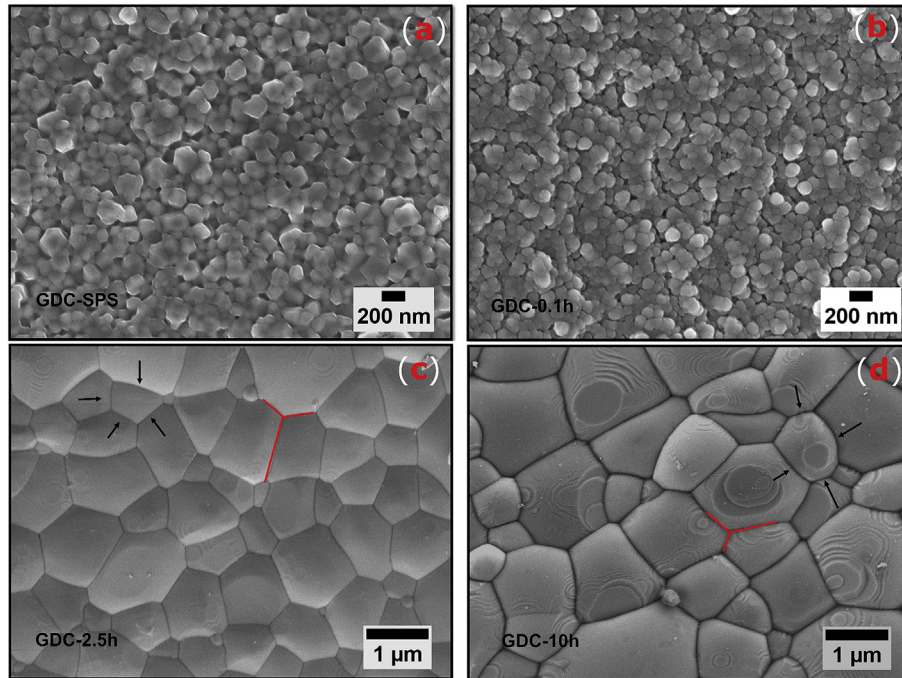


Fig. 3. SEM images of four different GDC samples, sintered in (a) SPS at 980 °C, 70 MPa (b) air at 1450 °C, for 0.1 h (c) air at 1450 °C, for 2.5 h (d) air at 1450 °C, for 10 h.

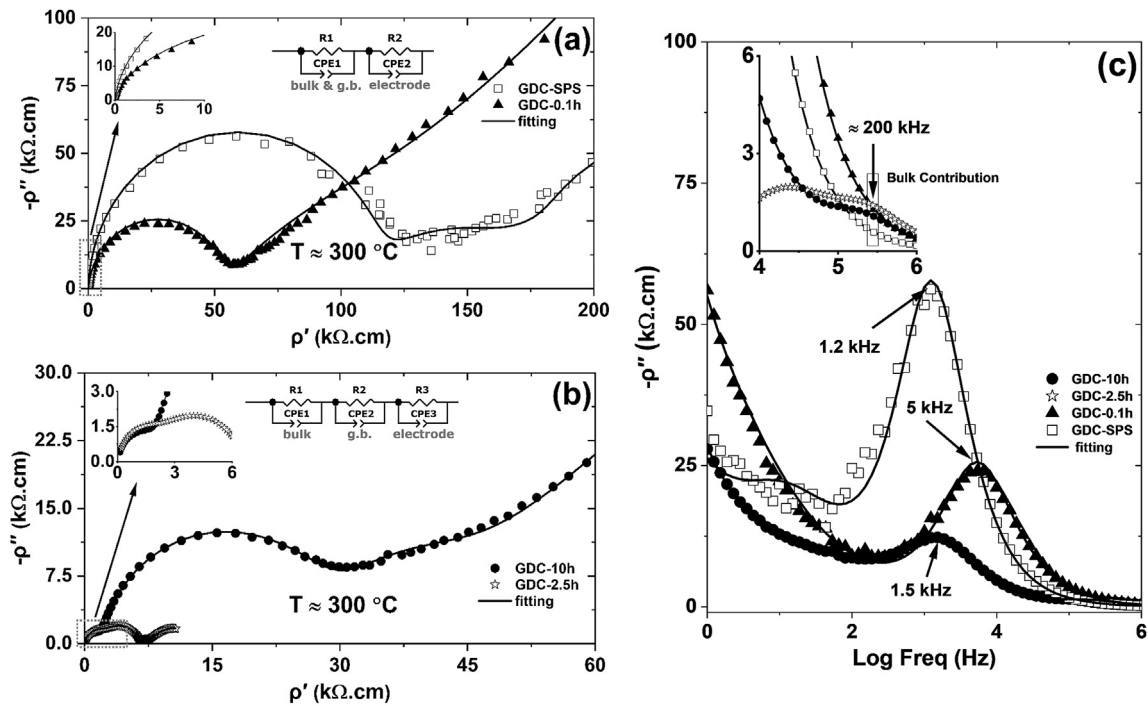


Fig. 4. Geometry normalized (a) Nyquist plot ( $\rho'$  vs  $\rho''$ ) of GDC-SPS and GDC-0.1 h samples, (b) Nyquist plot ( $\rho'$  vs  $\rho''$ ) of GDC-10 h and GDC-2.5 h samples, (c) imaginary  $\rho''$  vs log frequency ( $f$ ) plots of all the GDC samples, measured at 300 °C.

resistance is characterized by the grain boundary blocking factor ( $\alpha_{gb}$ ), which is defined as the ratio of grain boundary resistance to the total resistance ( $\alpha_{gb} = \frac{R_{gb}}{R_{bulk} + R_{gb}}$ ) [47]. The grain boundary blocking factor ( $\alpha_{gb}$ ) is estimated as  $\approx 0.65$  and  $\approx 0.9$  for GDC-2.5 h and GDC-10 h at 300 °C, respectively. Comparing the microstructure, such behavior is unexpected as GDC-10 h has larger grain size, *i.e.* lower gb/grain geometrical ratio, than GDC-2.5 h sample.

Similar results were previously reported, where long-term thermal treatment, *i.e.* 36 h, possesses a detrimental effect on the blocking factors for low dopant concentration, *e.g.* for the conventional sintering for 10 h [3]. Furthermore, a significantly higher resistance in GDC-SPS compared to GDC-10 h indicates a field assisted trapping of oxygen vacancies in the lattice during SPS. High electric fields in SPS can result in a frozen non-equilibrium dopant

distribution, which could decrease the possible vacancy mobility in the nanometric polycrystalline materials. Moreover, one report suggests that the chemical reducing condition occurring during the SPS can also create a large number of  $Ce^{3+}$  species that remain confined at the grain boundary, even after long time re-oxidation [36], resulting in an increment of grain boundary space charge potential. As mentioned before, nanostructures in SPS create a high density of grain boundaries, which act as a high blocking barrier to charge migration [48,49]. Although having similar nanostructure like GDC-SPS, fast firing sample, *i.e.* GDC-0.1 h presents an intermediary behavior between GDC-SPS and GDC-10 h. To sum up, all the samples possess similar density and exactly same dopant concentration, however, they develop quite different grain boundary resistance (blocking barrier), an effect that is ascribed to dissimilar oxygen vacancy configurations. In a broader sense, various sintering mechanisms lead to govern unlike oxygen vacancy configurations in the material, as well as dissimilar ordering of vacancies and defect hopping probabilities, which could be attributed to the nature of solute drag effect due to various thermal treatments.

In Fig. 4c,  $\rho''$  vs frequency plots elucidate the distribution of charge transport by means of its relaxation frequency. Both GDC-10 h and GDC-2.5 h expose a bulk relaxation frequency around ~200 kHz, while, grain boundary relaxation frequency exhibits around 1.5 kHz and 20 kHz (data not shown here), respectively. Such a low grain boundary frequency response is attributed to high blocking barrier effect in the GDC-10 h compound. GDC-SPS and GDC-0.1 h show an overlapped relaxation frequency at 1.2 kHz and 5 kHz, respectively. This overlay behavior is ascribed to different charge transport mechanism, as resulting from unrelaxed microstructure and non-equilibrium fast thermal treatment. Above all, comparative analysis of high frequency response (see inset Fig. 4c) suggests that possible bulk relaxation behavior of GDC-0.1 h is equivalent to GDC-10 h sample, while GDC-SPS show very limited response.

Table 1 summarizes the capacitance, relaxation frequency values of the samples at 300 °C, along with average grain size. These values are calculated from the constant phase element with the 1/RC relationship from the fitted plots.

The temperature dependence of the total electrical conductivities ( $\sigma = 1/\rho'$ ), *i.e.* bulk plus grain boundary is illustrated with an Arrhenius plot in Fig. 5a. As anticipated and observed, conventionally sintered microcrystalline samples display superior electrical conductivity than non-conventional nanocrystalline materials. Additionally, it is worth mentioning that at high doping content such as 10 mol% Gd, electronic conductivity is negligible at atmospheric pressure [50], therefore it can be assumed that total electrical conductivity (bulk and grain boundary) in air is solely controlled by the migration/mobility of  $V_O^{\bullet}$ . GDC-2.5 h displays highest electrical conductivity among all of them, whereas, GDC-SPS reveals the minimum, which is directly interlinked with activation energy values. The high activation energy in GDC-SPS is also consistent with the existence of a large density of blocking barrier illustrated in Fig. 4, an effect conceivably caused by vacancy

trapping or/and vacancy clustering mechanisms. The minimum activation energy observed in GDC-2.5 h could be of different grain boundary composition (uniform dopant distribution) due to short thermal treatment. GDC-0.1 h shows similar conductivity of previous work (see Fig. 5a), however, as expected, GDC-10 h sample displays much higher conductivity than GDC-36 h [3]. At the same time, Fig. 5b distinguishes between bulk and grain boundary conductivity for GDC-10 h and GDC-2.5 h samples. In this case, the resistivity of the two contributions is normalized by the actual volume of bulk and grain boundaries, as reported in Ref. [50]. According to expectations, microcrystalline samples show a similar trend in bulk conductivity. A significant difference is determined in grain boundary conductivity value, which is linked to the grain boundary blocking factor. Low grain boundary conductivity in GDC-10 h also confirms that oxygen vacancy at the grain boundary is less mobile than GDC-2.5 h sample. The most substantial result is that measured ionic conductivity of GDC-0.1 h lies in between grain boundary conductivity of GDC-10 h and GDC-2.5 h samples, at these temperatures range. This outcome further presupposes that grain boundary blocking factor ( $\alpha_{gb}$ ) in GDC-0.1 h sample might be in between 0.65 and 0.9. Additionally, it supports the hypothesis that the conduction mechanism in nanocrystalline ceria is ruled by grain boundary blocking factors.

The electrostrictive strain as a function of applied electric field square is presented in Fig. 6. All the compounds exhibit negative longitudinal strain that agrees with previous reports of GDC thin films and bulk materials [10,12]. They respond at the second harmonic of the applied electric field with different frequency within the applied range, further confirming its electrostriction behavior. Besides, the graph explains the following trends *i.e.* at low frequency, the strain saturates with increasing electric field amplitude, whereas with increasing frequency magnitude of strain value declines dramatically. The strain saturation behavior empirically fits the following equation:

$$u(E^2) = M_{33} \cdot E_{sat}^2 \cdot \left[ 1 - \exp\left(-E^2/E_{sat}^2\right) \right] \quad (1)$$

Where  $M_{33}$  is the electrostriction 3-3 strain coefficient and  $E_{sat}$  is the saturation electric field. Beyond the saturation point, the linear relationship between electrostriction strain vs  $E^2$  is no longer valid. At certain electric field and frequency, GDC-10 h shows maximum electrostrictive strain among all the samples, which has a high bulk and low grain boundary relaxation frequency (see Fig. 4c). Surprisingly, GDC-2.5 h, with low blocking barriers, exhibits  $M_{33}$  value much smaller than GDC-10 h. Furthermore, it does not show any strain saturation behavior, and strain linearly increases with  $E^2$ . The reason for this effect could be of high grain boundary conductivity, which leads to a marginal voltage drop at bulk grain. On the other hand, being nanostructured and having higher blocking effect compared to GDC-2.5 h sample, GDC-0.1 h generates much higher electrostriction than counterpart does. The most surprising result is observed with GDC-SPS sample. The electromechanical response of this sample is significantly lower compared to others, for instance, electrostrictive strain coefficient ( $M_{33}$ ) value being one order of magnitude lower than GDC-10 h. The small value of the former is not due to its unrelaxed grain size but connected to trapped ionic/electronic defects-cation association and its interaction with the electric field. These defect-complexes are neutral and do not respond at low electric fields, suggesting super blocking behavior at the grain boundary.

This significantly highlights the flexibility of the blocking barrier in tuning the electrostrictive strain. For high electrostriction, the barriers should block oxygen vacancy migration without meaningfully decreasing the potential drop and vacancy should resonate

**Table 1**  
Grain size, capacitance and relaxation frequency response of the samples.

Sample ID	$C_{total}$ (F)	$f_{total}$ (Hz)	Grain Size (nm)		
GDC-SPS	$2.0 \times 10^{-11}$	$1.2 \times 10^3$	200 ± 25		
GDC-0.1 h	$3.5 \times 10^{-11}$	$5.0 \times 10^3$	170 ± 20		
	$C_{Bulk}$ (F)	$C_{G.B.}$ (F)	$f_{Bulk}$ (Hz)	$f_{G.B.}$ (Hz)	Grain Size (μm)
GDC-10 h	$1.2 \times 10^{-11}$	$3.0 \times 10^{-10}$	$2.0 \times 10^5$	$1.5 \times 10^3$	2.0 ± 0.3
GDC-2.5 h	$2.9 \times 10^{-11}$	$4.0 \times 10^{-10}$	$2.0 \times 10^5$	$2.0 \times 10^4$	1.5 ± 0.2

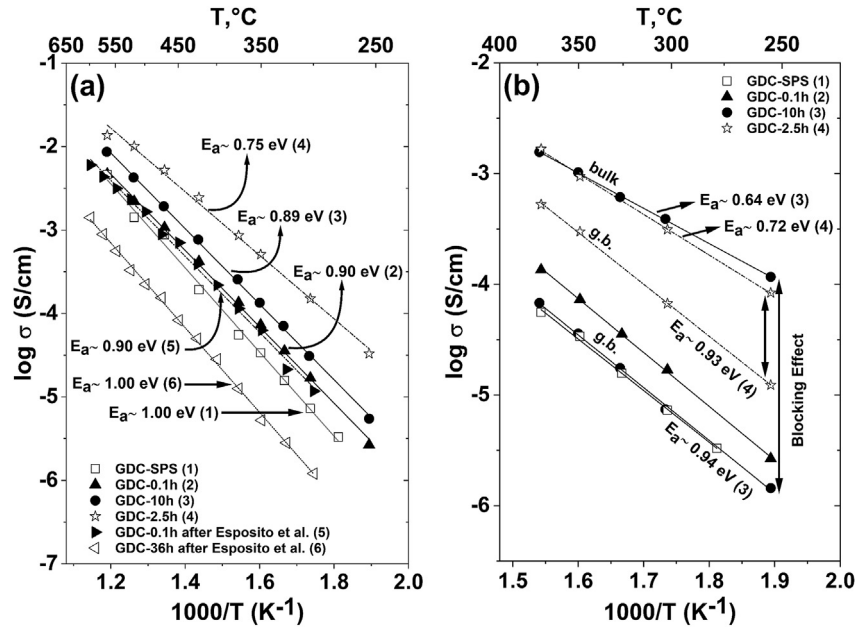


Fig. 5. Arrhenius plot (a) for the estimation of total electrical conductivities of the samples, results are compared with the literature [3], (b) for the bulk and grain boundary conductivities of conventionally sintered GDC-10 h and GDC-2.5 h samples; entire experiments are carried out in air.

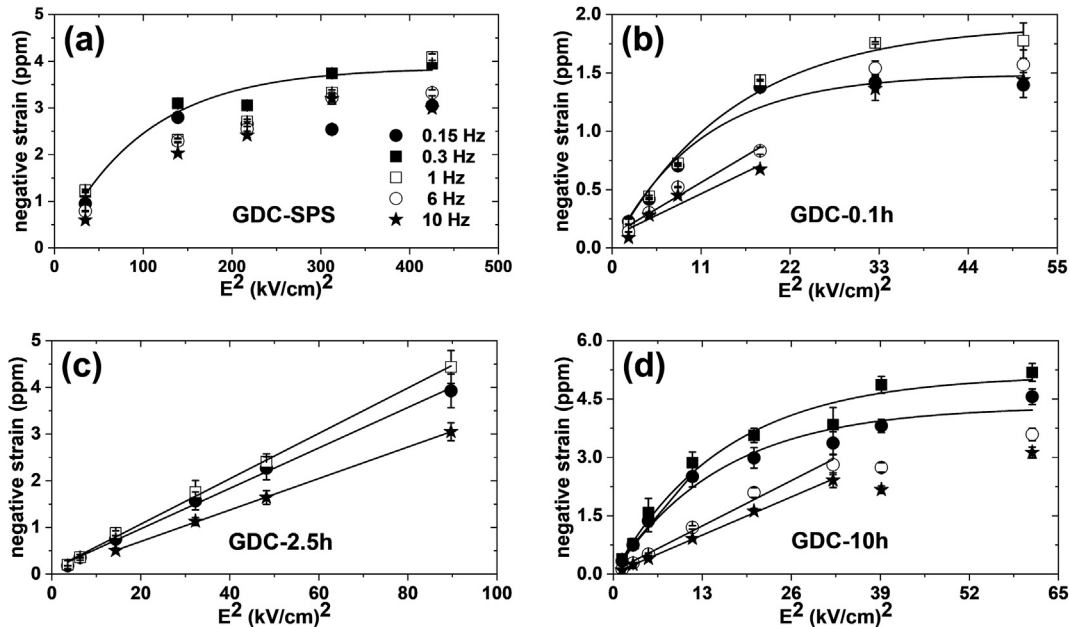


Fig. 6. Electrostrictive negative strain as a function of applied electric field square at frequencies 0.15–10 Hz, showing strain saturation behavior at a lower frequency.

within the lattice, as per the model described by Lubomirsky et al. [16].

Fig. 7 demonstrates the declining trend of electrostrictive strain coefficient ( $M_{33}$ ) with increasing frequency. This type of electrostriction relaxation with frequency can be fitted by (non-ideal-Debye) following function:

$$M_{33}(f) = \frac{M_{33}^0}{\sqrt{1 + (\tau \cdot f)^{2+\alpha}}} + M_{33}^\infty \quad (2)$$

Here,  $M_{33}^0$  and  $M_{33}^\infty$  are frequency independent electrostriction coefficient,  $\tau$  is the relaxation time and  $\alpha$  is denoted as a non-

ideality factor. Both the saturation and relaxation phenomena are observed in the recent publication of Yavo et al. [12], specifying that both mechanisms are intrinsic properties of electromechanical behavior of gadolinium doped ceria. Moreover,  $M_{33}$  values are approximately in order of  $\geq 10^{-18}$  (m/V)<sup>2</sup> at 10 Hz for all the samples, which are still one order of magnitude higher than the classical electrostriction model.

Table 2 describes the comparative analysis of grain boundary resistivity and electrostriction coefficient among the samples. Finally, by correlating experimental findings, it can be concluded that electrostriction in GDC materials increases with grain boundary blocking factor up to a certain level (below super blocking

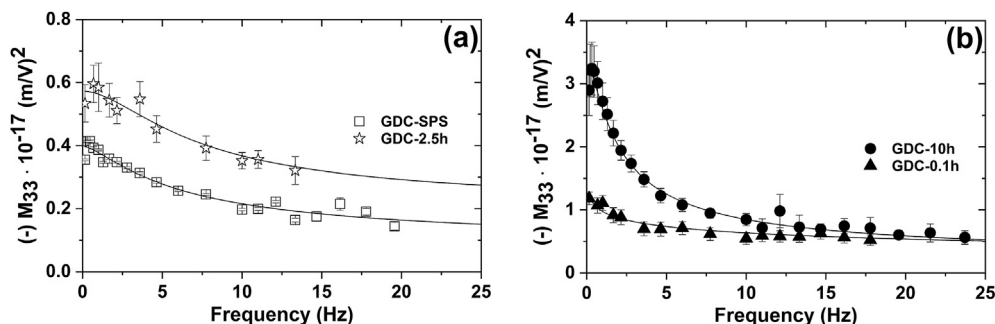


Fig. 7. Frequency dependent relaxation of electrostriction strain coefficient ( $M_{33}$ ), for conventional and non-conventional sintered samples, for frequencies  $0 < f < 25$  Hz.

Table 2

Comparative analysis of grain boundary resistivity and electrostriction coefficient between samples.

Material Properties	Nano size grain		Micron size grain	
	GDC-SPS	GDC-0.1 h	GDC-10 h	GDC-2.5 h
G.B. Resistivity ( $\approx 300$ °C) [ $\Omega \cdot \text{cm}$ ]	$\sim 100000$	$\sim 50000$	$\sim 30000$	$\sim 3500$
Electrostriction ( $\approx 1$ Hz) ( $\text{m/V}^2$ )	$0.4 \cdot 10^{-17}$	$1.0 \cdot 10^{-17}$	$2.8 \cdot 10^{-17}$	$0.6 \cdot 10^{-17}$

region) and then decreases dramatically. The effect of blocking in electrostriction is also schematically presented in Table 2. The blocking diagram and the data strongly suggest that electrostriction is not dependent on the geometrical ratio between bulk and grain boundary. Microstructure does not necessarily influence the electromechanical properties. Additionally, it also confirms that the nominal oxygen vacancy concentration is not a true parameter that controls electrostriction. In conclusion, it is the blocking barrier at the grain boundaries, which regulates the electrostrictive properties. The blocking barrier is tuned by the configuration of oxygen vacancy within the grain boundary. Despite more uniform oxygen vacancy distribution, both GDC-SPS and GDC-0.1 h materials show considerably limited electromechanical activity compared to GDC-10 h with a low density of large blocking barriers. These results finally conclude the dominant distribution of oxygen defect configuration to the electromechanical properties.

#### 4. Conclusion

In this work, highly dense GDC ceramic pellets were fabricated by both non-conventional and conventional sintering methods. Non-conventional sintering was performed by SPS and fast firing to achieve similar nanometric microstructures with tuned oxygen vacancy configurations, with the same nominal oxygen vacancy concentration. The resulting polycrystalline materials exhibit unrelaxed microstructure with nano-grains, while the samples sintered in conventional method exhibits equilibrium grain of micron size. Surprisingly, electro-chemo-mechanical properties of the samples did not follow a mere geometrical grain size dependency. They show a strict dependency on ionic migration blocking barriers

built in the materials by the different sintering processes. Furthermore, all the compounds show non-classical giant electrostriction with a strong dependency on the frequency and electric field amplitude. Above all, it was observed that sample with high bulk and low grain boundary relaxation frequency exhibits large electrostrictive coefficient, which is further related to the distribution of oxygen vacancies. In summary, the oxygen defects configuration rather than their nominal concentration in the bulk controls the electromechanical behavior in Gd-doped ceria.

#### Acknowledgements

This research was supported by DFF-Research project grants from the Danish Council for Independent Research, Technology and Production Sciences, June 2016, grant number 48293 (GIANT-E) and the European H2020-FETOPEN-2016-2017 project BioWings, grant number 801267. The authors would like to thank Massimo Rosa for assistance in TEM.

#### References

- [1] H.L. Tuller, A.S. Nowick, Doped ceria as a solid oxide electrolyte, *J. Electrochem. Soc.* 122 (1975) 255–259.
- [2] H. Inaba, H. Tagawa, Ceria-based solid electrolytes, *Solid State Ionics* 83 (1996) 1–16.
- [3] V. Esposito, E. Traversa, Design of electroceramics for solid oxides fuel cell applications: playing with ceria, *J. Am. Ceram. Soc.* 91 (2008) 1037–1051.
- [4] M. Mogensen, N.M. Sammes, G.A. Tompsett, Physical, chemical and electrochemical properties of pure and doped ceria, *Solid State Ionics* 129 (2000) 63–94.
- [5] S.R. Bishop, T.S. Stefanik, H.L. Tuller, “Electrical conductivity and defect equilibria of  $\text{Pr}_{0.1}\text{Ce}_{0.9}\text{O}_{2-\delta}$ ”, *Phys. Chem. Chem. Phys.* 13 (2011) 10165–10173.
- [6] D. Pérez-Coll, D. Marrero-López, P. Núñez, S. Piñol, J.R. Frade, Grain boundary

- conductivity of  $\text{Ce}_{0.8}\text{Ln}_{0.2}\text{O}_{2-\delta}$  ceramics (Ln = Y, La, Gd, Sm) with and without Co-doping, *Electrochim. Acta* 51 (2006) 6463–6469.
- [7] A. Arabaci, Effect of Sm and Gd dopants on structural characteristics and ionic conductivity of ceria, *Ceram. Int.* 41 (2015) 5836–5842.
- [8] H.L. Tuller, A.S. Nowick, Small polaron electron transport in reduced  $\text{CeO}_2$  single crystals, *J. Phys. Chem. Solids* 38 (1977) 859–867.
- [9] T.S. Stefanik, H.L. Tuller, Nonstoichiometry and defect chemistry in praseodymium-cerium oxide, *J. Electroceram.* 13 (2004) 799–803.
- [10] R. Korobko, A. Patlolla, A. Kossoy, E. Wachtel, H.L. Tuller, A.I. Frenkel, I. Lubomirsky, Giant electrostriction in Gd-doped ceria, *Adv. Mater.* 24 (2012) 5857–5861.
- [11] M. Hadad, H. Ashraf, G. Mohanty, C. Sandu, P. Murali, Key-features in processing and microstructure for achieving giant electrostriction in gadolinium doped ceria thin films, *Acta Mater.* 118 (2016) 1–7.
- [12] N. Yavo, O. Yehekel, E. Wachtel, D. Ehre, A.I. Frenkel, I. Lubomirsky, Relaxation and saturation of electrostriction in 10 mol% Gd-doped ceria ceramics, *Acta Mater.* 144 (2018) 411–418.
- [13] V. Shelukhin, I. Zon, E. Wachtel, Y. Feldman, I. Lubomirsky, Low temperature dielectric properties of  $\text{Ce}_{0.8}\text{Gd}_{0.2}\text{O}_{1.9}$  films, *Solid State Ionics* 211 (2012) 12–19.
- [14] R.E. Newnham, V. Sundar, R. Yimnirun, J. Su, Q.M. Zhang, " Electrostriction, Nonlinear electromechanical coupling in solid dielectrics, *J. Phys. Chem. B* 101 (1997) 10141–10150.
- [15] N. Yavo, A.D. Smith, O. Yehekel, S. Cohen, R. Korobko, E. Eachtel, P.R. Slater, I. Lubomirsky, Large nonclassical electrostriction in (Y, Nb)-stabilized  $\delta\text{-Bi}_2\text{O}_3$ , *Adv. Funct. Mater.* 26 (2016) 1138–1142.
- [16] Y. Li, O. Kravynis, J. Kas, T. Weng, D. Sokaras, R. Zacharowich, I. Lubomirsky, A.I. Frenkel, Geometry of electromechanically active structures in Gadolinium - doped Cerium oxides, *AIP Adv.* 6 (2016), 055320–7.
- [17] A.S. Nowick, B.S. Berry, J.L. Katz, Anelastic relaxation in crystalline solids, *J. Appl. Mech.* 42 (1975) 750.
- [18] S.K. Kim, S. Khodorov, C.T. Chen, S. Kim, I. Lubomirsky, How to interpret current-voltage relationships of blocking grain boundaries in oxygen ionic conductors, *Phys. Chem. Phys.* 15 (2013) 8716–8721.
- [19] S. Kim, S.K. Kim, S. Khodorov, J. Maier, I. Lubomirsky, On determining the height of the potential barrier at grain boundaries in ion-conducting oxides, *Phys. Chem. Chem. Phys.* 18 (2016) 3023–3031.
- [20] A.D. Ushakov, E. Mishuk, E. Makagon, D.O. Alikin, A.A. Esin, I.S. Baturin, A. Tselev, V.Y. Shur, I. Lubomirsky, A.L. Kholkin, Electromechanical properties of electrostrictive  $\text{CeO}_2$ :Gd membranes: effects of frequency and temperature, *Appl. Phys. Lett.* 110 (2017) 142902–142904.
- [21] P.L. Chen, I.W. Chen, Grain growth in  $\text{CeO}_2$ : dopant effects, defect mechanism, and solute drag, *J. Am. Ceram. Soc.* 79 (1996) 1793–1800.
- [22] P.L. Chen, I.W. Chen, Role of defect interaction in boundary mobility and cation diffusivity of  $\text{CeO}_2$ , *J. Am. Ceram. Soc.* 77 (1994) 2289–2297.
- [23] V. Esposito, D.W. Ni, Z. He, W. Zhang, A.S. Prasad, J.A. Glasscock, C. Chatzichristodoulou, S. Ramousse, A. Kaier, Enhanced mass diffusion phenomena in highly defective doped ceria, *Acta Mater.* 61 (2013) 6290–6300.
- [24] D.W. Ni, D.Z. de Florio, D. Marani, A. Kaiser, V.B. Tinti, V. Esposito, Effect of chemical redox on Gd-doped ceria mass diffusion, *J. Mater. Chem.* 3 (2015) 18835–18838.
- [25] F. Teocoli, D.W. Ni, S. Sanna, K. Thydén, F.C. Fonseca, V. Esposito, Fast mass interdiffusion in ceria/alumina composite, *J. Mater. Chem.* 3 (2015) 17135–17143.
- [26] D.W. Ni, J.A. Glasscock, A. Pons, W. Zhang, A. Prasad, S. Sanna, N. Pryds, V. Esposito, Densification of highly defective ceria by high temperature controlled re-oxidation, *J. Electrochem. Soc.* 161 (2014), F3072–F3078.
- [27] B. Feng, N.R. Lugg, A. Kumamoto, Y. Ikuhara, N. Shibata, Direct observation of oxygen vacancy distribution across Ytria-Stabilized Zirconia grain boundaries, *ACS Nano* 11 (2017) 11376–11382.
- [28] D.V. Quach, S. Kim, R.A. De Souza, M. Martin, Z.A. Munir, Grain size effect in the electrical properties of nanostructured functional oxides through pressure modification of the spark plasma sintering method, *Key Eng. Mater.* 484 (2011) 107–116.
- [29] X. Guo, R. Waser, Electrical properties of the grain boundaries of oxygen ion conductors: acceptor-doped zirconia and ceria, *Prog. Mater. Sci.* 51 (2016) 151–210.
- [30] X. Guo, J. Maier, Grain boundary blocking effect in zirconia: a Schottky barrier analysis, *J. Electrochem. Soc.* 148 (2001) E121.
- [31] S. Kim, J. Fleig, J. Maier, Space charge conduction: simple analytical solutions for ionic and mixed conductors and application to nanocrystalline ceria, *Phys. Chem. Chem. Phys.* 5 (2003) 2268–2273.
- [32] J. Maier, Ionic conduction in space charge regions, *Prog. Solid State Chem.* 23 (1995) 171–263.
- [33] X. Guo, W. Sigle, J.U. Fleig, J. Maier, Role of space charge in the grain boundary blocking effect in doped zirconia, *Solid State Ionics* 154–155 (2002) 555–561.
- [34] S. Kim, J. Fleig, J. Maier, Space charge conduction: simple analytical solutions for ionic and mixed conductors and application to nanocrystalline ceria, *Phys. Chem. Chem. Phys.* 5 (2003) 2268–2273.
- [35] J. Fleig, The grain boundary impedance of random microstructures: numerical simulations and implications for the analysis of experimental data, *Solid State Ionics* 150 (2002) 181–193.
- [36] U. Anselmi-Tamburini, F. Magila, G. Chiodelli, A. Tacca, G. Spinolo, P. Riello, S. Bucella, Z.A. Munir, Nanoscale effects on the ionic conductivity of highly doped bulk nanometric cerium oxide, *Adv. Funct. Mater.* 16 (2006) 2363–2368.
- [37] C. Plapcianu, C. Valsangiacom, J.E. Schaffer, A. Wieg, J. Garay, L. Stanciu, Spark plasma sintering studies of nanosize lanthanidoped ceria obtained by sol-gel method, *J. Optoelectron. Adv. Mater.* 13 (2011) 1101–1108.
- [38] O. Guillon, J.G. Julian, B. Dargatz, T. Kessel, G. Schierming, J. Raethel, M. Herrmann, Field-assisted sintering technology/spark plasma sintering: mechanisms, materials, and technology developments, *Adv. Eng. Mater.* 16 (2014) 830–849.
- [39] J.A. Glasscock, V. Esposito, S.P.V. Foghmoes, T. Stegk, D. Matuschek, M.W.H. Ley, S. Ramousse, The effect of forming stresses on the sintering of ultra-fine  $\text{Ce}_{0.9}\text{Gd}_{0.1}\text{O}_{2-\delta}$  powders, *J. Eur. Ceram. Soc.* 33 (2013) 1289–1296.
- [40] M.I. Mendelson, Average grain size in polycrystalline ceramics, *J. Am. Ceram. Soc.* 52 (1969) 443–446.
- [41] A.L. Patterson, The scherrer formula for X-ray particle size determination, *Phys. Rev.* 56 (1939) 978–982.
- [42] M.C. Göbel, G. Gregori, J. Maier, Electronically blocking grain boundaries in donor doped cerium dioxide, *Solid State Ionics* 215 (2012) 45–51.
- [43] G. Gregori, B. Rahmati, W. Sigle, P.A. Van Aken, J. Maier, Electric conduction properties of boron-doped ceria, *Solid State Ionics* 192 (2011) 65–69.
- [44] H.L. Tuller, Ionic conduction in nanocrystalline materials, *Solid State Ionics* 131 (2000) 143–157.
- [45] X. Guo, S. Mi, R. Waser, Nonlinear electrical properties of grain boundaries in oxygen ion conductors: acceptor-doped ceria, *Electrochem. Solid State Lett.* 8 (2004) J1.
- [46] D.Z. de Florio, R. Muccillo, V. Esposito, E. Di Bartolomeo, E. Traversa, Preparation and electrochemical characterization of Perovskite/YSZ ceramic films, *J. Electrochem. Soc.* 152 (2004) A88.
- [47] K. Neuhaus, R. Dolle, H.-D. Wiemhöfer, Assessment of the effect of transition metal oxide addition on the conductivity of commercial Gd-Doped Ceria, *J. Electrochem. Soc.* 165 (2018), F533–F542.
- [48] A. Hara, Y. Hirata, S. Sameshima, N. Matsunaga, T. Horita, Grain size dependence of electrical properties of Gd-doped ceria, *J. Ceram. Soc. Japan* 116 (2008) 291–297.
- [49] E.C.C. Souza, W.C. Chueh, W. Jung, E.N.S. Muccillo, S.M. Haile, Ionic and electronic conductivity of nanostructured Samaria-doped ceria, *J. Electrochem. Soc.* 159 (2012) K127.
- [50] M.G. Bellino, D.G. Lamas, N.E.W. De Reça, Enhanced ionic conductivity in nanostructured heavily doped ceria ceramics, *Adv. Funct. Mater.* 16 (2006) 107–113.



# The role of oxygen defects on the electro-chemo-mechanical properties of highly defective gadolinium doped ceria

Ahsanul Kabir<sup>a,b,\*</sup>, Jin Kyu Han<sup>a</sup>, Benoit Merle<sup>b</sup>, Vincenzo Esposito<sup>a,\*</sup>

<sup>a</sup> Department of Energy Conversion and Storage, Technical University of Denmark, Frederiksborgvej 399, Roskilde 4000, Denmark

<sup>b</sup> Materials Science & Engineering I, University Erlangen-Nürnberg (FAU), Cauerstr. 3, 91058 Erlangen, Germany

## ARTICLE INFO

### Article history:

Received 8 December 2019

Received in revised form 5 February 2020

Accepted 10 February 2020

Available online 11 February 2020

### Keywords:

Defects

Blocking barriers

Ionic conductivity

Creep

Electrostriction

## ABSTRACT

In light of the recent discovery of giant electrostriction in defective fluorites, here we investigate the interplay between mechanical, electrochemical and electromechanical properties of oxygen defective ceria compositions ( $\text{Ce}_{1-x}\text{Gd}_x\text{O}_{2-\delta}$ ) as the effect of Gd-doping ( $x = 0.05\text{--}0.3$ ) at low temperatures. Highly dense polycrystalline ceramics are prepared as micron-size grains with a minimized grain boundary extent. Electrochemical ionic migration by impedance spectroscopy reveals that dopant content controls the oxygen vacancies association in the samples. Interestingly, we observe that electromechanical activity is strongly controlled by the local oxygen vacancy configuration rather than on its nominal concentration. The primary creep at room temperature indicates a declining viscoelastic trend with increasing oxygen defects.

© 2020 Elsevier B.V. All rights reserved.

## 1. Introduction

Electromechanically active materials have shown growing interests in a wide range of sensing and actuating applications including consumer electronics, ultrasound transducers, sonar, etc. [1]. Electrostriction is the second-order electromechanical coupling developed in all insulators, with a strong dependency on materials dielectric permittivity ( $\epsilon$ ) and elastic compliance ( $S$ ). A recent investigation illustrates that specific orientated thin films of highly defective Gd-doped cerium oxides ( $\text{Ce}_{0.8}\text{Gd}_{0.2}\text{O}_{1.9}$ ) display a non-classical giant electrostriction response with  $M_e \approx 6.5 \times 10^{-18} \text{ m}^2/\text{V}^2$  at 0.1 Hz, which is at least two orders of magnitude larger than classical prediction [2]. Moreover, the polycrystalline bulk form of GDC and another similar oxide ( $\text{Bi}_2\text{O}_3$ ) also exhibit similar results of even higher magnitudes [3–5]. The atomistic mechanism of such mechanism is attributed to the presence of electroactive elastic dipoles ( $\text{Ce}_{\text{Ce}}\text{-O}_\text{O}$ ) that changes their bond length under an external electric field [2,6]. Despite experimental shreds of evidence indicating that oxygen vacancies-cation complexes, i.e. vacancies associations, play a key role in the electromechanical properties, the concentration of the defects is generally considered the primary parameter in

controlling the electrostriction in defective fluorites [4,7]. Similar to electrostriction,  $\text{Ce}_{\text{Ce}}\text{-O}_\text{O}$  dipole rearranges under mechanical load, exhibiting an unusual primary creep behavior at room temperature in nanoindentation measurement [4]. Moreover, oxygen defects can take different configurations in the fluorites, especially in polycrystalline materials with different degrees of disorder and composition inside the grains and at grain boundaries [8]. These effects are observed for oxygen ionic conductivity [8] as well as for cation diffusion at high temperatures [9–11], where both electrostatic and steric effects between dopants and oxygen defects can control the energetic barrier of such processes [12]. In this work, we demonstrate the role of oxygen vacancies on the electrical, mechanical and electromechanical properties of Gd-doped ceria, highlighting their concentration/configuration dependency on each effect.

## 2. Experimental procedure

The nanometric gadolinium doped ceria (GDC) powders with composition  $\text{Ce}_{1-x}\text{Gd}_x\text{O}_{2-\delta}$  where  $x = 0.05\text{--}0.3$  were synthesized by the co-precipitation method, as described elsewhere [5,8]. The powders were uniaxially cold-pressed at 200 MPa and subsequently sintered at 1450 °C in air for 10 h. The density of the pellets was measured by the Archimedes method in deionized water. The crystallographic phase purity was analyzed by the X-ray diffraction (XRD) technique (Bruker D8, Germany). The microstructure was characterized by a high-resolution scanning electron microscope

\* Corresponding authors at: Department of Energy Conversion and Storage, Technical University of Denmark, Frederiksborgvej 399, Roskilde 4000, Denmark (A. Kabir).

E-mail addresses: [ahsk@dtu.dk](mailto:ahsk@dtu.dk) (A. Kabir), [vies@dtu.dk](mailto:vies@dtu.dk) (V. Esposito).

(SEM; Zeiss Merlin, Germany). The electrical conductivity was measured by electrochemical impedance spectroscopy (EIS) Solartron 1260 (UK) in a temperature range of 300–450 °C for a frequency distribution of 0.01–10<sup>7</sup> Hz in air. The electromechanical property is examined in a nano-vibration analyzer with a single-beam laser interferometer (SIOS, Germany). The mechanical properties of the samples were investigated by nanoindentation technique (KLA G200, USA), using Berkovich indenter at room temperature. The creep measurements were based on a typical trapezoidal load-hold-unload system with a loading/unloading rate of 15 mN/s (fast) or 1.5 mN/s (slow) and holding at load 150 mN or depth of 1000 nm for 20 s duration (see Fig. 2a). During holding, the creep relaxation of the material was recorded as a progressive increase in displacement. The elastic modulus and nano-hardness of the material were determined by the Oliver-Pharr analysis [13]. For the local strain rate sensitivity measurement, the strain rate was varied between 0.001 s<sup>-1</sup> and 0.1 s<sup>-1</sup> and evaluated from the resulting jump in hardness [14,15].

### 3. Results and discussion

The XRD patterns reveal characteristic cubic fluorite structure (Fm – 3 m), confirming a formation of a single-phase solid solution (see Fig. S1.a). A highly dense microstructure was observed, which agrees with the results of experimental density (>95% of theoretical density).

The thermal (binding) energy and mobility of oxygen vacancies is characterized by complex impedance spectroscopy and Fig. 1a demonstrates the typical impedance plot (Nyquist formalism) at 300 °C in ambient air. The semicircles at the high and intermediate frequency refer to bulk and grain boundary impedance, respectively. The plot highlights the arising of ion blocking factors, usually associated with the disorder at the grain boundary (g.b.) [8,16]. The ion-blocking effect is generally characterized by the grain boundary blocking factor ( $\alpha_{g.b.}$ ) where  $\alpha_{g.b.} = \frac{R_{gb}}{R_{bulk} + R_{g.b.}}$  [8]. Despite the parameter ( $\alpha_{g.b.}$ ) is namely related to the grain boundary and grain size it can also collect other blocking factors such as the oxygen vacancies associations, porosity, segregations, etc. [17,18]. All these can control the defect migration mechanism in the materials [8]. In the previous work, we have demonstrated that the evolution of the ion-blocking barrier is strictly dependent on the way the defects are organized and can be modified by the sintering process *i.e.* microstructural features [5,8]. The present results are consistent with previous literature [16] showing that increasing the dopant concentration reduces the blocking factor (inset Fig. 1b), where the grain growth is obtained by long thermal treatments at high temperatures.

The temperature dependence total electrical conductivity ( $\sigma$ ) of the sample is shown in Fig. 1.b in an Arrhenius plot. The result illustrates that GDC-10 and GDC-20 samples possess maximum conductivity which is half-one order higher than counterparts are, associating to low activation energy value ( $\approx 0.9$  eV) in the

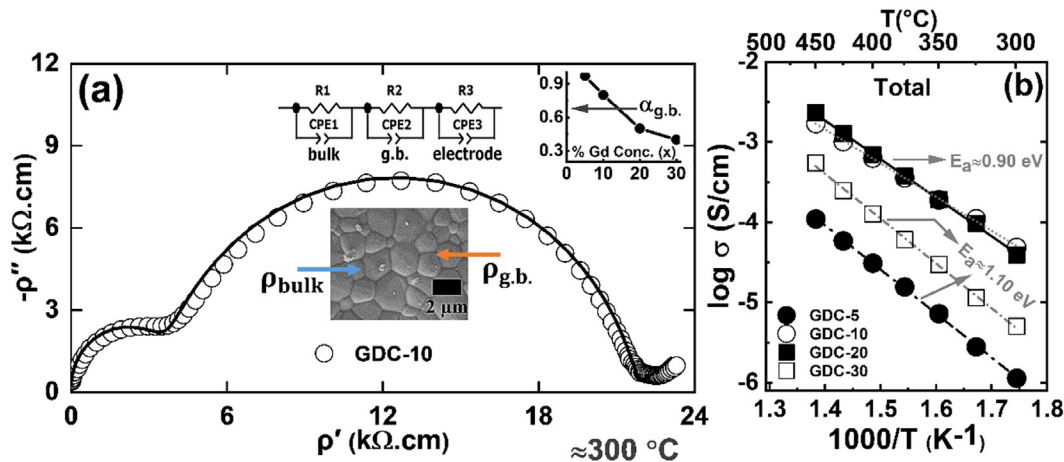


Fig. 1. (a) Illustration of a characteristic impedance spectrum of GDC-10 sample, measured at 300 °C in air with silver (Ag) electrode. The inset plot shows the relation of the ion-blocking factor as a function of dopant concentration. (b) The Arrhenius plot for the estimation of total electrical conductivities of the sintered GDC pellets.

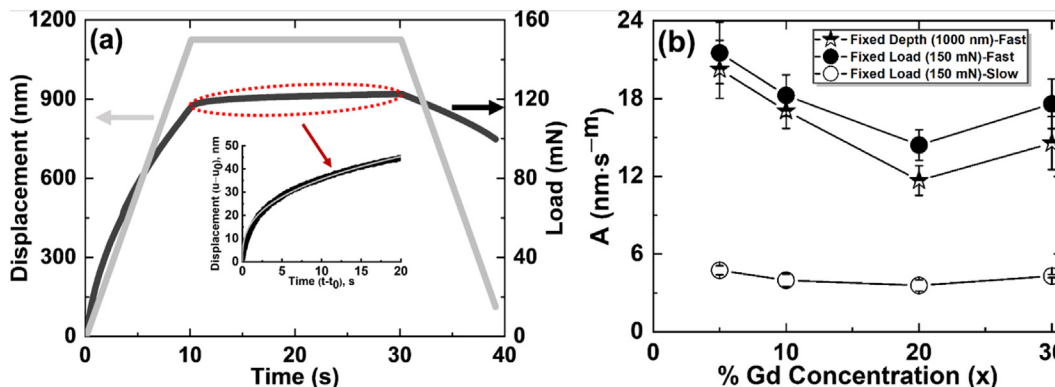
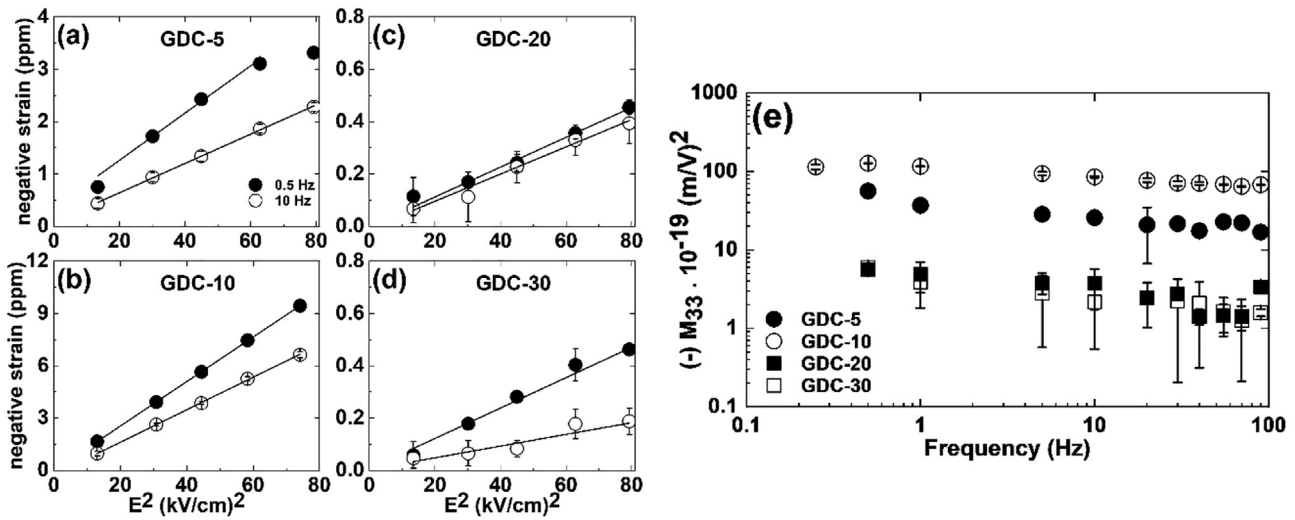


Fig. 2. (a) The representative load–time and displacement–time curve of a GDC-10 sample in the nanoindentation fast loading approach. The inset shows a non-linear displacement–time plot in the holding segment, indicating a primary creep. (b) The creep constant ( $A$ ) as a function of Gd-doping in ceria compositions under fixed depth (fast) and fixed load (fast/slow) mode.



**Fig. 3.** (a–d) The electrostrictive negative strain with the response to the external electric field at frequencies 0.5 and 10 Hz for GDC samples (Gd = 0.05–0.3), electrode material: Gold (Au). (e) The electrostrictive strain coefficient ( $M_{33}$ ) as a function of frequencies ranging from 0.15–100 Hz.

materials. Fig. S2 describes how the total conductivity is controlled by the g.b. blocking effects. For instance, the GDC-5 sample has low bulk migration energy but a high blocking factor, leading to lower-most ionic conductivity.

All investigated samples display noticeable creep behavior during the hold section of the measurement under fast loading. The holding time dependence of the displacement shows a non-linear relation, following an empirical formula  $(u - u_0) = A(t - t_0)^m$  where  $u_0$  is the initial displacement at time  $t_0$  at the holding segment,  $A$  is defined as creep constant and  $m$  the fitting exponent. The creep constant  $A$  is shown in Fig. 2b as a function of Gd-concentration.  $A$  decreases linearly for  $0.05 < \text{Gd} < 0.2$ , in agreement with previous reports, suggesting that the increased interaction between cations and oxygen vacancies is responsible for the lesser creep and the increasing hardness [19,20]. These results are consistent with the impedance, where high dopant content reduces the conductivity at the bulk (see Fig. S2). The augmented value for GDC-30 could be attributed to the possible local double fluorite structure of the material [21]. As expected, the creep constant is considerably higher for a fast pre-loading than for the slow mode. Its value hardly depends on whether the creep segment starts after reaching 150 mN or 1000 nm. The exponent  $m$  ranges between 0.3 and 0.6  $\text{nm}\cdot\text{s}^{-m}$  and slightly decreases with Gd-content, similar to the strain rate sensitivity (see Figs. S4 and S5).

Fig. 3a–d shows that all samples strained negatively at the second harmonic of the applied electric field, verifying the electrostriction behavior of ceria, as reported in [2,4]. A large strain is noticed for low-doped samples that contain large blocking barrier effect ( $\alpha_{g.b.} > 0.8$ ) as well as low oxygen vacancy ordering. As noticed, the strain value is higher at 0.5 Hz than 10 Hz for all investigated samples. The electrostrictive coefficient ( $M_{33}$ ) shows to decrease gradually with increasing frequencies (Fig. 3e). As observed, the samples with large ion-blocking effects represent high  $M_{33}$  value. Moreover,  $M_{33}$  still has an order of  $\approx 10^{-18}$  (m/V)<sup>2</sup> at higher frequency e.g. 50 Hz for GDC-5 and GDC-10 samples that is still one order higher than classical model estimation.

#### 4. Conclusion

Highly dense GDC ceramics were successfully produced via conventional sintering with micron-size grains. These samples develop

a different blocking effect that scaled-down with Gd concentration, affecting the total ionic conduction as well as electrostriction. High electrostriction is measured for the samples with a large ion-blocking effect. They also display non-linear creep properties at room temperature with a strong dependence on nominal Gd content.

#### CRediT authorship contribution statement

**Ahsanul Kabir:** Conceptualization, Experimental work, Writing - original draft. **Jin Kyu Han:** Experimental work (electromechanical). **Benoit Merle:** Experiment work (mechanical characterization), draft revision. **Vincenzo Esposito:** Conceptualization, Methodology, draft supervision.

#### Declaration of Competing Interest

The authors declare that they have no known competing financial interests or personal relationships that could have appeared to influence the work reported in this paper.

#### Acknowledgments

This research was supported by DFF-Research project grants (GIANT-E, 48293) June 2016, partially by European H2020-FETOPEN-2016-2017 project BioWings (# 801267) and the center for Nanoanalysis and Electron Microscopy (CENEM) and the interdisciplinary center for nanostructured films (IZNF) at University Erlangen-Nürnberg (FAU).

#### Appendix A. Supplementary data

Supplementary data to this article can be found online at <https://doi.org/10.1016/j.matlet.2020.127490>.

#### References

- [1] R.E. Newnham, V. Sundar, R. Yimnirun, J. Su, Q.M. Zhang, Electrostriction: Nonlinear Electromechanical Coupling in Solid Dielectrics, *J. Phys. Chem. B* 101 (1997) 10141–10150.
- [2] R. Korobko, A. Patlolla, A. Kossov, E. Wachtel, H.L. Tuller, A.I. Frenkel, I. Lubomirsky, Giant electrostriction in Gd-doped ceria, *Adv. Mater.* 24 (2012) 5857–5861.

- [3] N. Yavo, O. Yeheskel, E. Wachtel, D. Ehre, A.I. Frenkel, I. Lubomirsky, Relaxation and saturation of electrostriction in 10 mol% Gd-doped ceria ceramics, *Acta Mater.* 144 (2018) 411–418.
- [4] Y. Nimrod, A.D. Smith, Y. Ori, C. Sydney, K. Roman, W. Ellen, P.R. Slater, L. Igor, Large Nonclassical Electrostriction in (Y, Nb)-Stabilized  $\delta$ -Bi<sub>2</sub>O<sub>3</sub>, *Adv. Funct. Mater.* 26 (2016) 1138–1142.
- [5] A. Kabir, S. Santucci, N. Van Nong, M. Varenik, I. Lubomirsky, R. Nigon, P. Mural, V. Esposito, Effect of oxygen defects blocking barriers on gadolinium doped ceria (GDC) electro-chemo-mechanical properties, *Acta Mater.* 74 (2019) 53–60.
- [6] R. Korobko, A. Lerner, Y. Li, E. Wachtel, A.I. Frenkel, I. Lubomirsky, In-situ extended X-ray absorption fine structure study of electrostriction in Gd doped ceria, *Appl. Phys. Lett.* 106 (2015) 042904.
- [7] M. Hadad, H. Ashraf, G. Mohanty, C. Sandu, P. Mural, Key-features in processing and microstructure for achieving giant electrostriction in gadolinium doped ceria thin films, *Acta Mater.* 118 (2016) 1–7.
- [8] V. Esposito, E. Traversa, Design of electroceramics for solid oxides fuel cell applications: Playing with ceria, *J. Am. Ceram. Soc.* 91 (2008) 1037–1051.
- [9] V. Esposito, D.W. Ni, Z. He, W. Zhang, A.S. Prasad, J.A. Glasscock, C. Chatzichristodoulou, S. Ramousse, A. Kaiser, Enhanced mass diffusion phenomena in highly defective doped ceria, *Acta Mater.* 61 (2013) 6290–6300.
- [10] D.W. Ni, D.Z. de Florio, D. Marani, A. Kaiser, V.B. Tinti, V. Esposito, Effect of chemical redox on Gd-doped ceria mass diffusion, *J. Mater. Chem. A* 3 (2015) 18835–18838.
- [11] D.W. Ni, J.A. Glasscock, A. Pons, W. Zhang, A. Prasad, S. Sanna, N. Pryds, V. Esposito, Densification of Highly Defective Ceria by High Temperature Controlled Re-Oxidation, *J. Electrochem. Soc.* 161 (2014) F3072–F3078.
- [12] P.-L. Chen, I.-W. Chen, Role of Defect Interaction in Boundary Mobility and Cation Diffusivity of CeO<sub>2</sub>, *J. Am. Ceram. Soc.* 77 (1994) 2289–2297.
- [13] G.M. Pharr, An improved technique for determining hardness and elastic modulus using load and displacement sensing indentation experiments, *J. Mater. Res.* 7 (1992) 1564–1583.
- [14] B. Merle, W.H. Higgins, G.M. Pharr, Critical issues in conducting constant strain rate nanoindentation tests at higher strain rates, *J. Mater. Res.* 34 (2019) 3495–3503.
- [15] V. Maier, C. Schunk, M. Göken, K. Durst, Microstructure-dependent deformation behaviour of bcc-metals – indentation size effect and strain rate sensitivity, *Philos. Mag.* 95 (2015) 1766–1779.
- [16] H.J. Avila-Paredes, K. Choi, C.-T. Chen, S. Kim, Dopant-concentration dependence of grain-boundary conductivity in ceria: a space-charge analysis, *J. Mater. Chem.* 19 (2009) 4837.
- [17] V. Esposito, M. Zunic, E. Traversa, Improved total conductivity of nanometric samaria-doped ceria powders sintered with molten LiNO<sub>3</sub> additive, *Solid State Ionics.* 180 (2009) 1069–1075.
- [18] Z.P. Li, T. Mori, G.J. Auchterlonie, J. Zou, J. Drennan, Direct evidence of dopant segregation in Gd-doped ceria, *Appl. Phys. Lett.* 98 (2011) 093104.
- [19] R. Korobko, C.T. Chen, S. Kim, S.R. Cohen, E. Wachtel, N. Yavo, I. Lubomirsky, Influence of Gd content on the room temperature mechanical properties of Gd-doped ceria, *Scr. Mater.* 66 (2012) 155–158.
- [20] R. Korobko, S.K. Kim, S. Kim, S.R. Cohen, E. Wachtel, I. Lubomirsky, The role of point defects in the mechanical behavior of doped ceria probed by nanoindentation, *Adv. Funct. Mater.* 23 (2013) 6076–6081.
- [21] M. Varenik, S. Cohen, E. Wachtel, A.I. Frenkel, J.C. Nino, I. Lubomirsky, Oxygen vacancy ordering and viscoelastic mechanical properties of doped ceria ceramics, *Scr. Mater.* 163 (2019) 19–23.